Technische Universität München

TUM School of Natural Sciences

Consequences of lattice dimensionality in solid state magnetism

An investigation using high resolution neutron scattering and magnetometry

Lukas Beddrich

Vollständiger Abdruck der von der TUM School of Natural Sciences der Technischen Universität München zur Erlangung eines

Doktors der Naturwissenschaften (Dr. rer. nat.)

genehmigten Dissertation.

Vorsitz:		Prof.	Dr.	Frank Pollmann
Prüfer*innen der Dissertation:				
	1.	Prof.	Dr.	Peter Böni
	2. apl.	Prof.	Dr.	Rudolf Hackl

Die Dissertation wurde am 30.01.2023. bei der Technischen Universität München eingereicht und durch die TUM School of Natural Sciences am 16.02.2023. angenommen.

Abstract

Magnetism in solid matter affects the macroscopic world, even though it is inherently a quantum phenomenon. At first glace, interest in quantum magnetism seems to be purely academic, however, it enables transformative technologies such as digital memory storage or electronic sensor devices. One of the most fundamental and influential parameters of any magnetic system is the dimensionality of its exchange interactions as it determines the stability of magnetic order and its fluctuations.

In this work, two magnetic materials, which are nickel (Ni) and $Cu(C_4H_4N_2)_2(H_2O)_2Cr_2O_7$ (Cu-pyz), of different dimensionality have been investigated to further the understanding of their microscopic interactions and the resulting magnetic properties. Nickel, one of the archetypical, room temperature ferromagnets is known to behave as predicted for a 3D isotropic Heisenberg system, but ought to exhibit dipolar behavior in the vicinity of the Curie temperature T_C.

High resolution neutron spectroscopy was employed to investigate the critical dynamics and the signature of dipolar coupling at the smallest wavevector transfer q and energy transfer ΔE studied to date. Even though the measure of strength of the dipolar interaction, the dipolar wavevector q_D, was found to be a factor of 2 smaller than previously reported, extensive modeling confirmed its necessity to explain the observed spin wave dispersion. At the same time, the dynamical scaling behavior of the linewidth of the paramagnetic fluctuations adhered to the purely isotropic Heisenberg model, which is consistent with mode-coupling calculations of Résibois & Piette. This apparent discrepancy with the observation of a signature of dipolar coupling in the spin wave dispersion is resolved by an extension of the mode-coupling equations considering anisotropic dipolar interactions. According to Frey and Schwabl, dipolar contributions enter the dynamical scaling function of the transversal fluctuations only if $q \lesssim q_D/10$, which was not accessible in this measurement.

Inelastic neutron scattering at the three-axis spectrometer IN12, played an integral role in validating the antiferromagnetic 2D Heisenberg model proposed for the metal-organic hybrid system $Cu(C_4H_4N_2)_2(H_2O)_2Cr_2O_7$. Previous susceptibility measurements performed with a 9 T physical property measurement system (PPMS) strongly suggested the 2D nature of the exchange coupling and set the energy scale of the in-plane exchange constant to $J_{2D} = 0.5\,\text{meV}$. Similarly, magnetization curves confirm this notion through their upward bending, characteristic shape at 2 K. The negligible out-of-plane coupling compared to the strong in-plane coupling is plausible due to the excellent separation of magnetically active copper ions along the a axis. Evaluation of the spin wave dispersion in the bc-plane tied together these results establishing Cu-pyz as a 2D quantum Heisenberg antiferromagnet. These results lay the foundation for future studies under high pressure, which allows tuning of the dimensionality of the Cu-pyz system.

Zusammenfassung

Magnetismus in Festkörpern ist ein makroskopisches Phänomen, dessen Ursprung jedoch nur auf Basis quantenmechanischen Eigenschaften auf atomarer Ebene erklärbar ist. Obwohl dies von rein akademischem Interesse zu sein scheint, dient Magnetismus als Basis for mannigfaltige, moderne Technologie, wie beispielsweise Festplatten und Sensorik. Einer der elementarsten Parameter eines magnetischen Systems ist die Dimensionalität seiner Austauschwechselwirkung, welche maßgeblich die Stabilität der magnetischen Struktur und deren Fluktuationen beeinflusst. In dieser Arbeit wurden zwei magnetische Systeme mit unterschiedlicher Dimensionalität der interatomaren Wechselwirkungen untersucht um deren Einfluss auf die resultierenden, magnetischen Eigenschaften zu verstehen.

Nickel, einer der archetypischen Raumtemperaturferromagneten, lässt sich mithilfe des 3D isotropen Heisenberg Models beschreiben, wobei Nickel in der Nähe der Curie-Temperatur T_C dipolares Verhalten zeigen sollte. Hochauflösende Neutronenspektroskopie wurde eingesetzt, um die kritische Dynamik und die Signatur der dipolaren Kopplung bei den kleinsten bisher untersuchten Wellenvektorüberträgen q und Energieüberträgen ΔE zu messen. Der dipolare Wellenvektor q_D, welcher die Stärke der dipolaren Wechselwirkung parameterisiert, konnte im Experiment bestimmt werden. Der dabei erhaltene Wert ist um einen Faktor 2 kleiner als der bisher in der Literatur publizierte Wert, jedoch bestätigte eine umfassende Modellierung seine Notwendigkeit, um die beobachtete Spinwellendispersion zu erklären.

Im Gegensatz dazu stimmt das dynamische Skalierungsverhalten der Linienbreite der paramagnetischen Fluktuationen mit den Lösungen der Modenkopplungsgleichungen von Résibois & Piette überein, welche auf Basis des rein isotropen Heisenberg-Modells berechnet werden. Diese scheinbare Diskrepanz mit der Beobachtung einer Signatur der dipolaren Kopplung in der Spinwellendispersion wird durch eine Erweiterung der Modenkopplungsgleichungen unter Berücksichtigung anisotroper dipolarer Wechselwirkungen gelöst. Nach Frey und Schwabel gehen dipolare Beiträge nur dann in die dynamische Skalierungsfunktion der transversalen Fluktuationen ein, wenn $q \lesssim q_\mathrm{D}/10$. Dieser Messbereich war im Rahmen des durchgeführten Experiments nicht zugänglich.

Inelastische Neutronenstreuung am kalten Dreiachsenspektrometer IN12 spielte eine wesentliche Rolle bei der Validierung des vorgeschlagenen antiferromagnetischen 2D-Heisenberg-Modells für das metallorganische Hybridsystem $Cu(C_4H_4N_2)_2(H_2O)_2Cr_2O_7$ (Cu-pyz). Vorangegangene Suszeptibilitätsmessungen, die mit einem 9 T 'Physical Property Measurement System' (PPMS) durchgeführt wurden, deuten stark auf die 2D-Natur der Austauschkopplung hin und legten die Energieskala der Austauschkonstante in der Ebene auf $J_\mathrm{2D} = 0.5\,\mathrm{meV}$ fest. Zusätzlich bestätigen die Magnetisierungskurven diese Vermutung durch ihre charakteristische, positiv gekrümmte Form bei 2 K. Die Auswertung der Spinwellendispersion in der *bc*-Ebene vereint diese Ergebnisse, die Cu-pyz eindeutig als 2D-Quanten-Heisenberg-Antiferromagneten identifizieren.

für Reini

Acknowledgment

First and foremost, my gratitude goes to my PhD supervisor Peter Böni. You have been unbelievably supportive towards any project I conjured up in the past few years and let me pursue my own interests. Even though the pandemic made personal meetings difficult for quite some time, your openness to take video calls at any time, was integral to pull me onto the right path in case I got lost in the swamp that is data analysis. Your stories of programming triple-axis resolution calculations on punch cards made me appreciate the convenience of modern computing. Nevertheless, your tips and tricks on experiment planning and data reduction have been more valuable than any supercomputer. I very much enjoyed the work we did and the discussions we had for the nickel project, which I hope to continue in some form.

My Family

More than anyone else, I want to thank my family, who are fundamentally responsible for me writing these lines. From the beginning, my parents always conveyed to me the importance of and the freedom granted by education, without ever imposing constraints or setting expectations. I was free to choose and supposed to find my own way. I can gladly say: 'I did!'

Mum und Reini, ihr habt mich immer unterstützt auf meinem Weg hierher. Mit den Freiheiten, die ihr mir gelassen habt, habe ich meine Berufung gefunden. Ihr hattet immer ein offenes Ohr für mich, unabhängig davon, ob ich mit Verzweiflung oder Begeisterung von meiner Arbeit berichtet habe. Euer Glauben an mich und meine Fähigkeiten hat mich auch in den schwersten Zeiten bestärkt durchzuhalten und soweit zu kommen. Ich kann euch nie genug dafür danken!

Jonas, auch wenn du der 'kleine' Bruder bist, werde ich wohl immer zu dir aufschauen. Du warst mir nicht nur der beste Mitbewohner, den man sich für eine Pandemie wünschen kann, du hast mir immer geholfen vor lauter Arbeit nicht dem Wahnsinn zu verfallen. Vor allem unsere ausladenenden Gespräche, in denen wir versuchen dem jeweils anderen zu erklären woran wir im Moment herumdoktoren, sind für mich unersetzlich. Ich danke dir so sehr für deine Unterstützung.

Experiment Teams

Science is a team effort, a fact, which can not be stressed enough. It could not be more true for the work presented here, as well. This is why, I want to thank all my colleagues and collaborators, who helped me over the past four and a half years conducting my research.

MIRA

In particular, I want to thank my colleagues in the MIRA instrument group. My office buddy Christoph Herb has probably suffered through and endured the most hours of nighttime experiments with me. Even though nothing works as expected, you were a reliable partner and full of ideas to get the job done, against all odds. Discussions with you are always fun, sometimes absurd and still fruitful.

Without any doubt, Henrik Gabold has been the social dark matter and center of gravity of the PhD candidates at MIRA. Rightfully so, since his willingness to support his colleagues with his expertise and practical skills is unmatched. On top of that, he managed to break through our solitary attitude creating a relaxing work atmosphere, which is best represented by the daily coffee break in his office. I want to thank you for being open for any scientific discussion, for your great effort to proofread my thesis, and for the many helpful comments.

Also many thanks go to Alexander Book, who has shared his mathematical prowess to help me with the intricate analysis of the nickel data. Deeply appreciated is your enthusiasm to torture your X-ray diffractometer with tedious single crystal orientation measurements, whenever the X-ray Laue is not operational. Similarly, I want to thank Ran Tang, for being a dependable supporter and humorous conference attendee. I look forward to our discussions about 2D magnetism, whenever you decide to write up your thesis. It will be fun. Last but certainly not least, I thank Maryna Kovalchuk, my former working student, who has entertained us more than anyone with crazy everyday life stories. I guess student life has become even more adventurous now. Your help with all the weird simulation and technical drawing tasks is highly valued. Maybe we get to shoot neutrons at this treacherous pressure cell at some point.

Especially, I am indebted to the senior members of the MIRA team Robert Georgii, Markos Skoulatos and Jonathan Frank. Robert, I thank you for your continued support and supervision of my PhD work and your valuable feedback for writing my thesis. Your insight into experimental pitfalls, help with instrument operation and your pinch of optimism were decisive for maintaining my sanity during beam times. Markos, without your proposal to look at these greenish crystals, I would never have been introduced to the wondrous world of 2D magnetism. Frankly, my thesis would miss a chapter and a topic, which I have found a lot of interest in. I hope we can continue to unravel the mysteries of Cu-pyz, as I enjoy our collaboration on neutron experiments and the promising work at the new DynaCool. Thanks for guiding me through this exciting project and reading all the pages I wrote about it. The one person, without whom every experiment is doomed, is Jonathan. Your expertise of MIRA made the experiments possible, since I, a freshly baked PhD student was ill-equipped to handle this myself. Thanks for always being ready to help out, even though I sometimes called at ungodly hours.

RESEDA

Many thanks go to the colleagues at RESEDA, Johanna Jochum, Christian Franz, Steffen Säubert, Christian Fuchs and Milan Antic, who enabled me to measure the critical fluctuations in nickel at RESEDA. Not only is this instrument a sexy fever dream gone

nuclear, you made the experiment look easy. Even though it took several years and many iterations to get the data analysis right, you were always eager to discuss the current status and support my efforts for such a long time. Now, I am very happy to have joined the team and work with you.

IN12

For the great support regarding the neutron scattering experiments on Cu-pyz performed at the cold three-axes spectrometer IN12 (ILL), I want to thank Karin Schmalzl. In the midst of the COVID-19 pandemic, Karin enabled us to measure such a delicate system in a complex sample environment from the safety of our homes. Without having been present in France, I can only commonly thank the supporting staff, who contributed to the success of this measurement.

The FRM II and Physics department community

Finally, I want to thank the many colleagues at the FRM II and the Physics Department at TUM. The readiness to help is a common denominator of the ANTARES instrument group, the sample environment group at the FRM II and the colleagues from E21 and E51, which I appreciate very much.

Contents

List of Abbreviations

AFM	antiferromagnet(ic)
ARG	asymptotic renormalization group (theory)
BZ	Brillouin zone
Cu-pyz	$Cu(C_4H_4N_2)_2(H_2O)_2Cr_2O_7$
DB	direct beam
DCS	differential cross section
DDCS	double differential cross section
DSF	dynamical scaling function
DST	dynamical scaling theory
E51	Chair for the Topology of Correlated Systems
FRM II	Research neutron source Heinz Maier-Leibnitz
ILL	Institute Laue-Langevin
(I)NS	(inelastic) neutron scattering
LF	laboratory frame
LRO	long range order
MC	mode-coupling (theory)
MIEZE	modulation of intensity with zero effort
MLZ	Heinz Maier-Leibnitz Zentrum
MOC	metal-organic compound
NRSE	neutron resonance spin echo

PG	pyrolitic graphite
PPMS	physical property measurement system
PSD	position sensitive detector
QCP	quantum critical point
(QE)NS	(quasi-elastic) neutron scattering
2D QHAF	two-dimensional quantum Heisenberg antiferromagnet
RESEDA	NRSE & MIEZE spectrometer at FRM II
ROI	region of interest
RS	reciprocal space
SANS	small angle neutron scattering (instrument)
SN	signal to noise ratio
SRO	short range order
TA(S)	triple-axis (spectrometer/spectroscopy)
VCM	vibrating coil magnetometer
VSM	vibrating sample magnetometer
pyz	pyrazine ($C_4H_4N_2$)
rlu	reciprocal lattice units

1. Introduction

Magnetism in solid materials is by nature a phenomenon involving many interacting particles on the microscopic scale. Therefore, it is not surprising that classical theories like the *mean field theory* only manage to reproduce experimental results in the crudest approximation, often far from quantitative agreement. Even more though, a rigorous proof, led by van Leeuwen [1, 2], shows unmistakably that a classical theory is unable to account for solid state magnetism, but requires an entirely new physical framework on the microscopic scale.

A remarkably successful model put forward by W. Heisenberg, hence bearing his name, considers magnetic ions on different lattice sites and their microscopic, pairwise interaction. Treating the spins as quantum mechanical operators the Hamiltonian of the *Heisenberg model* reads

$$\mathscr{H} = -\sum_{i,j} J_{ij}\ \boldsymbol{S}_i \cdot \boldsymbol{S}_j\ . \tag{1.1}$$

Here, $\boldsymbol{S}_i$ is the spin operator located on lattice site i, J_{ij} is the exchange constant determining the preferred alignment of coupled spins. Although one may worry whether the Heisenberg model is an oversimplification of reality, it has proven to reasonably describe many magnetic properties in systems with localized magnetic moments and itinerant systems alike [3].

Going beyond the isotropic Heisenberg Hamiltonian, a plethora of lattice models emerge from changing the type of coupling (nearest-neighbor, next-nearest-neighbor, anisotropy), spin-dimensionality ($n = 1, 2, 3$), spin value ($S = \frac{1}{2}, 1, \frac{3}{2}, \ldots$) or the lattice-dimensionality ($d = 1, 2, 3$). In case of a two-dimensional (2D) lattice model, the sum over i, j only runs over positions of spins in a single plane. A graphical representation of models of differing lattice dimensions is depicted in figure 1.1, where the colored lines indicate the exchange coupling J_{ij} of neighboring spins within the crystal. Evidently, (a) shows the standard Heisenberg model with nearest neighbor coupling in three dimensions, (b) a planar and (c) a 1D spin-chain model.

Studying the influence of dimensionality on magnetic systems has shown that features of the thermodynamic quantities and parameters vary drastically. Exemplarily, the 3D and 2D Heisenberg models are known to harbor an ordering phase transition, even though in the 2D case it is theoretically located at $T = 0\,\mathrm{K}$ [4], whereas the 1D spin-chain model never achieves magnetic long-range order (LRO). This is owed to the enhancement of fluctuations and short-range order effects, which leave their mark most prominently in the 'high-temperature tail' of thermodynamic quantities just above the transition temperature and has been verified by theoretical calculations [5, 6] and experiments alike. Intriguing examples of real world materials well described by the 3D, 2D and 1D Heisenberg models are $RbMnF_3$ [7–10], $CuF_2(H_2O)_2(pyz)$ [11, 12] and $Cu(NH_3)_4SO_4$

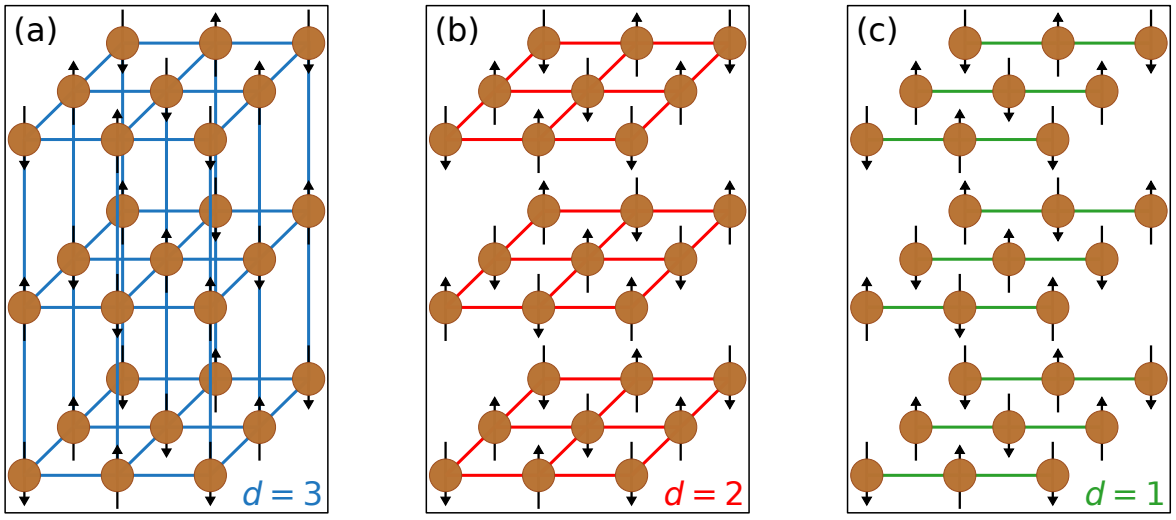

Figure 1.1.: Schematic visualization of the isotropic Heisenberg model in 3D, 2D and 1D for an antiferromagnetic system. The connecting lines represent the exchange pathways for the coupling J_{ij}. In (b), (c) the planes or chains are isolated from each other. A major challenge for experimental studies is the identification and preparation of suitable model systems.

[13, 14] or $KCuF_3$ [15, 16], respectively. Among those $CuF_2(H_2O)_2(pyz)$ is especially fascinating as it exhibits a dimensionality change from a planar Heisenberg to a 1D spin chain system under hydrostatic pressure. Naturally, the examples given above are anything but an extensive list, whereas the review on low-dimensional magnetism by de Jongh provides an in-depth resource on this matter and is highly recommended [3] for reading. As a result, interest in low-dimensional magnetic materials is diverse. They serve as proofing ground for scaling theory predictions [8, 17], new territory for novel non-classical ground states and magnetic phenomena [18–20], systems with an intricate connection to high temperature superconductivity [21–25] or candidates for technical application in sensor and spintronic devices [26, 27].

The projects of this thesis pick up the topic of dimensionality in magnetism from a fundamental research perspective. On the one hand, we concern ourselves with nickel (Ni), one of the three known ferromagnets exhibiting its properties in elemental form at room temperature. The reported magnetic dynamics of Ni at small momentum transfers are well described by the 3D isotropic Heisenberg model, even though it is an itinerant system. Close to T_C, critical exponents derived from the Heisenberg Hamiltonian should govern the dynamical scaling behavior in Ni. The study of related systems has shown that the pure Heisenberg behavior is altered by long range, anisotropic dipolar forces, which ought to be present in Ni, however, to a much more subtle degree. High resolution, inelastic neutron scattering experiments have been carried out to investigate the influence of dipolar coupling on spin waves and critical fluctuations.

On the other hand, the metal-organic compound $Cu(C_4H_4N_2)_2(H_2O)_2Cr_2O_7$ (Cu-pyz) was mentioned to be a potential 2D quantum Heisenberg antiferromagnet (2D QHAF) by Goddard *et al.* [28] based on its structural resemblance to other 2D organic hybrid systems. Using magnetic bulk measurements and inelastic neutron scattering, we aimed to clarify the magnetic properties of this spin-$\frac{1}{2}$ system and build a Hamiltonian as a

baseline model. This provides the necessary understanding for future investigations on superconductivity and pressure induced dimensionality change.

The performed investigations relied heavily on neutron scattering techniques, which are often the sole direct probe of magnetism on the atomic scale. As aptly phrased by Lowde in the concluding remarks of his comprehensive study on nickel:

> 'Our final conclusion, therefore, must be that neutron inelastic scattering techniques offer the means of probing quite deeply into the behavior of the electron gas; it is much to be hoped that the possibilities thereby opened up will lead to new insights in the difficult field.' [29]

This unique suitability is owed to the magnetic moment of the neutrons interacting directly with the magnetism inducing electrons. Subsequently, the static and dynamic correlation of these electrons determine the measured neutron scattering cross section, which allows reconstruction of the magnetic properties of a sample from the observed intensity signal. As mentioned before, for this work, the properties of interest encompass the spin wave dispersion relation in a low-dimensional antiferromagnet or the linewidth of critical fluctuations of an isotropic Heisenberg system.

Outline of this thesis

The manuscript is structured as follows. Due to its outstanding importance, chapter 2 is dedicated to elucidate the basic principles of neutron scattering. Given the sensitivity of neutrons to nuclear and magnetic potentials, we introduce the thereof derived double differential cross section and discuss the scattering expected from single crystalline magnetic matter. Furthermore, the susceptibility of neutrons to magnetic fields in free space and the resulting propagation of its spin states is presented in terms of the spinor formulation. The latter plays a major role in understanding the MIEZE technique, a high resolution neutron spectrometry method based on radio frequency spin manipulation, which is one of the two neutron scattering techniques utilized for the study of critical, magnetic fluctuations in the ferromagnet nickel. Together with three-axis spectrometry, the second neutron scattering method, MIEZE is explained in detail in chapter 3. This includes the measurement principle, the modes of operation of both techniques and the introduction of both instruments RESEDA and IN12, where the measurements have been performed. In addition, the final part of chapter 3 is concerned with the measurement of magnetic bulk properties as these techniques played an integral part of investigating the characteristics of the metal-organic spin-$\frac{1}{2}$ compound Cu-pyz. Chapter 4 is dedicated to the dynamical behavior of magnetism in the archetypal ferromagnet nickel. We address the collective spin wave excitations below T_C and the critical fluctuations at $T = T_\mathrm{C}$ and above, in the attempt to elicit a behavior consistent with the notion of the previously immeasurably small dipolar interaction. In chapter 5, we establish Cu-pyz to be a pristine example of a two-dimensional quantum Heisenberg antiferromagnet based on susceptibility, magnetization and complementary inelastic neutron scattering measurements.

2. The physics of neutron scattering - Unraveling solid state magnetism

In solid state physics, neutron scattering has been established as an invaluable method to probe matter on the microscopic scale. Due to its lack of electrical charge, a free neutron interacts with surrounding matter only via the strong nuclear force or magnetic fields coupled to its magnetic moment. This sensitivity to magnetic potentials makes neutron scattering a unique tool for the study of static magnetic order, magnetic interactions and the resulting dynamics. Measurements can be understood in terms of the microscopic spin-spin correlation function and the macroscopic generalized magnetic susceptibility, which reflect the magnetic properties of a system. This chapter intends to elucidate the mathematical description of neutron scattering and illustrate the signal expected from magnetic systems.

2.1. Neutrons interacting with matter

The properties and phenomena exhibited by solid materials are tightly connected to their microscopic arrangement of atoms and interaction between them. To understand the neutron scattering pattern produced by the microscopic structure a whole, knowledge of the interaction potential between neutrons and the constituent atoms is indispensable.

Starting with the discovery of the neutron itself, Chadwick *et al.* used the scattering of an unknown form of radiation, now known as a neutron, from hydrogen atoms to determine its properties [30, 31]. Nuclear scattering, which is mediated by the strong nuclear force, is in this case mathematically described in the form of the *Fermi pseudopotential*

$$V_{\mathrm{nuc}} = \frac{2\pi\hbar^2}{m_{\mathrm{n}}}\, b\, \delta\left(\mathbf{r}\right). \tag{2.1}$$

Here, b is the *scattering length* of the scattering nuclei and $\delta\left(\mathbf{r}\right)$ the three-dimensional Dirac delta distribution, which models the short range interaction of neutrons and the atomic nuclei. There is, as mentioned above, a magnetic potential created by the spin and angular momentum of the electrons inside any material, but as a starting point, the following discussion is limited to nuclear scattering.

Numerous authors, Lovesey [32], Squires [33], Sivia [34] and Shirane [35] to name a few, have written extensive literature on the theory of neutron scattering whose insights will be summarized in the following sections.

2.1.1. Fundamental scattering theory

In the field of physics, the expression *scattering* describes a wide variety of processes, which make a moving wave or particle deviate from its unperturbed trajectory through the medium of propagation . Scattering is caused by local inhomogeneities in the medium or free particles in the volume traversed by the radiation. Given by the fundamental conservation laws, in the scattering process the total momentum and total energy of the system remains constant, while the quantities of each individual partner is subject to change.

In the case of neutron scattering three quantities, namely the momentum $\boldsymbol{p} = \hbar\boldsymbol{k}$, the energy $E = \hbar\omega = \hbar^2\boldsymbol{k}^2/2m_\mathrm{n}$ and the spin $\boldsymbol{\sigma}$ fully determine the state of the neutron probe. Knowledge about the initial state of the neutron and gaining knowledge of the final state through a measurement, allows the reconstruction of the scattering process and the interaction potentials involved therein.

The basic quantity for the description of any scattering is the double differential cross section

$$\frac{\mathrm{d}^2\sigma}{\mathrm{d}\Omega\ \mathrm{d}E_\mathrm{f}} = \frac{\begin{array}{c}\#\text{neutrons per second scattered into solid angle } \mathrm{d}\Omega \text{ in the} \\ \text{direction } \theta,\ \phi \text{ with final energy between } E_\mathrm{f} \text{ and } E_\mathrm{f} + \mathrm{d}E_\mathrm{f}\end{array}}{\Phi\ \mathrm{d}\Omega\ \mathrm{d}E_\mathrm{f}}, \tag{2.2}$$

which describes the frequency of the incoming neutrons with $|\boldsymbol{k}_\mathrm{i}\,\boldsymbol{\sigma}_\mathrm{i}\rangle$ being scattered into a final state $|\boldsymbol{k}_\mathrm{f}\,\boldsymbol{\sigma}_\mathrm{f}\rangle$. This implies the change of a neutron's momentum and energy, where we use the convention 'initial minus final', meaning

$$\hbar\boldsymbol{Q} = \hbar\boldsymbol{k}_\mathrm{i} - \hbar\boldsymbol{k}_\mathrm{f} \qquad \text{and} \qquad \Delta E = \frac{\hbar^2}{2m_\mathrm{n}}\left(\boldsymbol{k}_\mathrm{i}^2 - \boldsymbol{k}_\mathrm{f}^2\right). \tag{2.3}$$

A graphical representation of such a scattering process, confined to two dimensions, is depicted in Fig. 2.1. An incoming neutron from the left side might be scattered under an angle 2θ into a solid angle $\mathrm{d}\Omega$ element and a width $\mathrm{d}\boldsymbol{k}_\mathrm{f}$.

Therefore, understanding the double differential cross section (DDCS) is integral to the interpretation of any neutron scattering experiment. For low energy neutrons, small samples and the absence of nuclear resonances, the DDCS can be derived using *Fermi's golden rule* [33] or by introducing the *scattering amplitude* $f\,(\lambda, \theta)$ in a general scattering theory formalism [34]. Independent of the approach, we arrive at a mathematical expression for the DDCS, for the purpose of further discussion is taken from Squires [33]:

$$\frac{\mathrm{d}^2\sigma}{\mathrm{d}\Omega\ \mathrm{d}E_\mathrm{f}} = \frac{k_\mathrm{f}}{k_\mathrm{i}}\left(\frac{m_\mathrm{n}}{2\pi\hbar^2}\right)^2 \left|\langle\boldsymbol{k}_\mathrm{f}\,\boldsymbol{\sigma}_\mathrm{f}, \Psi_\mathrm{f}|\, V\, |\boldsymbol{k}_\mathrm{i}\,\boldsymbol{\sigma}_\mathrm{i}, \Psi_\mathrm{i}\rangle\right|^2 \delta\left(E_{\Psi_\mathrm{i}} - E_{\Psi_\mathrm{f}} + E_\mathrm{i} - E_\mathrm{f}\right). \tag{2.4}$$

This equation expresses the dependence of the DDCS on the combined initial state of the neutron and the scattering system, $|\boldsymbol{k}_\mathrm{i}\,\boldsymbol{\sigma}_\mathrm{i}, \Psi_\mathrm{i}\rangle$, interacting via a potential V that leaves the the total system in a state $|\boldsymbol{k}_\mathrm{f}\,\boldsymbol{\sigma}_\mathrm{f}, \Psi_\mathrm{f}\rangle$. The term in $|...|^2$ is called the matrix element, a well known concept in quantum mechanics, in which the wave function of the scattering system is denoted by Ψ. Finally, the Dirac delta distribution enforces energy

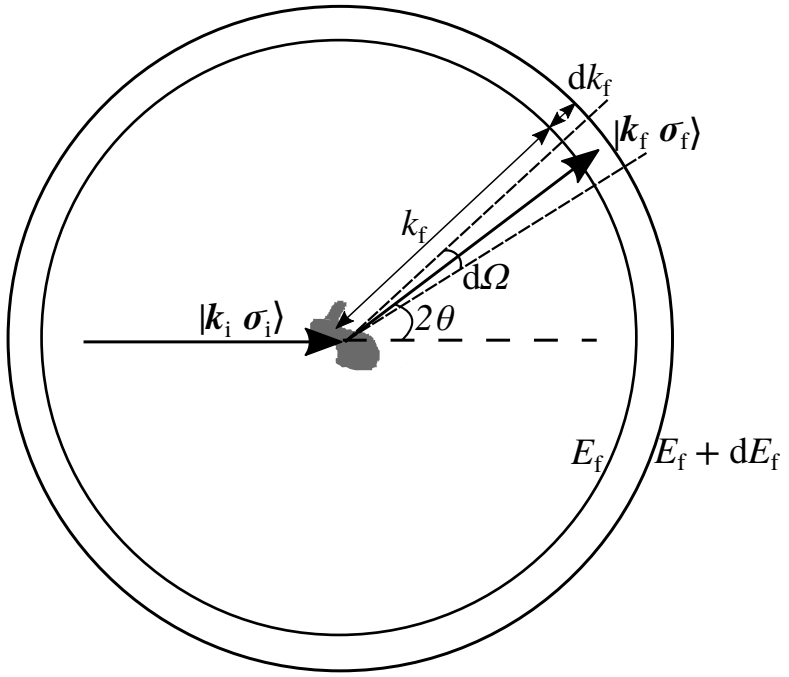

Figure 2.1.: Visualization of a general scattering geometry and definition of the double differential cross section. Incoming neutrons $|\boldsymbol{k}_\mathrm{i}\,\boldsymbol{\sigma}_\mathrm{i}\rangle$, whose states are completely described by wavevector $\boldsymbol{k}$ and spin $\boldsymbol{\sigma}$, interact with the sample represented by the gray area in the center. The double differential cross section expresses the frequency of these neutrons to scatter under the angle 2θ into a solid angle segment $\mathrm{d}\Omega$ and a wavevector interval $[\boldsymbol{k}_\mathrm{f}, \boldsymbol{k}_\mathrm{f} + \mathrm{d}\boldsymbol{k}_\mathrm{f}]$. Here we omit a possible azimuthal angle ϕ dependency. Adopted from [36].

conservation in the scattering process and gives us immediately an expression for the differential cross section (DCS)

$$\left(\frac{\mathrm{d}\sigma}{\mathrm{d}\Omega}\right) = \int_0^\infty \left(\frac{\mathrm{d}^2\sigma}{\mathrm{d}\Omega\ \mathrm{d}E_\mathrm{f}}\right) \mathrm{d}E_\mathrm{f} \tag{2.5}$$

applicable for experiments integrating over all energy transfers.

Equation 2.4 is the corner stone for any theoretical treatment of a physical system, such as a single atom or more practically a crystal of 10×10^{23} atoms with possibly magnetic ions inside. In subsequent sections, we consider a few systems that are relevant for instructive purposes and data analysis in later chapters, to calculate the expected neutron scattering signal.

2.1.2. Elastic neutron scattering

One of the descriptive examples, which is invaluable for crystal structure analysis, is nuclear scattering from a periodic arrangement of atoms inside a sample. Starting from the general equation for the DCS 2.5 it can be shown that the matrix element can be rewritten in terms of the Fourier transform of the real space potential. This further requires the assumption of plane wave like neutron wave functions and the

scattering potential's independence on the neutron's energy and spin state. Expressing the scattering system as

$$V = \sum_j V_j \left(\boldsymbol{r} - \boldsymbol{R_j} \right) \tag{2.6}$$

where $V_j \left(\boldsymbol{r} - \boldsymbol{R}_j \right)$ is the jth atom's potential located at position $\boldsymbol{R}_j$ and interacting with the neutron at position $\boldsymbol{r}$, we get

$$\langle \boldsymbol{k}_\mathrm{f}, \Psi_\mathrm{f} | \, V \, | \boldsymbol{k}_\mathrm{i}, \Psi_\mathrm{i} \rangle = \sum_j V_j \left(\boldsymbol{Q} \right) \langle \Psi_\mathrm{f} | \exp \left(i \boldsymbol{Q} \boldsymbol{R}_j \right) | \Psi_\mathrm{i} \rangle \, . \tag{2.7}$$

As indicated beforehand, the Fourier transformed potential function $\sum_j V_j \left(\boldsymbol{Q} \right)$ can be extracted from the matrix element and in combination with the assumption of a Dirac delta interaction potential, as motivated in equation 2.1, yields a simple constant:

$$V_j \left(\boldsymbol{Q} \right) = \int V_j \left(\boldsymbol{x}_j \right) \exp \left(i \boldsymbol{Q} \boldsymbol{x}_j \right) \mathrm{d}\boldsymbol{x}_j \quad \xrightarrow{V_j(\boldsymbol{x}_j) = \frac{2\pi\hbar^2}{m_\mathrm{n}} b_j \delta(\boldsymbol{x} - \boldsymbol{x}_j)} \quad V_j \left(\boldsymbol{Q} \right) = \frac{2\pi\hbar^2}{m_\mathrm{n}} \, b_j \tag{2.8}$$

So far, the DDCS described the transition two specific state of the system, which represents a very unlikely scenario for a real life experiment. As final steps to gain an expression for the *measured* DDCS the δ distribution in equation 2.4 needs to be replaced by its equivalent integral form, the scattering potential is rewritten as shown in equation 2.7 and we need to sum over all possible final wave functions $|\Psi_\mathrm{f}\rangle$ as well as average over all initial states $|\Psi_\mathrm{i}\rangle$ of the scattering system. It is reasonable to expect the initial states to be distributed according to Boltzmann. This leads to

$$\frac{\mathrm{d}^2\sigma}{\mathrm{d}\Omega \, \mathrm{d}E_\mathrm{f}} = \frac{k_\mathrm{f}}{k_\mathrm{i}} \frac{1}{2\pi\hbar} \sum_{jj'} b_j b_{j'} \int_{-\infty}^{\infty} \langle \exp \left(-i \boldsymbol{Q} \boldsymbol{R}_{j'}(0) \right) \exp \left(i \boldsymbol{Q} \boldsymbol{R}_j(t) \right) \rangle \cdot \exp \left(-i\omega t \right) \mathrm{d}t, \tag{2.9}$$

describing the entirety of neutron scattering processes from an assembly of atomic nuclei. The sum over j, j' run over all atoms with their generally time dependent position operator $\boldsymbol{R}_j(t)$. Using a standard representation, introduced by Van Hove [37], we absorb the thermal average $\langle ... \rangle$ into the *dynamical scattering function*

$$S(\boldsymbol{Q}, \omega) = \frac{1}{2\pi\hbar N} \sum_{jj'} b_j b_{j'} \int_{-\infty}^{\infty} \langle \exp \left(-i \boldsymbol{Q} \boldsymbol{R}_{j'}(0) \right) \exp \left(i \boldsymbol{Q} \boldsymbol{R}_j(t) \right) \rangle \cdot \exp \left(-i\omega t \right) \mathrm{d}t, \tag{2.10}$$

also known as *dynamical structure factor*.

It is notable, that some calculation steps made use of the simplicity of the nuclear scattering potential, which is why other scattering phenomena, such as magnetic neutron scattering, need a deeper look at the interaction mechanism and subsequently lead to more complicated expressions. These aspects will be discussed in the upcoming subsection 2.1.3 with emphasize on inelastic scattering, a method which has been extensively used in the research presented in this thesis.

A more detailed account of the mathematics required to arrive at equation 2.9 can

be found in Squires's book [33] from which this overview has been derived and we recommend a deeper look into the thorough literature [32, 34, 35] on neutron scattering.

2.1.3. Inelastic magnetic neutron scattering

Having explained the general approach to understanding neutron scattering by the means of the DDCS, it is straightforward to realize the potential of elastic neutron scattering for the determination of the microscopic structure of solid materials. In this subsection, two extensions to the concept of neutron scattering will be made. First, the interaction potential for magnetic neutron scattering will be introduced and used to evaluate the matrix elements in this context. Secondly, the DDCS for coherent scattering from collective magnetic excitations, spin waves, will be motivated. Especially the last part is important for understanding the conclusions drawn from the inelastic neutron scattering measurements performed on a low-dimensional magnetic system.

Magnetic scattering cross section

As mentioned in the first paragraph, the neutron, being a Fermion, possesses a spin and an associated magnetic moment

$$\boldsymbol{\mu}_\mathrm{n} = -\gamma \mu_\mathrm{N} \boldsymbol{\sigma} \tag{2.11}$$

where

$$\mu_\mathrm{N} = \frac{e\hbar}{2m_\mathrm{p}} \tag{2.12}$$

is the nuclear magneton, m_p is the proton's mass, e the elementary charge, $\gamma = 1.913$ a constant value and $\boldsymbol{\sigma}$ the Pauli spin operator. In the presence of a magnetic field $\boldsymbol{B}$, the neutron is subjected to a potential

$$V_\mathrm{mag} = -\boldsymbol{\mu}_\mathrm{n} \cdot \boldsymbol{B} \tag{2.13}$$

as any classical magnetic dipole. Generally, the field can be external, produced by powerful magnets, which has applications in sample environment or specialized instrumentation or the field can be internal as created by the spin and angular momentum of unpaired electrons in a sample.

For the last case the magnetic potential in a sample with unpaired electrons has the aforementioned contributions such that the field can be written as

$$\boldsymbol{B} = \boldsymbol{B}_\mathrm{S} + \boldsymbol{B}_\mathrm{L} = \frac{\mu_0}{4\pi} \left[\underbrace{\nabla \times \left(\frac{\boldsymbol{\mu}_\mathrm{e} \times \boldsymbol{R}}{R^3} \right)}_{\text{spin contribution}} - \underbrace{\frac{2\mu_\mathrm{B}}{\hbar} \frac{\boldsymbol{p} \times \boldsymbol{R}}{R^3}}_{\text{ang. mom. contribution}} \right]. \tag{2.14}$$

In the formula, $\boldsymbol{\mu}_\mathrm{e} = 2\mu_B \boldsymbol{s}$ is an electron's magnetic spin moment, $\boldsymbol{p}$ is the electron's

momentum and $\boldsymbol{R}$ is the position at which the field is determined.

In a similar fashion to nuclear scattering, the magnetic potential assembled from equations 2.13 and 2.14 is put into the general expression for the DDCS 2.4 and can be processed using planar wave ansatz for the neutron's wave function. The DDCS now reads

$$\frac{\mathrm{d}^2\sigma}{\mathrm{d}\Omega\ \mathrm{d}E_\mathrm{f}} = (\gamma r_0)^2 \frac{k_\mathrm{f}}{k_\mathrm{i}} \left|\langle \boldsymbol{\sigma}_\mathrm{f}, \Psi_\mathrm{f}| \, \boldsymbol{\sigma} \cdot \boldsymbol{S}_\perp \, |\boldsymbol{\sigma}_\mathrm{i}, \Psi_\mathrm{i}\rangle\right|^2 \delta\left(E_{\Psi_\mathrm{i}} - E_{\Psi_\mathrm{f}} + E_\mathrm{i} - E_\mathrm{f}\right). \tag{2.15}$$

where the *magnetic interaction vector* represents

$$\boldsymbol{S}_\perp = \sum_j \exp\left(i\boldsymbol{Q}\boldsymbol{r}_j\right) \left[\hat{\boldsymbol{Q}} \times \left(\boldsymbol{s}_j \times \hat{\boldsymbol{Q}}\right) + \frac{i}{\hbar Q}\left(\boldsymbol{p}_j \times \hat{\boldsymbol{Q}}\right)\right], \tag{2.16}$$

with $\boldsymbol{r}_j$, $\boldsymbol{s}_j$ being the jth electrons position and spin vector, respectively. While $\boldsymbol{S}_\perp$ seems to be a technical and unintuitive quantity, it can be shown that it is directly related to the Fourier transform of a samples *magnetization* $\boldsymbol{M}(\boldsymbol{Q})$:

$$\boldsymbol{S}_\perp = \hat{\boldsymbol{Q}} \times \left(-\frac{1}{2\mu_\mathrm{B}} \boldsymbol{M}(\boldsymbol{Q}) \times \hat{\boldsymbol{Q}}\right). \tag{2.17}$$

In addition, from the definition of the magnetic interaction it can be directly inferred that magnetic neutron scattering only occurs if there is a perpendicular component of local magnetization with respect to the scattered neutron's momentum transfer. A fact, which can be used in the determination of the magnetic structure of a solid.

Any further step in the determination of the DDCS of a magnetic system requires assumptions on the state of the neutrons and sample. In a very general setting, such as an unpolarized neutron beam and a non-Bravais crystal the DDCS can be expressed as

$$\begin{aligned}\frac{\mathrm{d}^2\sigma}{\mathrm{d}\Omega\ \mathrm{d}E_\mathrm{f}} = \frac{(\gamma r_0)^2}{2\pi\hbar}\frac{k_\mathrm{f}}{k_\mathrm{i}} \sum_{\alpha\beta}\left(\delta_{\alpha\beta} - \hat{\boldsymbol{Q}}_\alpha \hat{\boldsymbol{Q}}_\beta\right) \sum_{l'd',ld} \frac{1}{4} g_{d'} g_d F^*_{d'}(\boldsymbol{Q}) F_d(\boldsymbol{Q}) \\ \cdot \int_{-\infty}^{\infty} \langle \exp\left(-i\boldsymbol{Q}\boldsymbol{R}_{l'd'}(0)\right) \exp\left(i\boldsymbol{Q}\boldsymbol{R}_{ld}(t)\right)\rangle \\ \cdot \left\langle \boldsymbol{S}^\alpha_{l'd'}(0) \boldsymbol{S}^\beta_{ld}(t)\right\rangle \exp(-i\omega t)\mathrm{d}t.\end{aligned} \tag{2.18}$$

Arriving at equation 2.18 needs a considerable amount of theoretical calculations, for which the reader is encouraged to look at the literature (e.g. Squires [33]). Nevertheless, the main points will be become clear after the explanation of the components in 2.18. First, the indices l',l indicate the unit cell in the crystal and d', d account for the position inside the cell. The factors of the form g_d are the *Landé splitting factors* necessary to describe coupling between spin and orbital moments within a magnetic ion. The *magnetic form factor* $F_d(\boldsymbol{Q})$ is a result of the spatial distribution of the electrons in orbitals around their atoms and is the Fourier transform of the normalized density of all unpaired electrons. The sum over $\alpha, \beta \in [x,y,z]$ is a alternative way to express the

magnetic interaction vector together with the thermal average over the time dependent spin components of two magnetic atoms $\left\langle \boldsymbol{S}^{\alpha}_{l'd'}(0)\boldsymbol{S}^{\beta}_{ld}(t)\right\rangle$.

For a system of localized spins, the averages over positional and spin correlations contains several contributions to the DDCS, such as the elastic magnetic scattering, inelastic spin wave scattering and contributions coupling lattice and spin components.

Inelastic magnetic scattering cross section

At the heart of understanding spin wave scattering lies the evaluation of the time-dependent matrix element contained in $\left\langle \boldsymbol{S}^{\alpha}_{l'd'}(0)\boldsymbol{S}^{\beta}_{ld}(t)\right\rangle$ and can not be done in all generality. It involves knowledge about the time evolution of the spins, a problem well understood in the framework of *linear spin wave theory*. As a starting point, we take the Heisenberg Hamiltonian already introduced in equation 1.1 of chapter 1

$$\mathscr{H} = -\sum_{mm'} J_{mm'}\boldsymbol{S}_m \cdot \boldsymbol{S}_{m'} \ , \tag{2.19}$$

a well proven microscopic model for a magnetic, solid state system. Choosing the *exchange coupling* or *exchange energy* $J_{mm'} > 0$ leads to parallel spin alignment and ferromagnetic ordering. This model is one of the instances, which can be solved analytically by employing a second quantization scheme. While the calculation in its entirety is beyond the scope of this introductory chapter, a few key computation steps, the result and the conclusion drawn from them will be presented here. They are insightful even for more complex systems.

In the first step, the spin operator $\boldsymbol{S}_m$ needs to be represented in terms of the creation and annihilation operators $a^{\dagger}_m$ and a_m, respectively. They create or destroy a deviation from the ferromagnetic ground state in the system. Then the Hamiltonian can be written as

$$\mathscr{H} = -NS^2\mathscr{J}(0) + 2S\mathscr{J}(0)\sum_m a^{\dagger}_m a_m - 2S\sum_{mm'} J_{mm'}a_m a^{\dagger}_m, \tag{2.20}$$

where

$$\mathscr{J}(\boldsymbol{q}) = \sum_{\boldsymbol{\rho}} J_{\boldsymbol{\rho}} \exp\left(i\boldsymbol{q}\cdot\boldsymbol{\rho}\right) \quad \text{with} \quad \boldsymbol{\rho} = \boldsymbol{R}_m - \boldsymbol{R}_{m'} \tag{2.21}$$

with $\boldsymbol{q}$ being in a vector in the first Brillouin zone, S being the total spin value of an atom and N being the number of atoms in the crystal. The second step is already hinted at in equation 2.20 since it is advantageous to change from real space to momentum space by Fourier expanding the operators a_m and $a^{\dagger}_m$ with their respective momentum space counterparts $b_{\boldsymbol{q}}$, $b^{\dagger}_{\boldsymbol{q}}$. The new representation of the Heisenberg Hamiltonian

$$\mathscr{H} = -NS^2\mathscr{J}(0) + \sum_{\boldsymbol{q}} \hbar\omega_{\boldsymbol{q}} b^{\dagger}_{\boldsymbol{q}} b_{\boldsymbol{q}} \tag{2.22}$$

contains the dispersion relation

$$\hbar\omega_{\boldsymbol{q}} = 2S\left(\mathscr{J}(0) - \mathscr{J}(\boldsymbol{q})\right), \tag{2.23}$$

which is of major importance, as it connects the momentum of a spin wave excitation quantum, also known as *magnon*, with its associated energy.

Finally, using the momentum space representation of $\mathscr{H}$ it is possible to calculate the time dependent form of the spin operators $\boldsymbol{S}(t) = (\boldsymbol{S}_x(t), \boldsymbol{S}_y(t), \boldsymbol{S}_z(t))$ in terms of $b_{\boldsymbol{q}}$, $b_{\boldsymbol{q}}^\dagger$ and thus allows the evaluation of the spin-spin correlation functions explicitly, because the states $|\Psi\rangle$ need to be eigenfunctions of the Hamiltonian. Leaving the detailed explanation to Squires [33], the ultimate expression for the DDCS of a ferromagnet is given by

$$\begin{aligned}\frac{\mathrm{d}^2\sigma}{\mathrm{d}\Omega\ \mathrm{d}E_\mathrm{f}} &= (\gamma r_0)^2 \frac{k_\mathrm{f}}{k_\mathrm{i}} \frac{(2\pi)^3}{v_0} \frac{1}{2} S^2 (1 - \hat{\boldsymbol{Q}}_z^2) \left| \frac{1}{2} g F(\boldsymbol{Q}) \right|^2 \exp(-2W) \\ &\quad \times \sum_{\boldsymbol{G},\boldsymbol{q}} \underbrace{\delta(\boldsymbol{Q} - \boldsymbol{q} - \boldsymbol{G}) \delta(\hbar\omega_{\boldsymbol{q}} - \hbar\omega) \left\langle n_{\boldsymbol{q}} + 1 \right\rangle}_{\text{spin wave creation}} + \underbrace{\delta(\boldsymbol{Q} + \boldsymbol{q} - \boldsymbol{G}) \delta(\hbar\omega_{\boldsymbol{q}} + \hbar\omega) \left\langle n_{\boldsymbol{q}} \right\rangle}_{\text{spin wave annihilation}} .\end{aligned} \tag{2.24}$$

It contains the *Deby-Waller factor* $\exp(2W)$, the *Boltzmann factor*

$$\langle n_{\boldsymbol{q}} \rangle = \frac{1}{\exp(\hbar\omega_{\boldsymbol{q}} / k_\mathrm{B} T) - 1} \tag{2.25}$$

and the unit cell volume v_0. Two terms contribute to the inelastic spin wave scattering spectrum. The first term represents spin wave creation, where the neutron loses energy of $\hbar\omega_{\boldsymbol{q}}$ when its momentum transfer matches $\boldsymbol{Q} = \boldsymbol{G} + \boldsymbol{q}$. Similarly the second term represents spin wave annihilation, a process during which the neutron gains energy according to the dispersion relation $\hbar\omega_{\boldsymbol{q}}$, while anywhere else in momentum-energy space, the inelastic neutron scattering cross section is zero. The Boltzmann factor determines the occupation number of a particular magnon state with the energy $\hbar\omega_{\boldsymbol{q}}$. Thus, the Boltzmann factor causes that at low temperatures, where few excitations modes are present in the sample, spin wave annihilation is suppressed. Scattering processes creating magnons are still allowed.

Clearly, INS is not confined to the study of collective magnetic excitations, but for more random dynamics of diffusion or spin fluctuations as well. Staying on the topic of magnetism, a useful approach to calculate the spin dependent part of equation 2.18 by relating it to the magnetic susceptibility tensor of the system. For the Fourier transformed dynamical spin-spin correlation function of a Bravais crystal with one magnetic atom in the unit cell we introduce

$$\mathcal{S}^{\alpha\beta}(\boldsymbol{Q}, \omega) = \frac{1}{2\pi} \sum_l \int_{-\infty}^{\infty} \exp\left(i\boldsymbol{Q}\boldsymbol{R}_l - i\omega t\right) \left\langle \boldsymbol{S}_0^\alpha(0) \boldsymbol{S}_l^\beta(t) \right\rangle \mathrm{d}t \ , \tag{2.26}$$

which contains the time independent and dependent contributions leading to magnetic Bragg scattering and inelastic diffusive scattering respectively. It can be shown, and has been comprehensively written up by Marshall and Lowde [38], that the dynamical spin correlation function is connected to the imaginary part of the dynamic susceptibility

$\Im\left(\chi^{\alpha\beta}\right)$ via the *fluctuation-dissipation theorem*:

$$\mathcal{S}^{\alpha\beta}(\boldsymbol{Q},\omega) = \frac{\hbar}{\pi}\frac{1}{g^2\mu_\mathrm{B}^2}\frac{1}{1-\exp\left(-\frac{\hbar\omega}{k_\mathrm{B}T}\right)}\Im\left(\chi^{\alpha\beta}(\boldsymbol{Q},\omega)\right) \ . \tag{2.27}$$

This equation concisely expresses the relation between the response of the macroscopic system (right side of equation 2.27) and the spectrum of the microscopic fluctuations (see equation 2.26). Going back to the previous derivation, in a magnetic system with LRO, the poles of $\Im\left(\chi^{\alpha\beta}(\boldsymbol{Q},\omega)\right)$ correspond to the spin wave spectrum.

Having motivated the INS cross sections, final remarks are due. The discussion of inelastic scattering was restricted to magnetic interactions between a ferromagnetic sample and neutrons, but the result is valid also without strict ferromagnetic order. This is related to the fact that under certain conditions non-ferromagnetic systems can be mapped onto a ferromagnetic state with an appropriate transformation. There, the dispersion is known and performing the inverse transformation yields the sought after excitation spectrum of the initial system [39]. As a side note, it should be mentioned that the ansatz of creation, annihilation operators can also be used to calculate scattering from collective lattice vibrations (phonons), which have not been addressed here. In both cases, INS instruments, such as triple-axis, time-of-flight or neutron spin echo spectrometers can be utilized to map the dispersion relation of the investigated system. Recalling the derivation steps above, it is evident that the dispersion relation is intimately tied to the Hamiltonian describing the magnetic or interatomic coupling. Therefore, INS data is invaluable to develop or refine models and coupling mechanisms in solid state physics, giving access to fundamental parameters.

2.2. Description of the neutron spin

A fundamental property of a neutron is its spin of value $\hbar/2$, which is why it is characterized similarly to the proton and electron as a *Fermion*. Just as the orbital momentum induces a magnetic moment so does the spin. In order to mathematically describe the interaction due to spins, the *spinor* formalism is highly useful [40].

Being an inherent quantum mechanical property, a spin-1/2 system has only two states corresponding to the *eigenvalues* of the operator $|\hat{\boldsymbol{e}},\pm\rangle$ with respect to an arbitrary quantization axis $\hat{\boldsymbol{e}}$. Without restrictions to generality, the choice of $\hat{\boldsymbol{e}} = \hat{\boldsymbol{z}}$ can be made. Therefore, applying the spin operator $\boldsymbol{S} = (S_x, S_y, S_z)$ to either of these two spin states results in

$$\boldsymbol{S}\cdot\hat{\boldsymbol{z}}\,|\pm\rangle = \pm\frac{\hbar}{2}\,|\pm\rangle \ . \tag{2.28}$$

$S_z = \boldsymbol{S}\cdot\hat{\boldsymbol{z}}$ is an observable, physical quantity the states $|\pm\rangle$ are constructed to be orthonormal and form the basis of the two component spinor space. A general wave function of a Fermion or neutron with an arbitrary spin state can be written as

$$|\boldsymbol{\Psi}(x)\rangle = \begin{pmatrix}\psi_+(x)\\ \psi_-(x)\end{pmatrix} \ , \tag{2.29}$$

obeying the normalization equation

$$\langle \mathbf{\Psi} | \mathbf{\Psi} \rangle = \int |\psi_+(x)|^2 + |\psi_-(x)|^2 \mathrm{d}x \ . \tag{2.30}$$

Having introduced the basic concept of the spinor space, which allows to describe any spin state in terms of a 2D vector, it is necessary to relate these states to the spin operator in the Cartesian laboratory frame. The link between the two representations is given by the *Pauli matrices*

$$\sigma_x = \begin{pmatrix} 0 & 1 \\ 1 & 0 \end{pmatrix}, \sigma_y = \begin{pmatrix} 0 & -i \\ i & 0 \end{pmatrix}, \sigma_z = \begin{pmatrix} 1 & 0 \\ 0 & -1 \end{pmatrix} \tag{2.31}$$

and the relation $S_i = \frac{\hbar}{2}\sigma_i$. The fact that σ_z is a diagonal matrix arises from the initial choice of the quantization axis. In a different setting (as in chapter 3.2.1), where $|\pm\rangle_x$ would the eigenstates with reference to $\hat{\boldsymbol{x}}$, the operators S_x, σ_x would be represented by the diagonal matrix [40, 41].

The spinor formalism allows to calculate the behavior of a neutron's spin state propagating through an experimental setup and how the state evolves under influence of polarizing devices and magnetic guide fields. The later can be treated by solving the Schrödinger equation for a static magnetic potential given by

$$i\hbar \frac{\partial}{\partial t} |\mathbf{\Psi}(x,t)\rangle = \left(\frac{\hbar^2 \nabla^2}{2m_\mathrm{n}} I_2 + \mu_\mathrm{B} \boldsymbol{\sigma} \cdot \boldsymbol{B} \right) |\mathbf{\Psi}(x,t)\rangle \ . \tag{2.32}$$

I_2 is the identity matrix of a 2D vector space.

As an example, a neutron, described by a plane wave traveling in y direction with polarization along x

$$|\mathbf{\Phi}\rangle = \frac{1}{\sqrt{2}} e^{-i(k_0 y - \omega_0 t)} \begin{pmatrix} 1 \\ 1 \end{pmatrix} \tag{2.33}$$

starts to evolve in time through the potential of a magnetic guide field $\boldsymbol{B} = B_z \hat{\boldsymbol{z}}$ dictated by equation 2.32. In classical terms this evolution is known as *Lamor precession* with a modified neutron wave function

$$|\mathbf{\Phi}\rangle = \frac{1}{\sqrt{2}} e^{-i(k_0 y - \omega_0 t)} \begin{pmatrix} e^{-i\omega_z y/v} \\ e^{i\omega_z y/v} \end{pmatrix} \ , \tag{2.34}$$

which represents a precession motion in the x-y-plane with an angular frequency $\omega_\mathrm{L} = 2\omega_z = 2\mu_\mathrm{B} B_z/\hbar$ [42].

A polarization analysis device projects the full wave function into the analyzed direction $|x\rangle \langle x|\mathbf{\Phi}\rangle$, here the polarization in x is chosen and only allows this part of the wave function to propagate further. The analyzed wave function behind the polarization analyzer reads

$$|\mathbf{\Phi}_x\rangle = \frac{1}{2\sqrt{2}} e^{-i(k_0 y - \omega_0 t)} \left(e^{-i\omega_z y/v} + e^{i\omega_z y/v} \right) \begin{pmatrix} 1 \\ 1 \end{pmatrix} \ . \tag{2.35}$$

As anticipated, depending on the Lamor frequency and the position of the polarization analyzer a different neutron polarization $\langle \mathbf{\Phi}_x | \sigma_x | \mathbf{\Phi}_x \rangle = \cos(\omega_\mathrm{L} y/v)$ would be measured. This phenomenon of Lamor precession is the basis of all polarization manipulating techniques in neutron scattering and therefore the fundamental principle behind high energy resolution neutron spin echo techniques, one of which will be discussed in section 3.2 in greater detail.

3. Instrumentation - At the heart of experiments

The experimental work performed for this thesis was concerned with studying the magnetic properties of the itinerant ferromagnet nickel and the low-dimensional magnet $Cu(C_4H_4N_2)_2(H_2O)_2Cr_2O_7$ (Cu-pyz) on the microscopic and on the bulk scale. The microscopic measurements employed different neutron scattering techniques namely triple-axis spectrometry (TAS) and modulation of intensity with zero effort (MIEZE). In chapter 2 the general theory of neutron scattering has been laid out, whereas this chapter addresses how the TAS and MIEZE techniques are implemented to acquire data of scattering processes between sample and neutrons. For the bulk properties of Cu-pyz measurements of the magnetization and the magnetic susceptibility were performed with a standard physical property measurement system (PPMS). In the following, the working principles will be addressed and the instruments used for data acquisition will be described in detail.

3.1. Triple-axis spectrometry

Triple-axis spectrometry is one of the oldest neutron scattering techniques invented by Brockhouse and Shull [43, 44], which allows systematic investigation of inelastic neutron scattering (INS) over a large domain in reciprocal space (RS). TAS completely determines the state of incoming and scattered neutrons, which is achieved by scattering the neutrons at the three, name giving, *scattering axis* of the instrument. Each axis is aligned perpendicular to the horizontal plane (ground) and is the pivoting axes of the rotational motors of the instrument. These motors are used to adjust the scattering angles at which neutrons traveling through the instrument are measured.

The reference book on triple-axis spectroscopy by Shirane *et al.* summarizes comprehensively the main equations of neutron scattering, TAS components, instrument resolution calculation and presents fitting examples for each topic under discussion [35]. Less comprehensively, this section will introduce the basic instrument layout and components of a triple-axis spectrometer and operational details in subsection 3.1.1 and 3.1.2, respectively.

3.1.1. A neutron's journey through a triple-axis instrument

When working with neutron scattering techniques, an important factor in experiment planing is the optimal neutron energy or wavelength to work with. Usually three regimes of energies are considered in the context of condensed matter research, which are dubbed *hot*, *thermal* and *cold* in reference to the temperature of the moderating material from which the neutrons are emitted. Example values of temperature T_{mod}, wavelength λ, wavevector k and energy E of each regime are summarized in table 3.1. These quantities

are related by

$$E = k_\mathrm{B}T \longrightarrow E\,[\mathrm{meV}] = T\,[\mathrm{K}]/11.605 \tag{3.1}$$

$$E = \frac{\hbar^2 k^2}{2m_\mathrm{n}} \longrightarrow E\,[\mathrm{meV}] = 2.072 \cdot (k\,[\mathrm{\AA}^{-1}])^2 \tag{3.2}$$

$$k = 2\pi/\lambda \longrightarrow k\,[\mathrm{\AA}^{-1}] = 6.283/\lambda\,[\mathrm{\AA}]\ . \tag{3.3}$$

	T_mod (K)	λ (Å)	k (Å^{-1})	E (meV)
hot	2300	0.642	9.780	198.2
thermal	300	1.779	3.532	25.85
cold	25	6.162	1.020	2.154

Table 3.1.: Energy regimes of neutrons accessible in modern neutron sources with secondary sources. Approximate values of the sources at the FRM II research reactor [45, 46].

Due to the strong variability of the interaction cross section between neutrons and matter, which depend on the neutron's energy, beam lines and instruments are typically tailored towards a restricted range of neutron energies. As IN12 and RESEDA both employ a cold neutron spectrum, only components and setups performing well in this energy range will be discussed.

In figure 3.1 the fundamental components of a TAS setup are depicted with neutrons (orange) entering from the left side through the neutron guide (pale blue). Neutrons encounter the first instrument component the *monochromator*, which reflects them towards the sample. The next sections describe the monochromator and the subsequent components the neutrons encounter.

The monochromator

At the first scattering axis, a narrow band of neutrons, coming from the source, is selected with a known wavelength λ_i, or in context of TAS a known wavevector $\boldsymbol{k}_\mathrm{i}$, bandwidth $\Delta\lambda/\lambda_\mathrm{i}$ ($\Delta k_\mathrm{i}/k_\mathrm{i}$), and with a finite divergence α_n via Bragg scattering

$$n\lambda_\mathrm{i} = n\frac{2\pi}{|\boldsymbol{k}_\mathrm{i}|} = 2d_\mathrm{M}\sin(\theta_\mathrm{M}) \tag{3.4}$$

from a well known single crystal, the monochromator. The equation 3.4 is known as *Bragg's law* and gives a relation between neutron wavelength λ_i, the angle θ_M enclosed by neutron flight path and the reflecting crystal planes and the distance d_M between those planes. Therefore, all neutrons with a wavevector are scattered under the angle $2\theta_\mathrm{M}$ from their initial trajectory, which is double the θ angle determined by Bragg's law. Hence, the direction and magnitude of $\boldsymbol{k}_\mathrm{i}$ is known and initial state $|\boldsymbol{k}_\mathrm{i}\rangle$ is almost fully

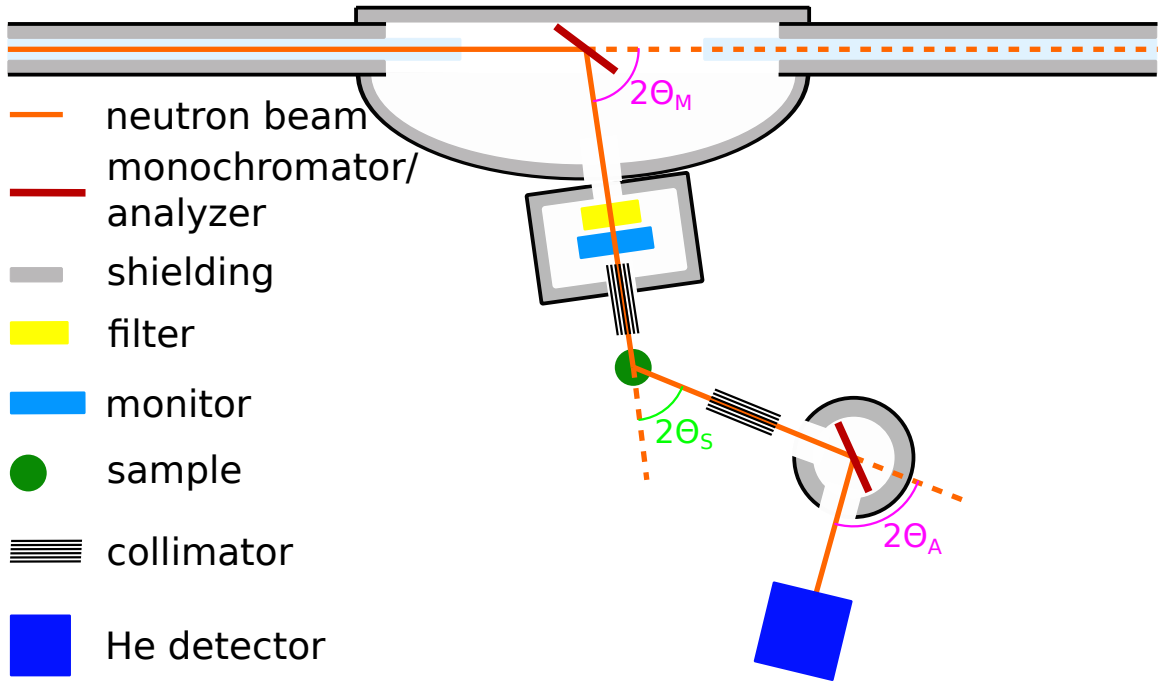

Figure 3.1.: Sketch depicting a common TAS setup. Starting left, the neutron beam (orange) travels along the guide from the source entering the monochromator assembly. At the monochromator (red) neutrons of the selected wavevector are scattered into the instrument, passing a filter (yellow), a intensity monitor (light blue) and a collimator (black lines) before interacting with the sample (green). Downstream of the sample, the analyzer assembly is placed in the desired position ($2\theta_S$) with an additional collimator in between. Finally, the neutron is detected in a $^3_2$He proportional counter (dark blue), if it satisfies the energy selection of the analyzer (red).

defined[1].

The higher order filter

However, Bragg's law allows neutrons with any integer fraction n of the selected wavelength to enter the instrument under the exact same scattering angle $2\theta_M$. The most dominant contribution to the *higher order contamination* arises from $\lambda_i/2$ and needs to be removed to obtain a well characterized neutron beam. Otherwise additional excitation peaks appear in inelastic neutron data or diffraction pattern making the analysis substantially more complicated. Filters eliminate higher order neutrons by absorption and elastic or inelastic scattering processes. In the thermal and cold neutron energy regime, Bragg scattering filters made from polycrystalline *pyrolitic graphite* (PG) and beryllium are employed. Based on Bragg's law 3.4 it becomes evident that neutrons with a wavelength $\lambda > \lambda_c = 2d_{max}$ do not scatter elastically in the filter material, while

1 The spin state is conveniently omitted. It is possible to use polarizing monochromators or special polarizing devices in conjunction with a guide field if spin dependent scattering is investigated. Here, this is not the case.

neutrons with $\lambda \leq \lambda_c$ do. Thus, higher order neutrons ($\lambda/2$ etc.) are scattered and thus removed by the randomly oriented domains in the filter material, whereas the neutrons possessing the desired wavelength are transmitted [35, 47, 48].

The intensity monitor

Following the monochromatizing components, intensity monitoring devices are often utilized as a reference for counting time during the experiment. As an example, reactor power, moderator efficiency or upstream instruments change the neutron over time making constant counting time inadequate. These monitors are required to be non-invasive regarding the incoming neutron beam, meaning they must not moderate or absorb neutrons to a noticeable degree. Fission chamber detectors with low detection efficiencies 10^{-7} to 10^{-3} can be used for this propose [49].

It is important to have a good understanding of the wavelength dependence of the detection efficiency, which comes down to the underlying absorption or conversion reaction used for neutron detection. Aforementioned fission chambers contain thin layers with trace amounts of ${}^{235}_{92}\mathrm{U}$, which capture neutrons before splitting in a general fission reaction like

$$ {}^{235}_{92}\mathrm{U} + {}^{1}_{0}\mathrm{n} \longrightarrow {}^{A'}_{Z'}\mathrm{X} + {}^{A''}_{Z''}\mathrm{Y} + \nu \cdot {}^{1}_{0}\mathrm{n} + Q \ . \tag{3.5} $$

Within the energy region of cold neutrons, the absorption cross section σ_A of ${}^{235}_{92}\mathrm{U}$ follows the $\propto 1/v$ - law well [50, 51]. Erratic changes in σ_A from nuclear resonances are mainly present at significantly higher neutron energies. Hence, even if energy of the incoming neutrons vary, monitors allow to account for intensity differences in the neutron flux by counting the correct number of incoming neutrons per measurement point. Extensive cross section and scattering length data on the reactions between neutrons and any isotope are investigated, archived and maintained e.g. by the *National Institute of Standards and Technology* (NIST) [52], the *International Atomic Energy Agency* (IAEA) [51] and the *Brookhaven National Laboratory* (BNL) [53].

The collimator

A collimator, also called *Soller* collimator, is a divergence control component used in X-ray and neutron scattering instrumentation. It consists of several parallel, radiation absorbing blades and removes all neutrons from the passing beam if their angle to the geometric beam axis α_n exceeds $\alpha = w/l$, where w is the distance between individual blades and l is the length of the blades. The transmission function of a Soller collimator [54, 55] has a triangular shape [56]

$$ T_\mathrm{coll}(\alpha_\mathrm{n}|\alpha) = T_0 \begin{cases} 1 - |\alpha_\mathrm{n}|/|\alpha|, & |\alpha_\mathrm{n}| < |\alpha|. \\ 0, & \text{otherwise.} \end{cases} \tag{3.6} $$

Shaping the neutron beam in this manner achieves higher momentum resolution and lower neutron background for the instrument at the cost of neutron intensity, as expected from Liouville's theorem. Starting from the neutron source, in a TAS there are four

standard positions, in front of and behind the monochromator and the analyzer, to insert collimators depending on experimental requirements. The implications of this kind of beam preparation on a TAS resolution function have been investigated thoroughly, because of its importance in data analysis for dynamic systems with a multitude of excitation bands and high resolution measurements [35, 57–60].

The sample

The second scattering event happens in the sample, during which the neutrons change their state according to the DDCS, which describes the partial currents of neutrons in $\mathrm{d}\Omega\ \mathrm{d}E_\mathrm{f}$. The aim is to measure the DDCS for specific points of interest in $\boldsymbol{Q}$-E-space, meaning the rate of neutrons needs to obtained at certain scattering angles θ_S, $2\theta_\mathrm{S}$ and neutron energies E_f. The scattering angle is defined by placing the neutron detector with respect to the sample position, but energy analysis is hard to implement in a neutron detector. With such a two-axis instrument that lacks energy resolution, only the energy integrated DCS can be measured.

The analyzer

For this reason, the third scattering axis adds an energy analyzing component, short *analyzer*, again consisting of another well known single crystal and operating exactly the same way as the monochromator. The instrument can be operated in two ways when investigating inelastic scattering signals. Evidently, the monochromator and analyzer need to be set to different neutron energies to measure a finite energy transfer. For a scan of energy transfer $\Delta E = E_\mathrm{i} - E_\mathrm{f}$ either the incident energy or the selected final energy needs to be varied. Both options are possible, but external constraints such as the available space or sharing the neutron guide with a downstream instrument might single out one option. To ensure consistent measurement results, it is preferable to fix the analyzer position because it operates with constant efficiency. In that configuration a monitor counter behind the monochromator can be used to ensure equal numbers of neutrons impinge the sample for each scan point. In contrast, if the constant k_i mode is chosen, the reflectivity $R_\mathrm{A}\left(k_\mathrm{f}\right)$ and the resolution volume of the analyzer changes with magnitude of the final wavevector $|\boldsymbol{k}_\mathrm{f}|$ and scattering angle $2\theta_A$, which has to be accounted for via the factor

$$F\left(k_\mathrm{f}\right) = R_\mathrm{A}\left(k_\mathrm{f}\right) k_\mathrm{f}^3 / \tan(\theta_\mathrm{A}) \ . \tag{3.7}$$

The detector

The research and operation of neutron detectors in itself justifies an entire thesis document, but in triple-axis spectrometry, simple He-3 proportional counters are used for detection of thermal to cold neutrons. The (n, p) reaction occurring upon neutron capture by He-3:

$$^3_2\mathrm{He} + {}^1_0\mathrm{n} \longrightarrow {}^1_1\mathrm{H} + {}^3_1\mathrm{H} + Q \ . \tag{3.8}$$

has a large cross section of 5330 b [52].

The charged reaction products inside the He-3 gas filled volume depose their energy via ionization of the surrounding gas. Arising charge pulses are picked up and processed by the electronics discriminating neutron interaction from secondary $\gamma-$radiation and other background events. Typically, He-3 detectors with a cylindrical detection volume are used. This includes IN12's detector with a height $h = 12\,\mathrm{cm}$ and diameter $d = 5\,\mathrm{cm}$ [61, 62].

Final remarks

While this concludes the introduction of the main TAS components, even aside from sample environment many more parts which expand the instruments capabilities. Those are polarizing devices, guide fields and spin flipper for polarization analysis [62–65], velocity selectors [62, 64] as an alternative to filters, apertures and beam stops [35]. This list is not exhaustive as there are many instruments with a plethora of experimental use cases.

3.1.2. TAS - Exploring reciprocal space step by step

Performing an experiment at a triple-axis spectrometer equates to studying the DDCS of a sample for different momentum and energy transfer values $\boldsymbol{Q}$ and ΔE. From sketch 3.1 it is evident, that the control of the neutron wave vector is confined to a plane parallel to the floor. The perpendicular component $\boldsymbol{Q}_z$ is not resolved and neutrons with large vertical divergence are suppressed. This plane is called *scattering plane* and a single crystal sample needs to be aligned such that the plane of interest in reciprocal space is parallel to this scattering plane.

If this prerequisite is met, on the instrument operation level, the experiment reduces to driving six rotation stages for the angles θ_M, $2\theta_\mathrm{M}$, θ_S, $2\theta_\mathrm{S}$, θ_A, $2\theta_\mathrm{A}$ and waiting a preset amount of time for the detector to count the arriving neutrons. By convention positive angles mean counter-clockwise rotation.

In the following it will be shown how the spectrometer angles connect to the reciprocal space position $(\boldsymbol{Q}, \Delta E)$ of the crystal under investigation. The presented formalism is follows the covariant vector formulation used by T. Weber [2] for the TA spectrometry planing software Takin [66, 67]. Another useful resource regarding the UB-matrix approach to inelastic neutron scattering calculations is the paper by Lumsden *et al.* [68].

We choose the coordinate system of the laboratory frame (LF) to be a right-handed, orthogonal system. In full generality, the unit cell, which builds up a single crystal, has lattice constants a, b, c and associated angles α, β, γ, as depicted in figure 3.2 (a). Further it is assumed that the vector $\boldsymbol{a}$, one of the basis vectors of the crystal coordinate system, is aligned parallel to the laboratory coordinate system. With this information, any point in the crystal can be expressed in the LF coordinates by

2 The details of the calculations have been presented as part of the HERCULES School 2019.

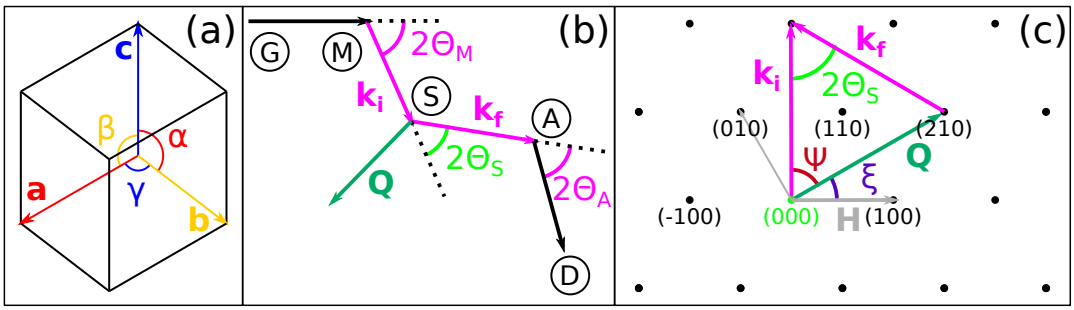

Figure 3.2.: Sketch depicting a general crystal system, a simplified TAS setup and a reciprocal space lattice with a scattering vector construction. In (a) the most general version of a crystal's unit cell is depicted with the lattice constants a, b, c and the angles α, β, γ, which define the basis of the crystal coordinate system and its reciprocal counterpart. (b) shows a TAS configuration with the three scattering axis that are passed by neutrons entering from the guide G and getting absorbed in the detector D. The three scattering angles $2\theta_i$ at the monochromator M, sample S and analyzer A determine the point (Q, E). (c) visualizes the scattering plane of a hexagonal crystal structure in reciprocal space. The vectors $\boldsymbol{k}_\mathrm{i}, \boldsymbol{k}_\mathrm{f}$ and $\boldsymbol{Q}$ are drawn together with the angles $2\theta_\mathrm{S}$, Ψ and ξ for elastic Bragg scattering from the (210) reflection. The known reference vector in the scattering plane to calculate θ_S for all other positions is $\boldsymbol{H} = (100)$.

$$\boldsymbol{a} = a \cdot \begin{pmatrix} 1 \\ 0 \\ 0 \end{pmatrix} \tag{3.9}$$

$$\boldsymbol{b} = b \cdot \begin{pmatrix} \cos(\gamma) \\ \sin(\gamma) \\ 0 \end{pmatrix} \tag{3.10}$$

$$\boldsymbol{c} = c \cdot \begin{pmatrix} \cos(\beta) \\ \frac{\cos(\alpha) - \cos(\gamma)\cos(\beta)}{\sin(\gamma)} \\ \sqrt{1 - \cos^2(\beta) - \left(\frac{\cos(\alpha) - \cos(\gamma)\cos(\beta)}{\sin(\gamma)}\right)^2} \end{pmatrix} . \tag{3.11}$$

Arranged into a matrix form $\underline{A} = \begin{pmatrix} \boldsymbol{a} & \boldsymbol{b} & \boldsymbol{c} \end{pmatrix}$ the $\underline{A}$ matrix transforms real space fractional coordinates of the crystal into the LF. Subsequently, we define the B-matrix $\underline{B}$, which is the transposed inverse of $\underline{A}$ leading to

$$\underline{B} = 2\pi \left(\underline{A}^{-1}\right)^T . \tag{3.12}$$

$\underline{B}$ transforms reciprocal space coordinates of the crystal in relative lattice units (rlu) to the LF with units of Å^{-1}. Using the B-matrix, the length of any reciprocal space vector $\boldsymbol{G}$ and the angle between two vectors in RS can be simply calculated, as they are seen

from the LF, via

$$|\boldsymbol{G}| = \sqrt{\boldsymbol{G}^{\mathrm{T}}\underline{B}^{\mathrm{T}}\underline{B}\boldsymbol{G}} \tag{3.13}$$

$$\measuredangle(\boldsymbol{G},\boldsymbol{H}) = \arccos\left(\frac{\boldsymbol{G}^{\mathrm{T}}\underline{B}^{\mathrm{T}}\underline{B}\boldsymbol{H}}{|\boldsymbol{G}|\cdot|\boldsymbol{H}|}\right) \ . \tag{3.14}$$

In both equations, $\underline{B}^{\mathrm{T}}\underline{B}$ is the *metric tensor* and accounts for the fact that the crystal coordinate system as well as its reciprocal counterpart are not necessarily orthogonal and the basis vectors have different magnitudes.

With this tool set the angles of a TAS, as the are shown in subplot (b) of figure 3.2, to reach a specific point in reciprocal space can be determined as follows. The monochromator and analyzer angles are given by Bragg's law (see equation 3.4) such that θ_{M} and θ_{A} satisfy the reflection condition for the required wavelength. Provided that the rotation stages for $2\theta_{\mathrm{M,A}}$ are properly aligned with the monochromator crystals, $2\theta_{\mathrm{M,A}} = 2\cdot\theta_{\mathrm{M,A}}$.

Next, the scattering angle at the sample $2\theta_{\mathrm{S}}$ can be computed from the crystals lattice constants, the selected wavevectors $|\boldsymbol{k}_{\mathrm{i,f}}| = \frac{2\pi}{\lambda_{\mathrm{i,f}}}$ and the chosen momentum transfer vector $\boldsymbol{Q}$ in the LF ($\mathrm{\AA}^{-1}$) via the cosine theorem

$$2\theta_{\mathrm{S}} = \pm\arccos\left(\frac{\boldsymbol{k}_{\mathrm{i}}^2 + \boldsymbol{k}_{\mathrm{f}}^2 - \boldsymbol{Q}^2}{2|\boldsymbol{k}_{\mathrm{i}}||\boldsymbol{k}_{\mathrm{f}}|}\right) \ , \tag{3.15}$$

where $\pm$ depends on the scattering sense of the instrument. The angle is positive, if $2\theta_{\mathrm{S}}$ is measured counter-clockwise.

Finally, the θ_{S} angle is not calculated by taking half of $2\theta_{\mathrm{S}}$, because the crystal is not necessarily perfectly aligned with the laboratory frame and angular offsets need to be considered. In its simplest form, θ_{S} is given in reference to a known Bragg reflection $\boldsymbol{H}$ in the scattering plane, which has to be determined and indexed in the experiment. Then θ_{S} is given by

$$\theta_{\mathrm{S}} = 90° - (\Psi + \xi) \tag{3.16}$$

$$\Psi = \measuredangle(\boldsymbol{Q},\boldsymbol{k}_{\mathrm{i}}) = \pm\arccos\left(\frac{\boldsymbol{k}_{\mathrm{i}}^2 - \boldsymbol{k}_{\mathrm{f}}^2 + \boldsymbol{Q}^2}{2|\boldsymbol{k}_{\mathrm{i}}||\boldsymbol{Q}|}\right) \tag{3.17}$$

$$\xi = \measuredangle(\boldsymbol{Q},\boldsymbol{H}) = \sigma_{\mathrm{QH}}\arccos\left(\frac{\boldsymbol{Q}^{\mathrm{T}}\underline{B}^{\mathrm{T}}\underline{B}\boldsymbol{H}}{|\boldsymbol{Q}|\cdot|\boldsymbol{H}|}\right) \tag{3.18}$$

in which Ψ is the angle between $\boldsymbol{k}_{\mathrm{i}}$ and $\boldsymbol{Q}$ in the LF ($\mathrm{\AA}^{-1}$) and ξ is the angle between $\boldsymbol{Q}$ and the known vector $\boldsymbol{H}$. For Ψ, the sign is the same as for $2\theta_{\mathrm{S}}$ and the sign σ_{QH} of ξ depends on the alignment of $\boldsymbol{Q}$ with $\boldsymbol{H}$. σ_{QH} is positive (negative), when the cross product $\boldsymbol{Q}\times\boldsymbol{H}$ is parallel (antiparallel) to the out of plane vector of the scattering plane coordinate system. The 90° offset in θ_{S} follows the convention of T. Weber in his implementation of the experiment planing software Takin and can take values like 180° depending on the source.

The derivation above neglects any misalignment between the crystal and the laboratory

frame thus presenting an idealized representation of an experiment. When accounting for tilts and rotational offset of the crystal, rotations need to be applied to align the crystal and laboratory coordinate system. For the inclined reader the paper by Lumsden *et al.* [68] is recommended for further study.

3.1.3. Scanning modes of triple-axis spectrometer

During a TAS experiment, several scanning modes have been established to systematically study neutron scattering around points of interest in reciprocal space. For elastic scattering modes, where $k_\mathrm{i} = k_\mathrm{f}$ two modes of operation are particularly useful. Starting from a reciprocal lattice point $\boldsymbol{G}$ (Bragg scattering), the '$\theta-2\theta-$ scan' probes momentum transfer (anti)parallel to $\boldsymbol{G}$ meaning that the reduced momentum transfer vector $\boldsymbol{q} = \boldsymbol{Q} - \boldsymbol{G}$ is (anti)parallel to $\boldsymbol{G}$. This scan direction is achieved, by incrementing θ_S by θ while adding adding $2 \cdot \theta$ to $2\theta_\mathrm{S}$ between each measurement point. Powder diffraction patterns and thin film reflectivity curves are obtained in this scanning mode as well.

Scanning reciprocal space perpendicular to a reference reciprocal lattice point is done by 'rocking' the sample around its vertical rotation axis with a fixed $2\theta_\mathrm{S}$ angle. Especially in single crystal diffraction the 'rocking−scan' is utilized, because the integrated intensity of the observed Bragg peak follows a known relation . From the acquired diffraction data, atomic positions within the crystals unit cell can be refined for crystallographic studies.

For inelastic neutron scattering either the $\boldsymbol{Q}$ position in RS is varied at a constant energy transfer or the momentum transfer vector $\boldsymbol{Q}$ is held constant and the energy transfer is scanned. Both modes require a combined movement of θ_S, $2\theta_\mathrm{S}$ and either the monochromator or analyzer angles depending on the fixation of $\boldsymbol{k}_\mathrm{i}$ or $\boldsymbol{k}_\mathrm{f}$, which has been elaborated on in section 3.1.1.

The non-uniform shape of the instrument resolution, in conjunction with the form of the dispersion surface, makes one of the scanning modes more applicable in comparison, depending on the specific experiment. Examples discussing the importance and influence of the instrument resolution on INS studies are ubiquitous. Educational ones can be found in [35, chapter 5] or more recent studies of the non-reciprocal spin waves in the chiral magnet MnSi [59, 60]

3.1.4. Triple-axis spectrometer IN12

The inelastic neutron scattering experiments were performed on the cold triple-axis spectrometer IN12 located at the Institute Laue-Langevin (ILL), that has been upgraded to its current state in 2016. A 115 m long 'S' shaped neutron guide section connects IN12, at the end position of the guide, to the in-pile *vertical cold source* of the ILL's reactor. Upstream of IN12, a velocity selector is employed, to mitigate higher order reflections from the vertically and horizontally focusing PG(002) monochromator. The end section of the neutron guide is laid out to utilize the *virtual source concept* by tapering down the neutron guide to create a focal area prior to the monochromator. Together with the double bending monochromator this arrangement maximizes neutron flux for small samples at the sample position while minimizing background events detected in a ${}^{3}_{2}\mathrm{He}$

detector ($d = 5\,\mathrm{cm}$ and $h = 12\,\mathrm{cm}$). In conclusion, IN12 is exceptionally suited to study magnetic and lattice excitations in single crystals even more due to its polarization analysis capabilities, which have not been used for the experiments (chapter 5.3) discussed in this thesis. A detailed description of IN12, its components and performance, has been published in Nuclear Instruments and Methods A by Schmalzl [61].

For the experiment performed at IN12 from the 9^{th} Sept. to 15^{th} Sept. 2020, the instrument was set up in unpolarized measurement mode with horizontal collimation of $80'$ behind the monochromator, fixed analyzer position at $k_{\mathrm{f}} = 1.5\,\mathrm{\AA}^{-1}$ and a cooled Be-filter for higher order filtering behind it. The sample environment consisted of a cryostat with dilution insert achieving temperatures as low as $T_{\mathrm{min}} = 38\,\mathrm{mK}$, at which all inelastic neutron data was gathered.

3.2. Modulation of intensity with zero effort (MIEZE)

Compared to long established neutron spectrometry techniques, such as the above discussed TAS, time-of-flight spectrometry, neutron backscattering or the interferometer like neutron spin echo technique (NSE) [69], the modulation of intensity with zero effort technique [70], abbreviated as MIEZE, is in its infancy. While initial concepts have been envisioned around 1992 during the further development of NSE to the neutron resonant spin echo method (NRSE) [71], fully functional MIEZE instruments have only come operational over the last decade [72, 73].

The motiviation behind this effort becomes clear if e.g. TAS is compared to spin echo techniques. Constrained by the Liouville's theorem, TAS gains resolution on the cost of neutron intensity, by restricting the divergence with collimators or using crystals with low mosaicity for its monochromator and analyzer. As a result, the energy resolution is limited to about $\approx 20\,\mu\mathrm{eV}$ [61, 63], beyond which the loss of neutron intensity becomes severe.

Spin echo methods circumvent this limitation by decoupling the energy resolution from the neutron intensity. To achieve this, the neutron spin or collectively the polarization of the neutron beam is used as an internal clock to determine minuscule changes to the energy of a neutron. However, this requires a well defined magnetic field environment that needs to be shielded from environmental factors like the earth's magnetic field, uncompensated stray fields, magnetized components and even the sample itself. Therefore considerable effort has to be undertaken in instrument design and experiment planing to mitigate these problems [74].

Utilizing resonant spin flippers at specific locations of the instrument for polarization manipulation, MIEZE is able to compensate for environmental factors such as stray fields. Even more importantly, depolarizing conditions at the sample position become tolerable, because the manipulation of the spin is performed only in the primary spectrometer arm, before interaction at the sample position occur. Similarly to NSE, a large neutron bandwidth can be used in a MIEZE instrument. These factors result in MIEZE being a versatile and capable method in studying weak and low energy magnetic dynamics [75]. The next chapters aim to elucidate the working principle of MIEZE, motivate the basic equation for the analysis of MIEZE data and introduce the instrument RESEDA [73].

3.2.1. Working principle

The MIEZE method uses two resonant spin flippers, which are tuned to different frequencies, to create a temporally periodic signal at an interference point downstream of the investigated sample. The ratio of the amplitude and the mean value of this oscillating intensity signal is called *contrast*. The contrast is the analogue to the polarization in a standard N(R)SE measurement. Perturbations in the flight time of the neutrons, e.g. through a transfer of energy at the sample, result in decoherence and subsequent reduction of the contrast signal.

The following paragraphs will give a rundown of the mathematical description for the MIEZE technique and motivate the relationship between sample properties and the observed contrast signal. Due to the large scope of the mathematical framework, the reader will be guided along the main points.

In addition, the sketch in Figure 3.3 shows the sequence of components a neutron encounters, as well as the reference coordinate system. The unpolarized neutron beam enters from the left side and is polarized at the polarizer P_1 [35, chapter 8] [76, 77] with its polarization vector pointing along the y direction. Due to the alignment of the guide field along the x direction, the spin rotates adiabatically to this direction as well. The $\pi/2$ flipper flips polarization by 90° away from x and starts its precession in the $y-z-$plane. Within the first resonant flipper the neutrons encounter a static field $\boldsymbol{B} = B_0 \boldsymbol{e}_x$ generated by the outer Helmholtz coils. At the center a rotating magnetic field is produced by a radio frequency coil, which gives a total magnetic field

$$B(t) = \begin{pmatrix} B_0 \\ 0 \\ 0 \end{pmatrix} + \begin{pmatrix} 0 \\ B_\mathrm{r} \cos(\omega_\mathrm{s} t) \\ B_\mathrm{r} \sin(\omega_\mathrm{s} t) \end{pmatrix}. \tag{3.19}$$

Understanding the time evolution of a neutron spin subjected to a time varying

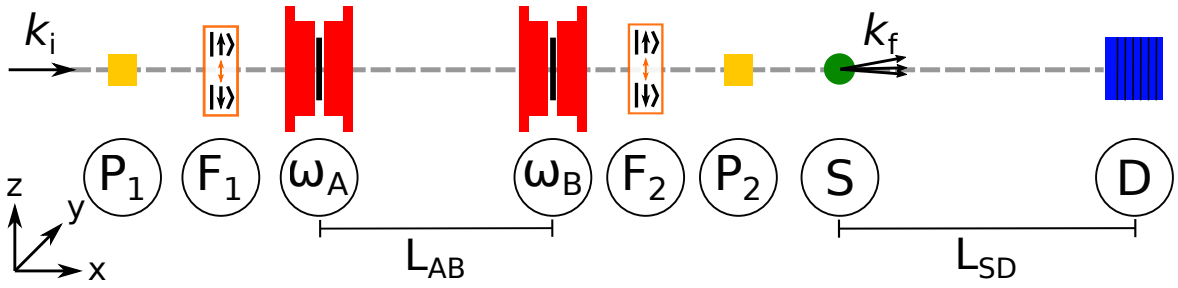

Figure 3.3.: Sketch depicting a reduced version of a MIEZE setup. From left to right, the components are the first polarizer (P_1), a $\pi/2$-spin flipper (F_1), the first resonant spin flipper (ω_A), the second resonant spin flipper (ω_B), which are separated by distance l_AB, a second $\pi/2$-spin flipper (F_2) and the final polarizer (P_2). At the detector position (D) the separated spin states interfere and create an intensity signal oscillating in time with a frequency $\omega_\mathrm{M} = 2(\omega_\mathrm{B} - \omega_\mathrm{A})$. Any perturbation to the kinetic energy of the neutrons at the sample position (S) reduces the contrast of this oscillation, which is defined as ratio of its amplitude to its mean value.

magnetic field is essential for the development of the NRSE and MIEZE technique. Several frameworks have been solving this problem in terms of a classical vector model [78], a quantum mechanical [79] or a plane wave propagation model [80], as well as a time evolution operator approach to the Heisenberg equation of the neutron's spin density operator [41]. In the following, the plane wave approach from [42] will be used to describe the time evolution of a neutron spin and the resulting intensity variation in a MIEZE spectrometer.

Utilizing the spinor notation introduced in section 2.2, the time evolution of a spin, which we express as the wave function

$$|\boldsymbol{\Psi}(x,t)\rangle = \begin{pmatrix} a_+ \\ a_- \end{pmatrix} e^{i(k_0 x - \omega_0 t)} \tag{3.20}$$

is governed by the Schrödinger equation with the time dependent potential introduced by the rotating magnetic field $V(t) = -\mu_\mathrm{n}\boldsymbol{\sigma}\cdot\boldsymbol{B}(t)$. The prefactors $a_\pm$ are complex numbers and adhere to the normalization $|a_+|^2 + |a_-|^2 = 1$. The Schrödinger equation with the time dependent potential in the Hamiltonian can be expressed as a two component vector equation for the general spin state (see equation 3.20). Then the Schrödinger equation reads

$$i\hbar\frac{\partial}{\partial t}|\Psi\rangle = -\frac{\hbar^2}{2m_\mathrm{n}}\frac{\partial^2}{\partial x^2}|\Psi\rangle + \begin{pmatrix} \omega_x & \omega_\mathrm{r} e^{-i\omega_\mathrm{s} t} \\ \omega_\mathrm{r} e^{i\omega_\mathrm{s} t} & -\omega_x \end{pmatrix}|\Psi\rangle\,. \tag{3.21}$$

Here, $\omega_x = \mu_\mathrm{n} B_0/\hbar$ is the *Lamor frequency* of the static field, μ_n the product of the nuclear magneton μ_N and the g-factor of the neutron g_n. ω_r is the Lamor frequency of the rotating field and ω_s is the angular frequency of the rotating field.

The problem formulated in equation 3.21 is known as *Krüger's problem* [42, 80] and has a known, analytical solution, which allows to transform the set of second order partial differential equations into algebraic ones. The used ansatz is given by

$$|\Psi(x,t)\rangle = \begin{pmatrix} A_\mathrm{n} e^{-i\omega_\mathrm{s} t/2} \\ B_\mathrm{n} e^{+i\omega_\mathrm{s} t/2} \end{pmatrix} e^{i(k_\mathrm{n} x - \omega_\mathrm{n} t)}\,, \tag{3.22}$$

which is essentially equal to a transformation into a coordinate system rotating at the same angular frequency as the time dependent field ω_s, and leads to

$$\begin{pmatrix} 0 \\ 0 \end{pmatrix} = \begin{pmatrix} [(k_\mathrm{n}^2 + \omega_x) - (\omega_\mathrm{n} + \omega_\mathrm{s}/2)]\cdot A_\mathrm{n} \\ [(k_\mathrm{n}^2 - \omega_x) - (\omega_\mathrm{n} - \omega_\mathrm{s}/2)]\cdot B_\mathrm{n} \end{pmatrix} + \omega_\mathrm{r}\begin{pmatrix} B_\mathrm{n} \\ A_\mathrm{n} \end{pmatrix}. \tag{3.23}$$

This equation is the basis for explicitly calculating the wave function of the spin states of a neutron in a region of space with static and rotating magnetic fields. Determination of the constants A_n, B_n, k_n and ω_n is possible via the initial, boundary and continuity conditions placed on the wave function by a specific magnetic field arrangement. Golub *et al.* calculated the solution for a scenario, which is depicted in figure 3.4. In regions I

and III the potential is due to the static magnetic field B_0, whereas in a comparably small region II the rotating magnetic field is superimposed. In each region, the total wave function is given by a linear combination of incoming, reflected and transmitted waves for each spin component, with coefficients determined by the boundary conditions.

Of interest is the part of the wave function in region III, which represents the time dependent spin components transmitted through the resonance flipper coil, and for an initial spin state $a_+ = 1$, $a_- = 0$ can be written as

$$|\Psi_{\mathrm{III}}(x,t)\rangle = \begin{pmatrix} T_0 e^{i\omega_x x/v} \\ T_1 e^{-i(\omega_\mathrm{s}-\omega_x)x/v} \end{pmatrix} e^{i(k_0 x-\omega_0 t)}. \tag{3.24}$$

The quantities k_0, ω_0 and v are the wavevector, angular frequency and velocity of the unperturbed neutron, respectively. T_0 and T_1 are transmission amplitudes given by

$$T_0 = e^{i\varepsilon d/v}\left[\cos\left(\omega_\mathrm{P} d/v\right) + i\frac{\varepsilon}{\omega_\mathrm{P}}\sin\left(\omega_\mathrm{P} d/v\right)\right] \tag{3.25}$$

$$T_1 = -i\frac{\omega_\mathrm{r}}{\omega_\mathrm{P}} e^{-i\varepsilon d/v}\sin\left(\omega_\mathrm{P} d/v\right) \tag{3.26}$$

with $\varepsilon = (\omega_\mathrm{s}/2 - \omega_x)$ and $\omega_\mathrm{P}^2 = \omega_\mathrm{r}^2 + (\omega_\mathrm{s}/2 - \omega_x)^2$ being shorthand notations for clarity purpose.

Having derived this general result, Golub *et al.* [42] discussed several use cases such as

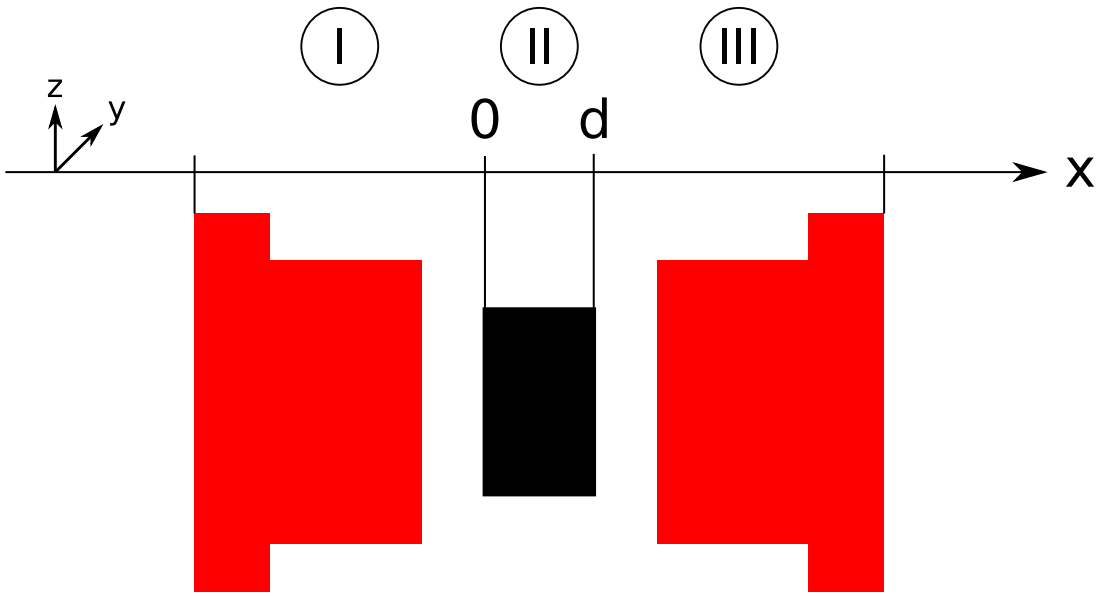

Figure 3.4.: Sketch of a single LNRSE coil showing the regions used in the calculation of Golub *et al.*. In region I ($x < 0$), the potential is given by the static magnetic field leading to a precession with $\omega_x = \mu_\mathrm{n} B_0/\hbar$. The rotating field is superimposed on the static field in region II ($0 \leq x \leq d$). Downstream in region III ($x > d$) the potential is again only due to the static field. The transition between all regions is assumed to be infinitely sharp. A solution of the Schrödinger equation needs to fulfill continuity at the boundaries between all regions.

the propagation of a neutron through two resonant coils tuned to two different frequencies $\omega_x \to \omega_\mathrm{A}, \omega_\mathrm{B}$ separated by a distance L_AB. In addition, we go from the general treatment to a case reflecting an actual experimental setup. First, we assume the resonance case $\omega_\mathrm{s} = 2\omega_x \equiv \omega_\mathrm{R} \to \omega_\mathrm{P} = \omega_\mathrm{r}$, second we assume the energy of the potential is small compared to the kinetic energy of the neutron $\omega_\mathrm{r}, \omega_x, \omega_\mathrm{s} \ll \omega_0$ and third we assume that the static magnetic field is confined to region II. The last assumption hold up, because the effect of the static field in front of and behind region II cancel out as the spin is flipped by the rotating field. The self correction effect is an inherent property of a longitudinal B_0 field configuration [81]. These assumptions simplify the calculation significantly and reproduce well known results. Hence, the wave function passing through a resonance flipper reads

$$|\Psi(x,t)\rangle = \frac{-i}{\sqrt{2}} e^{i(k_0 x - \omega_0 t)} \begin{pmatrix} a_- e^{+i\Phi(x,t)} \\ a_+ e^{-i\Phi(x,t)} \end{pmatrix}, \tag{3.27}$$

where

$$\Phi(x,t) = \omega_\mathrm{A} \left[\frac{x - d/2}{v} - t \right] \tag{3.28}$$

and ω_A is the Lamor frequency of the first coil. Equation 3.27 is the input for the second resonant flipper coil B (ω_B), but requiring a transform of the space coordinate x such that the new origin lies at the entry point of coil B. Shifting the wave function by $x' = x - L_\mathrm{AB}$ gives the input for the calculation at coil B. Finally, the wave function behind coil B is

$$|\Psi(x',t)\rangle = \frac{-i}{\sqrt{2}} e^{i(k_0 x' - \omega_0 t)} \begin{pmatrix} a_+ e^{+i\Theta(x',t)} \\ a_- e^{-i\Theta(x',t)} \end{pmatrix} \tag{3.29}$$

$$\Theta(x',t) = \frac{\Delta\omega x' - \omega_\mathrm{A}(L_\mathrm{AB} - d) - \Omega d}{v} - \Delta\omega t \tag{3.30}$$

$$\Delta\omega = (\omega_\mathrm{B} - \omega_\mathrm{A}), \quad \Omega = (\omega_\mathrm{B} + \omega_\mathrm{A})/2 \tag{3.31}$$

with d being the length of the resonance flipper coil (see figure 3.4). As seen from equation 3.30 there is a point behind the the second coil, where all velocity dependent terms cancel out. Without dephasing of neutrons with differing wavelength, at $x' = L_\mathrm{BD}$ a detector can measure a sinusoidally modulated neutron intensity signal oscillating with frequency $\omega_\mathrm{M} \equiv 2\Delta\omega$ in time. Fixing the distance between the resonance coil B and the detector, puts a constraint, known as the *MIEZE condition*, on the resonance flipper coils to create a measurable signal

$$\frac{\omega_\mathrm{B}}{\omega_\mathrm{A}} = \frac{L_\mathrm{AB} + L_\mathrm{BD} - d/2}{L_\mathrm{BD} - d/2}. \tag{3.32}$$

By putting a spin analyzing device before the sample, one polarization direction ($\langle\sigma_y\rangle$)

is selected and a signal of the form

$$I(t) = A\cos(\omega_{\mathrm{M}}t) + y_0 = \frac{I_0}{2}(1 + \cos(\omega_{\mathrm{M}}t)) \tag{3.33}$$

can be extracted. Having mentioned the contrast during the high level introduction of the MIEZE technique, we formalize this definition. The *contrast* C of the MIEZE signal, which is the MIEZE equivalent of the polarization for the N(R)SE [71, 78] techniques is defined as the ratio of the amplitude A and the mean value y_0 of the oscillating intensity signal on the detector. For the idealized undisturbed signal as described in equation 3.33 the contrast yields

$$C = \frac{A}{y_0} \xrightarrow{\text{eq 3.33}} \frac{I_0/2}{I_0/2} = 1. \tag{3.34}$$

The maximum contrast value of 1 is indicative of the neutrons not changing their kinetic energy while traversing a MIEZE instrument and can be observed in the direct neutron beam or with a sample scattering the neutrons elastically. With the MIEZE technique being a spectrometry method, a understanding is needed how the measured contrast changes due to finite energy transfers between neutrons and sample. The next subsection will elucidate the connection of contrast and dynamical structure factor.

3.2.2. Imprints of energy transfer in the MIEZE signal

Extensive literature has been written on the relationship of N(R)SE polarization and the dynamical structure factor often in terms of the *spin echo approximation*, which includes two assumptions on the scattering process [78, 82].

- The energy transfer is small compared to the neutron energy $\Delta E \ll E_{\mathrm{i}}$
- The dynamical structure factor $S(q, \omega)$ is symmetric in ω

However, the MIEZE technique has been applied to systems that do not satisfy these conditions. An example might be the non-reciprocal spin waves observed in the conical and skyrmion phase of MnSi [59, 60]. Especially in low temperature environments the *Bose factor* introduces asymmetry in $S(q, \omega)$ since scattering in conjunction with the annihilation of excitation quanta in the sample becomes suppressed. Furthermore, highly dispersive systems, which require large energy transfers [83], violate the spin echo approximation as well.

Therefore, we want to present a more explicit approach, which has already been used by Säubert *et al.* in the analysis of spin wave scattering in Fe [83, 84] and has been further refined by Jochum and Bender [85]. Starting from equation 3.33 the normalized signal at the detector

$$I(t_{\mathrm{D}})/I_0 = \langle \sigma_y \rangle_{\hbar\omega} = \frac{1}{2}\langle \cos(\omega_{\mathrm{M}} t_{\mathrm{D}}) + 1 \rangle_{\hbar\omega} \tag{3.35}$$

is influenced by the energy transfer with the sample. Here $\langle ... \rangle_{\hbar\omega}$ denotes the average over all possible energy transfers. Any delay or premature arrival of the neutrons by Δt_{D}

compared to the unperturbed flight time leads to a dephasing and subsequent reduction in the contrast signal with Δt_D being computed as

$$\Delta t_\mathrm{D} = L_\mathrm{SD}\left(\frac{1}{v} - \frac{1}{\sqrt{v^2 - 2\hbar\omega/m_\mathrm{n}}}\right). \tag{3.36}$$

The intensity observed at the detector depends on DDCS, which describes the number of neutrons scattered from the sample into the solid angle $\mathrm{d}\Omega$ and energy $\mathrm{d}E_\mathrm{f}$ normalized to the total number of incoming neutrons, as has been introduced in section 2.1.1. Including the DDCS, as the distribution of energy transfer to the neutrons, into equation 3.35 to expand the average over $\hbar\omega$, and applying the contrast definition in equation 3.34 results in

$$C(2\theta, \varphi, \omega_\mathrm{M}) = \frac{\int_{-\infty}^{\infty} \frac{\mathrm{d}^2\sigma}{\mathrm{d}\Omega \mathrm{d}(\hbar\omega)} \cos(\omega_\mathrm{M}\Delta t_\mathrm{D})\ \mathrm{d}(\hbar\omega)}{\int_{-\infty}^{\infty} \frac{\mathrm{d}^2\sigma}{\mathrm{d}\Omega \mathrm{d}(\hbar\omega)}\ \mathrm{d}(\hbar\omega)}. \tag{3.37}$$

Rewriting the DDCS in terms of the more commonly used dynamical scattering function and setting $E = \hbar\omega$ this becomes

$$C(2\theta, \phi, \omega_\mathrm{M}) = \frac{\int_{-\infty}^{\infty} \frac{k_\mathrm{f}}{k_\mathrm{i}} S(2\theta, \phi, E) \cos(\omega_\mathrm{M}\Delta t_\mathrm{D})\ \mathrm{d}E}{\int_{-\infty}^{\infty} \frac{k_\mathrm{f}}{k_\mathrm{i}} S(2\theta, \phi, E)\ \mathrm{d}E}. \tag{3.38}$$

At this point, it becomes necessary to account for instrumental details influencing the measurement in a real world setting. These corrections include the

- modification of the observed energy spectrum due to the energy dependent detection efficiency
- finite energy transfer from a neutron's kinetic energy
- bandwidth of incoming neutrons
- asymmetry of the measured double differential cross section

Finally, this leads to a description of the measured contrast signal

$$C(q, \omega_\mathrm{M}) = \int_0^\infty f(\lambda)\ N \int_{-\infty}^{E(\lambda)} P_\mathrm{det}(\lambda, E) \cdot \frac{k_\mathrm{f}}{k_\mathrm{i}} S(2\theta, \phi, E) \cos(\omega_\mathrm{M}\Delta t_\mathrm{D})\ \mathrm{d}E\, \mathrm{d}\lambda. \tag{3.39}$$

P_det is the generally energy dependent detector efficiency function of an instrument. The cut-off in the energy integral represents the fact that a neutron can not transfer more than its kinetic energy, while the factor N comes from the denominator in equation 3.37 and ensures that the energy spectrum is normalized. The integration over the wavelength λ with the wavelength distribution function $f(\lambda)$ accounts for the signal produced from neutrons with varying incident energy.

This formalism allows comprehensive analysis of MIEZE experiments beyond the spin echo approximation on the cost of extensive numerical computation. In the following,

the differences in the calculation's results prove the necessity of a framework beyond the Fourier transform approach. As an example, the simple magnon model will be revisited, which was derived in section 2.1.3. Thereby, the dynamical scattering function for magnetic inelastic scattering is given by

$$S(q,E) \propto \sum_{\boldsymbol{G},\boldsymbol{q}} \delta(\boldsymbol{Q}-\boldsymbol{q}-\boldsymbol{G})\delta(E_{\boldsymbol{q}}-E)\left\langle n_{\boldsymbol{q}}+1\right\rangle + \delta(\boldsymbol{Q}+\boldsymbol{q}-\boldsymbol{G})\delta(E_{\boldsymbol{q}}+E)\left\langle n_{\boldsymbol{q}}\right\rangle . \quad (3.40)$$

For simplicity, we restrict this discussion to a fixed $\boldsymbol{Q}$ position in reciprocal space, reducing the problem to the energy spectrum. It is represented by two Dirac-δ peaks at the values of positive and negative energy transfer. Infinitely sharp excitation peaks correspond to infinite lifetimes, which represent an unrealistic scenario in the physical world. In INS experiments, where the instrumental resolution often dominates the observed linewidth of an inelastic signal, the Dirac-δ peak model is sufficient. On the contrary, for a high resolution method such as MIEZE, it is inadequate and a *line shape function* has to be introduced. A *Lorentzian* peak shape

$$L(E) = \frac{1}{\pi}\frac{\Gamma_q}{(E-E_q)^2+\Gamma_q^2} \quad (3.41)$$

has proven to be suitable, while more elaborate line shape function can be derived depending on the system under investigation and will be discussed later in more detail (see section 4.1).

In figure 3.5 four $S(q,E)$ models are depicted and analyzed. It is shown how the inclusion of the corrections above change the numerically calculated contrast. All models use an initial wavelength $\lambda_\mathrm{i} = 6.0\,\text{Å}$, energy transfer of $E_q = 2.0\,\mathrm{meV}$ and linewidth $\Gamma_q = 0.25\,\mathrm{meV}$ and differ in:

- having Dirac-δ peaks
- being symmetric with respect to energy transfer
- being asymmetric due to inclusion of the Bose factor ($T = 15\,\mathrm{K}$)
- being 'one-sided', an extreme version of a non-reciprocal spectrum

From (b) to (d) corrections are introduced, which are firstly the energy-cutoff and $k_\mathrm{f}/k_\mathrm{i}$ factor, secondly the efficiency correction of the detector and lastly the average over the incoming wavelength spectrum, respectively. For clarity, (d1) and (d2) show two spectra with differing energy cut-offs. The subplots correspond to $\lambda_{\mathrm{d}1} = 4.5\,\text{Å}$ and $\lambda_{\mathrm{d}2} = 5.0\,\text{Å}$, where the cut-off point is indicated by the vertical, dotted lines. In the wavelength averaging process, several of these spectra are transformed and the results are averaged according to the weights of a triangular wavelength distribution.

Each correction reshapes the spectrum and improves the modeling of the neutron signal observed in the detector. Belonging to each $S(q,E)$ the prime labeled subplots (a') to (d') show the contrast curves, which are normalized to 1 and shifted for better visibility. With exception of (a') the contrast has been calculated via equation 3.39, while (a') was determined by numerical Fourier transform, as it would be appropriate for the SE approximation.

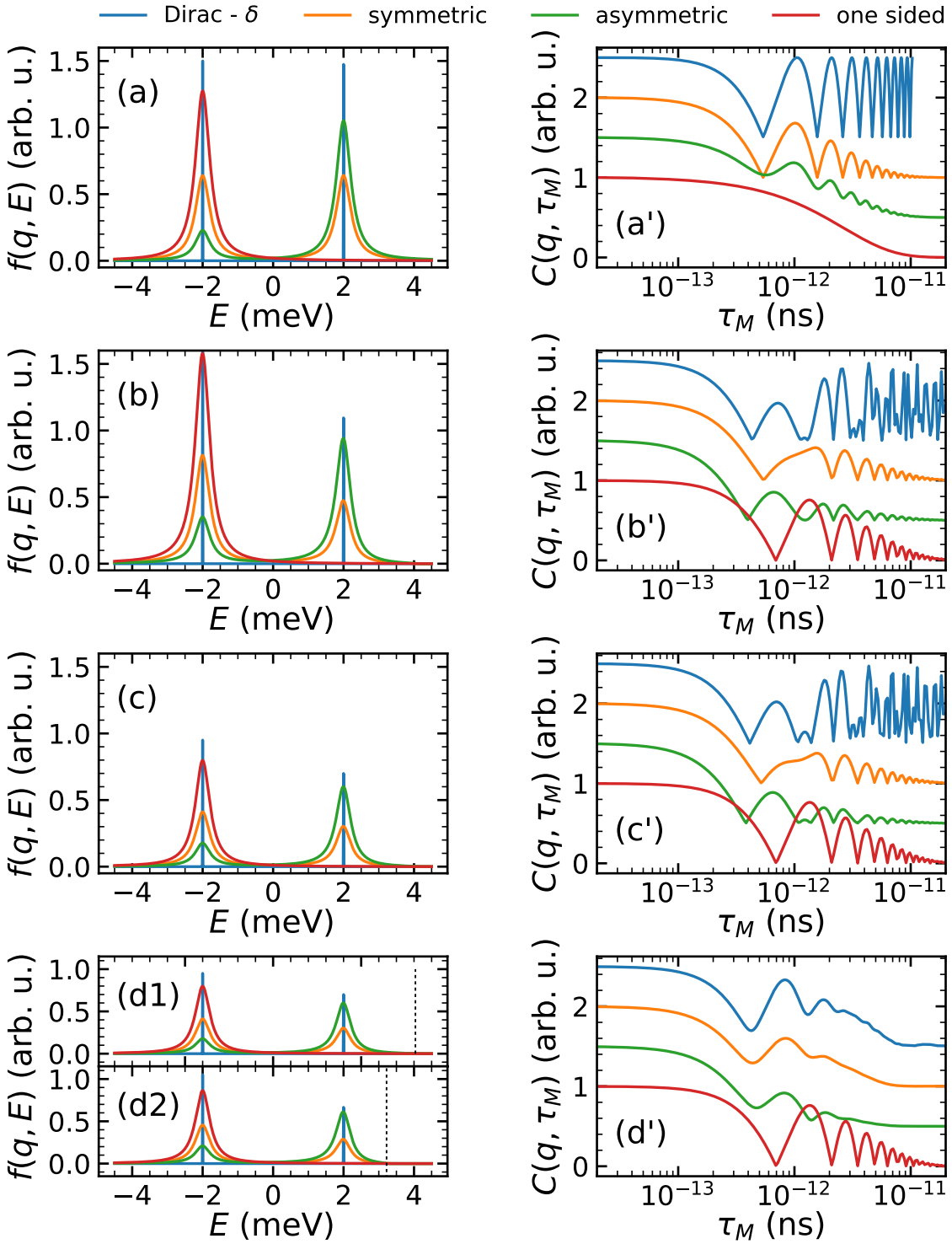

Figure 3.5.: The evolutionary steps in the MIEZE contrast calculation. On the left-hand side different $f(q,E)$ models are shown, including an increasing number of corrections from (a) to (d), while the primed plots on the right-hand side show the corresponding contrast curves. The blue lines show the Dirac-δ peak for the analytical spin wave model, the orange one is a symmetric excitation spectrum with finite linewidth, the green one depicts asymmetry introduced by the Bose factor and the red line shows a simple non-repciprocal model with only one peak. From (a) to (d) the $k_\mathrm{f}/k_\mathrm{i}$ factor and the energy cut-off, the detector efficiency and the triangular wavelength distribution is introduced.

Comparing (a') with (b'), (c'), (d') it becomes clear, that the SE approximations falls short in the description of MIEZE data with large energy transfers. Even though the model parameters have been chosen to highlight the differences, these energy transfers can be seen in real world samples and are of interest in context of critical dynamics in ferromagnets close to T_C as it will be explained in 4. This concludes the part discussing the theory behind the MIEZE technique and the contrast calculation required for data analysis.

3.2.3. MIEZE spectrometer RESEDA

The critical and spin wave scattering addressed in chapter 4 has been investigated with the MIEZE technique at the NRSE/MIEZE spectrometer RESEDA [73] located in the neutron guide hall of the Neutron Research Source Heinz Maier-Leibnitz (FRM II). Since the theoretical details of MIEZE have been discussed above, the instrument and the utilized setup will be introduced briefly.

For the study conducted in 2019, RESEDA was configured for MIEZE operation and equipped with a high temperature furnace (HTF-3 / TOF-TOF furnace), which uses resistive niobium heating elements. This setup provided access to the parameter set listed in table 3.2. RESEDA is connected to the curved cold neutron guide NL5-S with a $m = 2$ coating and $r = 1600\,\mathrm{m}$ radius. As an entry point to the instrument, the velocity selector provides a triangular shaped wavelength band with nominal wavelength $\lambda_0 = 3.5 - 22\,\text{Å}$ and a bandwidth $\Delta\lambda/\lambda_0 = 8.8 - 17.2\,\%$. Passing through the primary

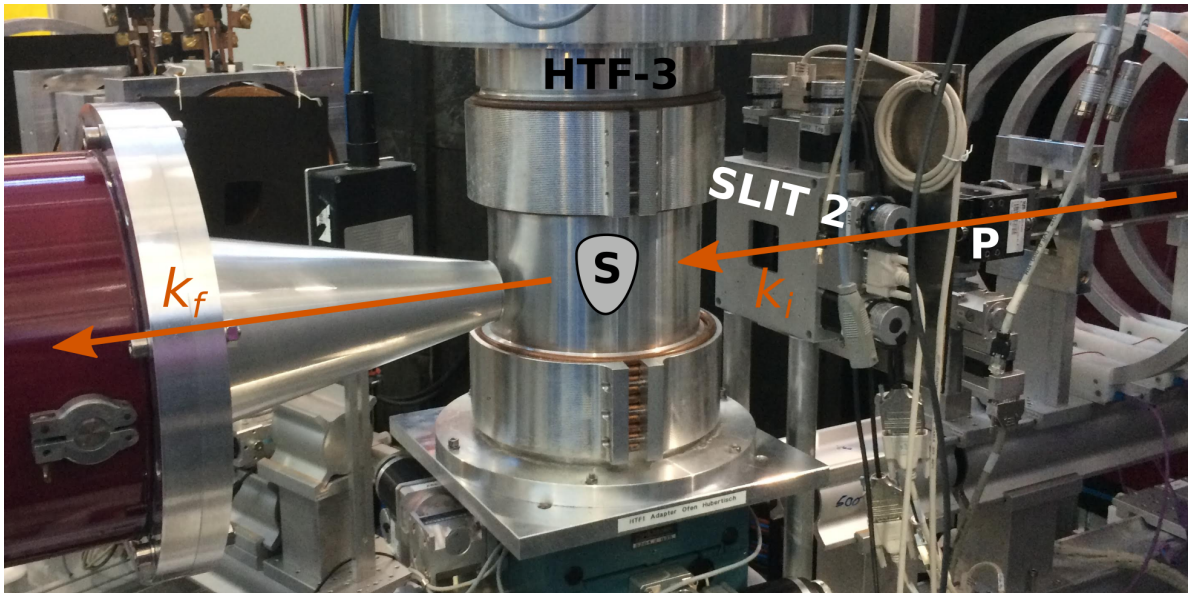

Figure 3.6.: RESEDA setup around the sample position. The image shows a cut-out of the RESEDA beamline with the upstream primary spectrometer arm on the right side, with the spin analyzer **P** and the subsequent second beam shaping slit (SLIT 2). The high temperature furnace (HTF-3), in which the single crystalline sample is mounted, is placed on the rotating goniometer table. After passing through the sample, neutrons enter the evacuated flight tube between sample and detector avoiding any further interaction, predominantly air scattering.

spectrometer arm, the neutron beam will be polarized and manipulated as described in subsection 3.2.1. Additionally, the beam divergence is restricted by means of a collimator and two aperture devices with rectangular window. The collimator, with exchangeable divergence acceptance of 20′, 40′ and 80′, suppresses double reflected neutrons coming from the neutron guide system. Both apertures have an individually adjustable width and height from 1 - 50 mm for beam shaping prior to the sample. Further neutron guide parts between all components in the primary arm reduce transport losses downstream.

Behind the sample position neutrons enter an evacuated flight tube up to the detector position. In between a circular beam stop ($d_{\mathrm{BS}} = 2.5\,\mathrm{cm}$) is mounted to block the direct beam from impinging on the detector. Together, the positioning of the detector with respect to the primary beam and the detector's active area, determine the scattering angle 2θ solid angle window $\mathrm{d}\Omega = A_{\mathrm{det}}/l_{\mathrm{SD}}^2$. The maximum scattering angle is $2\theta_{\mathrm{max}} = 55°$.

A comprehensive account of the available operation parameters of RESEDA can be found in publications of Franz *et al.* [73, 86] and online [87] A multitude of articles address the use cases of RESEDA [75], instrument specific derivation of the MIEZE signal with subtraction coils [88] and sample geometry dependent resolution effects [89–91], proving the capabilities and increasing maturity of RESEDA and the MIEZE technique in general.

Parameter	Value / Range
λ_0	6.0 Å
$\frac{\Delta\lambda}{\lambda_0}$	0.12
L_{SD}	3.43 m
τ_{M}	1.5×10^{-4} - 8.0×10^{-1} ns
T	300 - 700 K
A_{det}	$(20 \times 20)\,\mathrm{cm}^2$
α_{col}	40′
A_{ap}	$(10 \times 10)\,\mathrm{mm}^2$
2θ	$-1.5°$
L_{AB}	1.864 m
L_{ap}	4.35 m

Table 3.2.: Instrument parameters and accessible ranges for the measurement of magnetic dynamics in Ni at RESEDA.

3.3. Magnetization and magnetic susceptibility measurements

Material properties on the macroscopic scale, are the result of the intrinsic electronic states on the atomic scale. While the individual electrons can hardly be investigated, bulk measurements of the magnetization and magnetic susceptibility already indicate the character of electron spins inside. Being fairly standard, non-destructive and non-invasive both methods allow insight in properties readily and exclusively predicted by the laws of quantum mechanics.

Magnetization and static susceptibility

The magnetization of any material can be inferred from the stray fields produced by a magnetized sample. A convenient method to measure these fields is *vibration sample magnetometry*, which is based on *Farady's law of induction*

$$U_{\mathrm{ind}} = -\frac{\mathrm{d}}{\mathrm{d}t}\int \boldsymbol{B}\cdot \mathrm{d}\boldsymbol{A}\ , \tag{3.42}$$

where $\boldsymbol{B}$ is the magnetic stray field of the sample integrated over the area $\mathrm{d}\boldsymbol{A}$ of a pick-up coil called the magnetic flux Φ_{m}. A change in the magnetic flux over time induces a measurable voltage in the pick-up coil, which directly depends on the magnetization of the sample. In a vibrating sample magnetometer (VSM) [92] the time variation of Φ_m is produced by an oscillatory movement of the sample compared to a static pick-up coil. Similarly, the same induction is achieved if the coil setup is moved compared to a fixed sample in a vibrating coil magnetometer (VCM) [93]. However, VCM has an operational advantage in case additional sample environment is involved in the measurement such as pressure cells or sub-Kelvin temperature devices [84, 94].

For the exploration of a sample's magnetization $\boldsymbol{M}(T, \boldsymbol{H})$ as a function of temperature and external magnetic field it is convenient to define the static magnetic susceptibility

$$\chi_{ij}^{\mathrm{stat}}(T, \boldsymbol{H}) = \frac{\partial M_i(T, \boldsymbol{H})}{\partial H_j} \xrightarrow{\text{for simplicity}} \frac{M(T, \boldsymbol{H})}{H} \tag{3.43}$$

which generally is a tensor, but can be simplified to the ratio of the magnetization of the sample to field strength. Regarding systems with anisotropy or chirality, the off-diagonal terms are of great importance, however they will not be of interest in the context of this thesis.

AC-susceptibility

The static susceptibility represents the response of the magnetization of the sample to a unchanging, external magnetic field, meaning the frequency of the the field $\omega = 0$. This concept can be expanded straightforwardly, by adding a small additional magnetic field oscillating in time such that the sample is exposed to

$$\boldsymbol{H} = \boldsymbol{H}_0 + \boldsymbol{h}_{\mathrm{AC}}\cos(\omega t)\ . \tag{3.44}$$

Following this notion, it is expected, that the magnetic system responds at the same frequency, which is expressed in terms of the *AC-susceptibility* $\chi_{ij}^{\mathrm{AC}}(T, \boldsymbol{H}, \omega)$. It is linked to the measured induction voltage

$$U_{\mathrm{ind}}(t) = -N_{\mathrm{s}} \frac{\mathrm{d}\Phi_{\mathrm{m}}}{\mathrm{d}t} = \mu_0 H_0 \omega A N \sin(\omega t) \cdot (1 + \chi_{ij} f) \ , \tag{3.45}$$

where μ_0 is the magnetic permeability, N the number of windings and A the cross section area of the pick-up coil. f is the volume fraction occupied by the sample in comparison to the air. Generally, other filling media besides air are possible e.g. pressure transmitting fluids for AC-susceptibility measurements on samples under hydrostatic pressure. The suscepptibility contribution of such a filling medium χ_{fm} needs to be considered in the sum $(\chi_{\mathrm{fm}}(1-f) + \chi_{ij} f)$, which for air and small filling factors f breaks down to equation 3.45.

Since $f > 1$ and typical susceptibility values are small ($|\chi_{ij}| \ll 1$) the induction signal is dominated by the non-sample contribution. For this reason, the *mutual induction method*, a mitigation technique, is employed to minimize the background signal. Parallel to the sample encapsulating pick-up coil, a second empty, structurally identical one is measured. Except for small systematic deviations, a significant part of the background signal can be accounted for [95]. Such an AC-measurement assembly is sketched in figure 3.7, which shows a sample holder and sample being inserted into a reference coil and a pick-up coil. The external driving field $\boldsymbol{h}_{\mathrm{AC}} \cos(\omega t)$ is created by the excitation coil, which encloses the other two coils.

For the acquired induction voltage from an empty pick-up coil, a phase shift of $\pi/2$ in relation to the sinusoidal driving field $\boldsymbol{h}_{\mathrm{AC}}$ is expected. In contrast, the sample's contribution can be split into an in-phase and an out-of-phase signal in a way that the full susceptibility can be expressed as

$$\chi = \chi' + i\chi'' = \Re(\chi) + i\Im(\chi) \ . \tag{3.46}$$

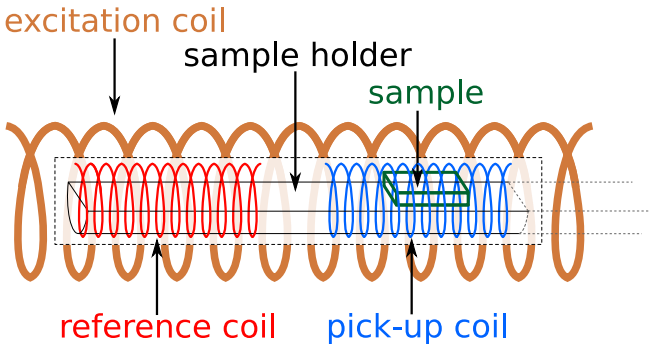

Figure 3.7.: Sketch depicting a mutual induction χ_{AC} measurement setup. The large excitation coil encloses the reference coil and pick-up coil to induce an induction voltage via a small driving field $\boldsymbol{h}_{\mathrm{AC}} \cos(\omega t)$. The difference in the measured voltage of both coils arises from the magnetic susceptibility of the sample. Thus the environmental background can be subtracted out.

The real part, in-phase with the time dependent magnetization, of the susceptibility is related to reversible dynamics of the magnetization of the sample at the probed frequency. However, the imaginary part $\Im(\chi) = \chi''$ is related to non-reversal or energy dissipating processes such as domain wall motion, spin-lattice relaxation, phase transitions or flux creep in superconductors [96].

Physical property measurement system

The static susceptibility and magnetization data of the metal-organic compound Cu-pyz (abbreviation for $Cu(C_4H_4N_2)_2(H_2O)_2Cr_2O_7$), which is discussed in chapter 5.2, was acquired with a *physical property measurement system* (PPMS) from the *Quantum Design AG* in the 9 T configuration [97] by means of VSM method [98]. The measurements were performed in collaboration with G. Benka of the chair for the Topology of Correlated Systems (E51) at the Department of Physics of the Technische Universität München.

4. Spin waves and critical fluctuations in nickel - A high resolution study using MIEZE

The study of solid state magnetism has always been strongly linked to phase transitions and their properties, hence the amount of papers published on the critical behavior around the phase transition temperature is, for practical purposes, uncountable. They discuss the key concepts of *critical scaling* and the categorization of systems based on *universality classes*. This approach to investigate magnetic materials has advanced the field substantially. A universality class is a set of *critical exponents*, which determine the power law behavior of the order parameter or response functions of a system. Within each class the exponents are interconnected via *scaling laws* allowing categorization and predictions of the other physical properties of any system [99].

More importantly, universality classes group systems together, which are according to their microscopic interactions, quite different only sharing commonality in few general parameters. Still, as only few of universality classes can be distinguished, it raises the question: Which features of these microscopic inter-particle forces are important for determining critical-point exponents and scaling functions, and which are unimportant? [99]

Naturally, this question is no less relevant for dynamic critical phenomena, which extend all of these concepts to time-dependent properties and their anomalous evolution close to the critical point. Bridging the world of theoretical consideration and experimental reality, physical systems and appropriate instrumentation has to be combined to test the predictions of idealized models. In recent years renewed interest in the critical dynamics of ferromagnetic systems arose from advances in inelastic neutron scattering techniques, which are uniquely qualified to probe these dynamic phenomena. Compared to other viable methods such as Brillouin light scattering or nuclear magnetic resonance, neutron scattering is well applicable in the long-wavelength regime $q \gtrsim 0$. The high energy resolution required at the same time has been achieved with the MIEZE measurement technique.

The ferromagnet nickel has a long history of studies investigating its spin wave and critical, paramagnetic scattering over a large range in temperature [29]. The current improvements in momentum and energy resolution of MIEZE enable the study of long-range dipolar interactions between the electrons in the system. Such a deviation from the prominent isotropic Heisenberg system has successfully been observed in the ferromagnetic systems Fe [83, 100, 101], EuO [102–104], EuS [103–105] and $LiTbF_4$ [106]. For this reason, we investigated the magnetic scattering in the vicinity of the ordering phase transition at T_C with energy and momentum transfers a factor of 10 lower then previously reported [107, 108].

In the following, the physics of critical dynamics of ferromagnets will be introduced, emphasizing the difference in behavior originating from dipolar coupling (section 4.1).

Section 4.2 is dedicated to the presentation of the MIEZE data describing the measurement, data reduction, physical parameter extraction and instrument resolution corrections. The acquired data will be compared to the theoretical models and the appropriate description will be discussed in section 4.3. Finally, a summary of the present and outlook on future studies will be given, cf. section 4.4.

4.1. Physics of dipolar ferromagnets

Fundamental to the theory of critical phenomena and scaling is a correlation function $C_\xi^{\boldsymbol{A}}(\boldsymbol{r}, t)$ of the operator $\boldsymbol{A}$ and its unique correlation length ξ, which approaches infinity at T_C and simultaneously is a measure of the deviation of the temperature from T_C such that $\xi = |t|^{\nu(\nu')}$ with $t = (T - T_\mathrm{C})/T_\mathrm{C}$ and ν, ν' being the associated critical exponents above and below T_C [109]. With regard to ferromagnetism, this abstract definition becomes more relatable, when specifying that $C^{\boldsymbol{A}}$ is related to the spin-spin correlation function $\left\langle S_i^\alpha S_j^\beta \right\rangle$. Since the range of temperatures T_C in real-world ferromagnets ranges over several orders of magnitude, it is not surprising that the *reduced temperature* t as defined before is the appropriate variable to describe those systems in context of critical phenomena.

In momentum and temperature space, the inverse correlation length $\kappa = \xi^{-1}$ defines three separate regions in the vicinity of T_C. Figure 4.1 shows the separation into the *spin wave region* ($q < \kappa$, $T < T_\mathrm{C}$), the *transition region* ($q \gg \kappa$) and the *hydrodynamic region* ($q < \kappa$, $T > T_\mathrm{C}$). Within each region, the investigated system exhibits differing dynamical behavior. Associating T_C with the Curie temperature and calling one region the spin wave region already specifies our interest on dynamic critical phenomena in magnetic materials, even though the formalism is applicable to a plethora of systems.

The dynamical behavior of a ferromagnet deep in the ferromagnetic state ($T \ll T_\mathrm{C}$) and far in the paramagnetic phase ($T \gg T_\mathrm{C}$) and consequently its observed response to NS is known from spin wave theory and statistical mechanics, respectively. Dynamical scaling theory (DST) extends this description and allows to predict the renormalization of the spin wave dispersion and the lifetime of paramagnetic fluctuations close to T_C. For each of the three distinct regions, the expected behavior will be presented for the subsequent comparison with high resolution neutron spectroscopy data of nickel.

4.1.1. Spin wave region

The basis for discussing the spin waves in nickel is a microscopic model describing a system of exchange coupled spins with dipolar anisotropy in an external magnetic field

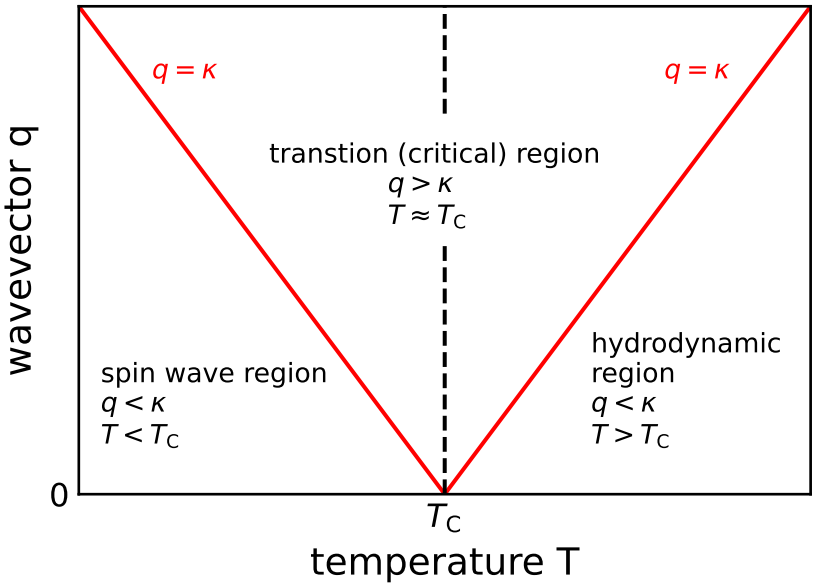

Figure 4.1.: Wavevector transfer vs temperature diagram in the vicinity of the critical temperature T_C. The red lines given by $q = \kappa(T)$ separate the space into three regions in which a system displays different, characteristic behavior. Corresponding to their names, in the spin wave region a magnetic system exhibits collective excitations, whereas spin diffusion is dominant in the hydrodynamic region. According to dynamical scaling theory, the asymptotic forms of two neighboring regions are assumed to merge at the boundaries. Both the inverse wavevector q^{-1} and correlation length $\xi(T) = \xi_0|1 - T/T_\mathrm{C}|^\nu$ are large compared to inter atomic distances.

H along the z axis. It is expressed by the Hamiltonian

$$\begin{aligned}\mathscr{H} &= \mathscr{H}_\mathrm{ex} + \mathscr{H}_\mathrm{dip} + \mathscr{H}_\mathrm{Zeeman} \\ &= -\frac{1}{2}\sum_{l,m}^{N} 2J_{lm}\boldsymbol{S}_l \cdot \boldsymbol{S}_m \\ &+ \frac{1}{2}\sum_{l,m}^{N} \frac{4\mu_\mathrm{B}^2}{R_{lm}^5}\left(R_{lm}^2 \boldsymbol{S}_l \cdot \boldsymbol{S}_m - 3\boldsymbol{S}_l \cdot \boldsymbol{R}_{lm}\boldsymbol{S}_m \cdot \boldsymbol{R}_{lm}\right) \\ &+ \sum_{l}^{N} 2\mu_\mathrm{B} H \boldsymbol{S}_l^z.\end{aligned} \tag{4.1}$$

Here, N is the total number of atoms, with l and m being summation indices from 1 to N omitting the case $l = m$. $\boldsymbol{R}_{lm} = \boldsymbol{R}_l - \boldsymbol{R}_m$ and $R_{lm} = |\boldsymbol{R}_{lm}|$ are the vector connecting the position of the atoms l, m and its magnitude, respectively. $\boldsymbol{S}_l$ denotes the spin angular momentum operator in units of $\hbar$ with J_{lm} being the exchange coupling constant of nearest neighbors.

Similar to the derivation of spin wave dispersion for a standard Heisenberg Hamiltonian (see subsection 2.1.3), Holstein and Primakoff [110] applied a technique now known

as *Holstein-Primakoff transformation* to express the Hamiltonian in terms of magnon creation and annihilation operators $a_{\boldsymbol{q}}^*$ and $a_{\boldsymbol{q}}$, respectively. As a result, the Hamiltonian takes the form

$$\mathscr{H} = C + \sum_{\boldsymbol{q}} A_{\boldsymbol{q}} a_{\boldsymbol{q}}^* a_{\boldsymbol{q}} + \sum_{\boldsymbol{q}} (\frac{1}{2} B_{\boldsymbol{q}} a_{\boldsymbol{q}} a_{-\boldsymbol{q}} + \frac{1}{2} B_{\boldsymbol{q}}^* a_{\boldsymbol{q}}^* a_{-\boldsymbol{q}}^*). \tag{4.2}$$

$$A_{\boldsymbol{q}} = 2SJq^2 + 2\mu_{\mathrm{B}} H + 4\pi\mu_{\mathrm{B}} M_0 \sin^2(\theta_{\boldsymbol{q}}) = A_{-\boldsymbol{q}} \tag{4.3}$$

$$B_{\boldsymbol{q}} = 4\pi\mu_{\mathrm{B}} M_0 \sin^2(\theta_{\boldsymbol{q}})\, e^{-2i\Phi_{\boldsymbol{q}}} = B_{-\boldsymbol{q}} \tag{4.4}$$

In these equations, q represents the reduced wavevector, which is required to be small compared to the total wavevector transfer in order for the expressions of $A_{\boldsymbol{q}}$ and $B_{\boldsymbol{q}}$ to be valid. M_0 is the saturation magnetization. The angles $\theta_{\boldsymbol{q}}, \Phi_{\boldsymbol{q}}$ parameterize the direction of the wavevector transfer $\boldsymbol{q}$ with respect to the magnetization (external field) direction. The spin wave dispersion deduced by determination of the eigenvalues of the Hamiltonian for a ferromagnetic state is given as:

$$\hbar\omega_{\boldsymbol{q}} = \sqrt{{A_{\boldsymbol{q}}}^2 - |B_{\boldsymbol{q}}|^2} = E_{\mathrm{HP}}(\boldsymbol{q}) \tag{4.5}$$

Changing to SI units and generalizing the magnetic moment of a spin to include the Landé-factor g the Holstein-Primakoff dispersion relation becomes

$$\begin{aligned} E_{\mathrm{HP}}(\boldsymbol{q}) &= \sqrt{(Dq^2 + g\mu_0\mu_{\mathrm{B}} H) \cdot (Dq^2 + g\mu_0\mu_{\mathrm{B}} H + g\mu_0\mu_{\mathrm{B}} M(T,H)\sin^2(\theta_{\boldsymbol{q}}))} \\ &= \sqrt{(E_{\mathrm{ex}} + E_H) \cdot (E_{\mathrm{ex}} + E_H + E_{\mathrm{dip}})}\ . \end{aligned} \tag{4.6}$$

Three terms contribute to the spin wave energy. $E_{\mathrm{ex}} = Dq^2$ goes back to the exchange coupling, with the material specific *spin wave stiffness* $D = 2a^2 JS$, where a is the lattice parameter of a cubic lattice. It leads to the well known $\propto q^2$ spin wave behavior of a ferromagnet for small q values. The Zeeman gap $E_H = g\mu_0\mu_{\mathrm{B}} H$ is introduced by an external magnetic field. Lastly, the dipolar term $E_{\mathrm{dip}} = g\mu_0\mu_{\mathrm{B}} M(T,H)\sin^2(\theta_{\boldsymbol{q}})$ reflects the strength of dipolar interactions and is related to the spin wave stiffness via the dipolar wavevector q_{D} via

$$E_{\mathrm{dip}} = D(T) \cdot q_{\mathrm{D}}^2\ . \tag{4.7}$$

In the special case $H = 0$, the Zeemann term vanishes and without intentional preparation the magnetic domains can be assumed to be randomly oriented. Then the average of $\theta_{\boldsymbol{q}}$ over all domains yields $\langle \sin^2\theta_{\boldsymbol{q}} \rangle = \frac{2}{3}$. Therefore, the dispersion becomes isotropic and the measured spin wave energy only depends on the magnitude of the wavevector transfer q.

The treatment of spin waves in a ferromagnetic material assumes an (almost) fully ordered magnetic state, such that spin wave stiffness D_0 and magnetization M_{sat} essentially represent the quantities at $T = 0$. However, dynamical scaling theory addresses the temperature dependence of these quantities close to T_{C} postulating a power law

relation and the appropriate critical exponents. Hence,

$$M\ (T) = M' \cdot \left(\frac{T_\mathrm{C} - T}{T_\mathrm{C}}\right)^{\beta} \tag{4.8}$$

$$D\ (T) = D' \cdot \left(\frac{T_\mathrm{C} - T}{T_\mathrm{C}}\right)^{\mu} \tag{4.9}$$

with β being the critical exponent of the magnetization and $\mu = \nu' - \beta$ being the exponent for the spin wave stiffness [109, 111] as derived from dynamical scaling theory. ν' is the critical exponent of the correlation length for $T < T_\mathrm{C}$. Here, the introduction of the *primed* quantities M' and D' highlights that they do not correspond to the $T = 0$ values, because the scaling behavior is only valid close to T_C.

The exact numerical value of any critical exponent needs to be calculated from microscopic theories for subsequent comparison with measurements. However, a variety of models lead to the same set of critical exponents and are subsequently grouped in universality classes. In this sense the critical exponents are denoted *universal*. Therefore, the numerical values of the critical exponents does not depend on the details of the microscopic interaction, but on fundamental properties such as the dimension of space and the dimension of the order parameter, which is here usually referred to as the spin dimensionality. Further important parameters are the range of the magnetic interactions and whether the order parameter is conserved.

The n-vector model covers many cases of microscopic model Hamiltonians [99] and using the results of Guillou *et al.* as an example we take $\nu' = 0.7054$ and $\beta = 0.3647$ to arrive at $\mu = 0.3407$ [112]. Instead of using elaborate renormalization group calculations for the 3D isotropic nearest neighbor Heisenberg model, Halperin estimated $\mu \approx 1/3$ from mean-field exponents [111]. Accordingly, a slight temperature dependence of $q_\mathrm{D}^2 \propto t^{\beta-\mu}$ would be expected.

Furthermore, deep in the spin wave region dynamical scaling theory predicts the dependency of the inverse lifetime or rather linewidth $\Gamma(\boldsymbol{q})$ of the spin waves on the correlation length ξ and the wavevector transfer q to be

$$\Gamma(\boldsymbol{q}) \propto \xi^2 q^2 \ . \tag{4.10}$$

This differs somewhat from the result of Harris [113], who derived a $q^4 \ln(1/q^2)$ dependency for a Heisenberg system in the long wavelength limit. In the case of small q the behavior approximately follows the expression

$$\Gamma(\boldsymbol{q}) = \Lambda q^{5/2} \ , \tag{4.11}$$

which is often referred to in spin wave damping studies [83, 114]. Consequently, the line shape function, which appears in the DDCS of INS from spin waves, can no longer be regarded as two symmetric Dirac-δ distributions in reciprocal space, but rather the function

$$f_{q\xi}(s) = \frac{1}{\pi} \frac{\eta_q}{(s^2-1)^2 + \eta_q^2} \ . \tag{4.12}$$

with $s = \omega/\omega_c$ being the ratio of scanned frequency ω and the characteristic frequency ω_c of a fluctuation mode of the system and η_q being the width parameter of the function. At this point it should be reiterated that the dynamical scaling theory predictions are ignorant regarding microscopic details of the model Hamiltonian. Therefore, experimental studies on dipolar ferromagnetic systems, where long range interactions are present, are of interest to test the limits and capabilities of dynamical scaling theory.

4.1.2. Transition region

Revisiting the definition above, the transition region as shown in figure 4.1 corresponds to $q > \kappa$ and $T \approx T_C$. Occasionally, it is also referred to as the *critical region*, which is more broadly used to describe a region where critical phenomena are pivotal to the behavior of the correlation function. Using this terminology, critical region corresponds to all portions in (q, T) space, where the length scales ξ and q^{-1} are macroscopic in relation to inter atomic or interaction distances.

As assumed in the framework of dynamical scaling, a system is fully characterized by its behavior in the three regions, which are depicted in figure 4.1. Any dominating mode, such as collective exciations in spin wave region, will continue arbitrary close to the critical temperature T_C without changing its fundamental character. However, when approaching T_C at fixed q, corrections on the order $(q\xi)$ become important. These correction terms can be suppressed by performing measurements at long enough wavelength. At the critical point, ξ diverges and the so far valid description breaks down. Besides this singularity, the dynamical scaling hypotheses rests on the assumption that anywhere else in the (q, T) plane $(q \neq 0)$, the correlation function varies smoothly. At the boarders $q = \kappa = \xi^{-1}$ separating the regions, the mathematical description of the system asymptotically matches. Therefore, if the asymptotic behavior of the characteristic frequency $\omega_c(\boldsymbol{q})$ in the spin wave region is known, it coincides with the characteristic frequency in the transition region [111]. Hence, the characteristic frequency of the magnetization, often interpreted as the inverse lifetime of the fluctuation of the order parameter, is expected to follow

$$\omega_c(q) = \Gamma(q) = \Lambda \cdot q^{(5-\eta)/2} + O\left(\frac{\kappa}{q}\right) \xrightarrow{T \to T_C} \Lambda \cdot q^{5/2} \ . \tag{4.13}$$

The critical exponent $\eta = 0.034$ is essentially negligible for a 3D Heisenberg system.

In contrast to the spin wave region (see equation 4.12), the scaling hypotheses does not specify the shape function $f_{q\xi}(x)$. Possible line shapes can be found in figure 3 of the publication by Halperin *et al.* [111]. Beyond that, renormalization group theory allows calculation of this very function in the limit of $T = T_C$ $(\xi \to \infty)$. The analytical representation given by

$$f_{q\xi=\infty}(q, \omega) = \frac{1}{\pi \cdot \Lambda q^{5/2}} \Re \left\{ \frac{1}{is + \alpha \left[1 + i(\alpha/a)s\right]^{-0.6}} \right\} \ , \tag{4.14}$$

where $\Re\{\cdots\}$ returns the real part of a complex function, $s = \omega/\omega_c$, $\alpha = 0.78$ and $a = 0.46$ [107, 115].

4.1.3. Hydrodynamic region

The hydrodynamic region (see figure 4.1) of a ferromagnet largely coincides with its paramagnetic state and describes the dynamical and transport properties of spin fluctuations. Here, the inverse lifetime of the critical fluctuations are slightly modified compared to the case of $T = T_C$ by introducing the *dynamical scaling function* (DSF) $\gamma(\kappa/q)$. Thus, the linewidth of an isotropic Heisenberg ferromagnet can be expressed as

$$\Gamma(q) = \Lambda\gamma(\kappa/q)q^{5/2} \ , \tag{4.15}$$

where Λ again determines the frequency scale of the decaying fluctuations and in case of magnetic systems contains the strength of the exchange interaction J.

Exploiting the fact that at the Curie temperature $\gamma(\kappa/q) = 1$, it is possible to extract the dynamical scaling function, by normalizing equation 4.15 to the linewidth at T_C (see equation 4.13) such that

$$\frac{\Gamma_{T^+}(q)}{\Gamma_{T_C}(q)} = \gamma(\kappa/q) \ , \tag{4.16}$$

which encapsulates the entire temperature dependence in terms of the inverse correlation length κ. T^+ indicates a temperature just above T_C. While dynamical scaling theory constraints the properties of $\gamma(\kappa/q)$ by requiring it to be a homogeneous function, which allows the determination of its asymptotic behavior, the form at any value of the scaled variable $x = \kappa/q$ is not known.

Using a mode-coupling (MC) approach for the treatment of the time dependent spin correlation function, Résibois and Piette deduced an integral equation for $\gamma(x)$ of an isotropic Heisenberg system that satisfies the asymptotic scaling behavior

$$\gamma(x) \to 1 \text{ for } x \to 0 \tag{4.17}$$

$$\gamma(x) \propto x^{1/2} \text{ for } x \to \infty \ , \tag{4.18}$$

but can only be computed numerically [116]. Studying the critical dynamics in iron, Mezei [100] proposed a useful analytic approximation of $\gamma(x)$ expressed as

$$\tilde{\gamma}(x) = 0.4284x^{1/2} + \exp\left(-0.4284x^{1/2} - 2.4x + 0.7x^2 - 0.2x^4\right) \ . \tag{4.19}$$

Similarly, Iro found a solution for $\gamma(x)$ via renormalization group theory calculations, which also yielded an expression for the dynamical shape function $f_{q\xi}(s)$ explaining the difference between measured neutron scattering intensity distribution and a Lorentzian peak used in the analysis. Since the expressions for $\gamma(x)$ and $f_{q\xi}(s)$ require a set of numerous equations, these have been put in appendix B.1 for clarity.

Increasing number of experimental results gathered on typical ferromagnets Fe [100], Co, Ni [107, 114], EuS [117] and EuO [118, 119] supported the general notion of the dynamical scaling hypotheses and the prediction of the dynamical scaling function by Résibois and Piette. Discrepancies however were especially dominant in systems EuO [103] and EuS [103, 117], which are known to harbor significant dipolar coupling besides

the dominant exchange interaction [105]. To resolve these issues, a theoretical framework for calculating the dynamical scaling function in the presence of dipolar interaction was developed by Frey and Schwabl on the basis of a mode-coupling ansatz.

The result, alike the ones before, can not be summarized in an analytical form, but only calculated numerically. The starting point is a set of two coupled integral equations, which express the inverse lifetime for longitudinal and transversal fluctuations $\Gamma^{\mathrm{L}}(x)$ and $\Gamma^{\mathrm{T}}(x)$ respectively, as a sum over all possible decay modes [120, 121]. In essence Frey and Schwabl predict, that the dipolar wavevector enters into the dynamical scaling function such that linewidth [101, 122] of the critical fluctuations ($\alpha = L, T$) is given by

$$\Gamma^{\alpha}(q) = \Lambda\gamma^{\alpha}(\kappa/q, q_{\mathrm{D}}/\kappa)q^{5/2} \ . \tag{4.20}$$

The ratio q_{D}/κ introduces a temperature dependence such that one obtains an array of curves, which reflects the observed critical dynamics well [101, 117, 122]. In the isotropic limit, meaning vanishing dipolar interactions, the theory of Frey and Schwabl reproduces the Résibois-Piette scaling function.

4.2. MIEZE measurements of Ni

Treating nickel as an isotropic Heisenberg type ferromagnet and subsequent interpretation of experimental results with the above introduced theoretical framework has produced good agreement over a large range of momentum and energy transfers above and below the Curie temperature [107, 108]. Given the fact that EuS, EuO and especially Fe clearly indicate the presence of dipolar contributions influencing their static and dynamic properties, Ni is expected to behave similarly. The lack of a pronounced signature could be explained by the comparably small value of $q_{\mathrm{D}} = 0.013\,\text{Å}^{-1}$ [123], which is on the limit of the instruments used in past measurements.

With increasing capabilities of modern neutron spectrometers, energy and momentum resolution became sufficient to reexamine the influence of dipolar interactions in nickel by MIEZE spectrometry. This chapter is concerned with presenting the measurements performed at the MIEZE spectrometer RESEDA at the Research Neutron Source Heinz Maier-Leibnitz (FRM II).

4.2.1. Nickel sample

The sample used in the presented study was a pure ^{64}Ni single crystal shaped like a droplet. The sample is 20 mm long with a diameter of about 13 mm for the thicker part of the drop shaped part, allowing for a $10 \times 10\,\text{mm}^2$ beam spot. The sample is a single crystal, but it has been mounted in an arbitrary orientation. Isotopic analysis shows 98.15 % purity of ^{64}Ni with any Ni isotope being less abundant than 0.85 % and any contamination of other elements < 0.2 %. An isotopically pure sample was chosen to minimize the isotope dependent absorption and nuclear coherent scattering cross section [52].

The sample holder, connecting crystal and high temperature sample environment, consisted of two stainless steel plates and four screws. A hole in the center of each

plate fixed the lateral movement of the sample after tightening the screws clamping it in place. The thicker, upper plate had an M8 inner thread to screw the sample holder onto the ceramic sample stick of the furnace. Being hollow, a thermocouple (type C) [46], which was 3 mm longer then the stick itself, was inserted through the sample stick to contact the sample. Since the thermocouple is rigid, fastening the sample tightly ensures thermal contact between sample and temperature sensor. A picture of the sample inside its holder is shown in figure 4.2 (a) and a sketch, which depicts the holder attached to the sample stick, is shown in figure 4.2 (b). A gray scale image taken by a neutron camera, which displays the sample in the neutron beam, is put beneath the sketch.

4.2.2. Experimental setup and data acquisition

RESEDA is set up in its standard SANS configuration, in which the primary spectrometer arm defines the geometry of the beam with two square slits, separated by 4.4 m. Both were set to $10 \times 10\,\mathrm{mm}^2$. A $40'$ collimator was used to remove the double reflection of the neutron guide.

For the experiment, pre-tuned MIEZE times τ_M could be used ranging from 10^{-4} ns to 1 ns. The triangular wavelength distribution of the velocity selector is centered at $\lambda_0 = 6.0\,\text{Å}$ and has an acceptance window of $\frac{\Delta\lambda}{\lambda} = 0.12$.

The fast, time resolving position sensitive detector (PSD), also referred to as CASCADE, is located 3.43 m behind the sample position with an active detection area of $200 \times 200\,\mathrm{mm}^2$. High neutron count rates can induce faulty signal in neighboring detector pixels, which is why the direct beam (DB) is blocked by a circular beam stop. The sketch in figure 4.3 shows the scattering geometry of the experiment. Neutrons scattered by a small angle $2\theta_\mathrm{S}$ pass the beam stop and get registered by the time resolving PSD. The colors indicate different values of the transverse momentum transfer $q_\perp$ with respect to the direct beam.

Experimental determination of T_C was done by observing the critical magnetic scattering integrated in a region of interest (ROI) around the direct beam spot on the CASCADE detector. As a function of temperature the intensity exhibits a maximum, as the magnetic susceptibility $\chi(T)$ diverges at T_C. The temperature was ramped with a rate of 0.2 K/min and a neutron counting time of 30 s per point. One cycle of cooling and heating through the Curie point is depicted in figure 4.4, as well as the ROI used for integration. While the signal is weak, but still unambiguous, no hysteresis was observed over several temperature sweeps confirming temperature stability.

The absolute value of the Curie temperature was 21.4 K lower then $T_\mathrm{C}^\mathrm{Ni} = 358.28(4)\,^\circ\mathrm{C} = 631.39(4)\,\mathrm{K}$ reported recently [124]. This discrepancy is attributed to the thermocouple being not properly contacted to the sample, but instead contacting the inner thread of the sample holder. The sample holder lies outside of the volume experiencing optimal heating[3]. Due to the small contact area with the sample heat is not well transported between sample and the holder. Since heat is transferred exclusively via radiation, it is plausible that the sample holder has a significantly lower temperature.

3 Private communication with sample environment responsible M. Antic.

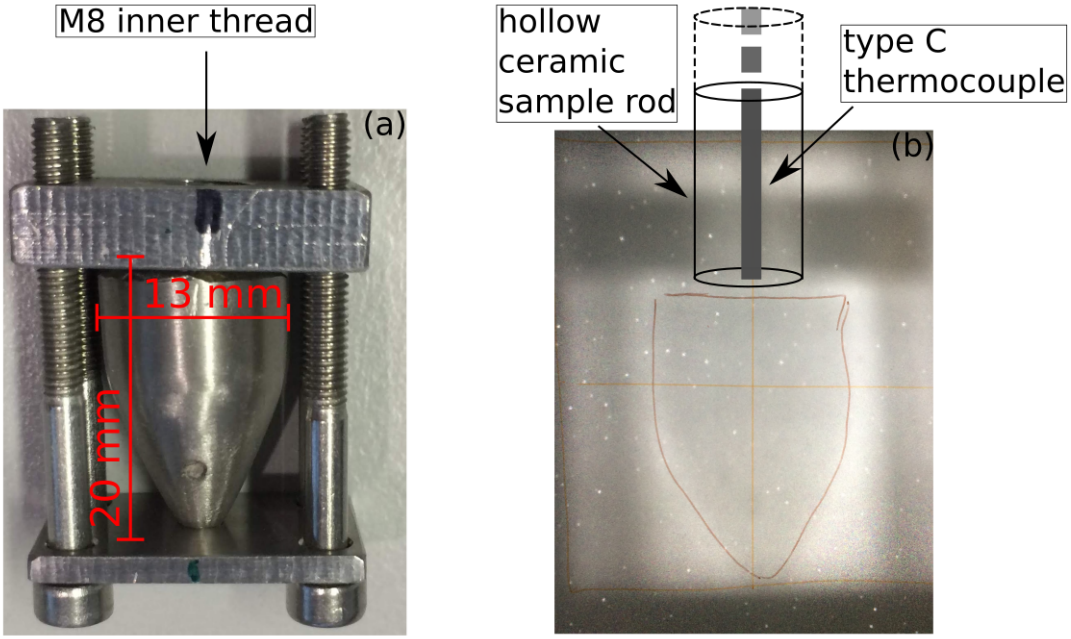

Figure 4.2.: The Ni sample has a drop like shape with a height of $20\,\mathrm{mm}$ and a diameter of $13\,\mathrm{mm}$ at the widest point. Depicted in (a), the sample was fixed in place by tightening four screws and clamping two plates with the sample in the middle together. Each plate had a hole in the center preventing lateral movement. The hole in the upper plate had an M8 inner screw thread, which could be connected to the ceramic sample stick of the furnace. This is indicated by the sketch in (b), where the type C thermocouple inside the sample stick is visualized as well. When screwing the sample to the stick, the thermocouple is pressed on top of the sample reading its temperature. In (b) the gray shaded areas show the sample inside the holder as seen by a neutron camera in transmission geometry.

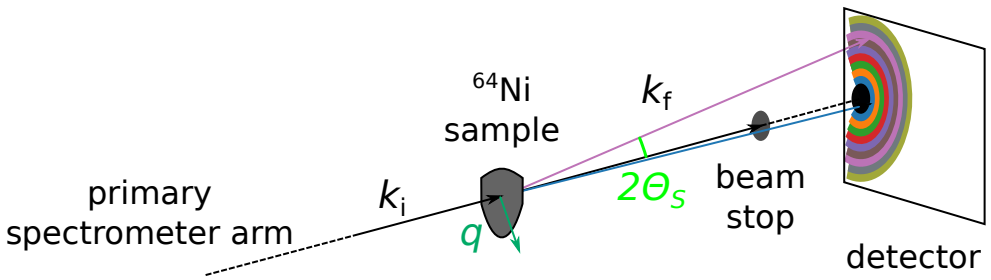

Figure 4.3.: Sketch of the experiment geometry. RESEDA is set up in a small-angle scattering geometry. After passing through beam preparation and collimation elements, the scattered neutrons, which experience a small transverse momentum transfer are detected by the PSD. Different $q_\perp$ values are indicated as colored rings on the detector area. Neutrons not deflected from the incoming beam direction are absorbed at the beam stop.

Repeated observations, which did not reveal any temperature drift over time, when changing temperature with small ramping speeds, indicated that the offset is constant and temperature independent in the narrow range around T_C relevant for the study.

In total, MIEZE data was acquired after adjusting the sample's temperature to a value $T = T_C + \Delta T$ with $\Delta T \in [-2\,\mathrm{K}, -1\,\mathrm{K}, 0\,\mathrm{K}, 1\,\mathrm{K}, 2\,\mathrm{K}, 4\,\mathrm{K}]$ and T_C is the experimentally detected temperature value by critical scattering. For each T and τ_M the counting time was set to 1 h, which achieves high enough counting statistics for a reliable contrast determination at large q values. Additionally, background data was recorded at $T = T_C + 30\,\mathrm{K}$, at which no magnetic dynamics could be observed and changes in the contrast originate from the geometry of the sample and the high temperature setup. Lastly, the time resolution of the instrument was measured with a graphite reference sample.

4.2.3. Data reduction

While being a powerful and versatile measurement technique, raw MIEZE data is significantly less intuitive to analyze than three-axis or diffraction data. At RESEDA, data acquisition for one τ_M value produces a four-dimensional data set, with one time dimension from binning the periodic intensity signal. Two dimensions correspond to the x and y coordinate of the PSD and the fourth dimension arises from the fact that within the detector 8 thin, boron coated foils are used to register the neutrons individually. Generally, it is necessary to measure a sample at many values τ_M to reconstruct its contrast function $C(\tau_M)$ adding one additional dimension. Transforming this space and time information into the more approachable momentum and energy domain requires four major processing steps to arrive at an interpretable result:

(i) The selection of ROIs on the detector area in which data processing should occur

(ii) The contrast $C(q, \tau_M)$ determination from the time modulated neutron intensity signal within these ROIs

(iii) The calculation of the associated wavevector transfer q.

(iv) The extraction of relevant physical quantities by fitting appropriate models to the $C(q, \tau_M)$ curves.

In the following paragraphs, the data reduction scheme for the performed experiment is elaborated on, as it encompasses a few non-standard steps for intricate data sets.

Regions of interest

The software package MIEZEPY [125] is a dedicated tool for processing the data contained in the *.tof* files, which are generated by the NICOS instrument operation software [126] from the raw data of the CASCADE detector. Therefore, MIEZEPY addresses the steps (i) and (ii) in the data reduction scheme. It groups a number of single files, classified by the same set of external parameter, such as temperature, B-field, etc., in addition to the underlying five-dimensional data set, which are the MIEZE time τ_M, index of the detection foil, index of the time bin and pixel coordinates in x, y.

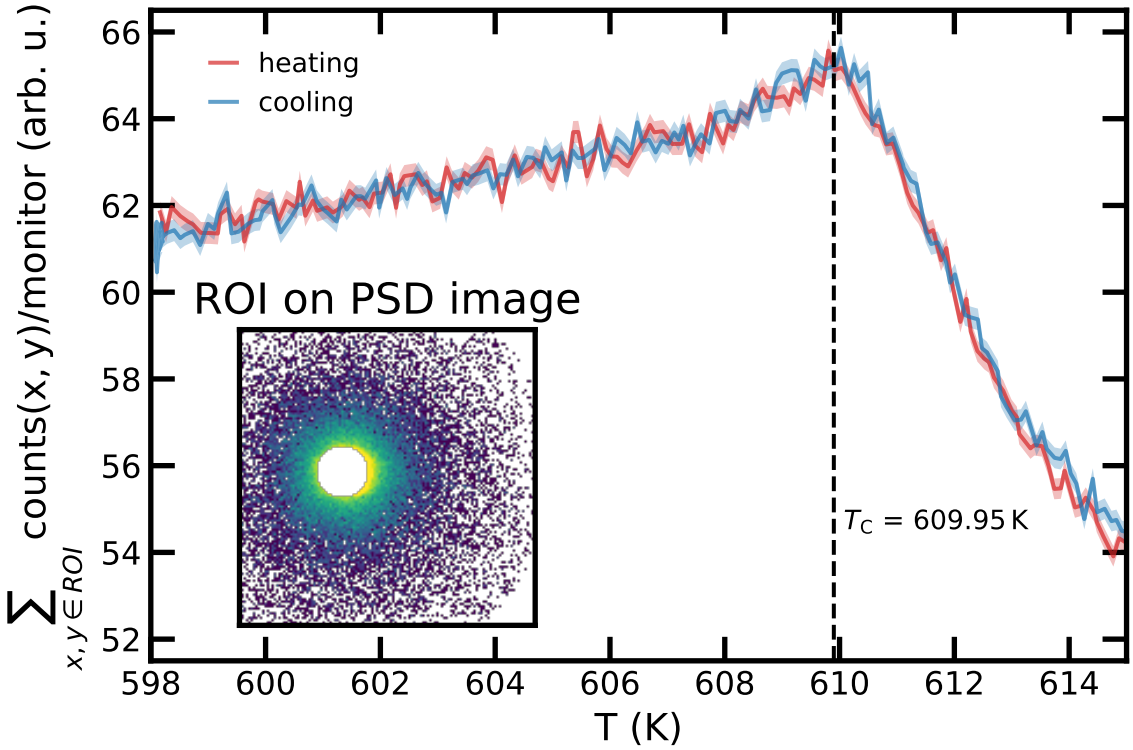

Figure 4.4.: Determination of the Curie temperature via critical, magnetic small angle scattering around the direct beam. With the static magnetic susceptibility χ diverging at the Curie temperature T_C critical scattering peaks at $T = 609.95\,\mathrm{K}$. Observed by varying temperature with a rate of $0.2\,\mathrm{K/min}$ and integrating all scattered neutrons in the region shown in the insert and over $30\,\mathrm{s}$, normalized to monitor. No hysteresis is apparent over multiple temperature cycles.

After organizing the data either manually in a graphical user interface (GUI) or scripting in the *Python* programming language, ROIs, also referred to as (q-)masks, are chosen. These ROIs generally serve two purposes. They are used to group pixels on the detector for phase correction calculations and also to integrate neutron counts prior to the contrast calculation. A graphical representation is shown in figure 4.5, which shows an exemplary 2D neutron distribution measured with the CASCADE detector. The data is overlaid with a set of circle segments, q-masks, utilized for the aforementioned integration of neutron counts. Each mask represents a different, average scattering angle or rather q value, which can be calculated via

$$q_{\mathrm{el}} = \frac{4\pi}{\lambda} \sin\left(\frac{2\theta}{2}\right) , \tag{4.21}$$

where the subscript 'el' expresses the assumption of strictly elastic scattering. As introduced in chapter 2, λ is the wavelength of the incoming neutrons and 2θ the scattering angle. In INS studies the energy transfer is per definition not negligible, which is why the correct momentum transfer can be determined after extracting the energy

transfer value. We will revisit this in step (iii).

The selection of ROIs is not a standardized procedure and needs to satisfy various constraints, which depend on the particular experiment and sample. Having nickel as a sample, where INS due to spin waves is expected below T_C, a mask corresponding to a q value should contain a signal corresponding to an energy transfer dictated by the dispersion relation. A broad ROI averages over a broad band of q values, which results in measuring an increasingly smeared out energy spectrum, and thus counterproductive for a high resolution measurement. In opposition, ROIs with a small area contain a less intense neutron signal, adversely affecting the contrast determination and extraction of physical parameters from the final $C(q, \tau_M)$ curves. Thus, a compromise between these inverse effects on signal analysis needs to be found. Lastly, the geometric shape of ROIs needs to reflect the symmetry of the measured system.

For that reason, the ROIs, depicted as colored areas in figure 4.5, are arcs of increasing radius with their center coinciding with the center of the DB. They describe areas of equal, total wavevector transfer q and take advantage of the isotropic scattering from randomly oriented magnetic domains ($T < T_C$) or unordered spins ($T \geq T_C$), by integrating the signal over a large area. The increasing width of the ROIs is owed to the decreasing neutron count rate further from the DB center.

Constrast fitting

Step (ii), the determination of the contrast in each ROI begins with a phase correction procedure. The phase correction is necessary to mitigate instrument dependent reduction in the contrast from flight time differences of the neutrons, which are solely determined by the instruments geometry and its components. Two main reasons, the flight path difference originating from a planar PSD and the height profile of the detection foils inside the CASCADE detector, have been identified. A detailed explanation of the correction techniques is given in [125].

At this point, a superficial description of these techniques should suffice. The ROI under investigation is subdivided into groups of multiple pixels, to which the phase correction scheme will be applied. The grouping needs to balance the number of pixels per group, which ensures higher counting statistics and thus improved reliability of the correction algorithm, against the inaccuracy of the correction result, which increases with the integration area on the detector. Therefore, in the high intensity regions on the detector 5-10 pixels per group are sufficient, while 30 or more pixels are required far from the beam center. As for the ROI selection, the exact grouping also depends on the individual experimental setup and sample. The correction is calculated and applied to each data set corresponding to τ_M individually. As a result, the time signal in each pixel is shifted, such that the time modulated signal everywhere has the same phase.

Subsequent to the phase correction of every data set, including background and resolution, the background is subtracted from the data, for each point in the 5D (τ_M, foil index, time bin index, x, y) parameter space. This procedure ensures that only the sample signal remains for further analysis.

In the next step, the contrast $C(\mathrm{ROI}, \tau_M)$ is calculated using the phase corrected and background subtracted data as well as the resolution data set. After the phase correction

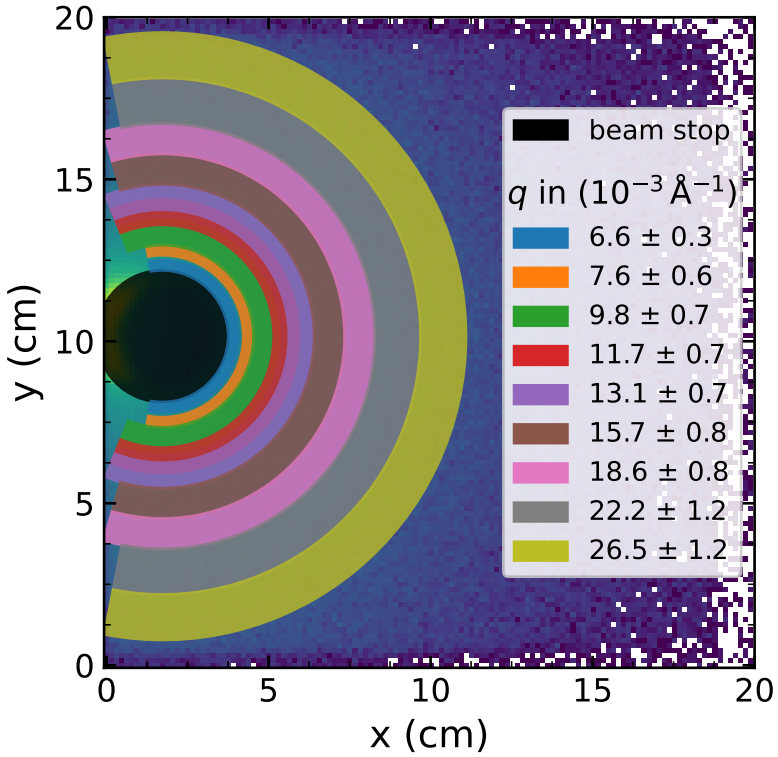

Figure 4.5.: Active detection zone of the CASCADE detector. The background shows a neutron distribution obtained by scattering from the Ni sample. The black, circular area represents an area, where no data reduction is performed and the direct neutron beam is blocked by a physical beam stop in front of the detector. The colored, concentric rings correspond to the ROIs (q-masks) utilized in the data reduction. The associated q_{el} values are calculated with equation 4.21.

the neutron data can be integrated over all pixels within one ROI, without averaging out the contrast signal in the process. This increases the neutron counts in each time bin significantly allowing a reliable fit of

$$N_{\mathrm{n}}(t_i) = A \cdot \sin\left(\frac{\pi}{8} t_i + \phi\right) + y_0 \tag{4.22}$$

to the data. A is the amplitude of the oscillation, y_0 the mean value and ϕ the phase. The frequency is fixed to $\pi/8$ because the detector was set up to record one period of the signal in 16 bins. As introduced in equations 3.33, 3.34 the ratio A/y_0 yields the contrast. Exemplarily, this process is shown in figure 4.6 for a simulated $C(\tau_{\mathrm{M}})$ curve in subplot (b). The contrast points colored red and blue in (b) correspond to the cosine signal in subplot (a), where the amplitude A and average value y_0 are drawn in.

The obtained contrast captures the dynamics of the sample, but is damped by the instrumental resolution, which is a function of (q, τ_{M}) and needs to be measured alongside

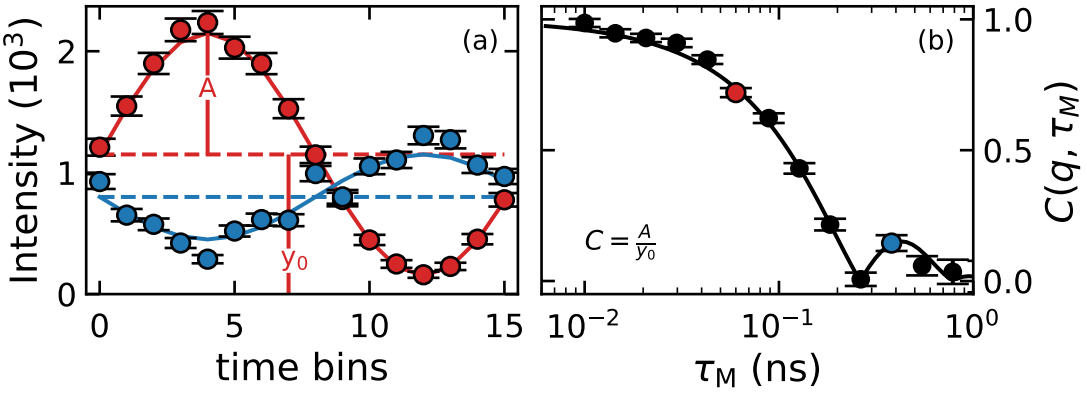

Figure 4.6.: Simulated MIEZE signal and data reduction visualization. (a) Shows the time binned MIEZE signal for two τ_M and the fitted cos curve. (b) Simulated $C(\tau_M)$ curve where the red and blue data points correspond to the contrast extracted in (a).

the actual sample to correct for the damping

$$C_{\text{sample}}(\text{ROI}, \tau_M) = \frac{C_{\text{measured}}(\text{ROI}, \tau_M)}{C_{\text{resolution}}(\text{ROI}, \tau_M)} \,. \tag{4.23}$$

As mentioned above, the resolution data were taken with a graphite reference, which scatters the neutrons elastically in forward direction and illuminates the detector homogeneously. This means, the energy spectrum is infinitely sharp at $\Delta E = 0$, which translates to a horizontal line ($C(\text{ROI}, \tau_M) = 1$) in the time domain measured with MIEZE. Every deviation from this behavior is a result of instrument performance that is corrected for by normalizing each contrast curve to the reference. All these steps are performed using MIEZEPY returning a $C(\tau_M)$ for each detection foil and ROI.

However, problems regarding the data acquisition in a particular foil or contrast fitting needed to be identified manually and the data of the affected detector foils is excluded if the error is not recoverable. The reliable contrast curves for each detector foil are averaged according to the total number of neutrons and the uncertainties are determined with inverse-variance weighting. The contrast curves $C\,(\text{ROI}, \tau_M \,|\, T, \boldsymbol{H}, p, ...)$ gained by the reduction process are ready to be analyzed to extract the physical parameters of interest.

Calculation of momentum transfer

Having touched on the determination of the momentum transfer q associated with a ROI, we will discuss the process in more detail, including a correction, which accounts for the deviations occurring for a planar detector rotatable around the sample position. The sketch in figure 4.7 serves as support for the explanation. It shows a top view of the scattering geometry behind the sample, where the dotted black line represents the DB passing through the sample, the blue line represents the planar detector surface and the green line a possible neutron flight path after scattering with angle 2θ. The orange line indicates the normal of the detection plane connecting its center with the sample

position. The sample-detector-distance is fixed to $l_{\mathrm{SD}} = 3.43\,\mathrm{m}$ under rotation of the secondary spectrometer arm by angle α. Finally, δ is the distance of any pixel on the detector to the DB center within the detection plane.

The wavevector transfer for a SANS-like instrument with a PSD can be computed as follows. Each pixel of a flat neutron detector can be associated with a scattering angle $2\theta = \arctan\left(\delta / l_{\mathrm{SD}}\right)$. With the assumption of $|\boldsymbol{k}_{\mathrm{i}}| = |\boldsymbol{k}_{\mathrm{f}}|$ the wavevector transfer is given by 4.21. Once $\alpha \neq 0$, δ is no longer perpendicular to the DB, which makes the arctangent relationship invalid. Instead simple geometric considerations yield a cumbersome determination equation for 2θ, which reads

$$\left(\frac{\delta}{l_{\mathrm{SD}}}\right)^2 = Z^2 - Z\frac{\cos(2\theta)}{\cos(\alpha)} + \frac{1}{\cos^2(\alpha)}, \tag{4.24}$$

with the Z being a representation for

$$Z = \left(\cos(2\theta)\cos(\alpha) + \sin(2\theta)\sin(\alpha)\cos(\Phi)\right)^{-1} \quad . \tag{4.25}$$

Except for special cases, equation 4.24 can not be solved analytically, but numerically, for the scattering angle 2θ and subsequently the wavevector transfer can be computed for each pixel on the detector. At that point, the average wavevector transfer $\bar{q}$ and its variance σ_q^2 can be calculated for each ROI, which is now also indicated by $C(\mathrm{ROI}, \tau_{\mathrm{M}}) \rightarrow C(q, \tau_{\mathrm{M}})$, where we omit the bar indicating the average. The interested reader will find a derivation of equation 4.24 in appendix B.3

Since we are measuring inelastic scattering from spin waves, it is necessary to go

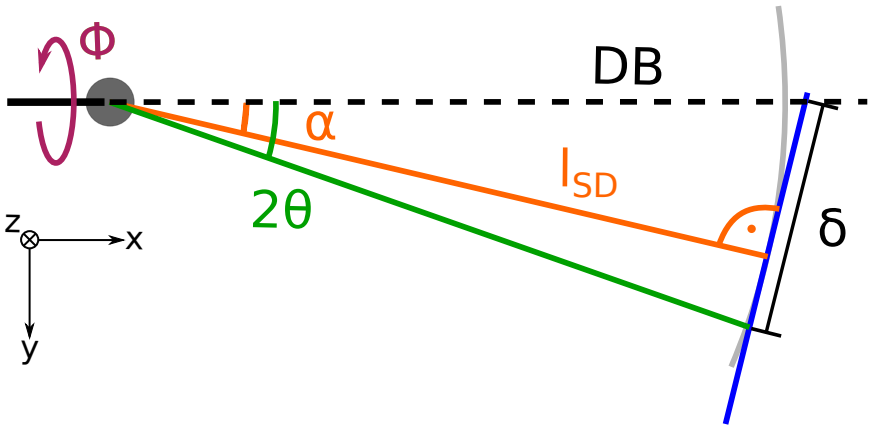

Figure 4.7.: Sketch of the secondary spectrometer arm of RESEDA for q_{el} calculation. The incoming neutrons from the left side are scattered at the sample position (dark grey circle) by an angle 2θ (and Φ) or transmitted before hitting the detector (blue line). The transmitted neutrons in the DB are indicated by the broken, black line. The distance δ between a neutron registered by the detector and the direct beam is used to calculate 2θ or rather q_{el} geometrically. As the center of the detector is rotated around the sample (grey curve), meaning $\alpha \neq 0$ and δ is no longer perpendicular to the DB, 2θ has to be a solution of equation 4.24 and needs to be calculated numerically. This gives small corrections to q computed from a simple $\arctan$ relation.

beyond the elastic limit and consider finite energy transfer. As a result, the final wavevector of a scattered neutron is calculated via

$$k_\mathrm{f} = \sqrt{\frac{2m_\mathrm{n}}{\hbar^2} \cdot \left(\frac{\hbar^2 k_\mathrm{i}^2}{2m_\mathrm{n}} - \Delta E \right)} \; . \tag{4.26}$$

Therefore, the wavevector transfer follows from the law of cosines

$$q_\mathrm{inel} = \sqrt{k_\mathrm{i}^2 + k_\mathrm{f}^2 - k_\mathrm{i} k_\mathrm{f} \cos(2\theta)} \; . \tag{4.27}$$

At this point, it is has to be noted, that for inelastic scattering step (iii) and step (iv), as defined at the beginning of section 4.2.3, are no longer independent of each other and a self consistent treatment might be necessary.

Physical parameter extraction

Analysis of the contrast curves $C(q, \tau_\mathrm{M})$ acquired by reduction of the raw MIEZE data can be done in various ways, e.g. having an appropriate description of the investigated system in the time domain allowing a direct comparison. It is equally possible to transform the contrast data into the (q, E) space achieving high resolution measurement of the dynamical structure factor $S(q, E)$. Here, we apply a third strategy, resembling the analysis of TAS data. Assuming a basic model for the dynamical structure factor $S(q, E)$ for the different temperature regimes discussed in 4.1, we extract the linewdith and excitation energy by transforming $S(q, E) \longrightarrow C(q, \tau_\mathrm{M})$, which is introduced in section 3.2.2, and fit the obtained contrast curve to the measured contrast data.

For the spin wave measurements at temperatures below T_C, the Lorentzian line shape was chosen, since it was repeatedly employed for similar investigations in ferromagnetic systems. Thus, comparability for the data analysis and subsequent discussion is assured. The line shape derived by Iro on the basis of asymptotic renormalization group theory (ARG) has been successfully employed by Böni *et al.* [107] in the analysis of paramagnetic scattering in Ni, therefore it is reasonable to utilize it here as well instead of the Lorentzian line shape. The ARG expression is valid for $T > T_\mathrm{C}$. To visualize the difference between these shape functions in figure 4.8, the approximation of equation B.1, which was proposed by Iro in [127] and the analytical expression for $T = T_\mathrm{C}$ (see equation 4.14) are compared to the Lorentzian distribution (see equation 3.41). All functions have a characteristic frequency $\omega_\mathrm{c} = \Gamma = 20\,\mu\mathrm{eV}$. Adequate for the study presented here, the temperature $T = T_\mathrm{C} + 1\,\mathrm{K}$, wavevector transfer $q = 0.01\,\mathrm{\AA}^{-1}$, inverse correlation length $\kappa(T) = 0.009\,\mathrm{\AA}^{-1}$ and the frequency scale $\Lambda = 350\,\mathrm{meV\AA}^{2.5}$ were chosen in compliance with the values published by Böni *et al.* [114] for nickel. This comparison demonstrates the importance of the suitable shape function to correctly extract the linewidth parameter. Even though each function was calculated with the same linewidth, the exact shape in the energy domain fundamentally changes the decay behavior observable in the time domain. The long tail of the Lorentzian shape function results in a more gradual decline in the corresponding contrast curve, compared to the two other functions, whose intensity of $S(q, E)$ drops to 0 exponentially.

While the theoretically calculated curves in the time and energy domain in figure

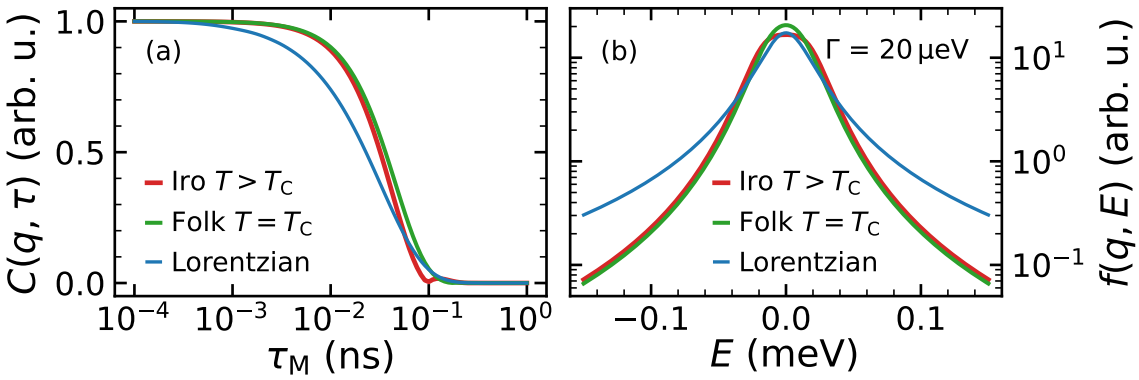

Figure 4.8.: Comparison of commonly used Lorentzian lineshape function with a lineshape derived by Folk [115] and Iro [127] based on renormalization group theory. Subplot (b) shows the (dynamical) line shape functions in energy space, as they would be observed in constant-Q scans on a TAS. The corresponding contrast curve in (a) can supposedly be measured at RESEDA, was calculated according to equation 3.39. All curves were calculated with the same characteristic frequency $\omega_c = \Gamma = 20\,\mu\text{eV}$. The temperature $T = T_C + 1\,\text{K}$, wavevector transfer $q = 0.01\,\text{Å}^{-1}$, inverse correlation length $\kappa(T) = 0.009\,\text{Å}^{-1}$ and the frequency scale $\Lambda = 350\,\text{meVÅ}^{2.5}$ were chosen in compliance with the values published by Böni *et al.* [114] for nickel. The integral of each curve in the depicted energy interval was normalized to 1.

4.8(a) and 4.8(b) respectively, can easily be distinguished visually if the number of calculated points is large enough, this is not necessarily the case when data is taken at an instrument. An observed signal is reliable, where the neutron intensity is large and thus the relative error low. For a MIEZE instrument this means small τ_M, where the contrast is high, whereas for TAS this region is around the peak center. That is why the MIEZE technique is sensitive to the tails of the dynamic structure factor, which can be associated with the onset of the decay of the contrast curve. At these high energy transfers, the counting statistics in a TAS experiment would make a distinction between the line shapes challenging. Converse to that, TAS might be better suited to resolve the peak shape close to the center. Due to the contrast value being similar to its uncertainty at large τ_M, this might be unfeasible with the MIEZE technique.

Figure 4.9 shows the results of fitting the linewidth and spin wave energy, if applicable, for three distinct temperatures $T - T_C \in [-2\,\text{K}, 0\,\text{K}, 1\,\text{K}]$, providing an example for each dynamical regime. The left column shows the MIEZE contrast data with the best fit acquired for equation 3.39 using the line shape functions described above. For the $T = T_C - 2\,\text{K}$, the peak position $(\pm)\,\omega_q$ and the linewidth Γ_q were taken as free parameters, while for $T \geq T_C$ only the characteristic frequency $\omega_c = \Gamma_q$ was fitted. Similar to the example shown in figure 4.8, Λ and $\kappa(T)$ have been taken from literature, whereas q was determined as explained in section 4.2.3. Since the Lorentzian line shape function, which is used for the analysis of the spin wave data, in itself is not directly dependent on q, no self consistent determination of q_{inel} is required.

The same procedure was used for the analysis of the remaining data at temperatures $T - T_C \in [-1\,\text{K}, 2\,\text{K}, 4\,\text{K}, 8\,\text{K}]$. Their visualizations have been put in the appendix

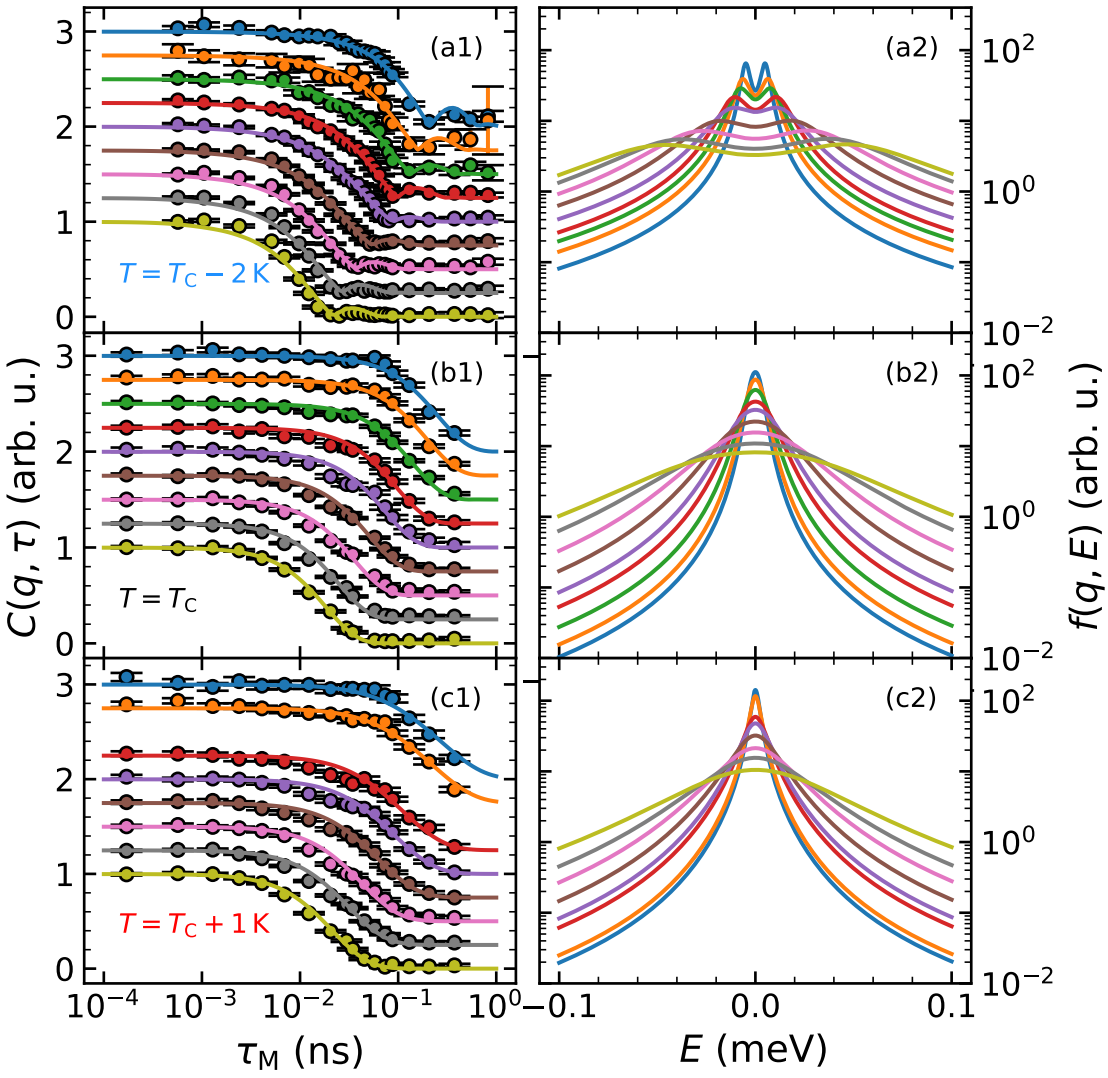

Figure 4.9.: Six panels showing the extraction of characteristic frequencies ω_c and spin wave excitation energies $\hbar\omega_q$. On the left side, panels (a1), (b1) and (c1) show the contrast data for the temperature values $T_C - 2\,K$, T_C and $T_C + 1\,K$, respectively, as examples. The solid lines within these plots show the best fit to the data and were calculated as described in 3.2.2 using the appropriate shape function, which was elaborated on in the text. The corresponding line shape functions are shown to the right. The color scheme of the curves match the one chosen in figure 4.5.

section B.4 together with tables listing all the numerical values of the fitted parameters and their uncertainties.

The code used to calculate the transformation from $S(E)$ to $C(\tau_{\mathrm{M}})$ and to subsequently fit the contrast data has been made publicly available over the GitHub repository: `https://github.com/LukasBeddrich/modelmiezelb.git`

Statistical analysis and uncertainty estimation

Considering the fact, that the analysis of MIEZE involves several steps of numerical fitting it seems inevitable to discuss the associated uncertainties and their propagation through the analysis. In general, the uncertainty of any measurement is of statistical or systematic nature. While the first is based on the statistics of the observable, the latter is the result of insufficient calibration, ignored external parameters influencing the measurement but also biases introduced by the observer / analysis [128].

Systematic uncertainties are notoriously hard to quantify, but we will give arguments at which points of the analysis biases are introduced, which influence the values of the determined contrast values. Easier to handle are the statistical uncertainties, which can be captured more easily by numerical estimates.

Each determination of a physical parameter is done by fitting an appropriate model function $f(\boldsymbol{x}_i \,|\, \boldsymbol{a})$ to the experimental data. Here $\boldsymbol{x}_i$ represents a set of measurement conditions under which the observation y_i is made. $\boldsymbol{a}$ is the parameter vector, whose entries are optimized such that the χ^2 cost function is minimized.

$$\chi^2 = \sum_{i=1}^{N} w_i \cdot \left[f(\boldsymbol{x}_i \,|\, \boldsymbol{a}) - y_i \right]^2 \longrightarrow \min \tag{4.28}$$

also includes a weight factor w_i, which expresses the reliability of the observation y_i. For every fit performed here, the optimal set of parameters has been determined by minimization of the χ^2 function in equation 4.28 using the a *Python* wrapper *iminuit2* of the *Minuit2*, which is part of the *ROOT* data analysis framework developed at CERN [129, 130]. The specific minimization algorithm is *MIGRAD*.

In theory, the weight of independent observations is equal to $w_i = k/\sigma_i^2$, where σ_i is the standard uncertainty of the distribution from which an observation y_i is drawn. In case the distribution is known $k = 1$, otherwise the σ_i express only a relative uncertainty between the observations. The least squares procedure yields an estimate of this factor k in terms of the *goodness-of-fit* measure

$$g_{\mathrm{fit}} = \frac{\chi^2}{n_{\mathrm{dof}}} = \frac{1}{n_{\mathrm{dof}}} \sum_{i=1}^{N} w_i \left[f(\boldsymbol{x}_i \,|\, \boldsymbol{a}) - y_i \right]^2 \ , \tag{4.29}$$

where n_{dof} is the number of degrees of freedom, meaning the number of observations is subtracted by the number of fitted parameters in $\boldsymbol{a}$ [128].

The fitting procedure returns the estimate $\hat{\boldsymbol{a}}$ of the optimal model parameters. The fitting algorithm *MIGRAD* also yields the uncertainties of the parameters σ_{a_j}, which

are calculated as square root of the diagonal elements of the Hessian matrix $\underline{H}$

$$\sigma_{a_j} = \underline{H}_{jj}^{1/2} \ . \tag{4.30}$$

If the uncertainty in the observations are underestimated and need to be adjusted by the factor $\sqrt{k} \approx \sqrt{g_{\text{fit}}}$, the parameter uncertainties need to be scaled by the same factor. This summarizes the uncertainty treatment regarding the fitted parameters starting with the parameter extraction from the contrast curves. Prior to this point, uncertainty calculation is performed by the MIEZEPY software. In the following we will describe the uncertainty estimation alongside the analysis steps.

The neutron intensity in each time bin is given by the square root of the detected neutrons $\sqrt{N_{\text{n}}}$ and follows from the variance of the Poisson statistics. These are included in the fitting of the contrast and is done by MIEZEPY. However, besides the statistical uncertainty, the contrast determination is subject to systematic uncertainty arising from the phase correction procedure, which is explained in section 4.2.3. Summarized briefly, the phase of the intensity oscillation varies more rapidly from pixel to pixel with increasing MIEZE time. Due to the fact that firstly, the time binning is limited to 16 channels and secondly the phase correction requires averaging over multiple pixels results in a slightly reduced contrast. While this systematic damping is corrected for by the resolution measurement, the exact contribution to the uncertainty is not quantifiable.

When fitting the contrast curves to determine linewidth and possibly spin wave energy, the uncertainty of each parameter is taken from the Hessian matrix and scaled by $\sqrt{g_{\text{fit}}}$ of the corresponding fit. Depending on the data set, the further treatment varies. In case of the dynamical scaling function, the square of the relative uncertainty is equal to the sum of the squared relative uncertainty of the individual linewidth parameters leading to

$$\Delta\gamma = \gamma \cdot \sqrt{\left(\frac{\Delta\Gamma(T)}{\Gamma(T)}\right)^2 + \left(\frac{\Delta\Gamma(T_{\text{C}})}{\Gamma(T_{\text{C}})}\right)^2} \ . \tag{4.31}$$

When further analyzing the spin wave dispersion an additional fit is performed, where the uncertainty is calculated exactly as described in the previous paragraph. In addition, we can estimate the uncertainty of such a fitted model $f(\boldsymbol{x} \,|\, \boldsymbol{a})$ via

$$\sigma_f = \sqrt{\sum_j \sigma_{a_j}^2 \cdot \left(\frac{\partial f}{\partial a_j}\right)^2 + 2 \sum_{j,k} \sigma_{a_j,a_k}^2 \cdot \left(\frac{\partial f}{\partial a_j}\right) \cdot \left(\frac{\partial f}{\partial a_k}\right)} \ , \tag{4.32}$$

where σ_{a_j,a_k}^2 expresses the covariance between the parameters a_j and a_k.

This concludes the general account of the uncertainty treatment. Wherever necessary, systematic influences, biases and limitations of this broad approach will be discussed in adequate detail.

4.3. Is Ni a dipolar ferromagnet?

Having extracted the spin wave energies and linewidths for the different temperatures, the results will be analyzed with respect to signatures consistent with the behavior of a dipolar Heisenberg ferromagnet. Hence, we use the Holstein-Primakoff theory to describe the observed spin wave dispersion for $T < T_C$ and deduce the influence attributed to the dipolar coupling in terms of the dipolar wavevector q_D.

As derived by Frey and Schwabl, it is to be expected that the dynamical scaling function is modified by dipolar coupling compared to the isotropic function put forward by Résibois and Piette or Iro. These predictions will be tested against the long wavelength or rather low-q measurements in the critical regime for $T \geq T_C$.

4.3.1. Spin wave dispersion of nickel in the long wavelength regime

An exact comparison to theory needs to incorporate the q resolution of the instrument, which for a SANS geometry is well established by analytic formulas found in Hammouda *et al.* [131]. According to their derivation, the resolution function is given by a Gaussian distribution

$$\mathscr{R}(q) = \left(\frac{1}{2\pi\sigma_q^2}\right)^{1/2} \exp\left(-\frac{q^2}{2\sigma_q^2}\right), \tag{4.33}$$

where the resolution defining standard deviation σ_q includes uncertainty due to a finite wavelength spread $\Delta\lambda$ of incoming neutrons, a contribution from geometric collimation in front of the sample and the size of pixels on the detector. The divergence is determined by two apertures of radii r_1, r_2, which are separated by the length L_{ap}. L_{SD} is the distance between sample and the detector. From these parameters σ_q was calculated using equation (5) in the paper published by Hammouda and Mildner. In their paper the nomenclature slightly differs, meaning $L_{ap} = L_1$ and $L_{SD} = L_2$.

Since the ROIs used for the MIEZE data reduction do not cover equal intervals of the scattering angle 2θ and therefore a larger spread in q, the resolution calculation was amended to take this fact into account. For each pixel within a ROI, the corresponding q value was calculated and the resulting distribution was binned into 4 to 15 bins of equal width depending on the with of the ROI. Using equation 4.33 the q resolution function was computed for each bin and averaged by the bins weight to acquire the final resolution function associated with the q value of a particular ROI. Based on the geometric parameters of RESEDA (see table 3.2) the FWHM_q of the Hammouda resolution function is around $0.01\,\text{Å}^{-1}$ and inclusion of the width of the ROI changes the result only by a few percent.

Ultimately, the measured dispersion relation for Ni is expected to match the convolution of the Holstein & Primakoff theory with the resolution function leading to

$$\mathscr{E}_{HP}(q) = \int_0^\infty \mathscr{R}(q') \cdot E_{HP}(q - q')\,\mathrm{d}q'. \tag{4.34}$$

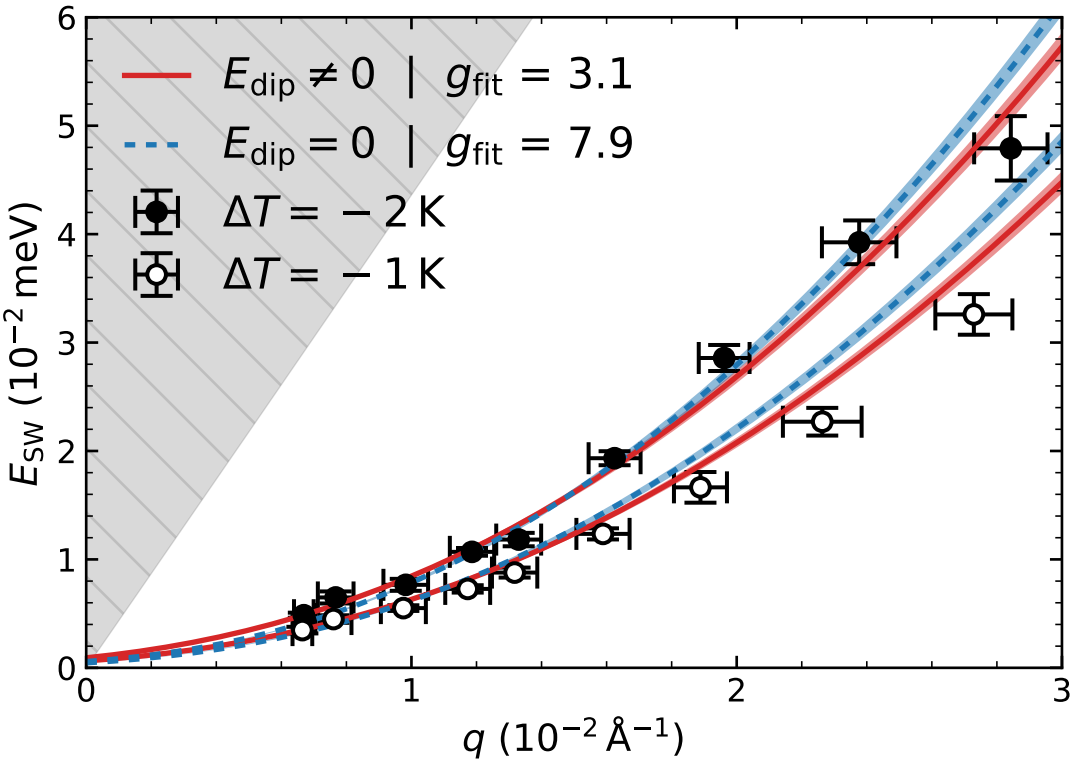

Figure 4.10.: Spin wave dispersion of nickel extracted from MIEZE data for $T = T_{\mathrm{C}} - 1\,\mathrm{K}$ and $T = T_{\mathrm{C}} - 2\,\mathrm{K}$. The dispersion data is shown on top of two models, which differ by inclusion of dipolar interactions (M4, red line) or by their neglection (M6, blue, broken line). A detailed description of methodology and nomenclature of the models is given in the text. The results of each model is underlaid with their 1σ uncertainty band in the appropriate colors. Model M4 with $E_{\mathrm{dip}} \neq 0$ achieves a much lower goodness-of-fit value g_{fit} strongly indicating the contribution of dipolar coupling in the system. However, the data is only consistent with a dipolar wavevetor $q_{\mathrm{D,exp}} = 0.007\,\text{Å} \approx q_{\mathrm{D,lit}}/2$ smaller than reported previously. The gray shaded area indicates the region inaccessible for INS due to constraints from momentum and energy conservation.

In total, the theory is determined by three parameters, D', q_{D} and μ. Because only two distinct temperatures had been investigated, deviations from the power law behavior in terms of the critical exponent μ could not be studied thoroughly. The variation observed in the spin wave dispersion (equation 4.6) due to temperature should be fully accounted for by the power laws in equations 4.9 and 4.8. In this analysis μ and β were fixed either to their mean-field values or the renormalization group values for a 3D Heisenberg model [112]. Therefore, it seemed reasonable to fit all data for $T < T_{\mathrm{C}}$ simultaneously. The associated χ^2 function was calculated as

$$\chi^2(D', q_{\mathrm{D}}) = \sum_{\Delta T, q} \left(\frac{E_{\Delta T, q} - \mathscr{E}_{\mathrm{HP}}(q|D', q_{\mathrm{D}})}{\sigma_E} \right)^2 . \tag{4.35}$$

$E_{\Delta T,q}$ represent the extracted energy values of the spin waves for a certain temperature

ΔT and wavevector transfer q with its respective standard deviations σ_E. The resolution convoluted, theoretical dispersion relation $\mathscr{E}_{\mathrm{HP}}(q|D', q_{\mathrm{D}})$ only depends on the spin wave stiffness D' and the dipolar wavevector q_{D}.

Figure 4.10 visualizes the measured spin wave dispersions at $T - T_{\mathrm{C}} = -2\,\mathrm{K}, -1\,\mathrm{K}$ as filled and empty circles respectively. The difference in q for two data points extracted from the same ROI on the detector is owed to the corresponding energy transfer, which in consequence changes k_{f} and q. As usual, the errorbar of the ordinate is the 1σ uncertainty of E as determined from the covariance matrix in the least-square optimization. In the abscissa, the error bar does indicate the standard deviation of the q distribution within a ROI. As σ_q is already considered in the resolution calculation, it is not directly included in the χ^2 computation e.g. via orthogonal distance regression [132].

The Holstein-Primakoff theory is plotted for two cases, with the red solid line representing the resolution convoluted dispersion including dipolar interaction, whereas the dotted blue line neglects the dipolar coupling. Drawing the 1σ confidence interval for both cases leads to the red and blue shaded areas beneath the curves. The grey shaded area on the left side of the graphic indicates the region on (q, E)-space not accessible to INS because in this region momentum and energy transfer can not be satisfied simultaneously.

Both models yield a different value for the spin wave stiffness D' amounting to $(431.1 \pm 10.0)\,\mathrm{meV\,\AA^2}$ and $(475.4 \pm 16.1)\,\mathrm{meV\,\AA^2}$, if dipolar interactions are included or neglected, respectively. The critical exponent was fixed at $\mu = 0.3407$. In the case where dipolar coupling is considered, the dipolar energy term equates to $E_{\mathrm{dip}}(\Delta T = -2\,\mathrm{K}) = 3.15\,\mu\mathrm{eV}$ and $E_{\mathrm{dip}}(\Delta T = -1\,\mathrm{K}) = 1.56\,\mu\mathrm{eV}$. Visually, both models seem equally plausible, describing the low q section of the dispersion sufficiently well. However, they have the tendency to overestimate the spin wave energy for $\Delta T = -1\,\mathrm{K}$ in a systematic manner, with the model, which has set $E_{\mathrm{dip}} = 0$ performing worse at larger q values. Overall, the data taken at $\Delta T = -2\,\mathrm{K}$ appears to be captured better by the $E_{\mathrm{dip}} \neq 0$ model.

As already introduced in section 4.2.3, a proven figure of merit to compare the descriptive power of competing models is the goodness-of-fit value $g_{\mathrm{fit}} = \chi^2/n_{\mathrm{dof}}$. By dividing the χ^2 value by the number of *degrees of freedom* n_{dof}, which is the number of data points minus the number of fitted parameters, we correct for the potential increase in χ^2 for more data points, while simultaneously punish overfitting with arbitrary, non descriptive parameters. The model achieving a smaller g_{fit} is more likely to be an adequate description of the data [128]. As a side note, the definition of g_{fit} makes it equal to the reduced chi-square value χ^2_{red}. The applicability of $g_{\mathrm{fit}} = \chi^2_{\mathrm{red}}$, utilized for the statistical χ^2-test, as a meaningful measure can be argued about, since the calculated values are significantly larger than 1, which is the value expected for data with Gaussian uncertainty and an appropriate model. It suffices as a qualitative indicator.

For a comprehensive analysis of the Holstein-Primakoff theory and temperature dependence as predicted by dynamical scaling theory, we created various models differing in the determination method of the dipolar energy contribution to the dispersion. In total, six models (MX) have been fitted to the data, with D' always being a fit parameter and q_{D} being treated as follows.

M1 The dipolar wavevector was taken from literature $q_{\mathrm{D}} = 0.013\,\mathrm{\AA^{-1}}$ [123] and the contribution to the dispersion was calculated according to equation 4.7.

M2 q_D and D' were treated as free fit parameters accounting for the dipolar energy as $E_\mathrm{dip} = D(T)q_\mathrm{D}^2$.

M3 q_D was determined according to the power law in equation 4.8 and $E_\mathrm{dip} = g\mu_0\mu_\mathrm{B}M(T)\sin^2(\theta_{\boldsymbol{q}})$. The constant M' was set to the value of the saturation magnetization $M_\mathrm{sat} = 4.91 \times 10^5\,\mathrm{A\,m^{-1}}$ [133].

M4 q_D was fixed by experimentally determined magnetization curves from Neugebauer [134] and again $M_\mathrm{sat} = 4.91 \times 10^5\,\mathrm{A\,m^{-1}}$. Further information is given in appendix B.5.

M5 $q_\mathrm{D}(\Delta T = -1\,\mathrm{K})$, $q_\mathrm{D}(\Delta T = -2\,\mathrm{K})$ and D' were fitted independently.

M6 Simple quadratic dispersion using $E_\mathrm{SW} = D(T) \cdot q^2$ neglecting dipolar interaction entirely.

Each model has been fitted to the data fixing the critical exponent μ (and β if contained in the model) to either the mean-field values or the renomalization group values. A summary of all fit parameters, their uncertainty estimates and g_fit are given in table 4.1. The assembled values allow to conjecture general trends and to draw conclusions on the validity of Holstein-Primakoff theory for dipolar ferromagnets.

To establish a baseline model, M4 was chosen to be the most representative one in this analysis, because it utilizes proven experimental knowledge in form of the temperature dependence of the magnetization. Simultaneously, M4 shows good agreement with the data based on its g_fit value. Regarding the g_fit value, M4 performs better compared to M3, in which q_D is determined via the power law of the magnetization as predicted by scaling theory. Notably, the values of q_D in model M4 are by a factor of 2 smaller than in M3 and the relative difference between $q_\mathrm{D}(\Delta T = -2\,\mathrm{K})$ and $q_\mathrm{D}(\Delta T = -1\,\mathrm{K})$ is larger because the experimental magnetization decreases slower then the power law with $\beta = 0.3647$. As a consequence, D' is significantly smaller for M3 since the dipolar contribution is considerably larger and the penalty to the χ^2 function is larger if the low q data is fitted insufficiently. In the comparison between M3 and M4, a lower q_D is supported by the data.

These observations extend to M1, which fixes q_D to its literature value $0.013\,\mathrm{Å}^{-1}$ and performs similar as M3. Comparing M1 and M2, M2 achieves better agreement with $q_\mathrm{D}(\mathrm{M1}) > q_D(\mathrm{M2})$ by again almost a factor of 2. Considering that model M5, puts the least constraints on its fit parameters, because $q_D(\Delta T = -1\,\mathrm{K})$ and $q_D(\Delta T = -2\,\mathrm{K})$ are assumed to be independent from each other, it is plausible that M5 achieves the best overall g_fit value. Somewhat expected, q_D for $\Delta T = -1\,\mathrm{K}$ is smaller than for $\Delta T = -2\,\mathrm{K}$ and both are smaller than the literature value.

Model M6, neglecting q_D entirely, returns D' values, which are slightly larger then those of the other models. The deviation from the dipolar behavior is best detectable at low q for the first 2 - 3 data points for each temperature. Crucially, this discrepancy results in the highest g_fit value for any dispersion model, making the inclusion of dipolar interactions favorable. Regardless of the model, we find that a larger μ leads to a smaller g_fit value indicating that the critical exponents as obtained by field-theoretical methods describe the data marginally better than the mean field values.

Model	D_0 (meV Å^2)	q_D (10^{-3} Å^{-1})	μ	g_fit
M1	333.2 ± 8.7	13.0 13.0	0.3333	4.9
	348.6 ± 8.0	13.0 13.0	0.3407	4.6
M2	382.8 ± 20.8	9.02 ± 1.50 9.02 ± 1.50	0.3333	3.7
	400.6 ± 21.3	9.02 ± 1.47 9.02 ± 1.47	0.3407	3.5
M3	343.5 ± 10.9	12.29 ± 0.20 12.29 ± 0.20	0.3333	4.4
	378.1 ± 10.4	10.75 ± 0.15 10.85 ± 0.15	0.3407	3.5
M4	412.1 ± 9.7	5.70 ± 0.07 7.22 ± 0.08	0.3333	3.2
	431.1 ± 10.0	5.71 ± 0.07 7.21 ± 0.08	0.3407	3.1
M5	381.6 ± 16.3	7.28 ± 0.81 10.66 ± 1.07	0.3333	2.3
	399.5 ± 16.9	7.33 ± 0.81 10.59 ± 1.06	0.3407	2.2
M6	454.4 ± 15.6	0.0 0.0	0.3333	8.1
	475.4 ± 16.1	0.0 0.0	0.3407	7.9

Table 4.1.: Parameters obtained by fitting the data using the Holstein & Primakoff theory. Each model has been evaluated with $\mu = 1/3$ and 0.3407 separately. Within one cell, the upper and lower q_D value corresponds to $\Delta T = -1\,\mathrm{K}$ and $\Delta T = -2\,\mathrm{K}$ respectively. In model M2 & M5 q_D was a fit parameter and its uncertainty could be estimated directly from the covariance matrix. For the models M3 & M4 the uncertainty Δq_D arises from $\Delta D'$ and was calculated via Gaussian error propagation. In model M1 & M6 q_D was fixed to $0.013\,\mathrm{Å}^{-1}$ and $0.0\,\mathrm{Å}^{-1}$, respectively.

Discussion of the dipolar contribution

In literature, the discussion of the influence of dipolar coupling on the critical dynamics has been focused on the temperature regime above T_C, with a limited amount of published experiments directly addressing the spin wave regime [83, 105]. Especially Ni has been disregarded in the past, because the combination of a large spin wave stiffness and an apparently small dipolar wavevector makes observations of q_D challenging. Instead it was regarded as a good testing ground for a purely isotropic ferromagnet when discussing spin wave dynamics and critical fluctuations from small to intermediate q values [29]. Nevertheless, measuring the spin wave energy below q_D should show a clear imprint leading to an approximately linear dispersion $E_{HP} \approx D(T)q_D \cdot q$. For this reason, the study is a novelty, as it directly probes inelastic scattering processes at q values smaller than in previous SANS studies [135, 136]. A linear contribution to the dispersion is not easily recognizable in figure 4.10, even though the lowest q value is a factor of 2 smaller then the reported $q_D = 0.013\,\text{Å}^{-1}$.

Figure 4.11 shows q_D and g_{fit} for the models M1 to M6. It is apparent that the measured dispersion is consistent with $0.006\,\text{Å}^{-1} < q_D < 0.011\,\text{Å}^{-1}$. Looking at the performance of M4 and M5, it is reasonable to assume a significant temperature dependence of q_D, which has already been pointed out be Böni *et al.* [105]. However, this dependence is more pronounced than expected from dynamical scaling theory with $q_D^2 \propto M/D \propto |t|^{\beta-\mu}$ ($\beta - \mu = 0.024$) for a 3D Heisenberg system [112]. Since only 2 different temperatures could be measured, a reliable analysis of the temperature dependence is not possible and requires a more comprehensive data set.

The evidence for dipolar interactions in nickel is circumstantial and additional measurements at even lower q could substantiate the understanding of related effects. Two routes for future experiments can be imagined. Firstly improvement of momentum transfer

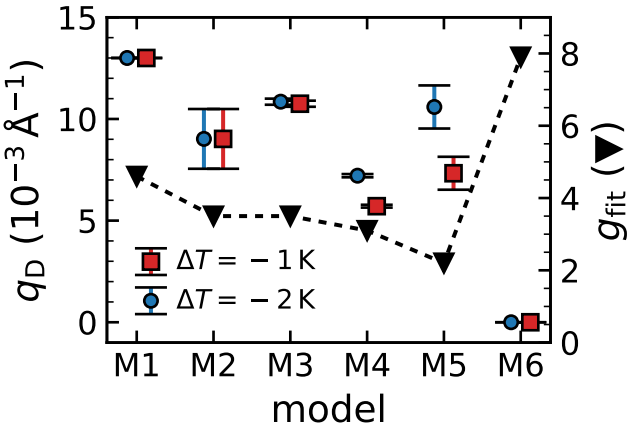

Figure 4.11.: Overview of the performance of Holstein-Primakoff models M1 - M6 employing various strategies to include the dipolar wavevector. The graphic depicts the $q_D(\Delta T)$ and g_{fit} for M1 to M6 using $\mu = 0.3407$ as a fixed value. The data suggests $q_D \approx 0.007\,\text{Å}^{-1}$, which is half of the literature value $0.013\,\text{Å}^{-1}$, but simultaneously rejects neglection of the dipolar contribution.

resolution could be achieved by using a longer wavelength e.g. $\lambda_0 = 8.0\,\text{Å}$ or adjustment of the collimation apertures and beam stop. Of course this needs to be planed correctly to prevent drastically longer measurement times. Secondly, temperatures closer to T_C flatten the dispersion branch. While it does not simplify the observation of q_D itself, because the dipolar contribution also decreases closer to T_C, as established before, the temperature dependence of q_D should become more apparent.

Discussion of the spin wave stiffness

Having decided to parameterize the temperature dependence close to T_C in terms of the power law $D(T) = D' \cdot (1 - T/T_C)^\mu$ with a fixed critical exponent instead of fitting D for each temperature individually, requires special care when comparing the result to literature. This is owed to the fact that the multitude of methods to determine the spin wave stiffness, e.g. TAS [108, 137, 138], SANS [135, 136] but also magnetization [139] and resonant inelastic X-ray scattering [140] measurements, have been applied to different regimes in T and q.

Over decades, spin wave measurements have been performed on nickel from $T = 4.2\,\text{K}$ to T_C. Up to now, there is no theoretical framework capable of unifying all the results from first principle calculations. The magnetization data published by Aldred *et al.* shows good agreement with spin wave theory and a $D(T) = D_0 - D_1 T^2$ relation from $5\,\text{K}$ to $300\,\text{K}$, when itinerant effects are included in their analysis procedure. The observed difference from pure spin wave theory was accounted for by single-particle Stoner excitations and the resulting holes induced in the spin-down bands. The gray shaded area with the black line in figure 4.12 (a) represents the 1σ band of this quadratic temperature dependence. The light gray line beneath is the best fit of Aldred's data neglecting Stoner single particle excitations [139].

Likewise, the $D(T)$ values of several neutron scattering studies have been visualized in the same figure (4.12 (a)) providing a remarkably consistent picture over the entire temperature regime from $T = 0\,\text{K}$ up to $T = T_C$. In their investigations, Pickart [135] and Stringfellow [136] used small angle neutron scattering to observe inelastic spin wave scattering down to $q = 0.02\,\text{Å}^{-1}$. Their ingenious method required no direct energy transfer detection, but only a measurement of the neutron intensity as a function of the scattering angle 2θ, when the sample was offset by an angle $\Delta\theta_S$ from the Bragg scattering condition. The angular width of the neutron signal as a function of $\Delta\theta_S$ is related to the spin wave stiffness $D(T)$. A detailed description of this method can be found in the publication by Alperin *et al.* [141]. In case of Stringfellow, $D(T)$ does not decrease down to 0 at the Curie temperature, which was not in line with related measurements, and at the time it was argued that the non-zero value of $D(T)$ originates from external magnetic fields.

More compatible with the understanding of dynamical scaling and spin wave theory is a TAS study by Minkiewicz [108] tracking spin wave dispersions from room temperature to T_C. Because their measurements were performed at a thermal TAS, the smallest wavevector transfer amounts to $q \geq 0.05\,\text{Å}^{-1}$, which is about a factor of 2 larger than the largest value acquired in the present study. From graph 4.12 can be seen that our results for $D(T)$ fit well to the previously reported experiments and extend them to

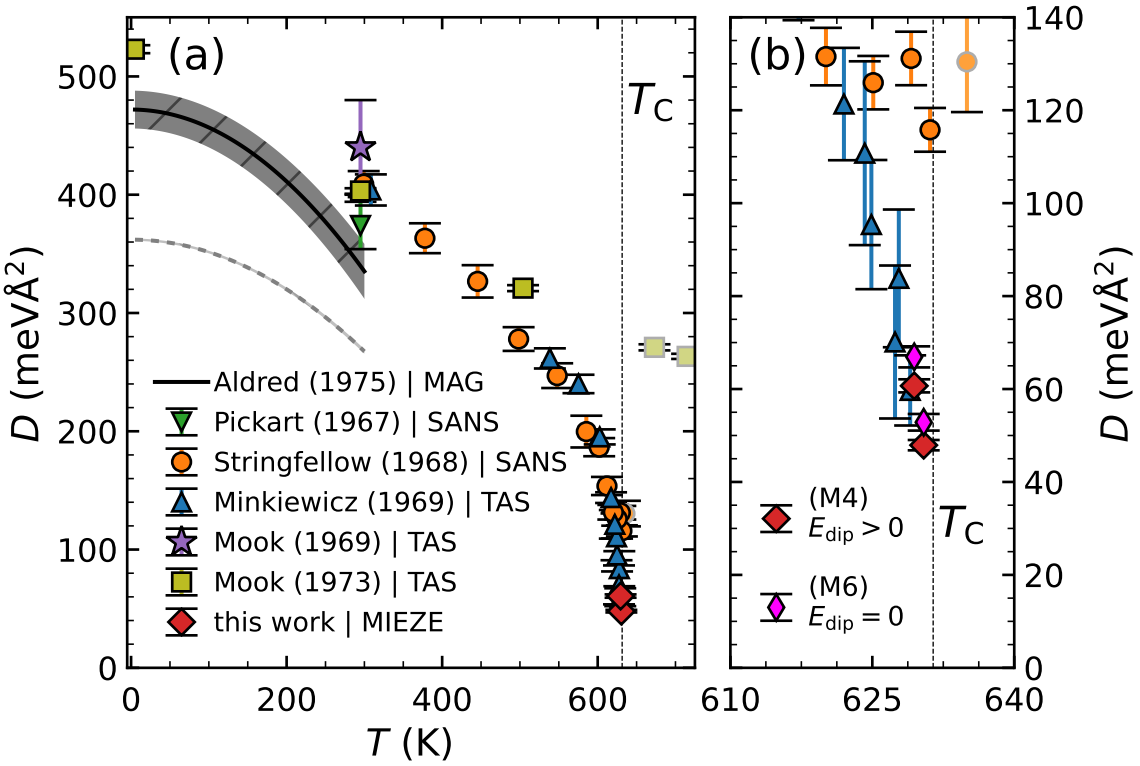

Figure 4.12.: Overview of the temperature dependent spin wave stiffness $D(T)$ combining the present and previously published results. The determination of the spin wave stiffness in nickel has been performed with a variety of techniques putting together a comprehensive picture of its temperature dependence from $T = 0\,\mathrm{K}$ up to T_C (see subplot (a)). The results of this study are remarkably consistent, support the notion of dynamical scaling theory that $D(T) \to 0$ at T_C and extend the extensive study of Minkiewicz *et al.* to temperatures closer to T_C. Uniquely, our data proves, at the currently lowest measured q and significantly increased accuracy, that the Heisenberg model with isotropic exchange coupling remains valid and the additional dipolar interactions do not fundamentally change this outcome. This can be inferred from the zoomed view in (b), where the results of models M4 and M6 are shown.

smaller q.

In the zoomed in view (figure 4.12(b)), the results of model M6 ($E_\mathrm{dip} = 0$) are drawn as well, unambiguously confirming the temperature behavior detected by Minkiewicz *et al.*. On the one hand, it successfully proofs the validate of high resolution MIEZE measurements of dispersive spin wave modes at very small momentum transfer. On the other hand, in the investigated q range, the simple, quadratic dispersion is an acceptable description such that $D(T)$ does not noticeably differ from prior measurements due to the smallness of E_dip.

4.3.2. Dynamical scaling of critical fluctuations in nickel

In this section, the measurements of the linewidth, or rather inverse lifetime of the critical fluctuations above and below T_C will be presented. With the high energy resolution and

sensitivity to the line shape of the critical fluctuations, the MIEZE technique allows precise determination of the dynamical scaling function at very low q values. First, the fluctuations in the temperature regime $T \geq T_C$ are considered to test the emergence of a q_D/κ dependence indicative of dipolar coupling. Second, the damping of spin waves will be addressed, in particular their temperature dependence.

Discussion of the dynamical scaling above the Curie-temperature

To elaborate on the conceptual (q, T) diagram in figure 4.1 and focus on the $T \geq T_C$ side, the figure 4.13 includes the boundary defined by $\kappa^2 + q^2 = q_D^2$ separating the regions of expected isotropic and dipolar critical behavior [117, 120, 123]. We drew boundaries for the literature values and previously estimated experimental values, neglecting a potential temperature dependence of q_D. In addition, the data points at which the critical linewidth could be extracted are drawn. The non-linearity of the temperature scale is dictated by the power law $\kappa = \kappa_0 |t|^\nu \propto T^\nu$.

We summarize the full results of the measured dynamical scaling function in figure 4.14, where the abscissa designates the dynamical scaling variable $x = \kappa/q$ and the ordinate the dynamical scaling function according to the scaling hypotheses $\gamma(\kappa/q) = \Gamma(q, T)/\Gamma(q, T_C)$. Using the same color scheme of the data points as in figure 4.13, the results for different temperatures are plotted together with previously published data by Böni *et al.* [107]. Visually, the measurements of the dynamical scaling function taken at $\Delta T \in [1\,\mathrm{K}, 2\,\mathrm{K}, 4\,\mathrm{K}] = [1.0016\,T_C, 1.0032\,T_C, 1.0063\,T_C]$ fall onto a universal curve. In regions where the different data sets overlap this holds true, with exception of the two points corresponding to the lowest q values at $\Delta T = 1\,\mathrm{K}$, which lie slightly higher (blue dots near $\kappa/q \simeq 1.2$). At low $\kappa/q \approx 1$ the current measurements are in agreement with the TAS data of Böni, which diverge to higher $\gamma(\kappa/q)$ incompatible within the uncertainty estimates of the data. Interestingly the same behavior is observed for the DSF at $\Delta T = 8\,\mathrm{K}$. However, for two reasons, which will be presented in more detail shortly, this agreement is most likely coincidental.

In the light of the previous spin wave analysis, that the dipolar wavevector q_D is considerably smaller then expected, we compared the results with the MC and ARG calculations by Résibois-Piette [116] and Iro [127], which are shown as the black, solid and broken line, respectively. Importantly, the curves of the theoretical dynamical scaling function have not been acquired by fitting of the data, but have been directly calculated from the equations 4.19 (Résibois-Piette) and B.3 (Iro). In general, the agreement is quite satisfactory. The mode-coupling result seems to approximate the data better at $\kappa/q < 1$, while the asymptotic renormalization group theory calculation fits better at higher κ/q. On the basis of the available data, it is unreasonable to give preference of one model over the other. The data up to $T_C + 4\,\mathrm{K}$ indisputably shows dynamical scaling behavior expected for an isotropic Heisenberg ferromagnet.

This leaves two questions open for debate: (i) Why are the measurements at $T_C + 8\,\mathrm{K}$ diverging from the otherwise consistent scaling behavior and can the reasoning be extended to the data of Böni *et al.*? (ii) Why is there no indication of dipolar coupling, which could be argued to influence the spin wave dispersion below T_C, and has been observed in other ferromagnetic systems?

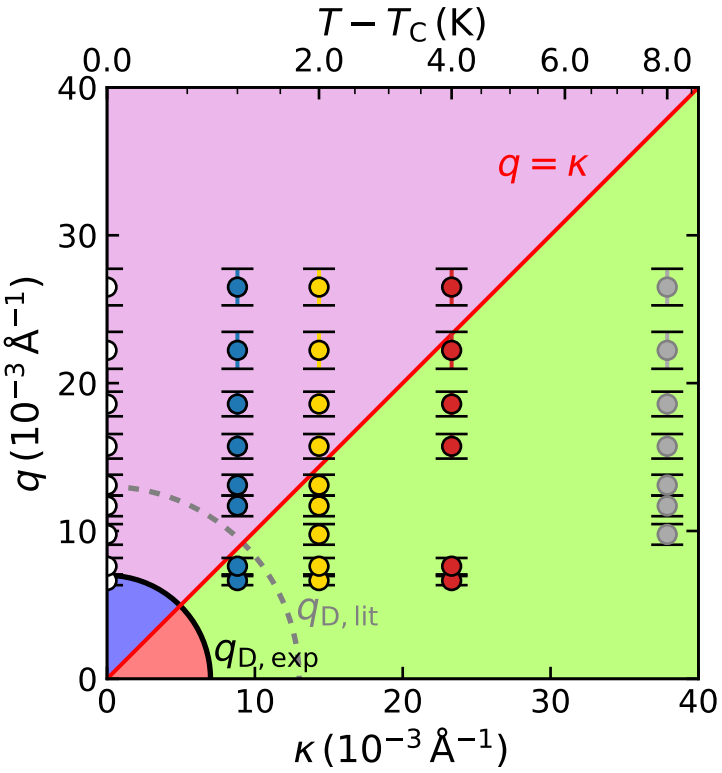

Figure 4.13.: $q-T$-diagram including the data of the MIEZE measurements in the temperature regime $T \geq T_C$. In addition, the sectors with radii $q_{D,exp}$ and $q_{D,lit}$ are marked, within which the influence of dipolar coupling should be visible. $q_{D,exp} \approx 0.007\,\text{Å}^{-1}$ was taken from the results in section 4.3.1, ignoring any temperature dependence, and severs foremost as an approximate border. Together with the condition $\kappa = q$, this quadrant into the *dipolar critical* (blue shaded), *dipolar hydrodynamic* (red shaded), *isotropic critical* (violet shaded), *isotropic hydrodynamic* (green shaded) regions governed by differing physical behavior, as discussed in the text.

Regarding (i), the MIEZE data at $\Delta T = 8\,\text{K}$ suffers from low magnetic scattering intensity introducing systematic uncertainties not captured by the error bars in figure 4.14. The analysis algorithm extracting the contrast values forces fitting of a sinusodial intensity distribution in time, even though in some instances, the raw data does not reflect the expected shape. A closer look at the reliability of this data is required to fully understand the behavior. The data is shown mostly for completeness. This reasoning, of course, cannot be extended to the data published by Böni *et al.*. Here, a different origin for the deviation from the universal dynamical scaling behavior is suspected. The data of Böni *et al.* lies, except for 1 point consistently outside of the critical region, defined by $q > \kappa(T)$, even more though for the lower q value. It has been taken at $q \in \left[0.09\,\text{Å}, 0.12\,\text{Å}\right]$ and $T \in [663.0\,\text{K}, 694.6\,\text{K}, 764.0\,\text{K}, 934.5\,\text{K}] = [1.05\,\text{T}_C, 1.10\,\text{T}_C, 1.21\,\text{T}_C, 1.48\,\text{T}_C]$. The ΔTs involved are orders of magnitude larger than the ones presented here. Naturally, DST predicts universal behavior, but DST cannot make a statement about its own range of validity, which is why comparability with the here presented data is questionable. While the exact conditions at which the dynamical scaling behavior in Ni breaks down

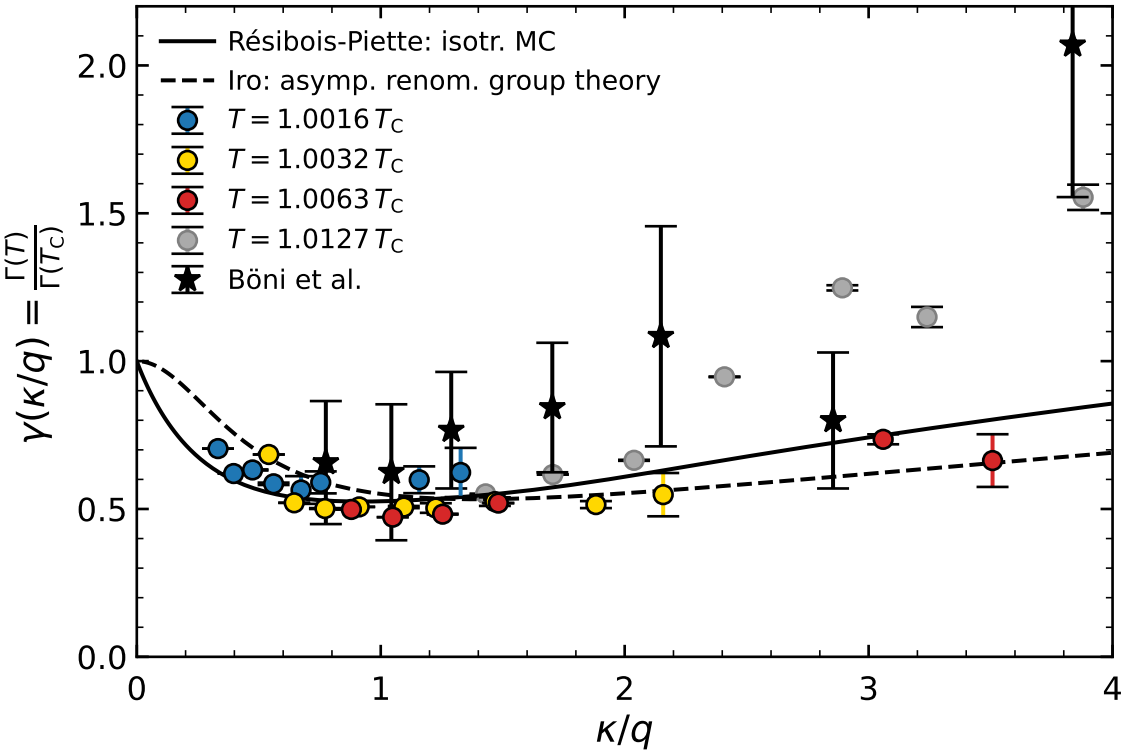

Figure 4.14.: Dynamical scaling function measured in nickel. Testing the dynamical scaling hypotheses, linewidth ratio $\Gamma_{T^+}(q)/\Gamma_{T_C}(q)$ is supposed to lie on a universal curve described by $\gamma(\kappa/q)$. Results acquired for ΔT being 1 K, 2 K and 4 K satisfy this expectation well, while at $\Delta T = 8$ K the deviation for large $\kappa/q > 2$ is significant. Comparing the findings with TAS data from Böni *et al.* [107] show good agreement for $\kappa/q \approx 1$. Most notably, the measurements match the dynamical scaling functions, which have been calculated by Résibois & Piette (solid line) and Iro (broken line) via mode-coupling and asymptotic renormalization group theory, respectively. Leaving aside the 8 K data, the MC theory fits better for small κ/q, whereas ARG captures the large κ/q behavior more accurately. The color scheme adheres to the one used in the (q, T)-diagram of figure 4.13.

is unknown, studies of critical scattering in Co [142] and Fe [143] show, that for $\kappa/q > 4$ the characteristic frequency reflects a quadratic relationship $\omega_c(q) = Dq^2$ with the spin-diffusion constant D. Hence, it is not inconceivable that the data by Böni *et al.* and possibly the MIEZE data at $\Delta T = 8$ K begin to display an intermediate behavior dubbed 'quasihydrodynamic' by Parette and Kahn [143]. It is indisputable that further research would be needed to clarify this hypothesis.

An answer to the lack of evidence for dipolar coupling in the dynamical scaling function (ii), is provided by theory calculations by Frey and Schwabl [120] and have been backed up by experimental investigations on ferromagnets with strong dipolar coupling such as EuO [118] and EuS [117]. In these publications it becomes clear, that the dynamical scaling function of the transverse spin fluctuations retains an isotropic shape even in the regime $q_D/10 \leq q < q_D$. Since the smallest q value was on the order of q_D determined by the spin wave measurements, the compatibility with Résibois-Piette and ARG scaling

functions is plausible.

However, the presented arguments become less consistent considering the recent MIEZE study by Kindervater *et al.* on iron [101], who report on the influence of dipolar interactions on the transverse fluctuations even though they do not achieve wavevector transfers below $q_\mathrm{D} \approx 0.033\,\text{Å}$. Quantitative agreement with MC computations, which include dipolar forces, is only achieved assuming a strong temperature dependence of q_D inexplicable by dynamical scaling theory. Damping by conduction electrons was given as a possible explanation. Following the chain of reasoning given by Kohgi *et al.* [144] spin fluctuations in $3d$ metals are damped by low-q spin-flip excitations in the conduction band. This leads to two noticeable consequences. First, the lifetime (linewidth) of spin fluctuations at low q should decrease (increase) compared to a purely localized system. Second, with increasing temperature this damping effect should become more prominent and extend to higher q values, due to the larger smearing of the Fermi-Dirac distribution around the *Fermi energy* E_F. This smearing scales approximately with $k_\mathrm{B}T$ and increases the number of accessible quantum states for spin-flip transitions. Arguably, the dipolar wavevector q_D at this point is only a way to parameterize the observed linewidth of the fluctuations instead a physical meaningful quantity, as was noted by Kindervater *et al.*

One step further, a comprehensive publication by Lowde and Windsor [29] concludes that the generalized dynamical susceptibility $\chi^{\alpha\beta}(\boldsymbol{Q},\omega)$ calculated on the basis of a random phase approximation treatment of the Hubbard Hamiltonian encompasses all essential effects of magnetism in nickel. Naturally, this comes with limitations on specific details. Therefore even though for the here presented study, a quantitative treatment of the itinerant effects has not been considered it might be worthwhile to use such a large-scale analysis approach on a more extensive data set in the future.

Discussion of the linewidth of the spin waves

Measuring the spin waves with the high resolution MIEZE method required temperatures up to T_C, since only the renormalization of the spin wave energy at high T made them observable at low q. Otherwise, the scattering triangle for inelastic spin wave scattering would not close. Besides the spin wave energy, this investigation revealed a strong dependence of the linewidth on the wavevector transfer, due to the excellent energy resolution of the instrument. This fact in itself is not surprising, because at high temperatures a multitude of magnon and longitudinal fluctuation states are occupied enabling decay resulting in a reduced lifetime of the excitations. The increase of the linewidth is a result of the reduced spin wave lifetime, as both quantities are inverse proportional to each other.

The recorded linewidth data lends itself to a comparison with the predictions of dynamical scaling theory (see equation 4.10) and the microscopic spin wave calculations by Harris, which is approximated by equation 4.11. The linewidth data for both temperatures, as well as the results of the analysis are shown in figure 4.15, whereas the numerical values for the fit parameters are summarized in table 4.2. The analysis procedure behind these results is explained in the next section.

As stated in the introduction on critical dynamics in ferromagnets (section 4.1), the

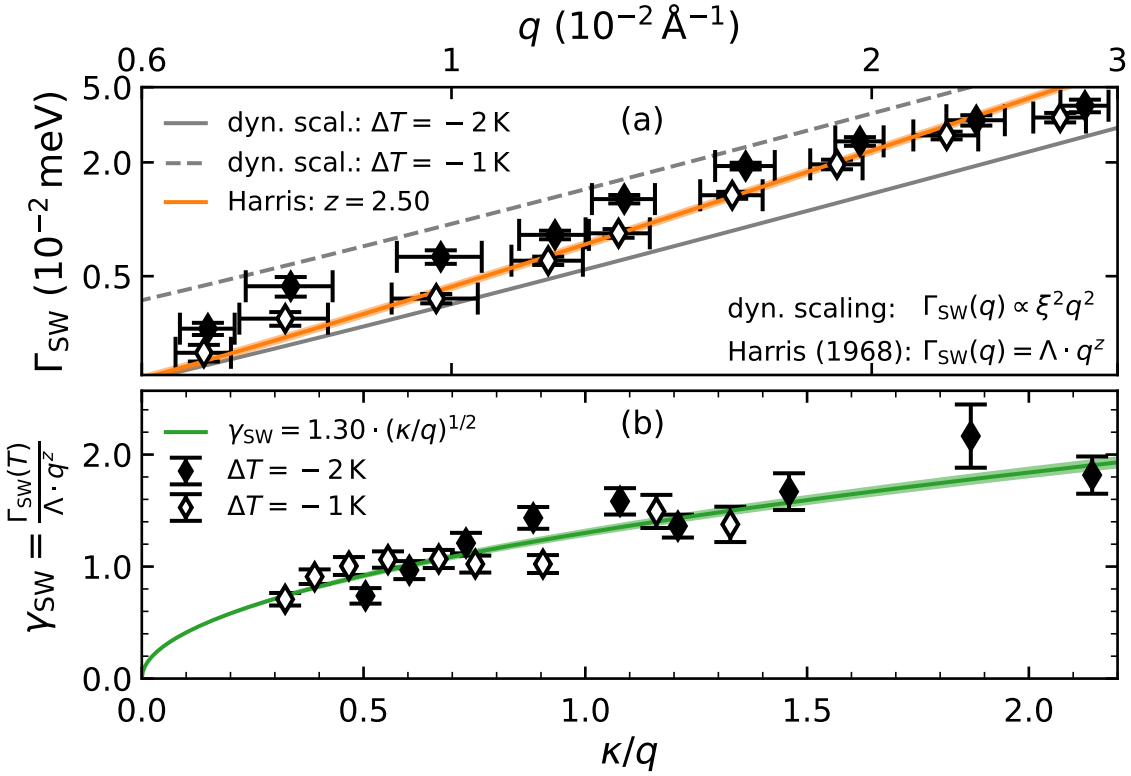

Figure 4.15.: Linewidth (a) and the dynamical scaling function (b) of the measured spin waves in nickel. In the log-log plot, the q-Γ points are expected to follow a linear relationship with a slope being equal to the exponent z if $\Gamma \propto q^z$. However, as visualized in (a), neither the slope of $z = 5/2$, which is an approximation to Harris spin wave theory calculations (orange solid line), nor the temperature independence of the frequency scale Λ as observed in past experiments on Fe [83] and Ni [114] fits the expectations. Understanding of the this behavior comes again from dynamical scaling theory. While the temperature dependence is not accounted for by the asymptotic behavior in the hydrodynamic regime, as explained in the text, the dynamical scaling function for $T < T_C$ (see equation 4.38) agrees well with the re-scaled data for $a = 1.30 \pm 0.04$.

Λ (meVÅ^z)	z	g_{fit}
396.4 ± 21.4	2.5	15.1
95.02 ± 47.10	2.14 ± 0.11	10.8

Table 4.2.: Parameters obtained by fitting the approximate equation of Harris (see equation 4.36) to the linewidth data of the spin waves.

DST predictions and the calculation by Harris are based on the isotropic Heisenberg model. Both computations assume long wavelength excitations, however, while DST is concerned with the temperature dependence close to T_C, the prediction by Harris are strictly speaking solely valid at low temperatures. For the analysis we use an approximation to the full expression of Harris

$$\Gamma_{SW}(q) = \Lambda \cdot q^z \quad | \quad z = 5/2 \ , \tag{4.36}$$

which has been shown to describe the q dependence of the linewidth of spin waves in nickel [114] and iron [83] well, with Λ being a constant independent of T. Coincidentally, the exponent of $z = 5/2$ in the equation 4.36 equals the exponent predicted by dynamical scaling theory, which should apply for $q > \kappa$ and $T < T_C$. The majority of the data points of the spin wave measurements fall in this region.

Optimizing the parameter Λ, as a temperature independent quantity, by least-square fitting of the entire linewidth data, we obtain $\Lambda = (396.4 \pm 21.4)\,\mathrm{meV\AA}^{5/2}$. The corresponding visualization can be seen as the orange solid line in figure 4.15 (a). The slope, which in double logarithmic scaling of the axis, is equal to the exponent $z = 5/2$, seems to be slightly too large to describe the data. While the value of Λ is not far from the value of the diffusion constant $\Lambda = 350\,\mathrm{meV\AA}^{5/2}$ at $T \geq T_C$ as published by Böni *et al.* [145], it deviates by almost a factor of 2 from the linewidth of the spin waves reported in [114]. When relaxing the constraint of the critical exponent $z = 5/2$, a better fit to the data is achieved according to the g_{fit} value, but both z and Λ, written in table 4.2, cannot be reconciled with previously published measurements.

Furthermore, the linewidth of the spin waves exhibit a systematic temperature dependence with $\Gamma(\Delta T = -2\,\mathrm{K}) > \Gamma(\Delta T = -1\,\mathrm{K})$ for each q, which has not been observed by TAS in Ni [114] or MIEZE in Fe [83]. This leads to the approach of including a T-dependence as predicted by DST for the spin wave region. Here, the temperature dependence of the linewidth is incorporated in the correlation length via $\xi = \xi_0 \cdot (1 - T/T_C)^{-\nu}$. Introducing a scaling factor c, in which the constant ξ_0^2 is absorbed, the DST equation 4.10 becomes

$$\Gamma_{SW,DST}(q,T) = c \cdot q^2 \left(1 - \frac{T}{T_C}\right)^{-2\nu} \ , \tag{4.37}$$

with c being the only free parameter in this parameterization. In figure 4.15 (a), the grey solid line and broken line show the result for $\Delta T = -2\,\mathrm{K}$ and $\Delta T = -1\,\mathrm{K}$, respectively, when $c = 0.01\,\mathrm{meV\,\AA}^2$ is used. This is not a fit to the data, but solely a visualization of the incapability of this model to describe the data. Since $\xi(T)$ diverges at T_C, the linewidth of $\Delta T = -1\,\mathrm{K}$, at the same q value, should always be larger. This predicted behavior would also be in agreement with calculations performed by Vaks *et al.* [146], but is clearly not consistent with the observation. The most likely explanation is, that the experimental parameters in q and $\kappa(T)$ do not sufficiently comply with the constraint $\kappa/q \gg 1$ [111].

An explanation to the issue of temperature dependence could be found by again formulating this dependence in terms of the dynamic scaling function, which has proven

to be a good descriptor. Thus, we rescaled the linewidth via $\gamma_{\mathrm{SW}} = \Gamma_{\mathrm{SW}}(T)/\Lambda q^z$, with Λ taken from literature, and the result can be seen in figure 4.15 (b). Here, the decision not to use the experimentally determined value of Λ is deliberate. Due to the finite energy transfer during spin wave scattering, the average momentum transfer for spin waves differs from the one for quasielastic critical scattering. For more details refer to section 4.2.3.

As a viable approach, the treatment by Tarvin *et al.* [147] seems to be the most appropriate to fit the data. They argued on the basis of dynamical scaling theory that γ_{SW} should be proportional to the square root of the scaling variable κ/q. Hence, we fit

$$\gamma_{\mathrm{SW}} = a \cdot \sqrt{\kappa/q} \tag{4.38}$$

to the data yielding $a = 1.30 \pm 0.04$ ($g_{\mathrm{fit}} = 2.2$), which is not far from the result of Böni *et al.* [114] and serves as a good parameterization of the linewidth data.

4.4. Conclusion and outlook

In this chapter, we have described the theoretical background of dynamical scaling, followed by explaining the pitfalls and careful considerations required for analyzing MIEZE data. Our results of the critical fluctuations in Ni were discussed with respect to theoretical predictions and the literature presenting studies of similar systems. This section summarizes the findings, points to current gaps in our understanding and addresses future investigations to resolve them.

We have shown the direct measurement of spin waves and critical fluctuations in nickel with the smallest wavevector transfer $q_{\mathrm{min}} = 6.6 \times 10^{-3}\,\text{Å}^{-1}$ and best energy resolution to date. From this data several results could be unequivocally drawn:

- Direct determination of the dipolar wavevector $q_{\mathrm{D}} \approx 7 \times 10^{-3}\,\text{Å}$ via measurement of the spin wave dispersion.
- Good agreement of the spin wave stiffness $D(T)$ and the dynamical scaling behavior of the spin wave linewidth $\gamma_{\mathrm{SW}}(\kappa/q)$ with dynamical scaling theory.
- Good agreement between the Résibois & Piette scaling function and the linewidth of the critical fluctuation.
- Absence of a signature originating from dipolar coupling in the dynamical scaling behavior above T_{C}

Nonetheless, the investigation was not without challenges. Misguided by initial literature research and having the benefit of hindsight, the lower limits for wavevector and energy resolution, which conversely corresponds to the upper limit of τ_{M}, have been chosen too high. This was partly owed to choosing an initial wavelength of $\lambda_{\mathrm{i}} = 6.0\,\text{Å}$ for higher flux compared to 8.0 Å. Given the fact, that a considerable amount of the data reduction and analysis procedure has been developed after performing the measurement, informed adjustment of the initial measurement plan was difficult. As a result of having

only conducted one experiment, due to an unforseen shutdown of the neutron source, the coverage in parameter space (q, T) lays a good foundation, but is not optimal to dispel all objections regarding the above presented conclusions.

Two main insights shape the conception process for future experiments on this topic. Firstly, access to smaller q needs to be achieved to definitively determine q_{D} in Ni. Secondly, a denser coverage of temperatures between $T_{\mathrm{C}} - 10\,\mathrm{K}$ and $T_{\mathrm{C}} + 10\,\mathrm{K}$ is required to address the critical exponents for the spin wave stiffness in detail, as well as ruling out or rather discovering non-scaling behavior around $\Delta T = 8\,\mathrm{K}$. The latter could in principle be studied using paramagnetic NSE, which is why an appropriate proposal has already been submitted. Due to the depolarizing conditions of a ferromagnetic Ni sample, the extension of the spin wave data is hopefully conducted at RESEDA in the not too distant future.

5. Probing the square lattice - Low-dimensional magnetism in a metal-organic framework

Low dimensional magnetism in historical context

Historically, research on 2D magnetic systems was of theoretical nature. About 80 years ago, Onsager predicted that an Ising-type magnet on a 2D lattice could harbor a phase transition to a long range order (LRO) state [148] at a finite temperature. The Ising model applies to systems with dominating anisotropy, where the spins can only be aligned parallel or antiparallel to an easy axis. For that reason, Onsager's prediction is not in conflict with the findings of Mermin and Wagner (1966), who could rigorously prove the absence of any ferromagnetic or antiferromagnetic LRO in a purely 2D, isotropic Heisenberg system [4].

Just a few months after the publication of Mermin's and Wagner's paper, one of the first experimental accounts of a 2D magnetic system came in the form of the compound K_2NiF_4 [149–151]. K_2NiF_4 can be classified as a *quasi-2D* magnet meaning that the crystal lattice itself is of three dimensional nature, while the interaction between magnetic ions within layers is strong compared to the interlayer interaction. This was convincingly demonstrated by neutron scattering on powder [149, 150] and single crystalline [152] samples. The study of the paramagnetic susceptibility generally supported neutron scattering results of Plumier et al. [150] by distinguishing two features at $T = 250\,\mathrm{K}$ and $T = 110\,\mathrm{K}$, which can be attributed to the emergence of in plane spin correlations and the onset of an anisotropic contribution [153], respectively. According to Lines [151] this is well aligned with calculations of a high temperature series expansion, which is commonly employed for the characterization of 2D magnetic systems. Characterization of low-dimensional magnetic systems requires the interplay of multiple, complementary techniques, to unravel the subtle differences between real world and idealized, theoretical systems. This is the case today, as well as half a century ago.

Nevertheless, having established the existence of low-dimensional magnetic systems, the field of research attracted broad interest again after the discovery of high temperature superconductivity in copper oxide materials, first in $Ba_xLa_{5-x}Cu_5O_{5(3-y)}$ [154, 155]. Shortly afterwards in 1987, the origin of the high T_c superconductivity was traced back by a combination of x-ray, susceptibility and resistivity measurements to a layered, K_2NiF_4-type structure in $La_{1-x}Ba_xCuO_4$ [156, 157]. Based on these discoveries, and notably the relation to K_2NiF_4, Anderson [18] argued for the applicability of the Resonant Valence Bond (RVB) model, which describes the emergence of cooper pairs from magnetic singlet pairs as a result of low dimensionality, low spin magnitude and magnetic frustration in the system.

These new concepts spurred the investigation of a multitude of physical phenomena connected to low-dimensional magnetism. Frustration in magnetic systems is a key

ingredient, as it profoundly influences the ground state resulting in strong fluctuations of the system in order to overcome it. This leads to states such as the Luttinger-liquid in $KCuF_3$ [158] and $Cu(NO_3)_2 \cdot 2.5D_2O$ [159] (1D), a spin-liquid phase initially thought to occur in $PbVO_3$ (2D) or a potential spin nematic phase in $BaCdVO(PO_4)_2$ (2D) [20]. Yet, to this date and specifically for square lattice arrangements, no J_1-J_2 model spin liquid has been found, despite plenty of theoretical predictions.

These novel magnetic states bring about *quantum critical points* (QCP) [158], provide insight in general properties in quantum critical phenomena and characterization of universality classes. Without a doubt, the few examples above are not an exhaustive list of references, which is why the review by Zhou *et al.* [160] or the book edited by Lacroix *et al.* [161] should provide a good starting point for reading.

Realization of 2D magnetism in metal-organic compounds

Indispensable in the search and study of quantum criticality are real world systems, which conform to the demanding requirements predicted by theoretical work. This is particularly true for investigations of low-dimensional magnetism, where samples are always 3D regarding their crystallography, but show reduced dimensionality in the magnetic sublattice. This can lead to dominant exchange pathways between the magnetic ions, which are confined in one layer (2D), along a ladder or chain (1D) [27, 162], or isolated pairs of ions forming dimers (0D) [163] in the crystal. *Metal organic magnets* can adopt relatively large and complex structures due to their unit cell size, with a variety of elements and molecular complexes involved. The magnetically active ions are often in the vicinity of not only oxygen ions as in inorganic oxides, but also with other elements (N, F...). Additionally the subtle role of the hydrogen bond adds yet another layer of complexity, leading to an enormous potential to host a variety of electronic and magnetic phases that originate from a strong interplay between the spin, orbital, and lattice degrees of freedom [164].

Coordination chemistry provides a versatile tool set for synthesizing a broad variety of low-dimensional magnetic systems connecting magnetic ions in high symmetry lattice positions with carefully selected complexes and separating the layers with additional ligands. An almost unlimited set of configurations is possible. While in $Cu_2(OH)_3(C_6H_{13}SO_3)$ the copper lattice planes are separated by long organic carbon chains and magnetic in-plane exchange is mitigated by (OH) groups [165], in $Cu(C_4H_4N_2)_2(ClO_4)_2$ the roles are inverse. Here, the magnetic interaction arises along the organic pyrazine ($C_4H_4N_2$) (pyz) constituents and the interplanar isolation is achieved with disordered ClO_4^- anions [166]. Therefore, a plethora of metal-organic compounds (MOC) with a diversity of structures, magnetic interaction pathways and predominantly antiferromagnetic properties can be acquired. In this loosely defined class of MOC, systems based on Cu^{2+} ions represent a prominent group, which brought forth well characterized compounds [160] and will be in the focus for the rest of this work.

One particular compound of this group, $Cu(pyz)F_2 \cdot (H_2O)_2$, is of special interest as it exhibits a transition from a 2D, planar magnetic coupled system to a 1D spin chain system under application of isotropic external pressure. The pressure anisotropically deforms the lattice structure resulting in a reorientation of the Jahn-Teller axis, which

is initially aligned with the $\boldsymbol{a}$ lattice vector along the pyrazine-copper chains, to be aligned with $\boldsymbol{c}$ and $\boldsymbol{b}$ depending on the pressure. Hence, the magnetic orbital of the Cu^{2+} ions switch orientation such that for $p = 6.1\,\mathrm{kbar}$ the 1D magnetic coupling was directly observed as a characteristic spinon continuum via inelastic neutron scattering by Skoulatos *et al.* [167]. This is but one example of uniform pressure leading to well defined deformation of the anisotropic octahedral environment in metal-organic perovskites [168].

The prospect of tailoring compounds with *switchable* magnetic dimensionality led to the effort of studying the MOC $Cu(C_4H_4N_2)_2(H_2O)_2Cr_2O_7$ (Cu-pyz) in search of a 2D to 1D pressure induced dimensionality change within the same crystallographic plane. First, in section 5.1 the implementation of 2D magnetic systems in the family of metal-organic systems will be discussed, how these systems can be characterized and why they are suitable for physical property engineering via external parameters. Section 5.2 addresses the magnetic bulk measurements, which give the base information required for further neutron scattering studies and modeling of microscopic behavior. Finally, section 5.3 presents the inelastic neutron scattering studies at sub-Kelvin temperatures and ambient pressure, as well as analysis of the observed spin wave dispersion by means of linear spin wave theory simulation with the *spinW* library.

5.1. Synthesis and structure of $Cu(C_4H_4N_2)_2(H_2O)_2Cr_2O_7$

Synthesis of a large portion of Cu^{2+} based MOC is done via wet chemistry. Generally, parent compounds in the form of water solvable salts are mixed in the stoichiometric ratio. The chemical reactions result in immediate precipitation of the wanted product or requires slow evaporation of the solvent with concurrent formation of crystals. Subsequent filtration separates solid crystals from the liquid phase and washing with appropriate cleaning liquids leaves back the intended product. The drying process, if applicable, is known to alter magnetic properties, as lattice water content can alter the magnetic behavior of the sample [165, p.1121 red line]. Since water molecules can serve as integral, structural part, out-diffusion of water changes the lattice internally and needs to be prevented through correct storage.

This general procedure has been successfully employed for carbon chain separated copper layers $Cu_2(OH)_3(C_nH_{2n+1}SO_4)$ [165], pyrazine connected ions in $Cu(pyz\text{-}d_4)_2(ClO_4)_2$ [166] and more [169–172], which are just a few selected examples. The crystals of $[Cu(C_4H_4N_2)_2(H_2O)_2]Cr_2O_7$ used in the described studies were grown similar to a method described in [28]. Pyrazine (0.48 g, 6 mmol) and ammonium dichromate (0.76 g, 3 mmol) were dissolved in 20 mL water. 0.5 g of nitric acid was added. A solution of copper(II) nitrate hydrate (0.89 g, 3 mmol) in 10 mL water was added. To grow single crystals, the mixture was heated up to 90 °C and slowly cooled down to room temperature. The crystal growth process yields depending on the amount of reactant a large variety of samples, with a wide range of sizes from tiny crystallites to single crystals of $(7 \times 7 \times 3)\,\mathrm{mm}^3$, which are well suited for magnetic bulk property measurements and inelastic neutron scattering, respectively [173].

The crystal structure of $Cu(C_4H_4N_2)_2(H_2O)_2Cr_2O_7$ is classified as orthorombic of space group #33, $Pna2_1$, with lattice parameters $a = (15.7236 \pm 0.0009)\,\text{Å}$, $b =$

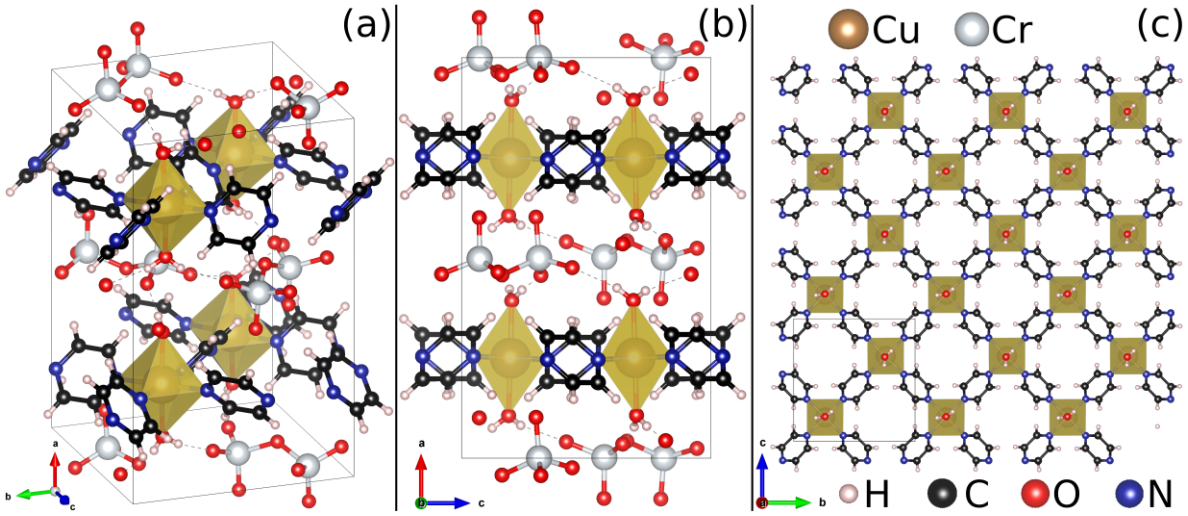

Figure 5.1.: Crystal structure of $[Cu(C_4H_4N_2)_2(H_2O)_2]Cr_2O_7$ in three different orientations. (a) depicts the conventional unit cell of Cu-pyz, which contains 4 formula units within it, each consisting of one magnetic Cu^{2+} ion, two pyrazine rings ($C_4H_4N_2$), two water molecules and a dichromate (Cr_2O_7) complex. In the bc-plane Cu^{2+} ions are coordinated with the pyrazine rings bonding to the nitrogen atoms on the opposing sides on the ring. Water molecules attach along the a direction. Thus the Cu^{2+} ions are surrounded by six ligands in an octahedral geometry elongated along the a-axis. (b) View along the crystals b-axis showing the separation of the Cu^{2+}-pyrazine layers with dichromate complexes in between. (c) View along the a-axis over 3 unit cells in b and c directions visualizing the copper square lattice with the pyrazine rings connecting adjacent ions.

(9.7063 ± 0.0006) Å, $c = (9.8112 \pm 0.0006)$ Å and has first been published by Goddard *et al.* [28, 174]. Figure 5.1 shows the structure as reconstructed by single crystal X-ray diffraction. In panel (a), on the left side, an overview of the whole unit cell is given, which contains 4 formula units. The magnetic Cu^{2+} ions are drawn within their respective coordination octahedra with pyrazine rings connecting the ions in the bc-plane and neighboring water molecules attached with the oxygen atom towards the copper ion along the a-axis. In between the copper layers, dichromate complexes (Cr_2O_7) serve as spacers. In the ac-plane, as depicted in figure 5.1 (b), the copper layers are well visible and the difference in distance between Cu^{2+} in the bc-plane in comparison to the a-axis becomes evident. Subplot (c) visualizes the square lattice arrangement of the copper ions over multiple unit cells, where the dichromate anions have been removed for clarity.

5.2. Magnetic bulk properties of $Cu(C_4H_4N_2)_2(H_2O)_2Cr_2O_7$

For the characterization of the bulk magnetic properties of Cu-pyz, measurements of the static susceptibility $\chi_{DC}(T, \mu_0 H)$ as a function of temperature, magnetization $M(\mu_0 H, T)$ as a function of external field as well as the AC-susceptibility $\chi_{AC}(T, \mu_0 H)$ under varying field and temperature have been performed. The bulk data is presented in the upcoming sections and discussed in the context of the properties expected for a 2D *quantum Heisenberg antiferromagnet* (QHAF). An important figure of merit for expressing the

degree of isolation between consecutive layers or the 'low-dimensionality' of a 2D QHAF is the ratio of the Néel ordering temperature and the intralayer exchange $T_N/|J|$. The results establish a baseline model of the magnetic interaction, which will be used for the analysis of the inelastic neutron data in chapter 5.3. For each data set, a qualitative description will be given in conjunction with extracted physical parameters via fitting of appropriate models. The quantitative results will be discussed in the context of contemporary literature.

All measurements conducted at ambient pressure conditions have been performed with the PPMS setup described in section 3.3 on instrumentation. A Cu-pyz single crystal with $m = 76\,\mathrm{mg}$ was aligned by hand with respect to the magnetic field of the setup, therefore an uncertainty of a few degrees cannot be ruled out.

5.2.1. Static susceptibility

The static susceptibility χ_{DC} was recorded with the external field along each of the crystal's main directions $\boldsymbol{a}, \boldsymbol{b}, \boldsymbol{c}$. The field was fixed at $\mu_0 H = 0.05$, 0.1, 0.5, 1.0, 5.0 and 9.0 T and simultaneously the temperature T was scanned from 2 K to 300 K.

In the following text the subscripts 'DC' and 'AC' might be dropped for simplicity, unless the distinction is not clear from context.

Experimental data

Following the common presentation of 2D QHAF magnets in the literature, an overview of the entire $\chi_{DC} = \frac{M}{H \cdot V}$ data is given in figure 5.2. Here, the unitless χ_{DC} is calculated, by normalizing the measured magnetization M to the external field H and sample volume V. For each field alignment and strength, the susceptibility χ_{DC} follows the same overall behavior with the susceptibility increasing as the sample temperature decreases. A clear hierarchy of χ_{DC} above $\mu_0 H = 0.05\,\mathrm{T}$ is visible, with $\chi_{\boldsymbol{H}\parallel\boldsymbol{a}} > \chi_{\boldsymbol{H}\parallel\boldsymbol{c}} \gtrsim \chi_{\boldsymbol{H}\parallel\boldsymbol{b}}$. At the lowest external field value $\mu_0 H = 0.05\,\mathrm{T}$ the order of $\chi_{\boldsymbol{H}\parallel\boldsymbol{b}}$ and $\chi_{\boldsymbol{H}\parallel\boldsymbol{c}}$ seems reversed, but simultaneously, the noise in the signal is significantly larger compared to the data at higher fields.

The susceptibility curves show a broad maximum peaking at around $T \approx 5\,\mathrm{K}$, sharply decreasing down to the lowest achievable temperature. The position in temperature of the maximum χ_{DC} value decreases drastically for $\mu_0 H \geq 5.0\,\mathrm{T}$ such that is hardly observable within the 2 K limit of the instrumentation. Additionally, a feature becomes visible at 50 K in $\chi_{\boldsymbol{H}\parallel\boldsymbol{c}}$. The bump appears at 0.5 T and becomes more pronounced with increasing external field strength.

An initial analysis and comparison with the Curie-Weiss law is shown in figure 5.3 where the inverse of the susceptibility $1/\chi_{DC}$ is depicted as a function of temperature. The exemplary data set was taken at 1 T with the field alignment along each crystal direction. In the temperature range from approximately 10 K to 45 K the inverse susceptibility follows a linear relationship with temperature independent of the alignment of $\boldsymbol{H}$ and complying with the Curie-Weiss law

$$\chi_{DC} = \frac{C}{T - \theta}\,, \tag{5.1}$$

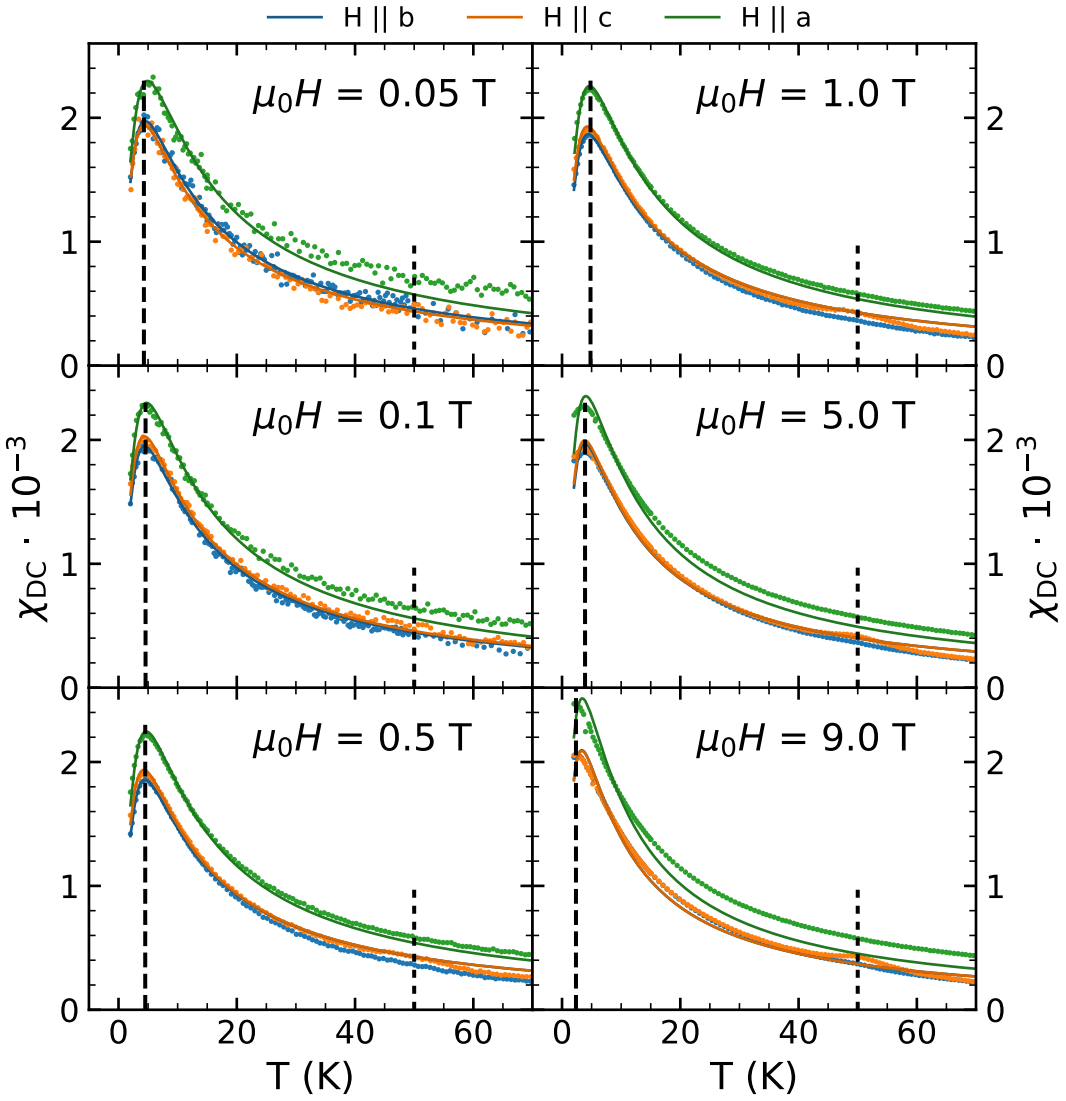

Figure 5.2.: Magnetic susceptibility over temperature for external magnetic fields up to $9\,\mathrm{T}$ along the main crystal axes. Independent of the external field strength $\mu_0 H$ the susceptibility shows the same overall curve shape. χ_{DC} increases with decreasing temperature reaching a maximum value at $T \approx 5\,\mathrm{K}$. This broad peak feature is indicative for emerging inplane spin correlations in a 2D QHAF before the system transitions to true magnetic LRO. LRO, as a result of the minuscule coupling between adjacent planes becomes relevant at $T \approx 0\,\mathrm{K}$. Furthermore the data shows a clear hierarchy with $\chi_{\boldsymbol{H}\parallel\boldsymbol{a}} > \chi_{\boldsymbol{H}\parallel\boldsymbol{c}} \gtrsim \chi_{\boldsymbol{H}\parallel\boldsymbol{b}}$. The two-point Padé approximation describes such a spin-$\frac{1}{2}$ Heisenberg system and each curve has been fitted with equation 5.2, with the results drawn as lines in the respective color. With increasing field, the susceptibility for $\boldsymbol{H} \parallel \boldsymbol{c}$ exhibits an unexpected bump, discussed in the main text.

which describes the magnetic susceptibility in the paramagnetic phase. Here, C is the *Curie* constant and θ is the *Curie-Weiss temperature*. Below 6 K, the data gradually diverges from the linear behavior, but not in a discontinuous way.

Fitting the Curie-Weiss law to the data reveals a negative value of θ. Furthermore, the fit parameters are similar for the data acquired with a field alignment parallel to the quasi-square plane (bc), but differ quite significantly for the perpendicular field alignment. Table 5.1 summarizes the fit results depicted in figure 5.3.

We will now attempt to fit an independent and more advanced model, as compared to the basic equation 5.1.

A theoretical description of 2D QHAF with isolated spins can be based on the isotropic Heisenberg model, which mathematically represents the spins of the Cu^{2+} ions ($S = \frac{1}{2}$) and the exchange coupling between them. Early on, a high-temperature series expansion approach to the spin-$\frac{1}{2}$ Heisenberg model on a square lattice yielded predictions of the thermodynamic properties χ_{DC} and the specific heat $\mathscr{C}$ [164, chapter by Navarro] [6, 175, 176]. In this context, the *two-point Padé approximation*

$$\chi_{DC}(T) = \frac{C}{T}\left[1 + \frac{\sum_{n=1}^{5} a_n \left(-J/T\right)^n}{1 + \sum_{n=1}^{5} b_n \left(-J/T\right)^n}\right], \tag{5.2}$$

being the ratio of two polynomials, is used to describe the magnetic susceptibility of a 2D QHAF as a function of J/T, where J is the coupling constant in units of K [166, 171]. Fitting expression 5.2, with two fit parameters, specifically the coupling constant J and the Curie constant C, to the susceptibility data shows good agreement as seen in the solid lines in figure 5.2. The prefactors a_n and b_n have been taken from Woodward *et al.* [171] and are listed in table A.1 of appendix A.1.

Evidently the descriptive power of equation 5.2 without adjustment to the coefficients is best for the low and intermediate field strength values. Figure 5.4 depicts a summary of the fit results to the $\chi_{DC}(T)$ curves. The subplots (a) and (b) show the optimal parameter values for the exchange constant J and Curie constant C respectively. In comparison, the results for C and J show an equal trend with increasing $\mu_0 H$, where the values hardly change up to 1 T but drop sharply for higher $\mu_0 H$. In case of the Curie constant, not only the trend is similar, but numerical values indicate $C_{\boldsymbol{H}\parallel\boldsymbol{b}} \simeq C_{\boldsymbol{H}\parallel\boldsymbol{c}}$. The values are tabulated in tables A.2, A.3 and A.4 of the appendix.

$\boldsymbol{H} \parallel$	$C \cdot 10^{-2}$ (K)	$\Delta C \cdot 10^{-3}$ (K)	θ (K)	$\Delta\theta \cdot 10^{-1}$ (K)
$\boldsymbol{a}$	3.48	0.15	-9.14	0.71
$\boldsymbol{b}$	2.28	0.17	-5.29	1.04
$\boldsymbol{c}$	2.47	0.18	-6.28	1.04

Table 5.1.: Fit results of the Curie-Weiss law fit of the 1 T data of Cu-pyz.

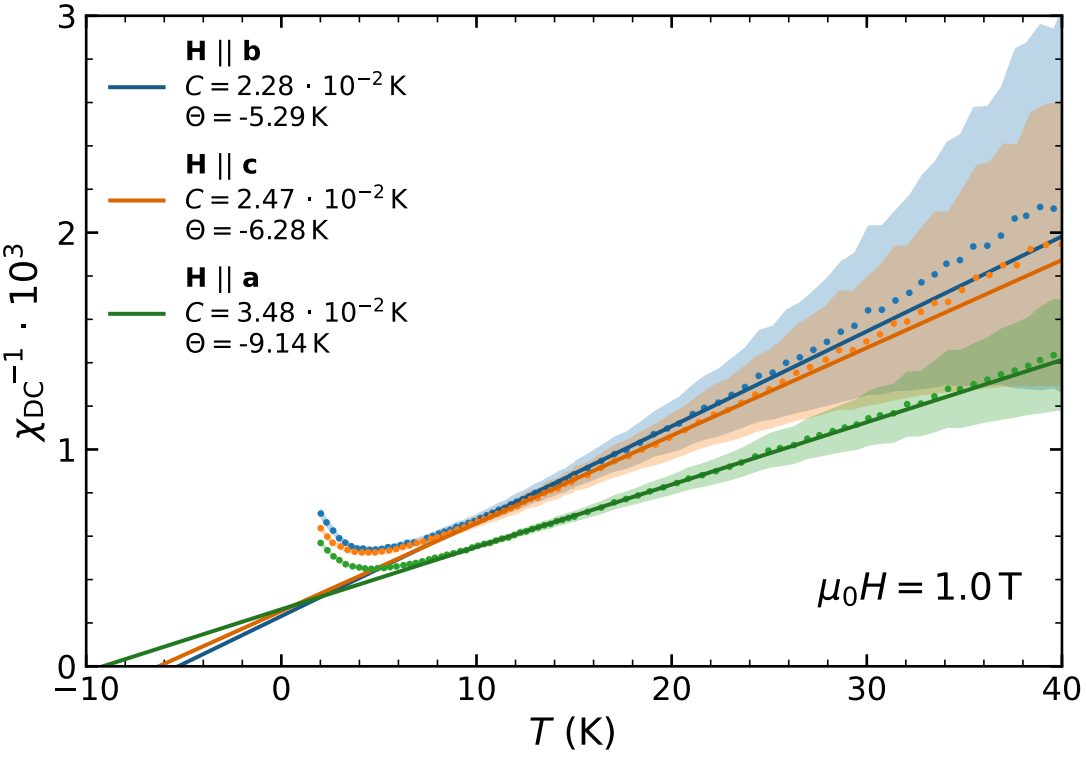

Figure 5.3.: Curie-Weiss plot of Cu-pyz at $\mu_0 H = 1\,\mathrm{T}$. The inverse static susceptibility, recorded for the external field aligned with each crystal axis, decreases linearly with T down to $6\,\mathrm{K}$. The shaded areas correspond to the measurement uncertainties of the identically colored data points. The Néel temperature for each direction is negative, as expected for a magnetic system with a dominant antiferromagnetic coupling. A small ferromagnetic component cannot be ruled out, based only on this data.

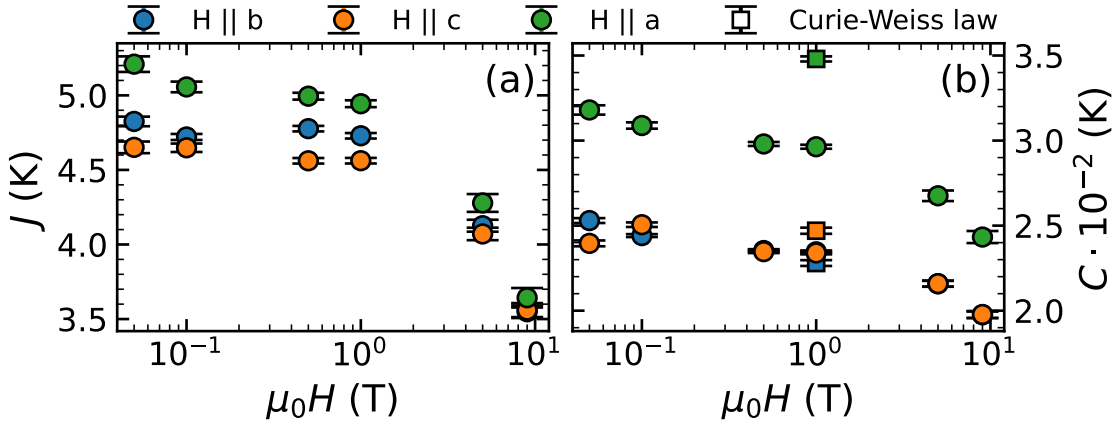

Figure 5.4.: Results from fitting the Padé approximation (equation 5.2) to the χ_{DC} data in figure 5.2. (a) depicts the optimal coupling constant J and (b) the associated Curie constant C as extracted from the fit for each $\mu_0 H$ value and field alignment to the crystal axes. The squares indicate the results obtained from fitting the Curie-Weiss law. The colors of the square markers retain their meaning.

Discussion

Looking at the Curie-Weiss analysis of the paramagnetic susceptibility as depicted in figure 5.3 and the extracted parameters in table 5.1, negative values of θ are consistent with the expectation of dominant antiferromagnetic exchange coupling in the system. With the Curie constant indicating a significant difference between the field alignment parallel ($C_\parallel$) and perpendicular ($C_\perp$) to the quasi square bc-plane, this can be explained in terms of the *g-factor anisotropy*

$$C_{\parallel(\perp)} = \frac{\bar{N} g_{\parallel(\perp)}^2 \mu_B^2 S(S+1)}{3k_B} \,, \tag{5.3}$$

which in case of Cu^{2+} can arise from crystal fields surrounding the ion [177, 178]. In a crystal lattice, structural constrains introduce an anisotropy potential, which lifts the degeneracy of the ground state of a magnetic ion and modifies the wave functions accordingly. The paramagnetic susceptibility of the system depends on the expectation values of the total angular momentum, which differs due to the new wave functions compared to the unperturbed magnetic ion.

Hence, g-factor anisotropy can be found in various metal-organic compounds such as $Cu(C_4H_4N_2)_2(ClO_4)_2$, described by F. Xiao *et al.* [179]. $C_{\parallel(\perp)}$ depends on the number density of magnetic ions $\bar{N}$, the anisotropy inducing g-factor $g_{\parallel(\perp)}$ and the spin S. Using equation 5.3 to analyze the fit values of the Curie constant obtained from the χ_{DC} data for $|\mu_0 H| \leq 1\,T$, the g-factors equate to $g_\parallel = 2.131 \pm 0.006$ and $g_\perp = 2.387 \pm 0.016$. Comparing again with Xiao's work, the anisotropy between parallel and perpendicular field alignment is similar. To put this in numbers, the relative difference $\delta g = (g_\perp - g_\parallel)/g_\perp = (11 \pm 1)\,\%$ for this work on Cu-pyz, whereas $\delta g = 9\,\%$ for $Cu(C_4H_4N_2)_2(ClO_4)_2$ in Xiao *et al.* Deeper insight into the exact values should be possible by analyzing the chemical environment of the Cu^{2+} ions, such as the bond length to the neighboring constituents. While this could lead to a better understanding of the electron orbital configuration and thus the exchange coupling pathways between the ions, it is beyond the scope of the presented work.

The *in-plane exchange coupling constant* J determines the energy scale of the interaction between neighboring Cu^{2+} ions in Cu-pyz. The ratio of the antiferromagnetic ordering temperature or *Néel temperature* T_N to J quantifies the 'two-dimensionality' of a system. In an isotropic, antiferromagnetic material, T_N can be identified by the diverging behavior of the susceptibilities $\chi_{DC,\parallel}$ and $\chi_{DC,\perp}$, which denote the susceptibility along and perpendicular to the preferred axis of spin alignment. According to molecular field theory, $\chi_{DC,\perp}$ stays constant down to $T = 0\,K$, $\chi_{DC,\parallel}$ decreases until it vanishes [180, chapter by F. Keffer]. Misalignment between external field and axis of the staggered magnetization can lead to mixing of both scenarios. In 2D QHAF, which inevitably ought to achieve 3D long range order (LRO), the differentiation between $\chi_{DC,\parallel}$ and $\chi_{DC,\perp}$ is expected and has been experimentally verified for a plethora of MOCs [28, 165, 166, 171, 172, 179].

However, $\chi_{\boldsymbol{H}\parallel\boldsymbol{a}}$, $\chi_{\boldsymbol{H}\parallel\boldsymbol{b}}$ and $\chi_{\boldsymbol{H}\parallel\boldsymbol{c}}$ do not exhibit any indication of transitioning to antiferromagnetic LRO down to 2 K. Subsequently, the determination of T_N and a distinction between easy and hard axis for the AFM alignment of spins can not be made

based on the χ_{DC} data alone. Therefore, we can only give an upper boundary for the ratio $T_{\mathrm{N}}/J \approx 0.42$, which is comparable to other low dimensional, copper based systems listed by Goddard *et al.* [28].

Even though, the susceptibility shows no clear transition to 3D antiferromagnetic LRO, the broad maxima, which are visible in each $\chi_{\mathrm{DC}}(T)$ curve of figure 5.2, are associated with the ordering of the strongly coupled Cu^{2+} ions within the bc-plane, while the individual planes are disordered with respect to their neighboring ones. This precedes the attainment of full 3D magnetic order in the sample, because the inter-plane coupling or potential single ion anisotropy is too small and easily overcome by thermal fluctuations even at the lowest attainable temperatures reached in our studies.

Further information on the ground state of the system could be discerned in the dynamic susceptibility χ_{AC} or neutron scattering measurements of Cu-pyz, observing the magnetic Bragg scattering to identify LRO on a microscopic level. Both subjects will be discussed in more detail in sections 5.2.3 and 5.3.1, respectively.

5.2.2. Magnetization

The bulk magnetization gives further valuable insights in the properties and the quality of a 2D QHAF system. The curve shape itself allows a unique distinction between mainly planar or 3D coupling between the magnetic ions.

Distinct features in a magnetization curve allow the determination of characteristic quantities such as the saturation magnetization m_{sat}, the saturation field strength $\mu_0 H_{\mathrm{c}}$ and the anisotropy field strength H_{A}. While the first two quantities are related to the high field behavior, the anisotropy field, which is usually much smaller than H_{c}, is indicated by a change of slope in the magnetization. At that point, the Zeeman energy overcomes the internal pinning potential, which is independent of its microscopic origin. The anisotropy field quantifies the resistance of the magnetization to align with the external field. Furthermore, the ratio $H_{\mathrm{A}}/H_{\mathrm{c}}$ is an important measure to characterize the divergence from an ideal isotropic 2D Heisenberg model system [166, 171, 179]. In the following the single crystal magnetization data of Cu-pyz up to 9 T with $\mu_0 \boldsymbol{H}$ parallel to each crystal axis and for three distinct temperatures $T \in [2.0\,\mathrm{K}, 5.0\,\mathrm{K}, 15.0\,\mathrm{K}]$ will be discussed.

Experimental data

For each temperature value and field alignment, magnetization curves were recorded starting from a zero-field cooled state. After an initial field sweep from 0 to 9 T, a complete hysteresis loop was performed going down to −9 T and again up to the 9 T. Looking at the data in figure 5.5, no saturation of the system is observed up to maximum available field for any curve. No hysteretic behavior is recognizable for any combination of external parameters. Similar to the susceptibility there is a hierarchy in the magnitude of the absolute values of the magnetization, with $|m_{\boldsymbol{H}\parallel\boldsymbol{a}}| > |m_{\boldsymbol{H}\parallel\boldsymbol{c}}| \geq |m_{\boldsymbol{H}\parallel\boldsymbol{b}}|$, which is shown in a more accessible depiction in figure A.1.

Most notable is the change in curve shape and its dependence on the temperature. While for $T \geq 5.0\,\mathrm{K}$ the magnetization is linear, but with differing slopes, as expected from susceptibility data, the magnetization at $T = 2\,\mathrm{K}$ deviates from this pattern. It

increases less steeply for small fields and bends upwards when $\mu_0 H$ becomes larger, with increasing slope. In figure 5.5 these two, differing field dependencies can be seen in subplots (a) and (b), when comparing the curve for $T = 5\,\mathrm{K}$ to $T = 2\,\mathrm{K}$. This behavior is a characteristic feature of 2D QHAF and will be discussed further in the next section. The fact that the system undergoes a change exactly in this region of temperature is strongly supported by the peaking susceptibility data (see. figure 5.2).

At exactly $\mu_0 H = \pm 1.0\,\mathrm{T}$ each magnetization curve exhibits a jump of the exact same magnitude and direction. This behavior is attributed to residual, captured flux in the pick up coil of the measurement setup[4]. For this mostly qualitative discussion of the magnetization data, the step is negligible and not further analyzed.

Discussion

The magnetization curves presented in figure 5.5 do not indicate saturation of the system up to 9 T. According to mean field theory calculations by Bonner and Fisher [5] the saturation field H_c can be calculated as

$$\mu_0 H_\mathrm{c} = \frac{z k_\mathrm{B} J}{g \mu_\mathrm{B}}, \tag{5.4}$$

where $z = 4$ for a Heisenberg model system. The other symbols retain their usual meaning: k_B is the Boltzmann constant, J is the coupling constant, g is the Landé factor and μ_B is the Bohr magneton. Equation 5.4 is widely used across the literature to estimate the saturation field of 2D magnets, the derivation by Bonner and Fisher (equation 4.7 in [5]) relates to an antiferromagnetic chain. The parameter z often interpreted to be the coordination number actually indicates the dimensionality of the spin coupling. According to Bonner and Fisher $z = 2(1 + \gamma)$, with $\gamma = 1$ and $\gamma = 0$ indicating Heisenberg or Ising-type couplings, respectively. However, no analytical equation for the 2D case is easily available. Hence, equation 5.4 will be used for further analysis. Taking the parameters for g and J as determined from the χ_DC analysis, we arrive at $\mu_0 H_{\mathrm{c},\boldsymbol{b}} = (13.42 \pm 0.08)\,\mathrm{T}$, $\mu_0 H_{\mathrm{c},\boldsymbol{c}} = (12.87 \pm 0.12)\,\mathrm{T}$ and $\mu_0 H_{\mathrm{c},\boldsymbol{a}} = (12.45 \pm 0.15)\,\mathrm{T}$ with an average of $\mu_0 \bar{H}_\mathrm{c} = (13.12 \pm 0.06)\,\mathrm{T}$. Considering that according to Goddard *et al.* the saturation field determined on a powder sample, has a value of $\mu_0 H_c = 13.3\,\mathrm{T}$, the estimated $\mu_0 \bar{H}_\mathrm{c}$ is in good agreement and explains why no saturation behavior is observed up to 9 T.

One of the indicators of a 2D QHAF seen in magnetization data is a *concave up* curvature up to the point of saturation, which was experimentally verified in various systems and is in good agreement with calculations by Zhitomirsky *et al.* [181] using a spin-wave expansion approach with second-order corrections. Strictly speaking, the theory is valid for $T = 0$, which is why the most fitting comparison is with the lowest temperature data at $T = 2\,\mathrm{K}$.

The upward curvature in the data is subtle and is expected to be largest close to $\mu_0 H_\mathrm{c}$, because the magnetization is supposed to diverge logarithmically at this point. Since $\mu_0 H_\mathrm{c}$ is about 50 % larger than the available external field magnitude, the divergence

4 Personal discussion with H. Gabold.

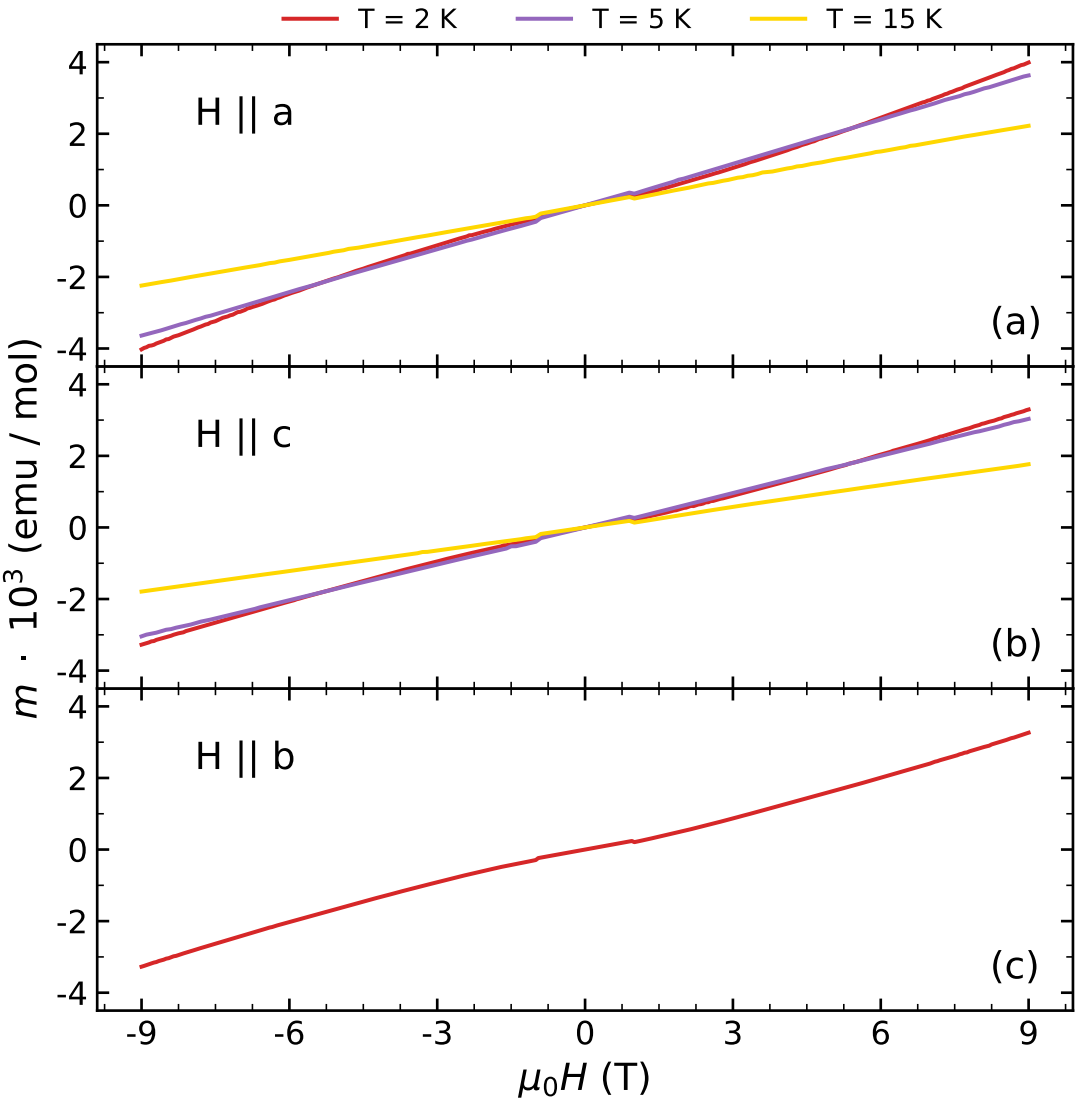

Figure 5.5.: Sample magnetization for different external field alignments and sample temperatures. Each panel shows the magnetization along one of the major crystallographic axis. For temperatures $\geq 5.0\,\mathrm{K}$ the relation between magnetization and external field is linear, while for $T = 2.0\,\mathrm{K}$ the curve bends steeper with increasing field. This behavior is representative for 2D magnetism and is discussed in the text. Panel (c) only contains data for $T = 2.0\,\mathrm{K}$.

and saturation is barely visible in the data. This distinctive curvature is subtle, but it becomes recognizable when comparing e.g. the magnetizations recorded at 2 K and 5 K, as can be seen in panels (a) and (b) of figure 5.5. The magnetizations at 5 K and 15 K essentially exhibits a linear dependence on external field over the measured range. In the following, the low and high field characteristics of the magnetization data of a 2D QHAF will be discussed more quantitatively.

According to the spin wave theory calculations of Zhitomirsky *et al.*, the low field

approximation yields

$$M(H) = \chi H + \frac{2}{\pi}\left(\frac{H}{H_c}\right)^2 \ , \tag{5.5}$$

where the second, non-linear term is a characteristic of a 2D QHAF spin system. Within the framework of Zhitomirsky, the susceptibility χ is expressed as a series up to second order in $1/(2S)$ and determined numerically. For intermediate values $0 < H < H_c$, no simple, analytical formula describing the magnetization could be extracted, however in the high field limit

$$M(H) = S\left[1 - \frac{h}{2S}\ln\left(\frac{\pi^2}{4h}\right)\right] \ , \tag{5.6}$$

with $h = 1 - H/H_c$ as the reduced field, the aforementioned logarithmically divergent behavior is obtained at the point of saturation.

Figure 5.6 brings together the low temperature magnetization data of Cu-pyz and puts it in relation to the theory prediction of Zhitomirsky *et al.* as well as data published by Woodward *et al.* [171], which show the entire magnetization curve of related compounds $(5MAP)_2CuBr_4$ and $(5CAP)_2CuBr_4$. The data is scaled with respect to the saturation magnetization m_{sat} and the saturation field $\mu_0 H_c$. For the present Cu-pyz data, the literature value of $\mu_0 H_c = 13.3\,T$ was used for normalization. Since the saturation magnetization of Cu-pyz is not known from this measurement, the qualitative agreement of the magnetization with theory and Woodward's data was taken as justification to estimate m_{sat} by scaling the data to fit the theory. This procedure yields $m_{sat,\boldsymbol{H}\|\boldsymbol{b}} = (5832 \pm 4)\,emu/mol$, $m_{sat,\boldsymbol{H}\|\boldsymbol{c}} = (5911 \pm 4)\,emu/mol$ and $m_{sat,\boldsymbol{H}\|\boldsymbol{a}} = (7124 \pm 4)\,emu/mol$, which ought to be verified in future experiments.

Turning towards the low field part of the data, the points for $\mu_0 H < 1\,T$ have been omitted due to the flux capture artifact shifting the curve. Hence, analysis of an existing anisotropy field, which is hallmarked by a deviation from a quadratic field dependence [171, 179], was not feasible. For 2D QHAF the anisotropy field in competition with the out-of-plane coupling are the driving forces of the emergent LRO and therefore of interest for a complete characterization of the system.

Finally, it is relevant to mention that beyond the theoretical description of idealized 2D QHAF at $T = 0\,K$, quantum Monte-Carlo simulations provide an excellent tool to study low-dimensional magnetic systems [28]. These models agree in the limit of $T = 0$ with analytical approaches, but the Hamiltonian can easily be extended with out-of-plane interactions, anisotropy and Zeeman terms, while simultaneously yielding results for finite temperatures.

As an example, promising results from the computational side have been produced by means of *stochastic series expansion* (SSE) quantum Monte Carlo methods. The partition function is calculated by expanding $e^{-\beta H}$ ($\beta \propto 1/T$) and decomposing higher orders of the Hamiltonian into *bond* operators, which describe the interaction between two spins S_i, S_j, effectively reducing the problem to a sum over products of permutation operators. Employing optimized update [182, 183] and tempering schemes (for finite T models), any thermodynamic property, such as heat capacity, magnetization [28, 182],

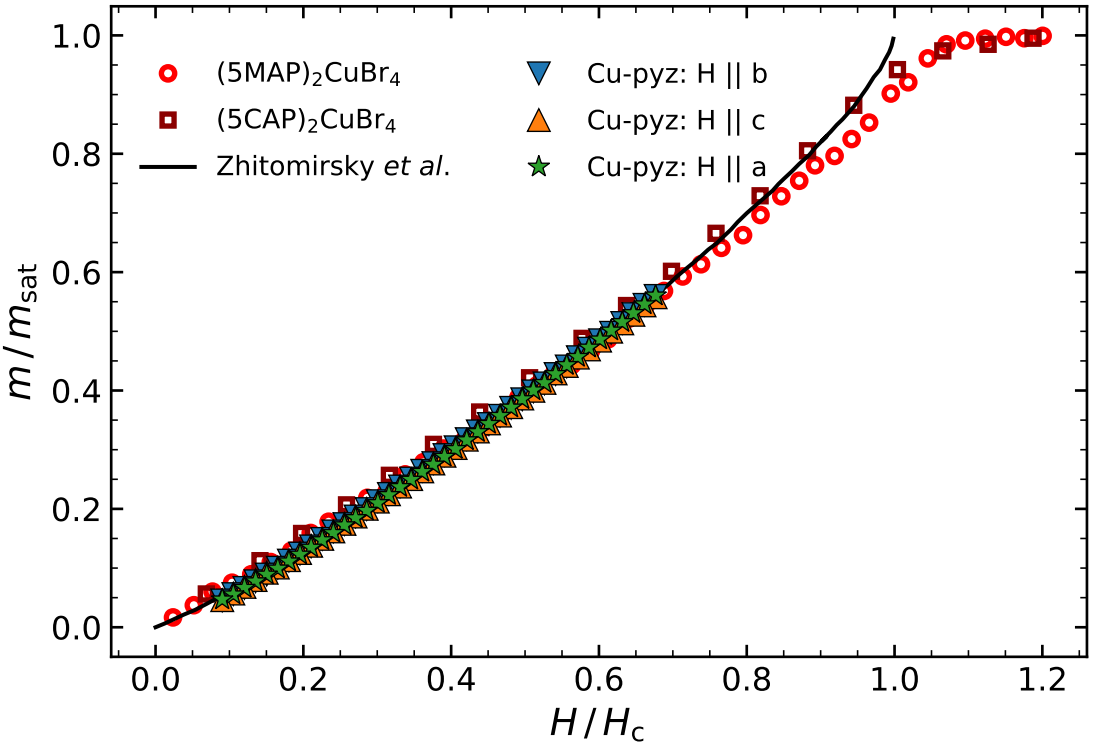

Figure 5.6.: Sample magnetization for different external field alignments of Cu-pyz at $T = 2\,\mathrm{K}$. The experimental conditions were not sufficient to saturate the magnetization of Cu-pyz, therefore the saturation magnetization m_{sat} and and saturation field H_{c} could not be directly observed. Based on the previously deduced g and C values, the latter can be estimated to be $(13.12 \pm 0.06)\,\mathrm{T}$. By normalizing the data to this value and comparing it to the expected magnetization curve of a 2D QHAF calculated by Zhitomirsky *et al.*, plausible estimates for m_{sat} were extracted. For consistency, we additionally compare our data with measurements by Woodward *et al.*. Data points for $(5\mathrm{MAP})_2\mathrm{CuBr}_4$, $(5\mathrm{CAP})_2\mathrm{CuBr}_4$ and the theoretical magnetization curve have been extracted from figure 6(b) in Woodward *et al.* [171].

susceptibility [182] or spin wave stiffness [183], of a 2D QHAF system can be computed.

5.2.3. Dynamic susceptibility

In parallel to the static susceptibility χ_{DC} and magnetization m, the AC-susceptibility χ_{AC} was measured. The χ_{AC} data presented in this chapter is of twofold interest. On the one hand, they contribute to the characterization of Cu-pyz as a 2D QHAF, but on the other hand, they serve as a baseline for studying the system under hydrostatic pressure since the AC measurement coils can be fit into large pressure cells. The next section provides an overview of the measurement.

Experimental data

The AC-susceptibility $\chi_{\mathrm{AC}} = \chi' + i\chi''$ was recorded at constant temperatures $T \in [2.0\,\mathrm{K}, 5.0\,\mathrm{K}, 15.0\,\mathrm{K}]$ over $-9.0\,\mathrm{T} \leq \mu_0 H \leq 9.0\,\mathrm{T}$ and constant field strengths $\mu_0 H \in$

$[0.05\,\mathrm{T}, 0.1\,\mathrm{T}, 0.5\,\mathrm{T}, 1.0\,\mathrm{T}, 5.0\,\mathrm{T}, 9.0\,\mathrm{T}]$ from 2 K to 300 K.

Introducing the field dependence of χ_{AC} first, in some cases, the data is dominated by noise, which is why the plots are cropped to the range, where useful information can be extracted. This can be seen in figure 5.7 exemplarily for $T = 2\,\mathrm{K}$, in which the dotted lines mark the point beyond which the χ' signal increasingly fluctuates. Hence, we limit our discussion to data within the marked $\mu_0 H$ range, but we try to reflect on the possible reasons for the increasing noise at large fields. The entire data set is depicted in the figures A.2 and A.3 of appendix A.2. Regarding the range $\mu_0 H$ in which noise appears, χ'' behaves similarly to χ'. However within the measurement uncertainty $\chi'' = 0$ for the entire region of interest (see figure A.3 in the appendix A.2).

In figure 5.8 the χ' measurements are grouped with respect to the alignment of $\boldsymbol{H}$ for different temperatures. As χ_{AC} is related to the magnetization via $\chi_{\mathrm{AC}} = \partial M/\partial H$, the difference in the magnetization curves is also reflected in the shape of χ', where for $T \geq 2\,\mathrm{K}$ it is essentially a constant with $\chi'_{\boldsymbol{H}\parallel\boldsymbol{a}} > \chi'_{\boldsymbol{H}\parallel\boldsymbol{c}}$, except for a small peak at 0 T, which is also visible at the lowest temperature. Since only 5 measurement points fall in the peak region, it is hard to determine the shape and width of this peak. In all cases, the peak height correlates positively with temperature, but not with field direction and decays completely for $|\mu_0 H| > 0.2\,\mathrm{T}$.

In comparison, the curve shape of χ' at 2 K is far from constant. Except for the peak, the signal increases with positive curvature up to an inflection point around 1.5 T. From this point it increases with a decreasing slope, but without leveling out completely up to 5 T. Beyond that, a trend of further increase of χ' can be postulated despite of the noisy signal (see figure 5.7). Lastly, it is notable, that $\chi'_{\boldsymbol{H}\parallel\boldsymbol{c}}$ is slightly larger than $\chi'_{\boldsymbol{H}\parallel\boldsymbol{b}}$ for low external field strengths.

As mentioned before, the temperature evolution of χ_{AC} has been measured for $|\mu_0 H| \in [0.05\,\mathrm{T}, 0.1\,\mathrm{T}, 0.5\,\mathrm{T}, 1.0\,\mathrm{T}, 5.0\,\mathrm{T}, 9.0\,\mathrm{T}]$ and is shown in figure 5.9. Consistent with the

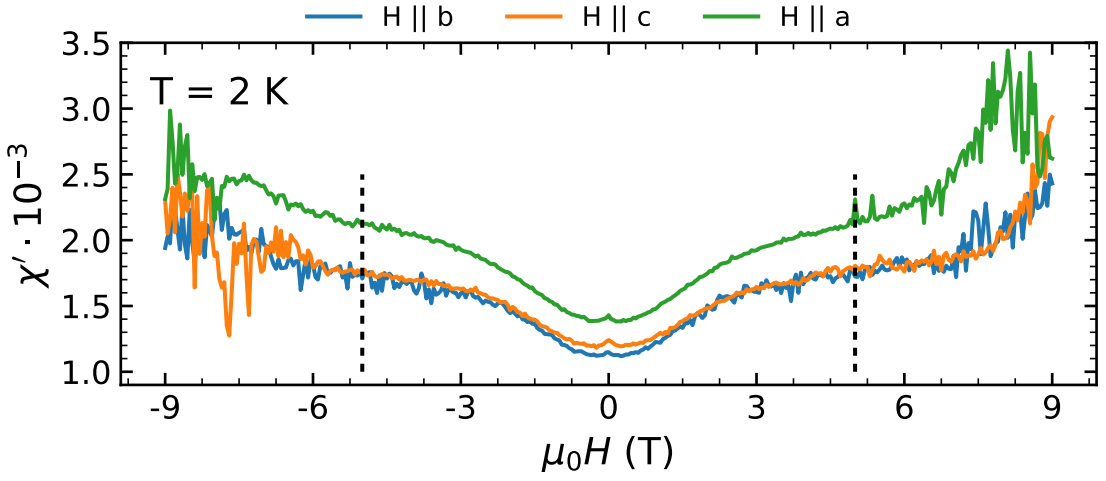

Figure 5.7.: χ' at $T = 2\,\mathrm{K}$ for $-9\,\mathrm{T} \leq \mu_0 H \leq 9\,\mathrm{T}$ along the main crystal axes. Exceeding $|\mu_0 H| \leq 5\,\mathrm{T}$, as marked by the dotted, vertical lines, the χ' signal becomes increasingly noisy. χ' exhibits a small peak at $\mu_0 H = 0\,\mathrm{T}$. For $|\mu_0 H| > 0.2\,\mathrm{T}$, the signal flattens and increases up to an inflection point at $\approx 1.5\,\mathrm{T}$, from where χ' increases with ever decreasing slope. For $|\mu_0 H| > 5\,\mathrm{T}$, the trend seems to change but the details are hidden in the noise.

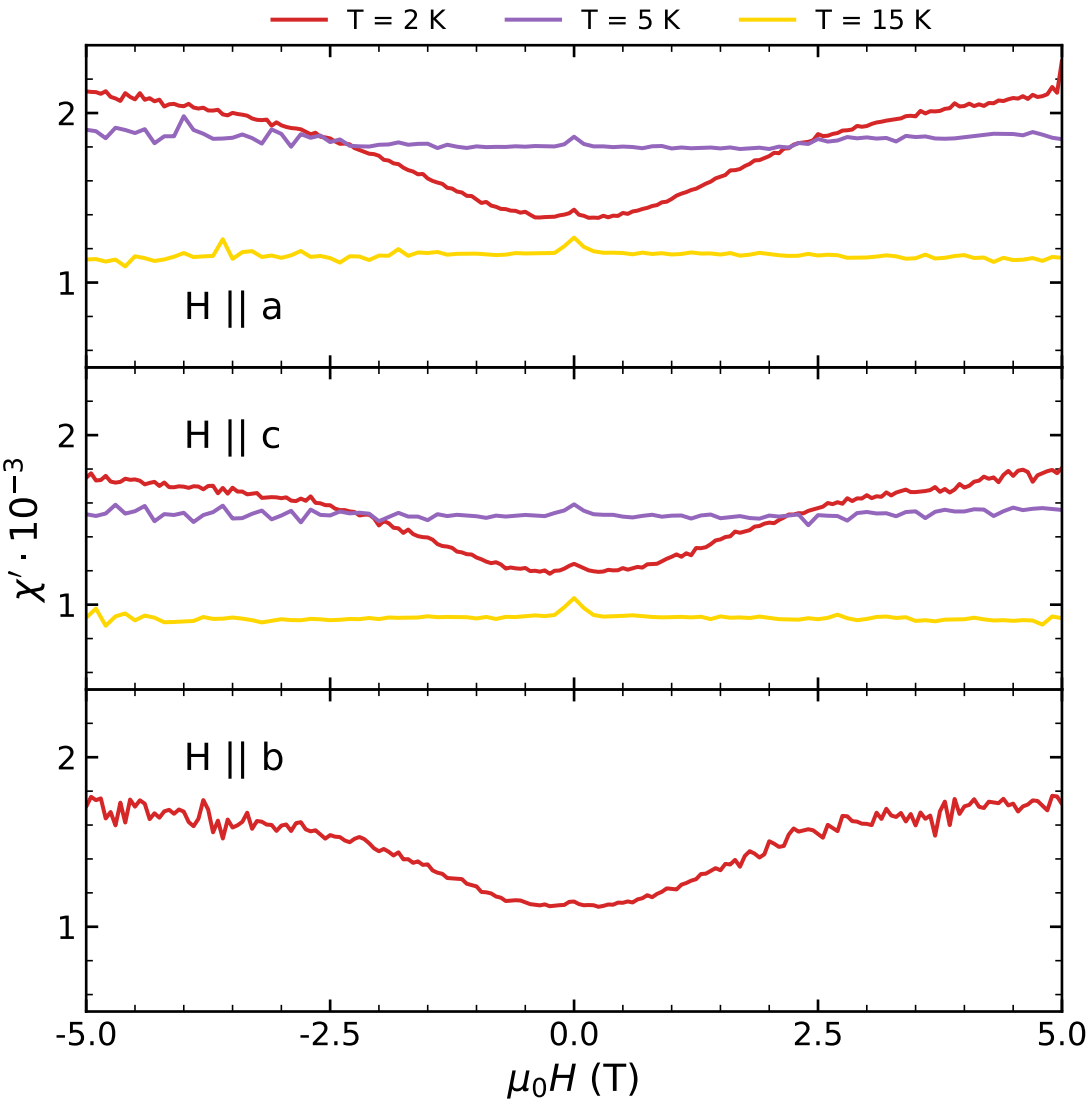

Figure 5.8.: χ' along all major crystal axes and temperatures $T \in [2.0\,\mathrm{K}, 5.0\,\mathrm{K}, 15.0\,\mathrm{K}]$. For the lowest $|\mu_0 H|$ values, χ' spikes sharply, whereby the amplitude of the peak decreases with decreasing temperature. Furthermore, at the lowest temperature, χ' behaves differently from being constant, which is the case for $T = 5\,\mathrm{K}$ and $15\,\mathrm{K}$. The signal $\chi'(2\,\mathrm{K})$ increases with a positive curvature up to an inflection point around $1.5\,\mathrm{T}$. Then, the sign of the curvature switches and χ' tends towards leveling out.

$\chi_{AC}(H)$ data, it is hard to extract meaningful information from the curves for $|\mu_0 H| > 5\,\mathrm{T}$, but are otherwise mostly congruent to the static susceptibility curves. Conversely, the bump at $T = 50\,\mathrm{K}$ is visible also for low fields and interestingly appears in the configuration $\boldsymbol{H} \parallel \boldsymbol{b}$ for 0.05 T and possibly 0.1 T. For higher fields, the signal is solely apparent for $\boldsymbol{H} \parallel \boldsymbol{c}$. At higher temperatures ($T > 200\,\mathrm{K}$) a broad feature and subsequently increased noise is present, almost identical in all curves.

Discussion

The AC susceptibility as a function of temperature is a good indicator of magnetic ordering phase transitions. Especially in the presence of an additional, small ferromagnetic exchange coupling, χ_{AC} has been successfully employed in identifying spin canting in antiferromagnetically dominated systems [172]. Even more intricate scenarios like a Kosterlitz-Thouless transition in a quasi-2D copper based MOC with XY anistropy were elucidated by determination of the critical exponent γ from χ_{AC} data [184–187]. However, the temperature dependent χ_{AC} curves in figure 5.9 show no signature of a phase transition consistent with antiferromagnetic order [179] or with occurrence of a spin canting resulting from weak, additional ferromagnetic coupling [172].

Therefore it is reasonable to assume that the ordering temperature $T_N < 1.8\,\mathrm{K}$ and thus gives an updated estimate for the figure of merit as $T_N/|J| = 0.377 \pm 0.001$, which was introduced in section 5.2.1. Still, for a more accurate categorization of Cu-pyz, the phase transition needs to be determined precisely with a temperature range extending below 1.8 K.

Finally, the AC-susceptibility gives a validation for the hypothesized instrument artifact detected in the magnetization curves at 1 T. Due to its direct relation to the sample magnetization $\chi_{AC} = \frac{\partial M}{\partial H}$, a sudden jump in the magnetization of the sample would have been registered as a peak in χ_{AC}. However, no such feature is visible in the field dependent data for neither field direction nor sample temperature. Therefore, the working hypothesis that the jump in the magnetization is a systematic instrument effect remains unchanged.

The χ_{AC} and χ_{DC} mutually exhibit a bump at 50 K, which is best visible in the configuration $\boldsymbol{H} \parallel \boldsymbol{c}$. A possible explanation are trace amounts of Fe (0.001 %) present in the dichromate salt used for the synthesis process. Fe is the only magnetically active impurity listed in the reacants, since within the Cr_2O_7 complexes the chromium ions are in the highest oxidation state lacking susceptible, unpaired electrons. However, it is unclear why the signal is seemingly anisotropic and why it appears at 50 K. Nevertheless, the fact that the signal becomes more pronounced, in shape and intensity, in the high field χ_{DC} data suggests that it is of non-diamagnetic origin. A spurious signal arising from trapped, solidifying oxygen, which has two phase transitions at 54 K from liquid to solid and at 44 K (γ to β phase), does not clearly fit the observed signal either [188, 189].

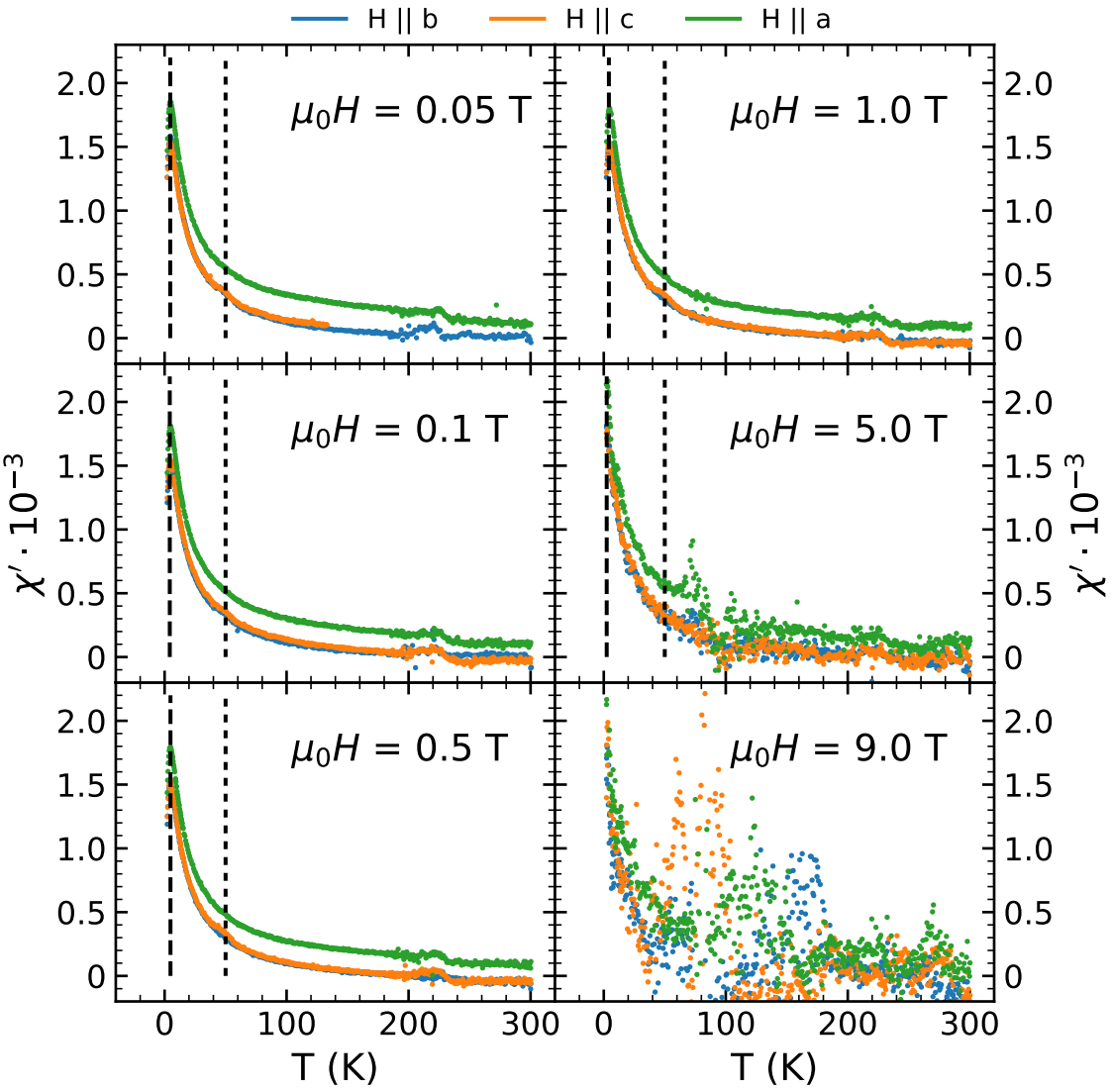

Figure 5.9.: χ' dependence on temperature with $\boldsymbol{H}$ along all major crystal axes and $|\mu_0 H| \in [0.05\,\mathrm{T},\ 0.1\,\mathrm{T},\ 0.5\,\mathrm{T},\ 1.0\,\mathrm{T},\ 5.0\,\mathrm{T},\ 9.0\,\mathrm{T}]$. The curve shape matches the χ_{DC} with a broad maximum around $4\,\mathrm{K}$ to $5\,\mathrm{K}$, the familiar hierarchy of signal strength and a bump at $50\,\mathrm{K}$, which is visible for low field values and $\boldsymbol{H} \parallel \boldsymbol{b}, \boldsymbol{c}$ configurations. Beyond $200\,\mathrm{K}$ all scans exhibit a broad double peak feature and more dispersed data points. High field values $|\mu_0 H| \geq 5.0\,\mathrm{T}$ lead to a noisy signal.

5.3. Magnetism in $Cu(C_4H_4N_2)_2(H_2O)_2Cr_2O_7$ - A study with neutron scattering

While bulk measurements at ambient pressure provide a consistent picture of the magnetic properties, neutron scattering is uniquely qualified to add complementary information. Therefore, (I)NS has been extensively involved in unraveling the structure [149, 152, 190] and dynamics [167, 191, 192] of many MOC that exhibit low-dimensional antiferromagnetism [3].

With the INS experiment conducted at the TAS IN12, we aimed to refine the underlying model describing the magnetism in Cu-pyz and establish the unknown magnetic structure. We fixed a Cu-pyz single crystal of approximately $(7 \times 7 \times 3)\,\mathrm{mm}^3$ on a sample holder by entwining it with $d = 0.5\,\mathrm{mm}$ thin aluminum wire. Figure 5.10 shows one example of a prepared sample. Two crystals have been prepared for the beam time, one with a sample holder made of copper and one made of aluminum. In the actual experiment, the copper sample holder was chosen for better heat conduction at mK temperatures. Further information on the instrument setup can be found in subsection 3.1.4.

Prior to mounting, the orientation of the crystals was determined via X-ray Laue measurements at the crystal lab of the Physics Department at the Technical University of Munich [193]. The geometric shape of the crystal was found to be within 5° to the microscopic structure. Perpendicular to the larger 'base' plane of the crystals was the a-axis, while b- and c- axes were parallel to the edges of the 'base' plane. The corresponding Laue patterns are shown in figure 5.10.

When investigating the magnetism of a new system with neutron scattering, the procedure for studying an antiferromagnet can be summarized as follows. Elastic neutron scattering is used to determine the transition to the ordered state at the Néel temperature T_N, by measuring the emergence of the order parameter. Under the assumption that the nuclear structure is known, determination of the propagation vector is the next step. This alone does not fully describe the magnetic structure of the system, but it allows to predict the emergence of magnetic scattering signal in reciprocal space. However, in our case, no magnetic Bragg scattering was detected. This indicates that 3D long range order has not been achieved in the sample, possibly halting further investigations.

Since in 2D QHAF the magnetic interaction is dependent on the direction of the exchange pathways in the crystal, long range correlations within planes of strongly coupled spins arise before 3D order is achieved. These correlations allow spin waves to propagate in these planes, which can be detected by INS. Requiring a fair amount of intuition and patience, since the magnetic propagation vector is unknown, the weak spin wave signal can still be picked up without complete prior knowledge of the magnetic structure yielding valuable insight unobtainable by diffraction methods.

In the first part of this section, the elastic scattering data will be discussed with respect to 2D magnetic systems. Subsequent to this, the mapping of the magnetic excitations along the high symmetry directions [010] and [001], will be analyzed based on linear spin wave theory applied to an AFM model, combined with the coupling parameters acquired from magnetic bulk measurements as an initial guess.

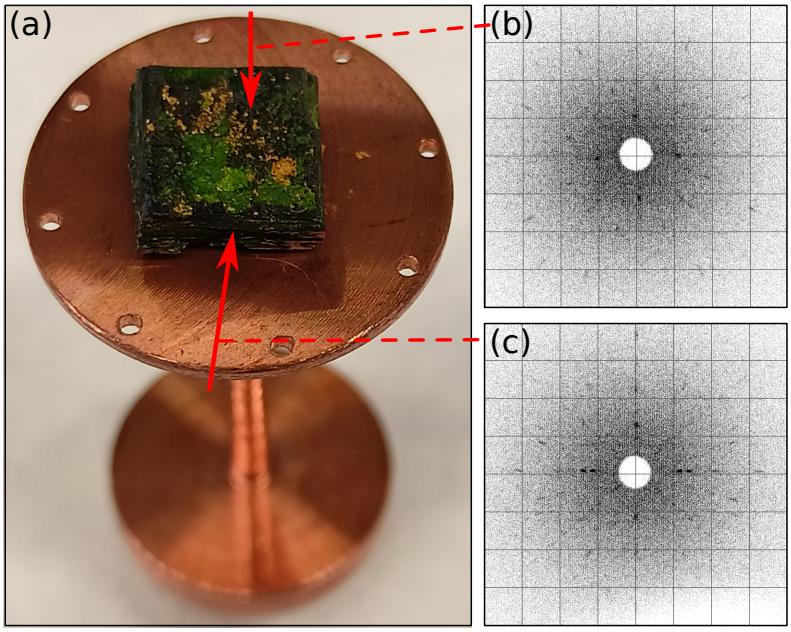

Figure 5.10.: Sample holder and preliminary X-ray Laue measurements. (a) shows a Cu-pyz single crystal mounted onto the sample holder for the INS measurements on IN12. (b) and (c) present the X-ray Laue images taken along the c axis and in the a-b plane, respectively. The sample was oriented with the surfaces of the cuboid perpendicular to the X-ray beam indicated by the red arrows. The red broken lines link them to the associated Laue image. The Laue data indicates that the macroscopic surfaces are well aligned with the lattice planes of the microscopic structure. Mismatch correction and distinction of the a and b directions was done during alignment on IN12.

5.3.1. Search for long range order via magnetic Bragg scattering

Following the general procedure for neutron scattering studies on magnetic materials, measurements at the cold triple-axis spectrometer PANDA at the FRM II were performed to determine the magnetic structure of Cu-pyz. A search for magnetic, elastic scattering signal at integer and half-integer positions was executed for temperatures between 0.06 K and 5 K. These positions correspond to a propagation vector (000) and $(\frac{1}{2}00)$, respectively. During this experiment, we found no evidence of elastic magnetic scattering contributions on top of the nuclear scattering signal. Two exemplary scans are shown in figure 5.11 (b) and (c) at the reciprocal lattice positions (011) and (400), respectively.

The graphic 5.11 (a) depicts data taken during a later experiment at IN12. Here, we show a scan of the (003) position, which is systematically extinct due to the lattice symmetry. The (003) reflection is especially important because as we will see later, this is precisely the zone center of inelastic scattering signal, which should exhibit a magnetic Bragg peak, if we were at absolute 0 temperature. Both data sets recorded at PANDA and IN12 were normalized to a background level to visualize the difference in intensity from nuclear scattering at allowed and forbidden Bragg peaks.

Given the unsuccessful attempts of detecting the magnetic structure in elastic scattering, we opted for directly studying the spin wave signal. Using PANDA in an inelastic scattering configuration at the lowest temperature setting $T = 0.06\,\mathrm{K}$, the signal of a

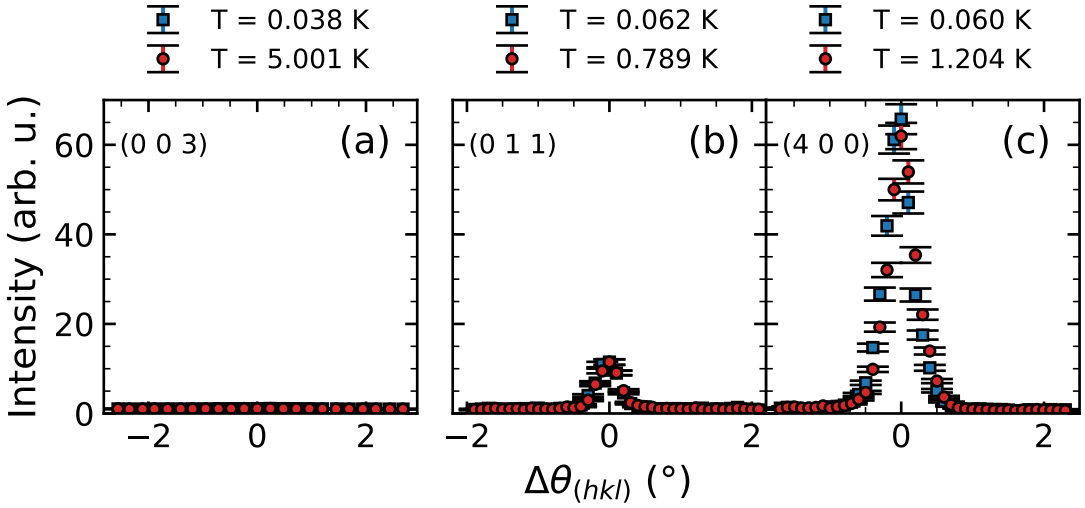

Figure 5.11.: Rocking scans of symmetry forbidden and allowed Bragg peak positions at the triple-axis spectrometers IN12 (a) and PANDA (b), (c). (a) shows a rocking scan around the (003) Bragg position, which is systematically extinct due to the lattice symmetry, with negligible signal to noise ratio (SN) of 1.1. In comparison, the Bragg peaks in (011) and (400) shown in (b) and (c), respectively, are substantially stronger with $\mathrm{SN}_{(011)} = 11.4$ and $\mathrm{SN}_{(400)} = 65.7$. The ratio of the peak amplitudes in (b), (c) fit well with the nuclear structure factor calculated from the crystal structure. Each scan was performed at base and elevated temperatures as indicated in the legend of each plot. In (a), the blue data points lie exactly behind the red ones, meaning that no additional magnetic scattering was detected in any case. In particular this should have been visible in panel (a) if the temperature was lowered to absolute 0.

slowly dispersing excitation originating from the $(00\bar{1})$ position was detected. According to the nuclear structure $\langle 001 \rangle$ is elastically forbidden, but the emergence of the dispersion signal at $(00\bar{1})$ requires it to be a putative zone center for magnetic Bragg scattering. While the inelastic scattering data will be discussed in more detail, this discovery justified the search for magnetic Bragg scattering at systematically extinct positions using IN12 in the second experiment. Therefore, several positions of potential magnetic peaks were scanned at 0.038 K and 5 K and the recorded scattering signal is depicted in figure 5.12. Due to limited beam time, the pair of scans in the upper three plots are incomplete. The nuclear Bragg peak (011) is shown for reference. Despite the peak shape detected at a few positions, it is to note that their signal to noise ratio $\mathrm{SN} < 2$. The measured intensity at these positions is a spurious signal, which is why the Bragg peak at (011) is substantially more intense.

For each reciprocal lattice position, the difference in sample temperature leads to a similar signal, whereby the low temperature scans do not contain extra intensity compared to the high temperature scans. This is not in line with a sought-after long range ordering transition between 0.038 K and 5 K.

The appearance of background neutron counts at forbidden positions is the result of a significant portion of hydrogen in the sample, which scatters incoherently across all directions. Subsequently, a background is expected over all reciprocal space. The

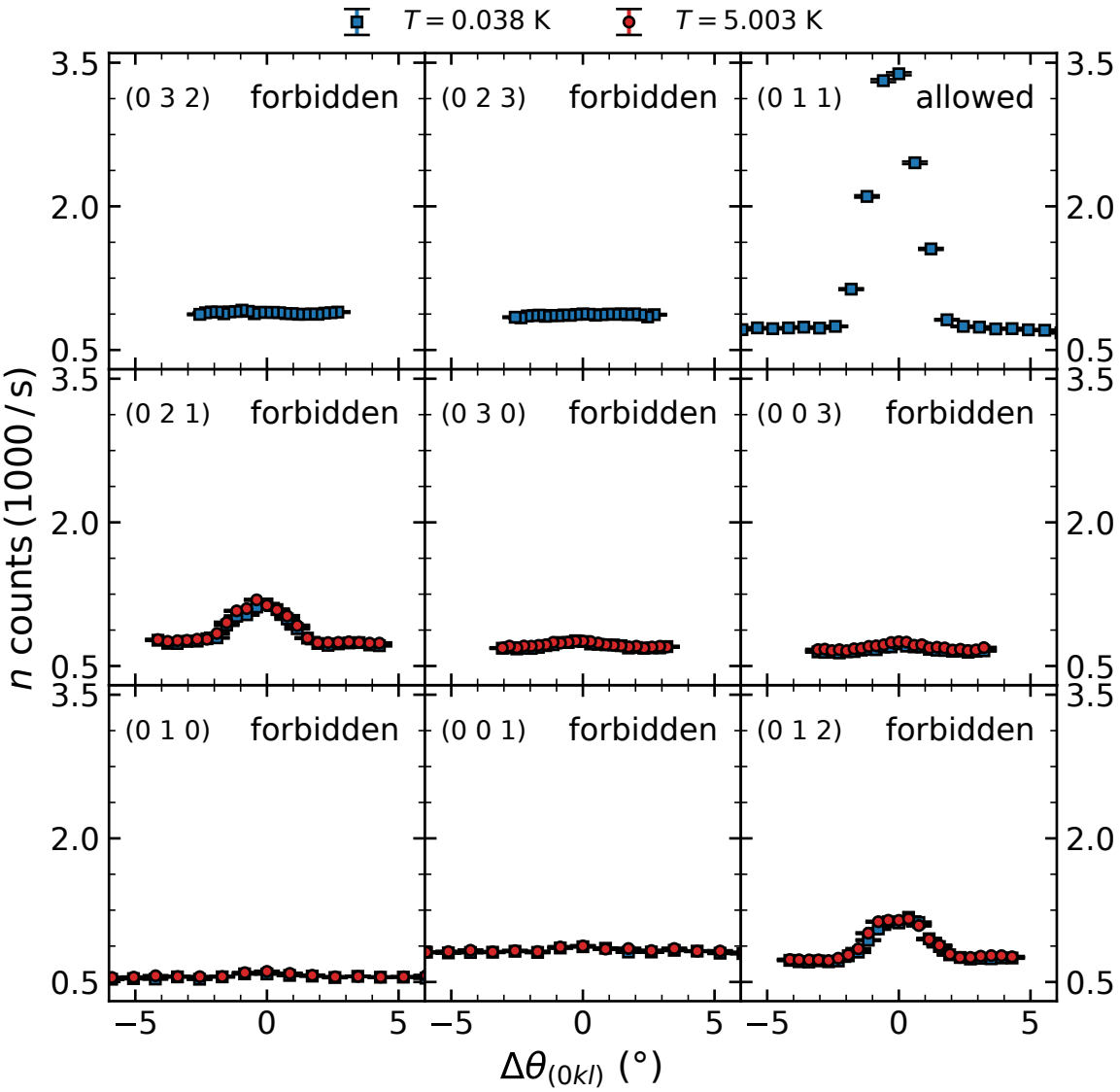

Figure 5.12.: Rocking scans of symmetry forbidden and allowed Bragg reflections at the triple-axis spectrometer IN12 at $0.038\,\mathrm{K}$ and $5.0\,\mathrm{K}$. Except for (011) in the upper right panel, no nuclear Bragg scattering is expected for the rest, due to systematic extinction rules. The measurement at two different temperatures yields no indication of magnetic Bragg scattering and subsequently magnetic LRO down to $0.038\,\mathrm{K}$. This is why the blue data points lie behind the red ones in the lower six panels.

peaked, low intensity above background at the investigated Bragg peak positions is not uncommon, but in general related to spurious effects. While the origin could arise from the sample itself, double scattering or higher order scattering, which is not entirely suppressed by the instrument, is also a potential source of the signal. Tying down the root cause is a complex issue and it is unlikely to yield valuable insight, which could change the interpretation described in this chapter. On the contrary, the absence of magnetic Bragg scattering can be reconciled with the observation of systematic inelastic neutron scattering is discussed in chapter 5.3.3.

5.3.2. Magnetic excitations studied with inelastic neutron scattering

Despite the negative results from the elastic NS study, which has been reported in the preceding section, INS was employed in the vicinity of (001) to validate the findings of PANDA and to comprehensively map the inelastic signal around this position. At the base temperature of 0.038 K, an inelastic scattering signal was observed at a energy transfer $\Delta E = 0.3\,\mathrm{meV}$ and reciprocal space position $Q_l = (0.913 \pm 0.003)\,\mathrm{rlu}$ in a constant energy scan. Figure 5.13 shows the aforementioned scan with a Gaussian fitted to the signal. The model consists of one peak on top of a sloped background, mathematically expressed as

$$\mathscr{G}(x|x_0, \sigma, A, m, b) = A \cdot \exp\left[-\frac{1}{2}\left(\frac{x - x_0}{\sigma}\right)^2\right] + xm + b\ . \tag{5.7}$$

The blue line represents the model equation evaluated with the optimal set of parameters and the black, broken line visualizes the sloped background in the scan. These parameters have been determined by minimization of the associated χ^2 function with a *Python* wrapper of the *Minuit2* algorithm, which is part of the *ROOT* data analysis framework developed at CERN [129]. In order to verify the magnetic nature of the signal, the scan was repeated at a temperature of 1.51 K, yielding an essentially linear slope lacking any evidence of a comparable signal. The overall neutron count rate increases slightly with temperature.

This analysis procedure has been applied to all the available INS data gathered at IN12. While the INS signal of a spin wave excitation is, under ideal circumstances, represented as a Dirac-δ distribution in Q-E-space (see 2.1.3 for context) the signal measured in reality is broadened by the resolution of the instrument. In case of a TAS, the resolution function is approximated by a 4D Gaussian distribution function, which when convolved with the spin wave signal results in a Gaussian peak [57, 58]. The underlying background was fitted with a simple linear model extending over the reasonably small interval of the scanned parameter. In figure 5.13 the assumption provides a reasonable description, but less so for other cases such as the $\Delta E = 0.7\,\mathrm{meV}$ scans in figures A.4 and A.6 of the appendix. Therein, the fitting of both peaks required a different linear background for each peak. Whenever possible the scattering signal recorded at one energy transfer value was fitted with one slope. Examples of the analysis results are shown in figure 5.14 for constant-Q scans and figure 5.15 for constant energy scans. All optimal fit parameters are tabulated and can be found in the appendix A.3.

Looking at the analysis results, the following observation can be made. At low energy

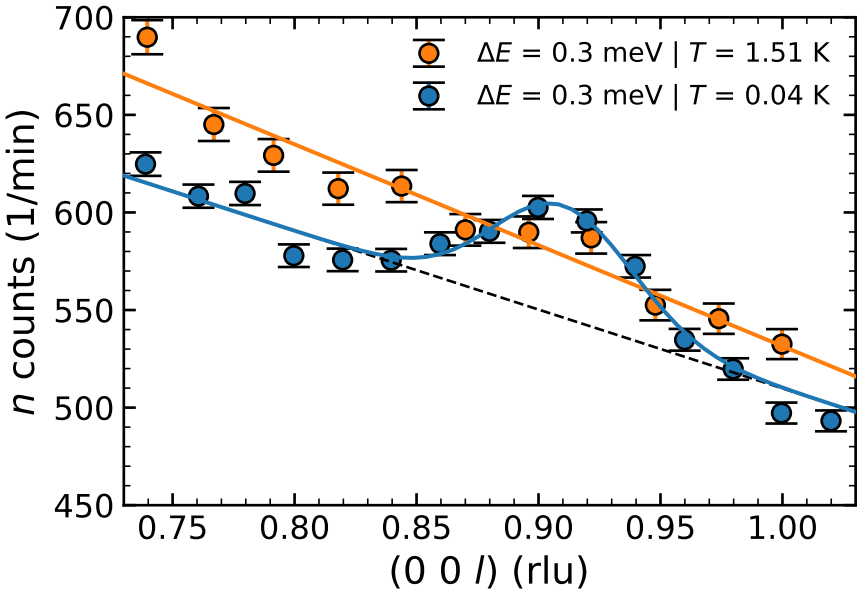

Figure 5.13.: Constant energy scans along the (00l) direction at the triple-axis spectrometer IN12 measured at 0.04 K and 1.51 K. A model consisting of a Gaussian peak with a sloped background has been fitted to the data. At base temperature this procedure yields a signal at $\Delta E = 0.3\,\mathrm{meV}$ and $Q_l = (0.913 \pm 0.003)\,\mathrm{rlu}$ in $\boldsymbol{Q}$-E-space, whereas at 1.51 K no comparable signal is observed.

values, the spin wave dispersion signal arises fairly symmetric around the (010) and (001) positions in reciprocal space. The background contributes a significant fraction up to the majority of the detected neutrons for each data point and changes drastically over reciprocal space. Close to the BZ center it is almost independent of q for small ΔE, but shows steep sloping and intensity contributions at intermediate energy transfers. For the highest ΔEs at the BZ boundary, the q dependence as well as the count rate are reduced again.

Regarding the intensity of the INS signal, several observations can be made. First, the intensity decreases with increasing energy transfer. Second, at large energy transfers and small momentum transfers the signal is not detectable. Third, for symmetric scans around BZ centers, as seen in the center plots of figure 5.15, the intensity differences indicate focusing and defocusing configurations of the three-axis spectrometer. This is related to the complex shape of the resolution function of a TAS, often represented by an ellipse contouring the half intensity boundary. The orientation and shape of the resolution function with respect to the dispersion leads to a shift, broadening and dilution of the true double differential scattering cross section. Fourth, intensity of the signal for $h, k > 1.5\,\mathrm{rlu}$ is reduced compared to the case of $h, k < 1.5\,\mathrm{rlu}$.

In a magnetic system, the observation of an inelastic signal in a constant-Q scan is a reliable indicator of a 'true' dispersing excitation, whereas constant-E scans can lead to similar signal shape originating from quasi-elastic scattering with a strongly momentum dependent linewidth instead of collective excitations. Hence, the constant-Q data presented in figure 5.14 provide good evidence for a collective excitation, the fit

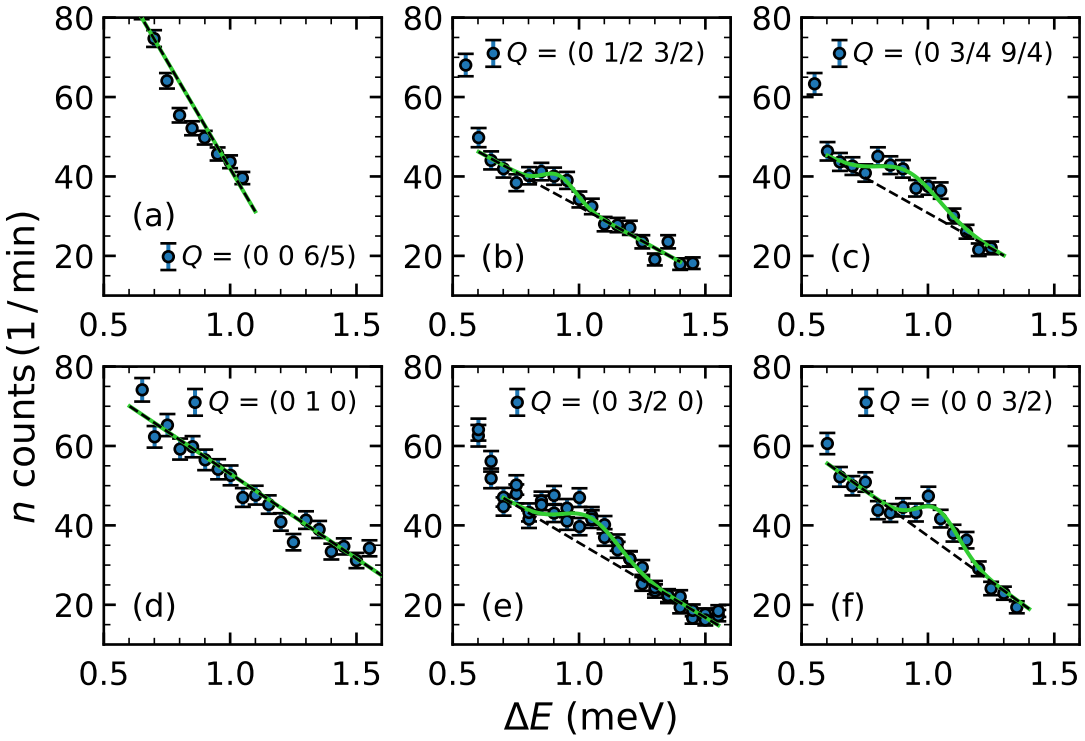

Figure 5.14.: Constant-Q scans in the range $0.4\,\mathrm{meV}$ to $1.6\,\mathrm{meV}$ are shown at various positions in reciprocal space, performed at the triple-axis spectrometer IN12. The six scans were performed at different positions in reciprocal space for measurement of the associated spin wave energy, only successful for panels (b), (c), (e) and (f). The spin wave signal was modeled by a Gaussian peak on top of a linear background, as stated in equation 5.7. In retrospect, there is no excitation signal visible in (a), because the scan range did not extend below $0.4\,\mathrm{meV}$. In case of (d) the $\boldsymbol{Q}$ matches the position of a putative magnetic Bragg peak, where no spin wave excitation is expected in the scanned energy range.

results of which can be seen as green lines. At the positions (001), (002), (0 0 1.2) and (010) no signal was detectable. The two last data sets depicted in figure 5.14 (a) and (d).

Summarizing the data from the Q-E-positions extracted from the INS scans in one plot, reveals the dispersion measured in the bc-plane. Figure 5.16 (a) shows the dispersion along the high symmetry $\langle 001 \rangle$ direction within this plane, whereas 5.16 (b) contains the excitation signal measured along the $[0\,\xi\,3\xi]$ direction. The color of each data point encodes the type of scan, which was used to detect it. Blue is used for constant-Q scans and red for constant-E scans. Seemingly, dispersions emerge from the (010) and (001) positions in reciprocal space, indicating a sinusodial relation. At low energy transfer values down to $\Delta E = 0.1\,\mathrm{meV}$, no gap of the dispersion is detectable within the energy resolution of IN12. Similarly, the two separate excitation peaks can not be resolved close to the elastic line, appearing as one peak around the Brillouin zone center.

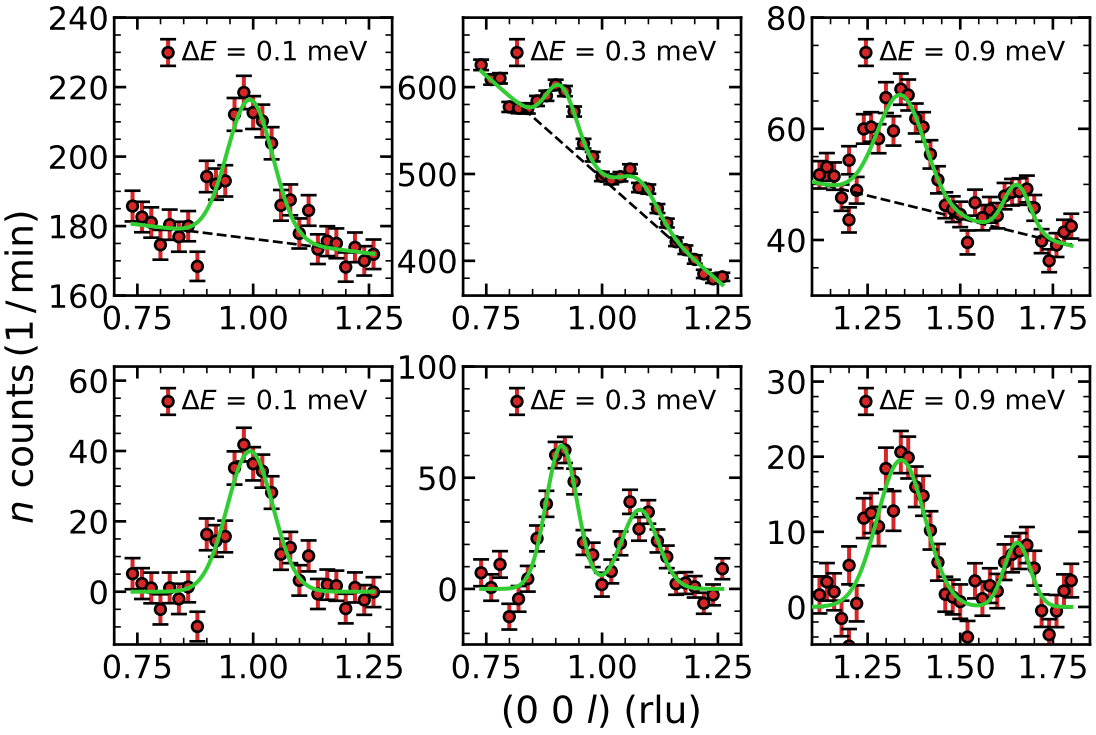

Figure 5.15.: Constant energy scans along the $(00l)$ direction measured at the triple-axis spectrometer IN12. Data taken at three different energy transfer values $\Delta E \in [0.1\,\mathrm{meV}, 0.3\,\mathrm{meV}, 0.9\,\mathrm{meV}]$ are shown together with the fitted Gaussian model (solid line). The lower three panels show the background subtracted INS signal corresponding to the curves above. The data at $\Delta E = 0.1\,\mathrm{meV}$ has been measured with $k_\mathrm{f} = 1.1\,\mathrm{\AA}^{-1}$, the other two data sets with $k_\mathrm{f} = 1.5\,\mathrm{\AA}^{-1}$. The small k_f value was used to improve the resolution at small energy transfers.

5.3.3. Inferring structure - Discussion of the neutron scattering results

The neutron data provides information on the spatial and time correlation of the magnetic moments of the Cu^{2+} ions. Models of the magnetic structure and coupling parameters built on the basis of the bulk measurement results can be tested against it. In this context, the expected magnetic Bragg scattering signal of a 2D magnetic system with strong intralayer coupling and therefore magnetically ordered planes are discussed and compared with the Cu-pyz system. Further, the shape of the spin wave dispersion encapsulates information on the coupling of spins, while the amplitude of the spin wave signal reflects the static magnetic structure. The simulation software spinW [39] is used to calculate the dispersion and spin-spin correlation function of a general magnetic structure and coupling model via linear spin wave theory, to be compared with the neutron data.

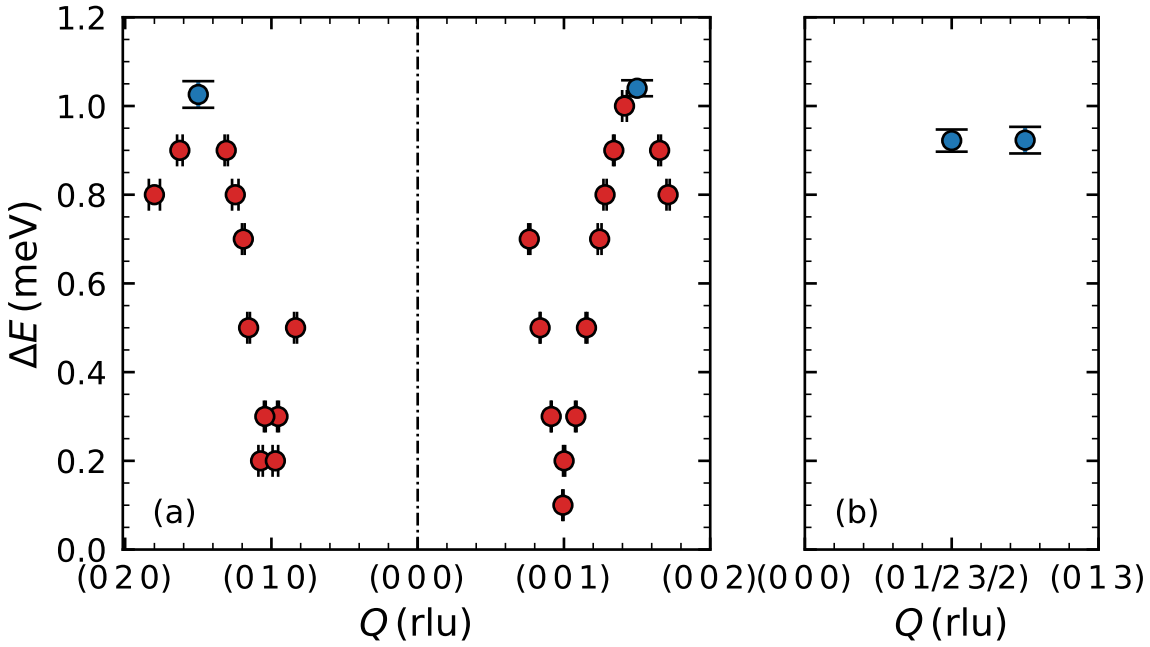

Figure 5.16.: Summary of the measured inelastic scans along $(0\,0\,l)$, $(0\,k\,0)$ and $(0\,\xi\,3\xi)$. The color of each data point corresponds to the type of scan it was extracted from, with red points yielded by constant-E and blue points yielded by constant-Q scans. The latter ones were only applicable in flat parts of the dispersion, while constant-E scans provided good results for steep slopes.

Elastic neutron scattering emerging from 2D long range order

First accounts of the 2D character in a layered magnetic system via (quasi)elastic neutron scattering were presented by Birgeneau *et al.* in 1969 in the layered perovskite material K_2NiF_4 [152]. In K_2NiF_4, NiF_2 planes with strong in-plane coupling between the Ni^{2+} ions are separated by two KF sheets, which suppress interlayer interaction between the Ni^{2+} ions due to the increase in interatomic distances [194]. A depiction of the nuclear and magnetic structure of K_2NiF_4 is shown in figure 5.17 (a). This suppression of magnetic interaction between two adjacent NiF_2 leads to the ordering of the in-plane spins at $T = 180\,\mathrm{K}$, with a transition to 3D LRO at $T_\mathrm{N} = 97.1\,\mathrm{K}$. Within this temperature region, where only long range spin correlations within the planes are present, elastic magnetic scattering intensity arises in the shape of *rods* instead of *points* in reciprocal space. These rods extend in the direction of disorder (perpendicular to the ordered planes) as can be seen from the fundamental equation describing the differential cross section of neutron scattering. Considering only the static part of the double differential cross section for magnetic scattering (see equation 2.18)

$$\left(\frac{\mathrm{d}\sigma}{\mathrm{d}\Omega}\right)_{\mathrm{Bragg}} = A(\boldsymbol{k}_\mathrm{i}, \boldsymbol{k}_\mathrm{f}) \sum_{\alpha\beta} \left(\delta_{\alpha\beta} - \hat{Q}_\alpha \hat{Q}_\beta\right) \sum_{\boldsymbol{R}} e^{i\boldsymbol{Q}\cdot\boldsymbol{R}} \langle S^\alpha_{\boldsymbol{0}} \rangle \langle S^\beta_{\boldsymbol{R}} \rangle \ , \tag{5.8}$$

where $A(\boldsymbol{k}_\mathrm{i}, \boldsymbol{k}_\mathrm{f})$ contains all neutron and sample related prefactors, the *rod* shaped intensity distribution in reciprocal space can be deduced by examining $\sum_{\boldsymbol{R}}$.

If only in plane correlations exist, spins in the same crystal plane contribute to the differential cross section via the vector product $\langle S_{\mathbf{0}}^{\alpha}\rangle\langle S_{\boldsymbol{R}}^{\beta}\rangle$, while contribution from different planes average to zero due to random angles between the spins. Hence, the differential cross section becomes independent of the value Q_z, the component perpendicular to the planes [194]. Figure 5.17 (b) shows the reciprocal space map of K_2NiF_4 in the $[001]\times[100]$ scattering plane, where double circled reciprocal lattice points indicate nuclear scattering and single circles represent magnetic Bragg points appearing below T_N. Above T_N magnetic correlations only exists within the the ab-plane, which is why the magnetic rod and therefore uniform magnetic scattering should appear along the l direction, designated *scan B* on the reciprocal space map. In contrast, scanning across the rods at any constant l value, labeled *scan A*, yields a localized magnetic scattering signal. Both scans are shown in figure 5.17 (c1) and (c2), respectively. The sample temperature was set to 99 K for the open circle data, 95 K for the open triangle data and 4 K for the filled circle data.

The appearance of this magnetic intensity rods was well demonstrated by Birgeneau *et al.* leading to the aforementioned conclusion that K_2NiF_4 is a good realization of a 2D AFM. In addition, two intriguing assessments can be made from the results published by Birgeneau. Even though the diffuse scattering intensity within the strongly coupled planes is centered around the reciprocal lattice points, the intensity distribution is broadened. Also, the integrated intensity is two orders of magnitudes smaller compared to the Bragg scattering arising at these positions after 3D LRO is established. Furthermore, the indicative rod shaped signal can be tracked over a wide range of temperatures up to the

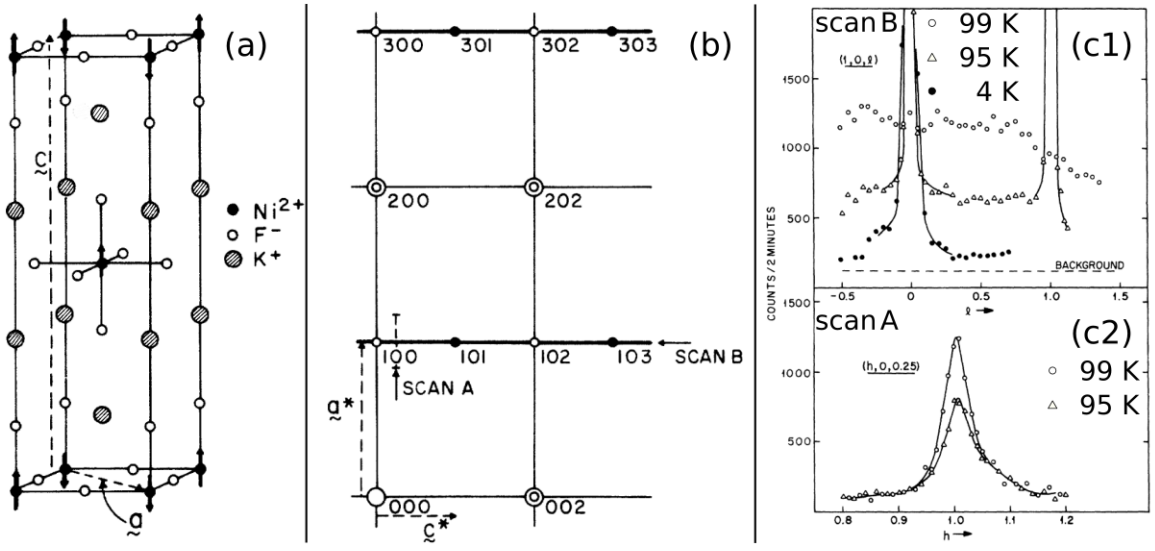

Figure 5.17.: Structure, reciprocal space map and measurement summary of K_2NiF_4. (a) shows the atomic positions of K_2NiF_4 in one unit cell, as well as the magnetic moments of the Ni^{2+} ions. (b) depicts the reciprocal space map of the ac-plane with double and single circles representing nuclear and magnetic Bragg positions, respectively. *Scan A* (c2) shows the scan range across the rod shaped magnetic intensity distribution, while *scan B* (c1) measures magnetic intensity along the rod. The graphic was composed from individual plots published in [152].

point where the in-plane correlations set in.

Comparing the behavior of the prototypical K_2NiF_4 system with Cu-pyz, which if aligned in the scattering plane [010] × [001], would result in the magnetic rods being perpendicular to the scattering plane, since the uncoupled copper planes are stacked in the $\boldsymbol{a}$ direction. Therefore, even above the Néel temperature an elastic magnetic scattering signal originating from the in-plane spin-spin correlations is expected to occur at the respective Bragg positions. Which is why, the scans presented in figure 5.12 should have picked up the scattering signal of the magnetic rods. Given the fact that the total magnetic scattering intensity is proportional to the square of the sublattice magnetization, within a certain temperature interval $T \gtrsim T_N$, the intensity accumulated in the point-like Bragg spots is redistributed over the magnetic rods. Using K_2NiF_4 as an example again, the expected neutron count rate from the rods is significantly reduced by a factor of ≈ 70 in comparison to the point-like Bragg scattering [195]. Thus, the rocking scans presented in figure 5.12, which cut through the intensity rods, collect only a small amount of the total magnetic scattering intensity. Since the sample contains non-deuterated molecules, the strong incoherent background signal makes the magnetic scattering undetectable within the counting time of 14 seconds per point.

Inelastic neutron scattering of 2D long range correlations

The literature on neutron scattering investigations of 2D magnetic systems provides a solid expectation of the elastic scattering signal to be observed in Cu-pyz. Since our diffraction data did not yield this sought-after information, we instead lean on the successfully performed spin wave measurements, which provides a good indication of the underlying magnetic structure. As the dispersion emerges at the positions (010) and (001) in reciprocal space these spots ought to be magnetic Bragg points. Conversely, at the positions (020) and (002) the spin-spin correlation function vanishes as indicated by the decreasing intensity of the high momentum transfer excitations. Below $\Delta E = 0.8\,\mathrm{meV}$ the signal was indistinguishable from the background.

In conjunction with the periodicity of the spin wave dispersion, which seems to complete its arch from BZ center to the next, the magnetic unit cell needs to match the nuclear unit cell to conform with measured data. Taking this assumption and prior knowledge obtained from the bulk measurements, a basic model can be set up for the linear spin wave calculation software library *spinW*. In summary, the model includes:

- An antiferromagnetic spin structure within the bc-plane
- A spin value $S = 1/2$ for each Cu^{2+} ion
- A strong intra-plane exchange coupling of $J_{2D} = 5\,\mathrm{K} \cdot k_B \approx 0.5\,\mathrm{meV}$
- A vanishing inter-plane exchange coupling of $J_\perp \approxeq 0\,\mathrm{meV}$

At the current state, the magnetic structure is undetermined and the ground state of the model is degenerate, with the sole assumption that neighboring spins are aligned anti-parallel. The spin alignment does not influence the form of the dispersion relation, but alters the relative, measured INS intensities due to the projection of the spin-spin

correlation function on the momentum transfer vector $\boldsymbol{Q}$. Therefore, careful analysis of the intensities of the spin wave signal aids the determination of the magnetic structure of the underlying ground state.

Since the ground state is not known, it is assumed that the spins are aligned parallel to the $\boldsymbol{a}$ direction of the crystal structure. Internally, *spinW* lifts the ground state degeneracy by adding a negligible energy award for the manually selected structure. Subsequently, the dispersion relation can be solved without introducing numerical singularities. Regarding the momentum projection, with the momentum transfer confined to $(0kl)$, there is no preferential direction as $\boldsymbol{Q}$ is always perpendicular to $\boldsymbol{S}$. By design, the spin-spin correlation function has the same magnitude for the directions k and l.

The results of the numerical calculation of the spin wave dispersion based on the aforementioned model are depicted in figure 5.18. Therein, data are also shown, along with the dispersion curve as the broken white line on top of the intensity map. The intensity map is obtained by convolving the spin-spin correlation function with a Gaussian distribution of $\Delta E_{\mathrm{FWHM}} \approx 100\,\mu\mathrm{eV}$ in energy space, which estimates an average energy resolution of IN12. Regarding the spin-spin correlation function, the underlying G-type antiferromagnetic structure as well as the intra-layer coupling is depicted in the insert (b) of figure 5.18. It shows a section of two stacked planes of Cu^{2+} ions as copper colored circles, which are connected within the planes by a red colored bond that represents the AFM Heisenberg coupling constant $J_{2\mathrm{D}}$. All non-magnetic ions have been removed in the abstraction process. The absence of connecting lines between planes signifies the lack of inter-plane coupling in our model.

With $J_{2\mathrm{D}}$ being the only free parameter of this model, an optimization was performed using the spinW *fitspec* routine. The best agreement between all data points of the measured dispersion and the model was achieved for $J_{2\mathrm{D}} = (0.52 \pm 0.03)\,\mathrm{meV}$. Comparing the results of this minimum viable model on the one hand already gives a good description of the observed spin wave spectrum, especially in the l direction. On the other hand, larger deviations from the simulated dispersion are seen along k, especially in the high energy transfer region. One possible explanation is the inferior statistics in the k data due to a factor of 2 difference in the counting time between the scans, owed to the limited beam time. This can be seen from the comparison of the error bars in the plots of the raw data A.5 and A.7. In case higher counting statistics confirms systematic differences between measured and modeled dispersions, additional contributions to the Hamiltonian of the system would need to be considered. Such corrections could be an extension of the magnetic square lattice model towards a rectangular system, where in plane coupling is described by two differing exchange constants. Subsequently, the shape of the dispersion along k and l would change accordingly. Whether this extension to the model has merit and can be reconciled with bulk data, the crystal symmetry and exchange pathways of the structure has yet to be determined. The same considerations would have to be made in relation to next-nearest neighbor interactions. In the spirit of *Occam's razor* current data are sufficiently explained by the minimum viable model with solely an intra-plane isotropic Heisenberg interaction.

The *fitspec* algorithm only accounts for the position of the measured excitations in Q-E-space but not the intensities of each excitation peak. Therefore, no conclusion can be drawn regarding the magnetic structure, which needs to be analyzed separately. For

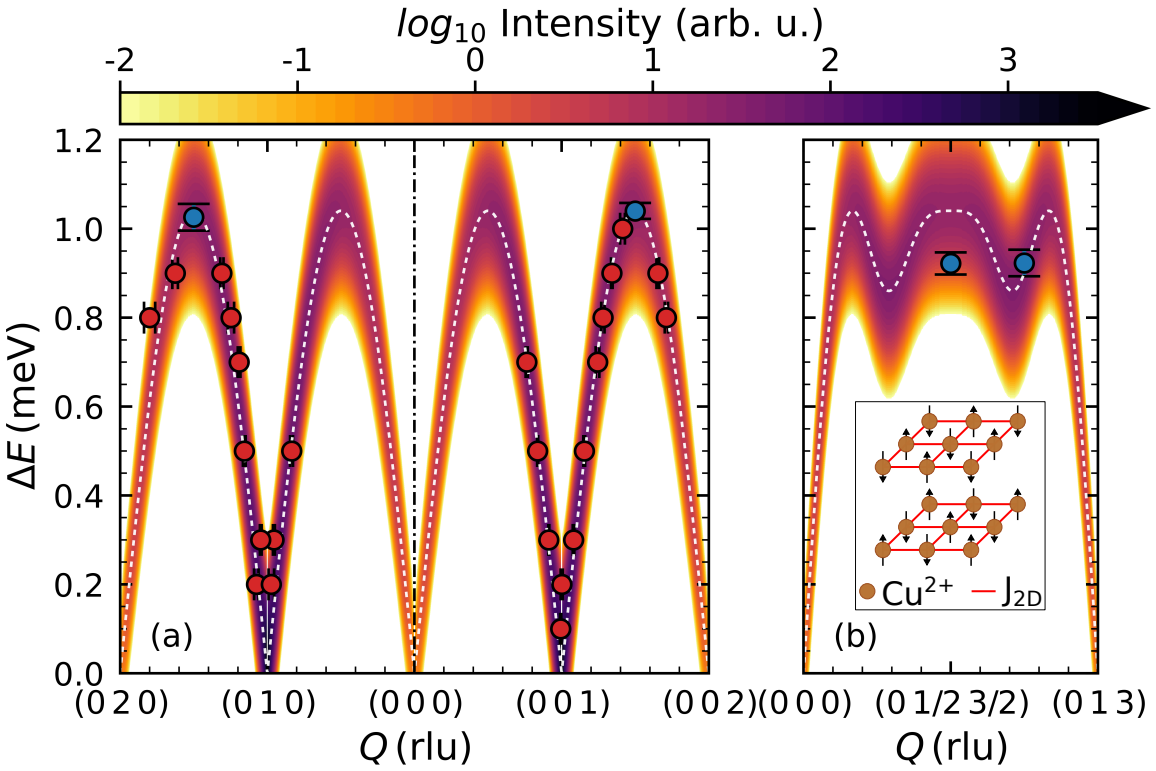

Figure 5.18.: Simulated and measured spin wave dispersion in Cu-pyz along $(0\,0\,l)$, $(0\,k\,0)$ in (a) and $(0\,\xi\,3\xi)$ in (b). The data depicted in (a) and (b) was fitted using a spin wave simulation of the dispersion of a spin-$\frac{1}{2}$ 2D QHAF yielding a strong in-plane coupling $J_{2D} = (0.52 \pm 0.03)\,\mathrm{meV}$, negligible out-of-plane exchange and a G-type antiferromagnetic structure with spins parallel to $\boldsymbol{c}$. The inset in (b) shows a graphic representation of this model. The calculated dispersion is plotted as white dashed lines achieving good agreement with the measurement. The underlying color map represents the expected neutron intensity from inelastic scattering and was computed from the spin-spin correlation function convolved with a Gaussian kernel ($\sigma = 0.1\,\mathrm{meV}$) to mimic the resolution of IN12.

a comprehensive treatment of the intensity, the instrument resolution effects need to be taken into account to correct for shifts or signal strength, which are introduced by the complex 4D resolution function of TAS. A combined model involving Monte-Carlo convolution of the TAS resolution function and the magnetic double differential cross section is under development.

Although the analysis of the spin wave dispersion can be easily performed, in the face of the fact that no magnetic LRO can be observed, this apparent discrepancy must be discussed. One of the first reports on this phenomenon is related to the archetypical 2D magnetic system K_2NiF_4 and was authored by Skalyo *et al.* [196]. On the one hand, their work unambiguously identifies the characteristic spin wave dispersion of a 2D AFM system with negligible inter-plane exchange coupling. The sought-after signal consists of clearly dispersing excitations for momentum transfer within the plane while along the direction with negligible coupling the excitation energy stays constant. On the other hand, they track the temperature dependence of the spin wave signal crossing from the

AFM LRO state below $T_N = 97.2\,K$ over the phase boundary to approximately $1.1\,T_N$, by means of a constant energy scan. Just from the data presented in their paper, a different interpretation is possible. For example, paramagnetic fluctuations with strongly momentum dependent lifetime create a similar peaked signal in the absence of dispersing spin wave excitations [145].

Still, the first explanation is supported by the findings of Birgeneau *et al.* in the related compound K_2MnF_4, which are well in line with the expected excitation spectrum of a quadratic anisotropic Heisenberg AFM, where the spin waves can be observed at $T \geq T_N$ [197]. Up to now, the persistence of magnetic excitations in 2D antiferromagnets has been observed in MOC ($Fe(NCS)_2(C_4H_4N_2)_2$) [198] and tapiolite ($FeTa_2O_6$) [199]. Therefore, interpreting the INS measurement in Cu-pyz in terms of propagating spin waves is put on firm ground.

5.4. Conclusion and outlook

In summary, the presented studies of Cu-pyz by means of magnetic bulk property measurements and triple-axis spectroscopy substantiate the notion of Cu-pyz being a two-dimensional antiferromagnet. The static susceptibility matches the expectations of a 2D QHAF system, as known from experimental and theoretical studies. Similarly, the magnetization data supports this conclusion and yields predictions for e.g. the critical field $\mu_0 H_c$, which ought to be tested in the near future. While the χ_{AC} data does not provide information beyond these prior insights, it is a valuable reference to compare to ongoing AC magnetometry studies of the properties of Cu-pyz under hydrostatic pressure. This is due to the fact that a quantitative measurement of χ_{DC} or m is hardly feasible in high pressure setups.

The data obtained by elastic neutron scattering are, as of writing, puzzling. Not only is the absence of 3D LRO down to 0.038 K observed, the signal expected from in-plane ordered spins is elusive as well. However, this could be reconciled with the hypothesis, that the diffusive magnetic scattering is overshadowed by the immense incoherent background originating from the hydrogen contained in the organic components of Cu-pyz. Nevertheless, successful mapping of the spin wave dispersion in the $[010] \times [001]$ scattering plane suggests long range correlations of the strongly coupled spins within the bc-plane. Furthermore, fitting a spin wave model to the three-axis data confirms antiferromagnetic exchange and determines the strength of the in-plane coupling $J_{2D} = (0.52 \pm 0.03)\,meV$ in agreement with the bulk measurements.

Indisputably, there are several open questions left to answer. Foremost, is it possible to achieve 3D magnetic long range order and more importantly determine the magnetic structure? Regarding easily available bulk measurement techniques, specific heat could aid in the detection of a phase transition, while a dedicated neutron diffraction experiment would be needed for structure determination. In case the phase transition to 3D LRO stays absent, diffuse magnetic neutron scattering from the internally ordered copper planes could provide insight on the magnetic structure via neutron Laue diffraction [200]. The emergence and fluctuation of the order parameter could be comprehensively studied with triple-axis or single crystal diffraction instruments [195]. The energy integrated structure factor of fluctuating magnetic short range order above T_N, as determined by

time-of-flight spectrometry, contains valuable information on the coupling and structure of the ground state [201–203].

In addition, a more comprehensive mapping of the spin wave spectrum, especially in low symmetry directions, would contribute to the determination of weak anisotropy terms or next nearest-neighbor couplings in the model Hamiltonian. A formidable example for such an investigation was published by Tsyrulin *et al.* in 2010 on the related copper pyrazine compound $Cu(C_4H_4N_2)_2(ClO_4)_2$ [192]. In this case, INS data was not only able to confirm the existence of a small XY anisotropy contribution resulting in a gaped magnon band structure at the Brillouin zone center, but also a next nearest-neighbor coupling term to be included in the spin wave dispersion calculation.

The endeavor of extensive neutron scattering investigations will be aided by the ongoing preparation of fully deuterated samples, which are expected to significantly reduce the background facilitating the study of diffuse and inelastic scattering more straightforward. However, due diligence is required to characterize a possible isotope effect and ensure the equivalency to the non-deuterated compound.

Finally, neutron scattering experimentation is going to play a critical part in the unraveling of the pressure induced variations at the atomic level. Combining high performance sample environment for hydrostatic pressure at sub-Kelvin temperatures with any neutron scattering instrumentation is as challenging as the prospect of finding quantum disordered, superconducting or dimensionality changing phases is enticing.

6. Conclusion and Outlook

Having presented our results of studying two rather different magnetic systems, a short summary and outlook of future work shall round off this thesis. As *dimensionality of magnetic systems* is the overarching theme of this work, we review its influence on the magnetic properties of the investigated systems Ni and Cu-pyz.

Starting with Ni, which is understood to be an itinerant ferromagnet, its magnetic properties in the vicinity of the Curie temperature T_C and small q can be adequately modeled using a 3D isotropic Heisenberg Hamiltonian. This is owed to the fact, that the microscopic details of the exchange interaction become less and less important close to T_C. Here, critical scaling theory describes the properties of Ni in the long wavelength regime. However, this is precisely where dipolar interactions are supposed to contribute to the critical dynamics of the system and are expected to modify the pure 3D Heisenberg behavior.

The inelastic neutron scattering measurements performed at the MIEZE spectrometer RESEDA, confirmed the validity of a 3D Heisenberg model with additional dipolar coupling due to the exceptional momentum and energy resolution of the instrument. The spin wave dispersion in nickel determined just below T_C revealed a dipolar wavevector $q_D = 7 \times 10^{-3}$ Å, which is at least a factor 2 smaller then previously reported. The spin wave stiffness $D(T|\mu)$ is strongly dependent on temperature, which fits well to the power law behavior suggested by dynamical scaling theory. In this context, the critical exponent $\mu = 0.3407$ used in the analysis was derived on the basis of field theory and the 3D Heisenberg Hamiltonian. In comparison, this value of μ leads to better agreement with the data than the mean field value $\mu = 1/3$. Since the spin wave energies can be understood with dynamic scaling theory in mind, it was mandatory to verify the agreement of the linewidth of the spin waves with DST as well. Absorbing the entire temperature dependence in the inverse correlation length κ and parameterizing the q dependence of the linewidth of the spin waves in terms of the dynamical scaling function $\gamma_{SW}(\kappa/q)$ leads to a successful reconciliation of the data with DST.

Using the same approach, the linewidths of the critical fluctuations of the order parameter have been investigated for temperatures above T_C. When extracting the linewidth of the quasi elastic scattering signal, meticulous analysis of the lineshape function, which close to the Curie temperature deviates from the commonly used Lorentzian distribution, is required. As a result, the renormalized linewidth values lie on a universal curve confirming a fundamental result of DST. Even more though, quantitative agreement with the parameter free Résibois-Piette scaling function is readily achieved. The sole underlying assumption of this prediction is that Ni can be modeled with the 3D isotropic Heisenberg Hamiltonian. The fact that dipolar interactions have seemingly no effect on the dynamical scaling behavior could be comprehended due to mode-coupling computations by Frey and Schwabl that included dipolar forces. Accordingly, deviations from the Résibois-Piette solution should arise only for wavevector

transfers of $q \leq q_D/10$, which are outside of the probed parameter space.

Hence, the dimensionality $n = d = 3$, as a fundamental input into the equations within the dynamical scaling theory framework, captures the entirety of the measured critical behavior of Ni below and above the Curie temperature and consolidates our current understanding of critical phenomena. Nevertheless, the work presented in this thesis would benefit greatly from an expansion of the current data set. Regarding the nickel sample, an extension of the measurement points in temperature would allow a more comprehensive analysis of the critical exponents μ, β, which has not been feasible so far. The possibility of reaching wavevector transfers a decade smaller than currently available is a major challenge for any active neutron spectrometer today. A promising contender might be the RESEDA instrument once the upgrade for small angle scattering studies is successfully deployed.

Changing dimensionality either of lattice or of spin degrees of freedom, has profound consequences for the behavior of magnetic systems. It effects the existence of a transition from an unordered to a long range ordered state and also the critical exponents associated with it. This is why a system that exhibits a change of its dimensionality, possibly controlled by an external parameter, promises an excellent opportunity to address this field of research. Metal-organic compounds, such as Cu-pyz, are known to deliver on this promise, but before studying the consequences of varying magnetic dimensionality, a good understanding of the system is required. The work done on Cu-pyz was dedicated to gain insight into its baseline, magnetic properties.

Magnetization, static and dynamic susceptibility measurements on single crystals of Cu-pyz substantially contributed to the characterization of Cu-pyz as a 2D quantum Heisenberg antiferromagnet. Broad peaks in the magnetic susceptibility data provided clear evidence of strong in-plane exchange coupling between the Cu^{2+} ions in a square lattice arrangement within the bc-plane. In contrast, the out-of-plane coupling is significantly weaker leading to an absence of 3D long range order down to 2 K justifying the classification of Cu-pyz as a 2D system. Magnetization data backs up this interpretation by showing remarkable agreement with the unique magnetization curve shape predicted for a 2D QHAF as calculated from second order spin wave theory.

Triple-axis spectroscopy enabled deeper insight into the magnetic interactions on the atomic scale. Even at the base temperature of the dilution fridge, $T = 0.038\,\mathrm{K}$, magnetic LRO was elusive in the elastic scattering data. However, the expected, strong in-plane correlation of the spins of the copper ions, could be readily observed in terms of propagating spin waves. Based on linear spin wave calculations, the data was best described using antiferromagnetically aligned spins within the square lattice, which are coupled by an exchange interaction $J_{2D} = (0.52 \pm 0.03)\,\mathrm{meV}$. Naturally, this result is in great agreement with the bulk magnetometry data.

Even though knowledge of the properties of Cu-pyz is far from complete, we established a baseline model upon which future experiments can be envisioned and to extend this model according to new findings. A combination of neutron scattering to uncover information on the magnetic structure and the interactions from diffuse and inelastic scattering as well as magnetometry techniques to detect phase transitions under hydrostatic pressure will be essential for future studies. With the affirmed anticipation of Cu-pyz being a excellent 2D model system, the influence and of dimensionality on

magnetic properties and its evolution is easily accessible and ought to be comprehensively investigated.

In the end, the systems, Ni and Cu-pyz, are only two examples in which dimensionality profoundly affects the magnetic properties and therefore plays an important role in characterizing them. However, not many systems are well understood in terms of their dimensionality and how it influences phenomena such as superconductivity, frustration and quantum disorder or short range order ground states. Therefore we conclude that it is of major importance to investigate the dimensionality of magnetic systems and its influence in condensed matter physics, material science and technology.

A. Supplementary data of the low-dimensional antiferromagnet Cu-pyz

A.1. Padé approximation: Tables of coefficients and fitparameters

n	a_n	b_n
1	0.998586	-1.84279
2	-1.28534	1.14141
3	0.656313	-0.704192
4	0.235862	-0.189044
5	0.277527	-0.227545

Table A.1.: Coefficients of the Padé approximation used in equation 5.2. These coefficients are not fit parameters, but are determined separately for each type of lattice. The presented values are taken from Woodward *et al.* [171].

$\mu_0 H$(T)	J(K)	$C \cdot 10^{-2}$(K)	g	$\mu_0 H_{\mathrm{sat}}$(T)	g_{fit}
0.05	5.129 ± 0.041	3.128 ± 0.023	2.447 ± 0.055	12.48 ± 0.30	6.7×10^4
0.1	4.975 ± 0.029	3.038 ± 0.016	2.411 ± 0.037	12.29 ± 0.20	4.9×10^5
0.5	4.952 ± 0.021	2.953 ± 0.011	2.377 ± 0.025	12.41 ± 0.14	1.1×10^8
1.0	4.899 ± 0.022	2.935 ± 0.012	2.370 ± 0.027	12.31 ± 0.15	2.0×10^9
5.0	4.141 ± 0.055	2.586 ± 0.031	2.225 ± 0.066	11.09 ± 0.36	9.9×10^{12}
9.0	3.502 ± 0.056	2.341 ± 0.032	2.117 ± 0.065	9.842 ± 0.340	1.6×10^{14}

Table A.2.: Results from fitting equation 5.2 to $\chi_{\mathrm{DC}}(T)$ in figure 5.2 for $\boldsymbol{H} \parallel \boldsymbol{a}$.

$\mu_0 H$(T)	J(K)	$C \cdot 10^{-2}$(K)	g	$\mu_0 H_{\mathrm{sat}}$(T)	g_{fit}
0.05	4.825 ± 0.030	2.532 ± 0.015	2.201 ± 0.031	13.05 ± 0.20	1.3×10^4
0.1	4.766 ± 0.019	2.463 ± 0.009	2.171 ± 0.018	13.07 ± 0.12	5.4×10^4
0.5	4.825 ± 0.012	2.377 ± 0.005	2.133 ± 0.011	13.47 ± 0.08	8.6×10^6
1.0	4.776 ± 0.012	2.386 ± 0.006	2.129 ± 0.012	13.36 ± 0.08	1.5×10^8
5.0	4.082 ± 0.042	2.133 ± 0.020	2.020 ± 0.038	12.03 ± 0.26	1.6×10^{12}
9.0	3.448 ± 0.040	1.921 ± 0.019	1.917 ± 0.035	10.71 ± 0.23	2.6×10^{13}

Table A.3.: Results from fitting equation 5.2 to $\chi_{\mathrm{DC}}(T)$ in figure 5.2 for $\boldsymbol{H} \parallel \boldsymbol{b}$.

$\mu_0 H$(T)	J(K)	$C \cdot 10^{-2}$(K)	g	$\mu_0 H_{\mathrm{sat}}$(T)	g_{fit}
0.05	4.663 ± 0.038	2.402 ± 0.018	2.144 ± 0.037	12.95 ± 0.25	1.5×10^4
0.1	4.593 ± 0.028	2.475 ± 0.014	2.176 ± 0.030	12.57 ± 0.19	1.9×10^5
0.5	4.537 ± 0.020	2.334 ± 0.010	2.113 ± 0.020	12.79 ± 0.14	3.9×10^7
1.0	4.560 ± 0.020	2.337 ± 0.009	2.114 ± 0.019	12.84 ± 0.13	4.7×10^8
5.0	4.012 ± 0.043	2.127 ± 0.020	2.017 ± 0.038	11.84 ± 0.26	1.6×10^{12}
9.0	3.447 ± 0.044	1.918 ± 0.021	1.916 ± 0.038	10.72 ± 0.25	2.8×10^{13}

Table A.4.: Results from fitting equation 5.2 to $\chi_{\mathrm{DC}}(T)$ in figure 5.2 for $\boldsymbol{H} \parallel \boldsymbol{c}$.

A.2. Additional magnetometry data

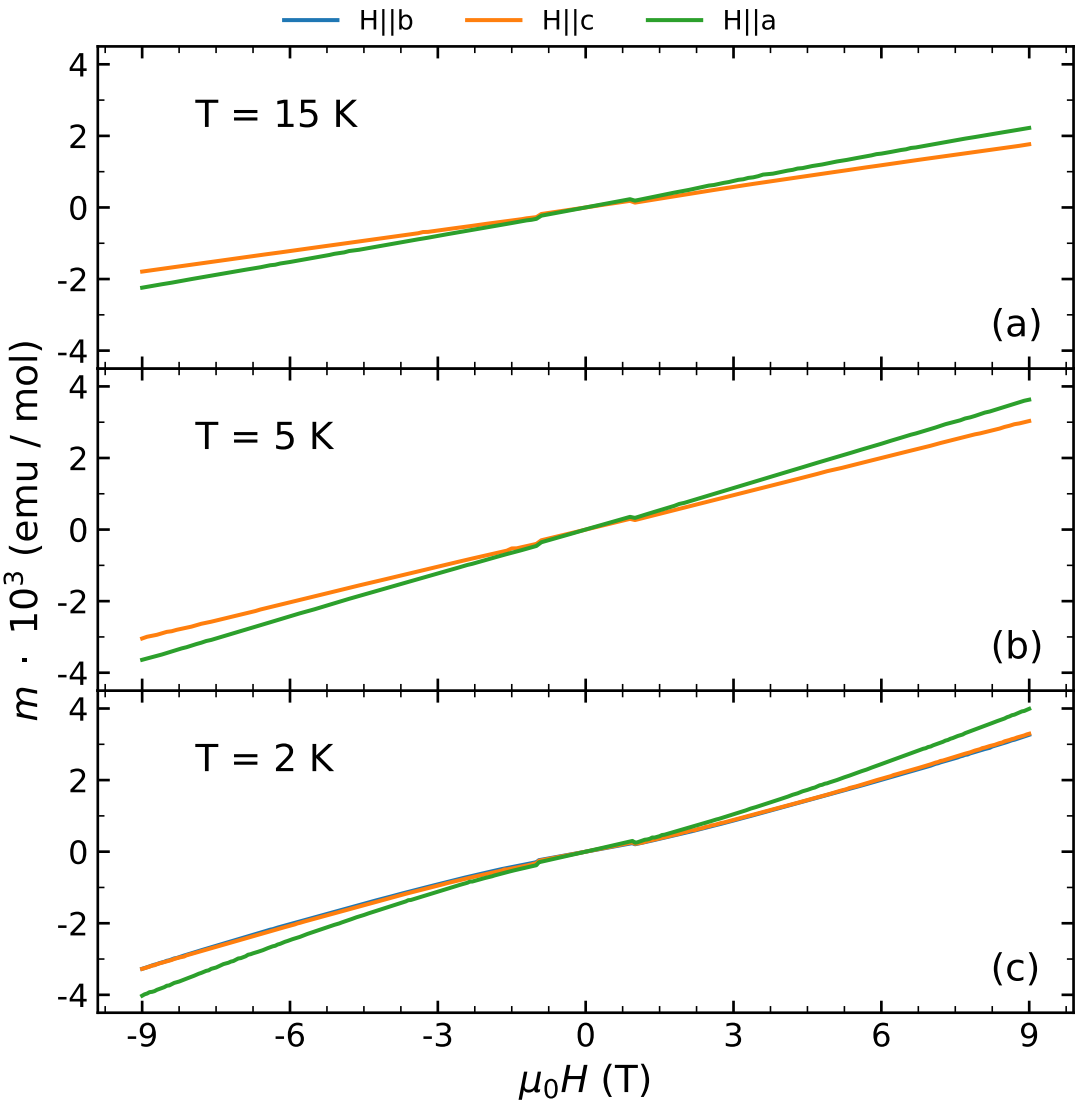

Figure A.1.: Sample magnetization for different external field alignments and sample temperatures. Each panel shows the magnetization at a constant temperature. For temperatures $\geq 5.0\,\mathrm{K}$ the relation between magnetization and external field is linear, while for $T = 2.0\,\mathrm{K}$ the curve bends with increasing field. Panels (b) and (c) do not contain data for $\boldsymbol{H} \parallel \boldsymbol{b}$.

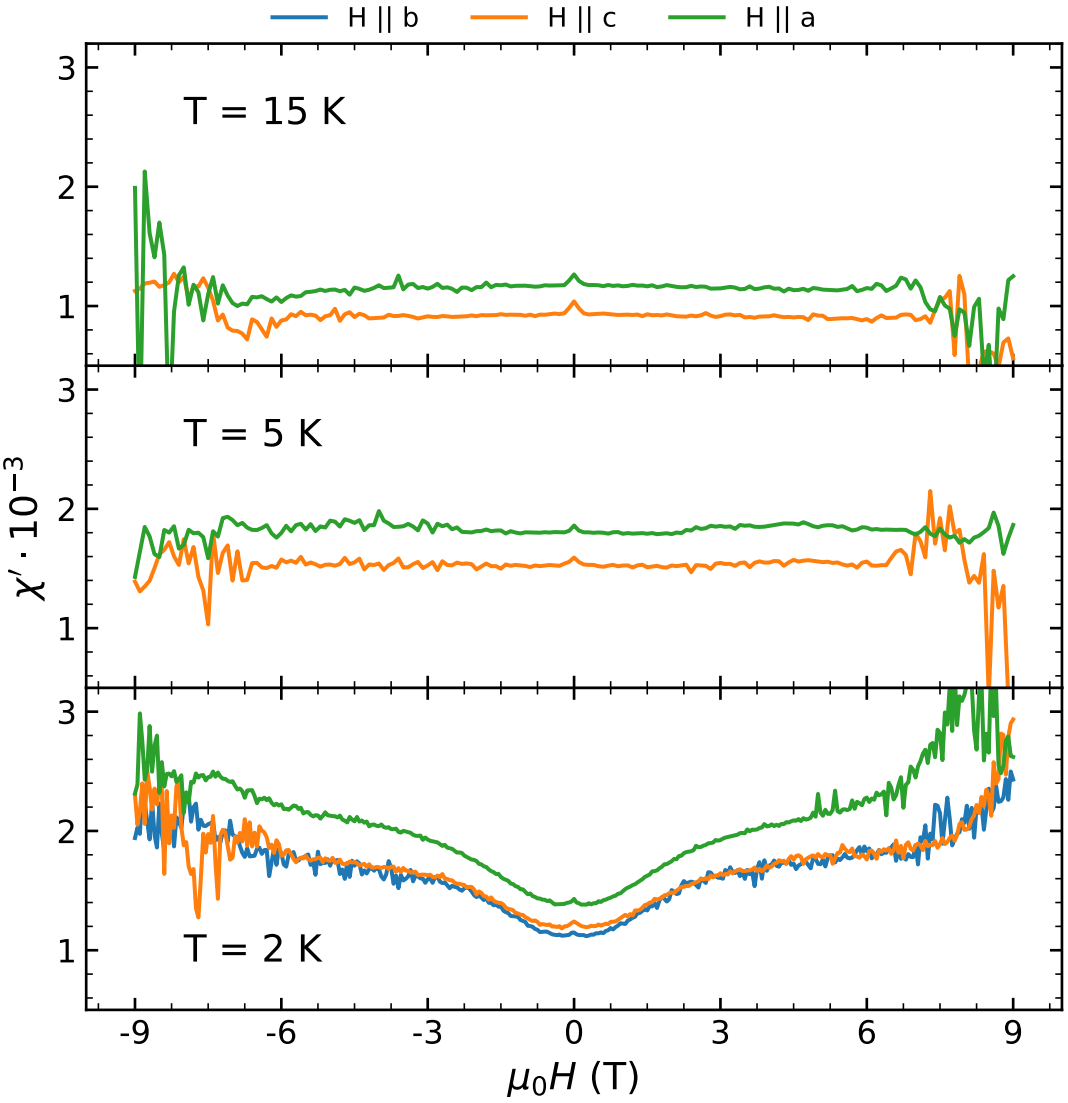

Figure A.2.: χ' for different external field alignments and sample temperatures.

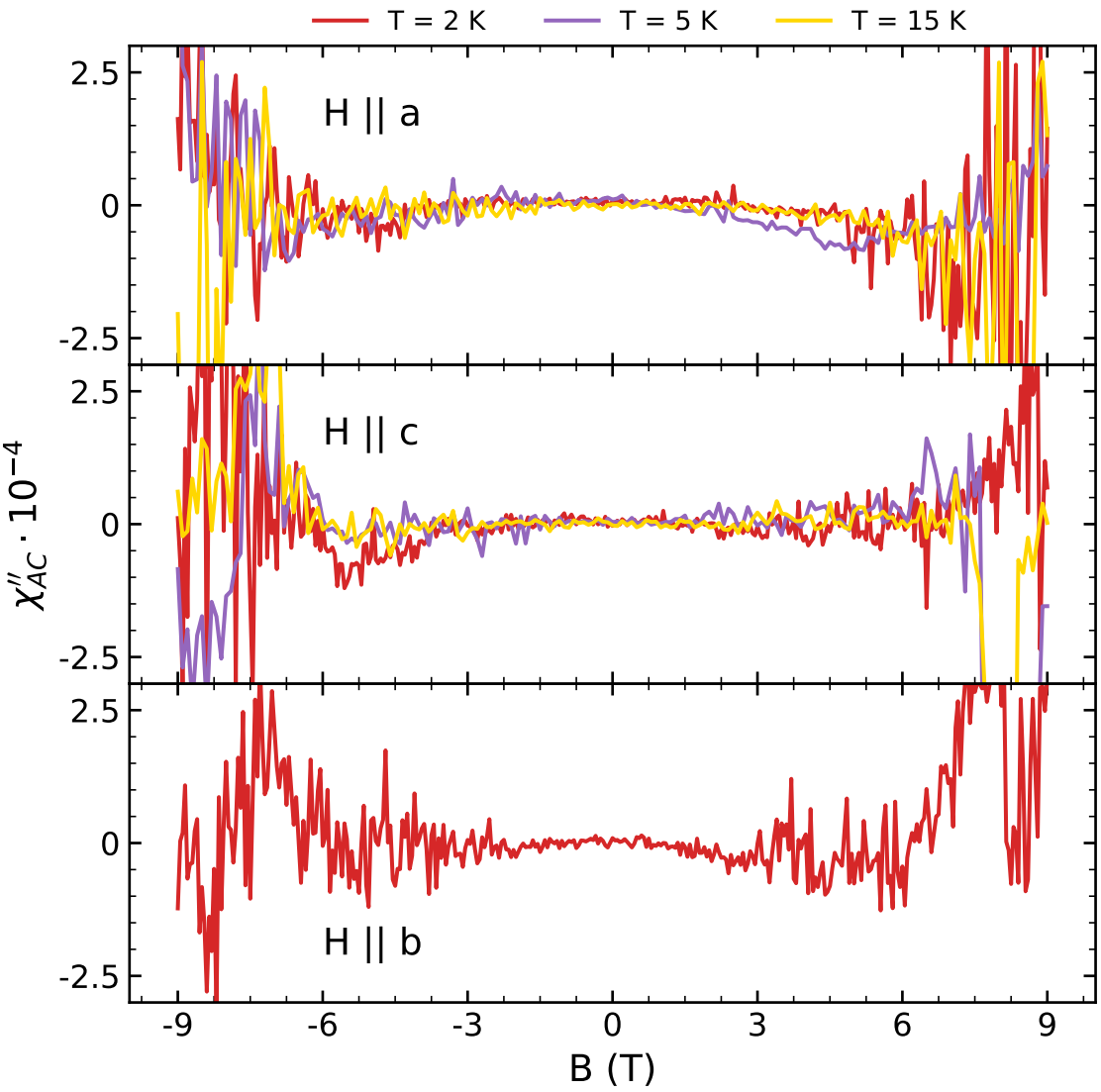

Figure A.3.: χ'' for different external field alignments and sample temperatures. Each panel shows χ'' for a particular alignment of $\boldsymbol{H}$ with respect to the lattice axis. For $|\mu_0 H| \leq 2.5\,\mathrm{T}$, χ'' is approximately constant with a value of 0 independent of T and the alignment of the external field. Above this threshold, the signal becomes increasingly noisy, with large fluctuations around 0 without any reliably detectable trend. In the $\boldsymbol{H} \parallel \boldsymbol{b}$ configuration, data is only available for $T = 2\,\mathrm{K}$.

A.3. Inelastic neutron data: Tables of fit parameters and plots

The following plots show the entirety of the inelastic neutron data recorded during the beam time at IN12. For each scan direction (k and l) two plots depict the raw data of the constant-E scans and the background subtracted data. The green, solid line represents the Gaussian peak of the fitted spin wave excitation. If the background is not subtracted, it is indicated by the black, broken line in the plot of the raw data.

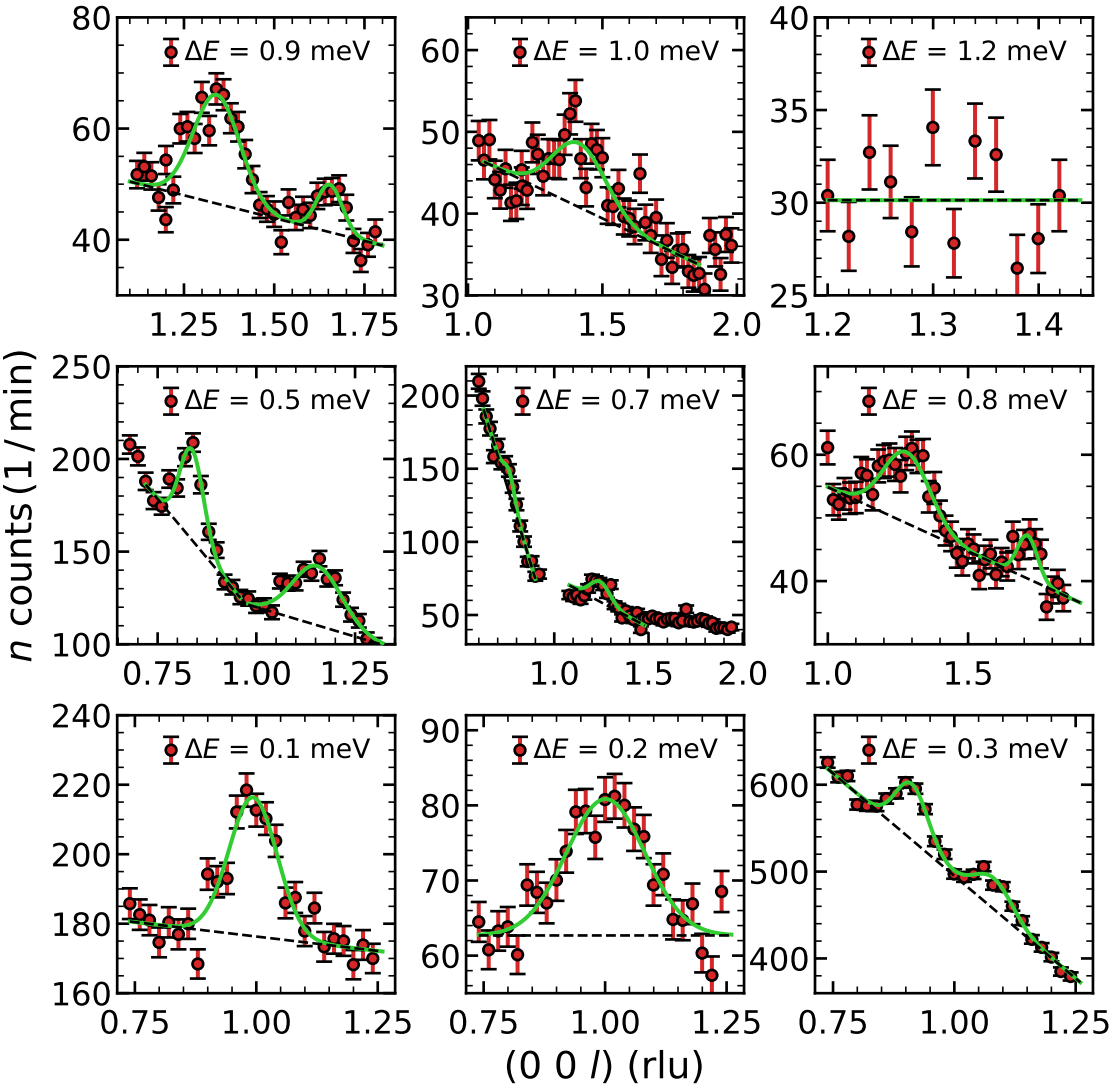

Figure A.4.: $(00l)$ TAS raw data with fit.

The fit parameters gathered by fitting equation 5.7 to the raw data are summarized in the tables A.5, A.7 for the constant-E scans and A.6 for the constant-Q scans.

Q_l (rlu)	ΔE (meV)	σ_Q (rlu)	A (min^{-1})	m ($\mathrm{min}^{-1}\mathrm{rlu}^{-1}$)	b (min^{-1})	g_{fit}
0.993 ± 0.004	0.1	0.049 ± 0.004	4.9 ± 0.5	-17 ± 6	193 ± 6	1.33
1.001 ± 0.007	0.2	0.081 ± 0.009	3.7 ± 0.5	0	62.7 ± 1.0	1.19
0.913 ± 0.003	0.3	0.034 ± 0.003	5.4 ± 0.5	-472 ± 8	957 ± 8	1.35
1.081 ± 0.005	0.3	0.039 ± 0.005	3.5 ± 0.5	-472 ± 8	957 ± 8	1.35
0.837 ± 0.003	0.5	0.030 ± 0.003	3.7 ± 0.4	-255 ± 17	370 ± 15	1.29
1.154 ± 0.006	0.5	0.062 ± 0.007	5.0 ± 0.8	-64 ± 11	184 ± 13	1.08
0.763 ± 0.002	0.7	0.029 ± 0.002	1.12 ± 0.08	-422 ± 3	454 ± 3	17.8
1.244 ± 0.013	0.7	0.053 ± 0.004	1.82 ± 0.33	-69 ± 8	144 ± 11	35.4
1.281 ± 0.011	0.8	0.083 ± 0.012	2.3 ± 0.4	-20.3 ± 2.0	75.2 ± 3.2	0.98
1.712 ± 0.011	0.8	0.036 ± 0.010	0.6 ± 0.2	-20.3 ± 2.0	75.2 ± 3.2	0.98
1.341 ± 0.005	0.9	0.065 ± 0.006	3.2 ± 0.4	-16.4 ± 2.7	68 ± 4	1.73
1.654 ± 0.009	0.9	0.035 ± 0.008	0.8 ± 0.2	-16.4 ± 2.7	68 ± 4	1.73
1.414 ± 0.016	1.0	0.099 ± 0.023	2.0 ± 0.5	-15.7 ± 1.7	63.0 ± 2.7	1.14
	1.2			0	30.1 ± 0.5	1.55

Table A.5.: Results from fitting equation 5.7 to the INS data in figure A.4 and A.5.

$\boldsymbol{Q}$ (rlu)	ΔE (meV)	σ_E (meV)	A (min^{-1})	m ($\mathrm{min}^{-1}\mathrm{meV}^{-1}$)	b (min^{-1})	g_{fit}
(010)				-42.7 ± 1.7	95.7 ± 2.1	2.82
$(0\frac{3}{2}0)$	1.050 ± 0.024	0.113 ± 0.027	2.3 ± 0.7	-37.7 ± 2.5	73.3 ± 3.4	0.40
$(00\frac{3}{2})$	1.040 ± 0.018	0.082 ± 0.015	1.7 ± 0.4	-45.8 ± 2.1	83.2 ± 2.4	1.68
$(00\frac{6}{5})$				-109 ± 3	151 ± 3	11.1
$(0\frac{1}{2}\frac{3}{2})$	0.922 ± 0.025	0.064 ± 0.022	0.83 ± 0.33	-34.7 ± 2.1	67.1 ± 2.4	1.17
$(0\frac{3}{4}\frac{9}{4})$	0.923 ± 0.030	0.124 ± 0.027	2.4 ± 0.8	-35.7 ± 3.3	67.0 ± 4.0	1.08

Table A.6.: Results from fitting equation 5.7 to the INS data in figure 5.14.

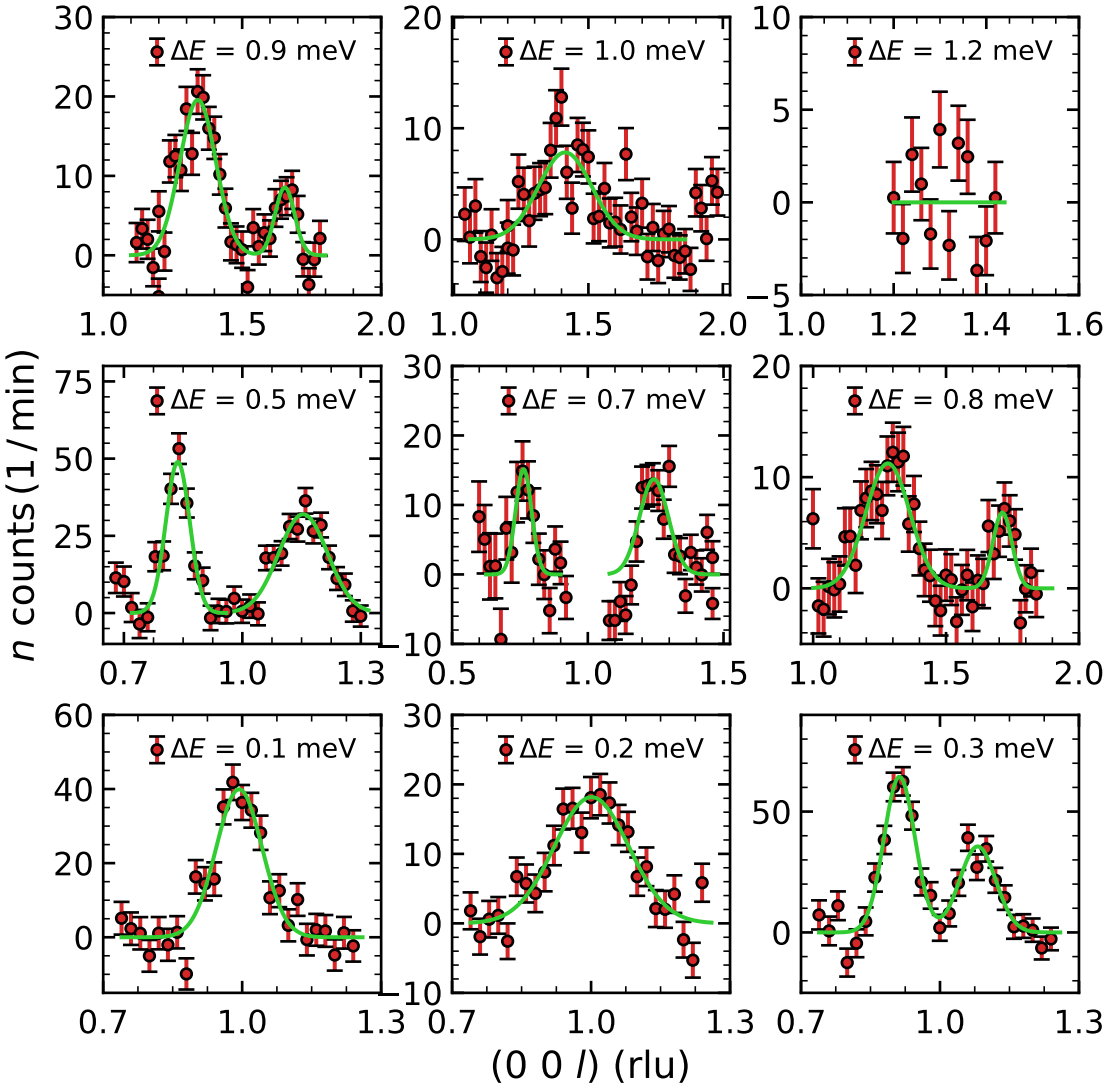

Figure A.5.: $(00l)$ TAS raw data with fit and background subtracted.

Q_k (rlu)	ΔE (meV)	σ_Q (rlu)	A (min^{-1})	m ($\mathrm{min}^{-1}\mathrm{rlu}^{-1}$)	b (min^{-1})	g_{fit}
1.074 ± 0.015	0.2	0.034 ± 0.019	1.2 ± 1.3	-13 ± 6	140 ± 6	0.82
0.973 ± 0.019	0.2	0.063 ± 0.018	5.8 ± 1.9	-13 ± 6	140 ± 6	0.82
0.955 ± 0.006	0.3	0.039 ± 0.008	3.3 ± 0.7	-523 ± 11	1102 ± 11	1.08
1.045 ± 0.006	0.3	0.035 ± 0.010	1.7 ± 0.6	-523 ± 11	1102 ± 11	1.08
0.835 ± 0.010	0.5	0.040 ± 0.012	1.5 ± 0.6	-173 ± 16	314 ± 15	1.14
1.156 ± 0.009	0.5	0.105 ± 0.010	7.2 ± 0.6	-144 ± 13	279 ± 20	2.31
1.192 ± 0.011	0.7	0.108 ± 0.019	5.2 ± 2.7	-1 ± 20	51 ± 28	0.99
1.235 ± 0.019	0.8	0.108 ± 0.019	2.7 ± 0.5	-12.9 ± 0.7	63.9 ± 1.0	0.79
1.840 ± 0.012	0.8	0.100 ± 0.021	0.57 ± 0.33	-12.9 ± 0.7	63.9 ± 1.0	0.79
1.309 ± 0.011	0.9	0.075 ± 0.016	1.8 ± 0.5	-13.0 ± 2.8	61.0 ± 4.6	0.96
1.626 ± 0.019	0.9	0.039 ± 0.018	0.33 ± 0.19	-13.0 ± 2.8	61.0 ± 4.6	0.96

Table A.7.: Results from fitting equation 5.7 to the INS data in figure A.6 and A.7.

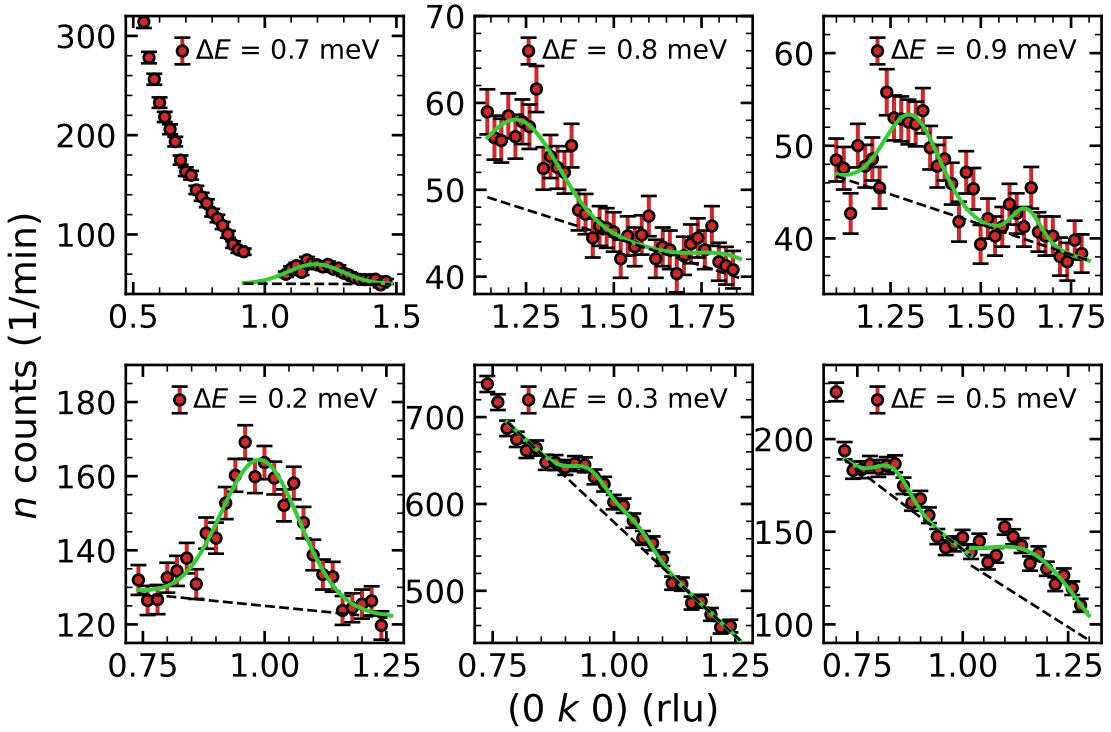

Figure A.6.: $(0k0)$ TAS raw data with fit.

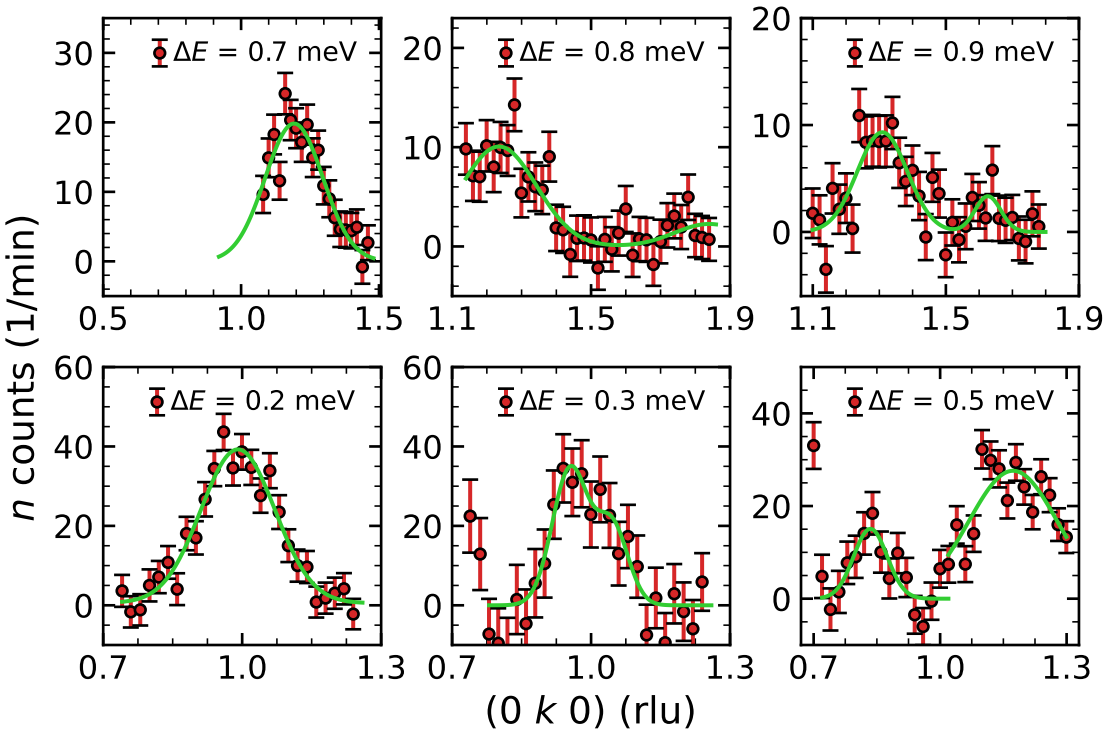

Figure A.7.: $(0k0)$ TAS raw data with fit and background subtracted.

B. Supplementary material for nickel

B.1. Renormalization group equations for isotropic ferromagnets

The dynamical shape function derived by Iro by means of renormalization group theory is

$$f_{q\xi}(x,s) = 2\Re\left\{\frac{1}{-is + \left[Z(x)\Pi_1\left(x, is\frac{Z(x)}{X(x)}\right)\right]^{-1}}\right\} \tag{B.1}$$

with Π_1 being the self-energy of the dynamic susceptibility and $Z(x)$ is an implicit function involved in the calculation of the characteristic frequency ω_c (linewidth) of the system. $X(x) = (1 + 1/x^2)^{-1}$ is the scaled magnetic susceptibility defined by $\chi(q,\xi) = q^{-2}X(q\xi)$ such that $x = q\xi$. Crucially, x is defined as the inverse compared to x in the entire section 4.1.

Iro proposed an analytical approximation to $Z(x)$, which otherwise can only be determined numerically. This yields

$$Z(x) = \left[1 - k\arctan\left(a\frac{1+1/x^2}{(1+b/x^2)^2}\right)\right]^{-1} \cdot \left(1 + \frac{b}{x^2}\right)^{\varepsilon/4} , \tag{B.2}$$

with $a = 0.46$, $b = 3.16$ and $k = 0.51$, being numerical parameters without direct physical interpretation. a is determined by a relaxation rate calculation performed by Bhattacharjee *et al.* [204]. b is chosen such that the dynamical scaling function $\gamma(x)$, which will be discussed below, asymptotically fits the behavior of the result of Résibois and Piette [116]. Subsequently, k takes the value to best approximate $Z(x)$ as defined by its implicit determination equation. The reader is revered to the original paper of Iro [205] and references therein. $\varepsilon = 6 - d = 3$ refers to the dimensionality of the renormalization group, where $d = 3$ is the dimensionality of space.

Iro also extracted the dynamical scaling function $\gamma(x)$ from his derivation of the magnetization correlation function. The scaling function is given by

$$\gamma(x) = \frac{Z(x)}{X(x)Z(\infty)} . \tag{B.3}$$

While the numerical values of the constants a, b and k have been chosen with reasonable assumptions in mind, e.g. asymptotic behavior for $x \to 0$, Iro argues that they can be used as fit parameters, when the theory is compared with experimental data.

B.2. Parametrizations for the Résibois & Piette dynamical scaling function

Glinka *et al.* used the approximation of

$$\tilde{\gamma}(x) = e^{-1.83x} + 0.43x^{1/2} \tag{B.4}$$

to parameterize the dynamical scaling function of Résibois & Piette [142].

B.3. Derivation of the correction of the momentum transfer for planar detectors

Here, we derive the equation 4.24 to determine the correct scattering angle 2θ assuming the direct beam position on the CASCADE detector of RESEDA is known. Then δ as defined in 4.2.3 can be calculated using the knowledge of pixel dimensions. Using the right-handed coordinate system introduced in figure 4.7, the $\hat{\boldsymbol{x}}$ is parallel to $\boldsymbol{k}_\mathrm{i}$, $\hat{\boldsymbol{z}}$ points into the plane of the sketch and $\hat{\boldsymbol{y}}$ is perpendicular to both.

The Hesse normal form of the detector plane, assuming the sample to be at the origin, is given by

$$\boldsymbol{r} \cdot \boldsymbol{n}_0 - l_\mathrm{SD} = 0 \longrightarrow x\cos(\alpha) + y\sin(\alpha) = l_\mathrm{SD} \ , \tag{B.5}$$

where $\boldsymbol{n}_0$ is the normal vector of the detector plane and $\boldsymbol{r}$ satisfies equation B.5 if it is a point in the plane. In the coordinate system, any normalized final wavevector of a neutron is parameterized by

$$\hat{\boldsymbol{k}_\mathrm{f}} = \cos(2\theta)\hat{\boldsymbol{x}} + \sin(2\theta)\cos(\Phi)\hat{\boldsymbol{y}} - \sin(2\theta)\sin(\Phi)\hat{\boldsymbol{z}} \ . \tag{B.6}$$

The point at which a neutron hits the detector is described by

$$\boldsymbol{h} = d \cdot \hat{\boldsymbol{k}_\mathrm{f}} = Z(2\theta, \alpha, \Phi) l_\mathrm{SD} \cdot \hat{\boldsymbol{k}_\mathrm{f}} \ , \tag{B.7}$$

where d the distance from the sample to this point is determined by inserting $d \cdot \boldsymbol{k}_\mathrm{f}$ in equation B.5. The sample-detector-distance can be factored out leaving the angle dependent part

$$Z(2\theta, \alpha, \Phi) = \left(\cos(2\theta)\cos(\alpha) + \sin(2\theta)\sin(\alpha)\cos(\Phi)\right)^{-1} \ . \tag{B.8}$$

As a consistency check, the direct beam ($2\theta = \Phi = 0$) intersects the detector plane at $\boldsymbol{h}_\mathrm{DB} = l_\mathrm{SD}/\cos(\alpha)\hat{\boldsymbol{x}}$.

The distance $|\boldsymbol{h} - \boldsymbol{h}_\mathrm{DB}| = |\boldsymbol{\delta}|$ is known from an observation of the DB position on the detector or in a less ideal case can be reconstructed if the angle α is known. For the performed experiment we have the first case. Equation 4.24 is recovered by squaring $\boldsymbol{\delta}$

leading to

$$\boldsymbol{\delta}^2 = l_{\mathrm{SD}}^2 \begin{pmatrix} Z\cos(2\theta) - \cos^{-1}(\alpha) \\ Z\sin(2\theta)\cos(\Phi) \\ -Z\sin(2\theta)\sin(\Phi) \end{pmatrix}^2 \tag{B.9}$$

$$= l_{\mathrm{SD}}^2 \left[Z^2\cos^2(2\theta) + \frac{1}{\cos^2(\alpha)} - 2Z\frac{\cos(2\theta)}{\cos(\alpha)} + Z^2\sin^2(2\theta)\left(\cos^2(\Phi) + \sin^2(\Phi)\right) \right] \tag{B.10}$$

$$= l_{\mathrm{SD}}^2 \left[Z^2 - 2Z\frac{\cos(2\theta)}{\cos(\alpha)} + \frac{1}{\cos^2(\alpha)} \right] \tag{B.11}$$

and dividing by l_{SD}^2. Potentially, this can be reduced to a more concise form, but finding numerical solutions for 2θ and choosing the result matching a positive angle appropriate for small angle scattering suffices.

B.4. Extracted parameters from MIEZE data analysis

The following tables summarize the results of the fits of the MIEZE contrast data as it was described in the paragraph addressing the extraction of physical parameters from section 4.2.3. Hence, for data measured below T_{C} the analysis yields:

- the mean wavevector transfer q_{el} as calculated under the assumption of elastic scattering and its standard deviation Δq_{el}
- the wavevector transfer q_{inel} adjusted for the energy transfer during spin wave scattering and its standard deviation Δq_{inel}
- the spin wave energy $\hbar\omega_q$ and its uncertainty $\Delta\hbar\omega_q$
- the linewidth of the spin wave excitations Γ_q and its uncertainty $\Delta\Gamma_q$

In case of data measured at $T \geq T_{\mathrm{C}}$ no propagating spin waves are observed, which is why only the parameters q_{el}, Δq_{el}, ω_{c} and $\Delta\omega_{\mathrm{c}}$ are listed in the tables. Here, the characteristic frequency ω_{c} is essentially the linewidth Γ.

q_{el} ($\mathrm{\AA}^{-1}$)	Δq_{el} ($\mathrm{\AA}^{-1}$)	q_{inel} ($\mathrm{\AA}^{-1}$)	Δq_{inel} ($\mathrm{\AA}^{-1}$)	$\hbar\omega_q$ (µeV)	$\Delta\hbar\omega_q$ (µeV)	Γ_q (µeV)	$\Delta\Gamma_q$ (µeV)
0.0066	0.0003	0.0067	0.0003	4.931	0.044	2.600	0.001
0.0076	0.0006	0.0078	0.0006	6.516	0.067	4.491	0.001
0.0098	0.0007	0.0098	0.0007	7.759	0.007	6.300	0.001
0.0117	0.0007	0.0119	0.0007	10.754	0.002	8.300	0.001
0.0131	0.0007	0.0133	0.0007	11.905	0.002	12.800	0.001
0.0157	0.0008	0.0162	0.0008	19.381	0.002	19.095	0.001
0.0186	0.0008	0.0196	0.0008	28.500	0.002	25.800	0.001
0.0222	0.0012	0.0238	0.0011	39.201	0.002	33.400	0.001
0.0265	0.0012	0.0284	0.0011	47.900	0.001	39.900	0.001

Table B.1.: Parameters extracted for $T = T_C - 2\,\mathrm{K}$ including the correct q_{inel} given the measured energy transfer.

q_{el} ($\mathrm{\AA}^{-1}$)	q_{el} ($\mathrm{\AA}^{-1}$)	q_{el} ($\mathrm{\AA}^{-1}$)	q_{inel} ($\mathrm{\AA}^{-1}$)	$\hbar\omega_q$ (µeV)	$\Delta\hbar\omega_q$ (µeV)	Γ_q (µeV)	$\Delta\Gamma_q$ (µeV)
0.0066	0.0003	0.0066	0.0003	3.510	0.192	2.000	0.001
0.0076	0.0006	0.0076	0.0006	4.503	0.001	3.062	59.923
0.0098	0.0007	0.0098	0.0007	5.579	0.002	3.810	0.001
0.0117	0.0007	0.0117	0.0007	7.390	0.003	6.000	0.001
0.0131	0.0007	0.0132	0.0007	8.871	0.002	8.400	0.001
0.0157	0.0008	0.0159	0.0008	12.300	0.001	13.400	0.001
0.0186	0.0008	0.0189	0.0008	16.600	0.002	19.500	0.001
0.0222	0.0012	0.0226	0.0012	22.699	0.002	27.800	0.001
0.0265	0.0012	0.0273	0.0012	32.603	0.003	34.500	0.001

Table B.2.: Parameters extracted for $T = T_{\mathrm{C}} - 1\,\mathrm{K}$.

q_{el} ($\mathrm{\AA}^{-1}$)	Δq_{el} ($\mathrm{\AA}^{-1}$)	ω_{c} (µeV)	$\Delta\omega_{\mathrm{c}}$ (µeV)
0.0066	0.0003	3.650	0.212
0.0076	0.0006	4.662	0.037
0.0098	0.0007	6.540	0.049
0.0117	0.0007	9.569	0.094
0.0131	0.0007	12.509	0.015
0.0157	0.0008	18.326	0.002
0.0186	0.0008	26.156	0.006
0.0222	0.0012	37.461	0.001
0.0265	0.0012	50.000	0.001

Table B.3.: Parameters extracted for $T = T_{\mathrm{C}}$.

q_{el} ($\mathrm{\AA}^{-1}$)	Δq_{el} ($\mathrm{\AA}^{-1}$)	ω_{c} (μeV)	$\Delta\omega_{\mathrm{c}}$ (μeV)
0.0066	0.0003	2.276	0.015
0.0076	0.0006	2.792	0.110
0.0098	0.0007	—	—
0.0117	0.0007	5.645	0.066
0.0131	0.0007	7.057	0.132
0.0157	0.0008	10.723	0.021
0.0186	0.0008	16.530	0.004
0.0222	0.0012	23.219	0.001
0.0265	0.0012	35.211	0.002

Table B.4.: Parameters extracted for $T = T_{\mathrm{C}} + 1\,\mathrm{K}$.

q_{el} ($\mathrm{\AA}^{-1}$)	Δq_{el} ($\mathrm{\AA}^{-1}$)	ω_{c} (μeV)	$\Delta\omega_{\mathrm{c}}$ (μeV)
0.0066	0.0003	2.002	0.018
0.0076	0.0006	2.400	0.007
0.0098	0.0007	3.433	0.003
0.0117	0.0007	4.815	0.031
0.0131	0.0007	6.336	0.003
0.0157	0.0008	9.292	0.003
0.0186	0.0008	13.116	0.004
0.0222	0.0012	19.511	0.002
0.0265	0.0012	34.213	0.001

Table B.5.: Parameters extracted for $T = T_{\mathrm{C}} + 2\,\mathrm{K}$.

q_{el} ($\mathrm{\AA}^{-1}$)	Δq_{el} ($\mathrm{\AA}^{-1}$)	ω_{c} (μeV)	$\Delta\omega_{\mathrm{c}}$ (μeV)
0.0066	0.0003	2.423	0.047
0.0076	0.0006	3.430	0.018
0.0098	0.0007	—	—
0.0117	0.0007	—	—
0.0131	0.0007	—	—
0.0157	0.0008	9.529	0.003
0.0186	0.0008	12.620	0.007
0.0222	0.0012	17.692	0.001
0.0265	0.0012	24.920	0.001

Table B.6.: Parameters extracted for $T = T_{\mathrm{C}} + 4\,\mathrm{K}$.

q_{el} ($\mathrm{Å}^{-1}$)	Δq_{el} ($\mathrm{Å}^{-1}$)	ω_{c} (µeV)	$\Delta\omega_{\mathrm{c}}$ (µeV)
0.0066	0.0003	—	—
0.0076	0.0006	—	—
0.0098	0.0007	10.163	0.002
0.0117	0.0007	10.997	0.002
0.0131	0.0007	15.609	0.003
0.0157	0.0008	17.352	0.002
0.0186	0.0008	17.383	0.001
0.0222	0.0012	23.094	0.001
0.0265	0.0012	27.552	0.001

Table B.7.: Parameters extracted for $T = T_{\mathrm{C}} + 8\,\mathrm{K}$.

B.5. Determination of the dipolar wavevector from magnetization curve

In model M4 of the spin wave analysis, the dipolar wavevector q_{D} is determined by extracting the magnetization $M(\Delta T)$ from experimental data. To evaluate the magnetization curve at arbitrary temperature values, the data points were interpolated using a power series optimized via linear regression. The full magnetization data set taken from a publication of Neugebauer [134] and *Magnetisierungskurve der Ferromagnetika* edited by Träuble [206]. The full data is shown in figure B.1. The inset of the same plot shows the result of the fit of the power series to the data close to T_{C} and also indicates the abscissa position and magnetization value for $\Delta T \in [-2\,\mathrm{K}, -1\,\mathrm{K}]$. These points yield $M(\Delta T = -1\,\mathrm{K}) = 14.75 \times 10^3\,\mathrm{A\,m^{-1}}$ and $M(\Delta T = -2\,\mathrm{K}) = 29.80 \times 10^3\,\mathrm{A\,m^{-1}}$

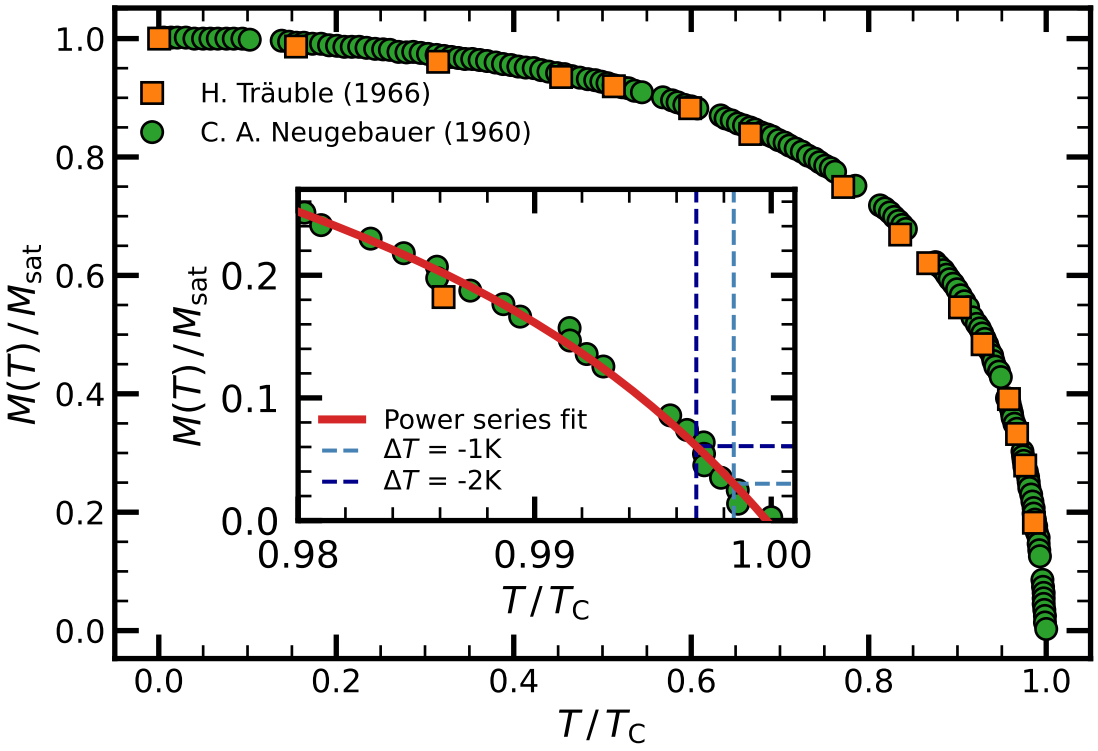

Figure B.1.: Experimentally determined magnetization curves of Ni taken from Neugebauer [134] and Träuble [206]. The plot shows the magnetization curves from $0\,\mathrm{K}$ to the Curie temperature $T_\mathrm{C} = (631.39 \pm 0.04)\,\mathrm{K}$, with the abscissa and ordinate being normalized to the Curie temperature T_C and the saturation magnetization M_sat, respectively. The inset shows a magnified section close to T_C, with the red solid line being the result of the fit of the power series expansion to the data. The vertical, broken lines indicate the position of $-1\,\mathrm{K}$ and $-2\,\mathrm{K}$ from T_C at which $M(T)$ is determined to calculate q_D.

Bibliography

[1] J. Van Vleck. *The theory of electric and magnetic susceptibility*. Oxford University Press, 1932.

[2] P. Mohn. *Magnetism in the solid state: an introduction*. Number 134 in Springer series in solid-state sciences. Springer, corrected 2nd printing edition, 2006. ISBN 978-3-540-29384-2.

[3] L. J. de Jongh. Experiments on simple magnetic model systems. *Advances in Physics*, 50(8):947–1170, 2001. doi: 10.1080/00018730110101412. URL https://www.tandfonline.com/doi/abs/10.1080/00018730110101412.

[4] N. D. Mermin and H. Wagner. Absence of ferromagnetism or antiferromagnetism in one- or two-dimensional isotropic Heisenberg models. *Physical Review Letters*, 17(22):1133–1136, 1966. ISSN 0031-9007. doi: 10.1103/PhysRevLett.17.1133. URL https://link.aps.org/doi/10.1103/PhysRevLett.17.1133.

[5] J. C. Bonner and M. E. Fisher. Linear magnetic chains with anisotropic coupling. *Physical Review*, 135(3):A640–A658, 1964. ISSN 0031-899X. doi: 10.1103/PhysRev.135.A640. URL https://link.aps.org/doi/10.1103/PhysRev.135.A640.

[6] G. A. Baker and H. E. Gilbert. On the two-dimensional spin-½ Heisenberg ferromagnetic models. *PHYSICS LETTERS*, 25(3):3, 1967. doi: 10.1016/0375-9601(67)90860-2. URL https://www.sciencedirect.com/science/article/abs/pii/0375960167908602?via%3Dihub.

[7] D. T. Teaney, M. J. Freiser, and R. W. H. Stevenson. Discovery of a simple cubic antiferromagnet: Antiferromagnetic resonance in $RbMnF_3$. *Physical Review Letters*, 9(5):212–214, 1962. ISSN 0031-9007. doi: 10.1103/PhysRevLett.9.212. URL https://link.aps.org/doi/10.1103/PhysRevLett.9.212.

[8] R. Coldea, R. A. Cowley, T. G. Perring, D. F. McMorrow, and B. Roessli. Critical behavior of the three-dimensional Heisenberg antiferromagnet $RbMnF_3$. *Physical Review B*, 57(9):5281–5290, 1998. ISSN 0163-1829, 1095-3795. doi: 10.1103/PhysRevB.57.5281. URL https://link.aps.org/doi/10.1103/PhysRevB.57.5281.

[9] D. P. Landau, S. Tsai, and A. Bunker. Magnetic excitations and critical dynamics in $RbMnF_3$ simulation versus theory and experiment. *Journal of Magnetism and Magnetic Materials*, page 3, 2001. doi: 10.1016/S0304-8853(00)00919-7. URL https://www.sciencedirect.com/science/article/abs/pii/S0304885300009197?via%3Dihub.

[10] J. C. López Ortiz, G. A. Fonseca Guerra, F. L. A. Machado, and S. M. Rezende. Magnetic anisotropy of antiferromagnetic $RbMnF_3$. *Physical Review B*, 90(5): 054402, 2014. ISSN 1098-0121, 1550-235X. doi: 10.1103/PhysRevB.90.054402. URL https://link.aps.org/doi/10.1103/PhysRevB.90.054402.

[11] J. L. Manson, M. M. Conner, J. A. Schlueter, A. C. McConnell, H. I. Southerland, I. Malfant, T. Lancaster, S. J. Blundell, M. L. Brooks, F. L. Pratt, J. Singleton, R. D. McDonald, C. Lee, and M. Whangbo. Experimental and theoretical characterization of the magnetic properties of CuF 2 (h 2 o) 2 (pyz) (pyz = pyrazine): A two-dimensional quantum magnet arising from supersuperexchange interactions through hydrogen bonded paths. *Chemistry of Materials*, 20(24): 7408–7416, 2008. ISSN 0897-4756, 1520-5002. doi: 10.1021/cm8016566. URL https://pubs.acs.org/doi/10.1021/cm8016566.

[12] P. A. Goddard, J. Singleton, C. Maitland, S. J. Blundell, T. Lancaster, P. J. Baker, R. D. McDonald, S. Cox, P. Sengupta, J. L. Manson, K. A. Funk, and J. A. Schlueter. Isotope effect in quasi-two-dimensional metal-organic antiferromagnets. *Physical Review B*, 78(5):052408, 2008. ISSN 1098-0121, 1550-235X. doi: 10.1103/PhysRevB.78.052408. URL https://link.aps.org/doi/10.1103/PhysRevB.78.052408.

[13] T. Watanabe and T. Haseda. Anomalous magnetic behavior in a single crystal of $Cu(NH_3)_4SO_4 \cdot H_2O$ at liquid helium temperatures. *The Journal of Chemical Physics*, 29(6):1429–1430, 1958. ISSN 0021-9606, 1089-7690. doi: 10.1063/1.1744748. URL http://aip.scitation.org/doi/10.1063/1.1744748.

[14] T. Haseda and A.R. Miedema. Specific heat of $Cu(NH_3)_4SO_4 \cdot H_2O$ below 1 K. *Physica*, 27(12):1102–1112, 1961. ISSN 00318914. doi: 10.1016/0031-8914(61)90051-9. URL https://linkinghub.elsevier.com/retrieve/pii/0031891461900519.

[15] D. Alan Tennant, Stephen E. Nagler, Detmar Welz, Gen Shirane, and Kazuyoshi Yamada. Effects of coupling between chains on the magnetic excitation spectrum of $KCuF_3$. *Physical Review B*, 52(18):13381–13389, 1995. ISSN 0163-1829, 1095-3795. doi: 10.1103/PhysRevB.52.13381. URL https://link.aps.org/doi/10.1103/PhysRevB.52.13381.

[16] D. Alan Tennant, Roger A. Cowley, Stephen E. Nagler, and Alexei M. Tsvelik. Measurement of the spin-excitation continuum in one-dimensional $KCuF_3$ using neutron scattering. *Physical Review B*, 52(18):13368–13380, 1995. ISSN 0163-1829, 1095-3795. doi: 10.1103/PhysRevB.52.13368. URL https://link.aps.org/doi/10.1103/PhysRevB.52.13368.

[17] A. R. Wildes, H. M. Rønnow, B. Roessli, M. J. Harris, and K. W. Godfrey. Static and dynamic critical properties of the quasi-two-dimensional antiferromagnet $MnPS_3$. *Physical Review B*, 74(9):094422, 2006. ISSN 1098-0121, 1550-235X. doi: 10.1103/PhysRevB.74.094422. URL https://link.aps.org/doi/10.1103/PhysRevB.74.094422.

[18] P. W. Anderson. The resonating valence bond state in La_2CuO_4 and superconductivity. *Science*, 235(4793):1196–1198, 1987. ISSN 0036-8075, 1095-9203. doi: 10.1126/science.235.4793.1196. URL https://www.sciencemag.org/lookup/doi/10.1126/science.235.4793.1196.

[19] Masari Watanabe, Nobuyuki Kurita, Hidekazu Tanaka, Wataru Ueno, Kazuki Matsui, and Takayuki Goto. Valence-bond-glass state with a singlet gap in the spin-1/2 square-lattice random J_1 - J_2 Heisenberg antiferromagnet $Sr_2CuTe_{1-x}W_xO_6$. *Physical Review B*, 98(5):054422, 2018. ISSN 2469-9950, 2469-9969. doi: 10.1103/PhysRevB.98.054422. URL https://link.aps.org/doi/10.1103/PhysRevB.98.054422.

[20] M. Skoulatos, F. Rucker, G. J. Nilsen, A. Bertin, E. Pomjakushina, J. Ollivier, A. Schneidewind, R. Georgii, O. Zaharko, L. Keller, Ch. Rüegg, C. Pfleiderer, B. Schmidt, N. Shannon, A. Kriele, A. Senyshyn, and A. Smerald. Putative spin-nematic phase in $BaCdVO(PO_4)_2$. *Physical Review B*, 100(1):014405, 2019. ISSN 2469-9950, 2469-9969. doi: 10.1103/PhysRevB.100.014405. URL https://link.aps.org/doi/10.1103/PhysRevB.100.014405.

[21] G. R. Stewart. Superconductivity in iron compounds. *Reviews of Modern Physics*, 83(4):1589–1652, 2011. ISSN 0034-6861, 1539-0756. doi: 10.1103/RevModPhys.83.1589. URL https://link.aps.org/doi/10.1103/RevModPhys.83.1589.

[22] John M. Tranquada, Guangyong Xu, and Igor A. Zaliznyak. Superconductivity, antiferromagnetism, and neutron scattering. *Journal of Magnetism and Magnetic Materials*, 350:148–160, 2014. ISSN 03048853. doi: 10.1016/j.jmmm.2013.09.029. URL https://linkinghub.elsevier.com/retrieve/pii/S0304885313006884.

[23] Pengcheng Dai. Antiferromagnetic order and spin dynamics in iron-based superconductors. *Reviews of Modern Physics*, 87(3):855–896, 2015. ISSN 0034-6861, 1539-0756. doi: 10.1103/RevModPhys.87.855. URL https://link.aps.org/doi/10.1103/RevModPhys.87.855.

[24] J. Herbrych, J. Heverhagen, N. D. Patel, G. Alvarez, M. Daghofer, A. Moreo, and E. Dagotto. Novel magnetic block states in low-dimensional iron-based superconductors. *Physical Review Letters*, 123(2):027203, 2019. ISSN 0031-9007, 1079-7114. doi: 10.1103/PhysRevLett.123.027203. URL https://link.aps.org/doi/10.1103/PhysRevLett.123.027203.

[25] T. Takenaka, K. Ishihara, M. Roppongi, Y. Miao, Y. Mizukami, T. Makita, J. Tsurumi, S. Watanabe, J. Takeya, M. Yamashita, K. Torizuka, Y. Uwatoko, T. Sasaki, X. Huang, W. Xu, D. Zhu, N. Su, J.-G. Cheng, T. Shibauchi, and K. Hashimoto. Strongly correlated superconductivity in a copper-based metal-organic framework with a perfect kagome lattice. *Science Advances*, 7(12):eabf3996, 2021. ISSN 2375-2548. doi: 10.1126/sciadv.abf3996. URL https://www.science.org/doi/10.1126/sciadv.abf3996.

[26] Nitin Samarth. Magnetism in flatland. *Nature*, 546(7657):216–217, 2017. ISSN 0028-0836, 1476-4687. doi: 10.1038/546216a. URL http://www.nature.com/articles/546216a.

[27] David L. Cortie, Grace L. Causer, Kirrily C. Rule, Helmut Fritzsche, Wolfgang Kreuzpaintner, and Frank Klose. Two-dimensional magnets: Forgotten history and recent progress towards spintronic applications. *Advanced Functional Materials*, 30(18):1901414, 2020. ISSN 1616-301X, 1616-3028. doi: 10.1002/adfm.201901414. URL https://onlinelibrary.wiley.com/doi/10.1002/adfm.201901414.

[28] P A Goddard, J Singleton, P Sengupta, R D McDonald, T Lancaster, S J Blundell, F L Pratt, S Cox, N Harrison, J L Manson, H I Southerland, and J A Schlueter. Experimentally determining the exchange parameters of quasi-two-dimensional Heisenberg magnets. *New Journal of Physics*, 10(8):083025, 2008. ISSN 1367-2630. doi: 10.1088/1367-2630/10/8/083025. URL https://iopscience.iop.org/article/10.1088/1367-2630/10/8/083025.

[29] R.D. Lowde and C.G. Windsor. On the magnetic excitations in nickel. *Advances in Physics*, 19(82):813–909, 1970. ISSN 0001-8732, 1460-6976. doi: 10.1080/00018737000101201. URL http://www.tandfonline.com/doi/abs/10.1080/00018737000101201.

[30] J. Chadwick. Possible existence of a neutron. *Nature*, 129(3252):312–312, 1932. ISSN 0028-0836, 1476-4687. doi: 10.1038/129312a0. URL http://www.nature.com/articles/129312a0.

[31] J. Chadwick. The existence of a neutron. *Proceedings of the Royal Society of London. Series A, Containing Papers of a Mathematical and Physical Character*, 136(830):692–708, 1932. ISSN 0950-1207, 2053-9150. doi: 10.1098/rspa.1932.0112. URL https://royalsocietypublishing.org/doi/10.1098/rspa.1932.0112.

[32] Stephen W. Lovesey. *Theory of neutron scattering from condensed matter. 2: Polarization effects and magnetic scattering.* Number 72 in International series of monographs on physics. Clarendon Pr, repr edition, 2003. ISBN 978-0-19-852029-0.

[33] G. L. Squires. *Introduction to the Theory of Thermal Neutron Scattering.* Cambridge University Press, 3 edition, 2012. ISBN 978-1-139-10780-8. doi: 10.1017/CBO9781139107808. URL http://ebooks.cambridge.org/ref/id/CBO9781139107808.

[34] D. S. Sivia. *Elementary scattering theory: for X-ray and neutron users.* Oxford University Press, 2011. ISBN 978-0-19-922867-6 978-0-19-922868-3. OCLC: ocn694227131.

[35] G. Shirane, S. M. Shapiro, and John M. Tranquada. *Neutron scattering with a triple-axis spectrometer: basic techniques.* Cambridge University Press, 2002. ISBN 978-0-521-41126-4.

[36] Lukas Beddrich. Magnetic excitations in the skyrmion phase of MnSi, 2018.

[37] Léon Van Hove. Correlations in space and time and born approximation scattering in systems of interacting particles. *Physical Review*, 95(1):249–262, 1954. ISSN 0031-899X. doi: 10.1103/PhysRev.95.249. URL https://link.aps.org/doi/10.1103/PhysRev.95.249.

[38] W Marshall and R D Lowde. Magnetic correlations and neutron scattering. *Reports on Progress in Physics*, 31(2):705–775, 1968. ISSN 00344885. doi: 10.1088/0034-4885/31/2/305. URL https://iopscience.iop.org/article/10.1088/0034-4885/31/2/305.

[39] S. Toth and B. Lake. Linear spin wave theory for single-q incommensurate magnetic structures. *Journal of Physics: Condensed Matter*, 27(16):166002, 2015. ISSN 0953-8984, 1361-648X. doi: 10.1088/0953-8984/27/16/166002. URL https://iopscience.iop.org/article/10.1088/0953-8984/27/16/166002.

[40] Franz Schwabl. *Quantenmechanik (QM I)*. Springer-Lehrbuch. Springer Berlin Heidelberg, 2007. ISBN 978-3-540-73674-5. doi: 10.1007/978-3-540-73675-2. URL http://link.springer.com/10.1007/978-3-540-73675-2.

[41] Nikolas Arend. New aspects of the MIEZE technique, 2007. URL https://mediatum.ub.tum.de/doc/618189/document.pdf.

[42] R. Golub, R. Gähler, and T. Keller. A plane wave approach to particle beam magnetic resonance. *American Journal of Physics*, 62(9):779–788, 1994. ISSN 0002-9505, 1943-2909. doi: 10.1119/1.17459. URL http://aapt.scitation.org/doi/10.1119/1.17459.

[43] B. N. Brockhouse. Scattering of neutrons by spin waves in magnetite. *Physical Review*, 106(5):859–864, 1957. ISSN 0031-899X. doi: 10.1103/PhysRev.106.859. URL https://link.aps.org/doi/10.1103/PhysRev.106.859.

[44] Bertram N. Brockhouse. Lattice waves, spin waves, and neutron scattering, 1961. URL http://www.osti.gov/servlets/purl/4693264/.

[45] Forschungs-Neutronen-Quelle Heinz Maier-Leibnitz. Sekundäre Quellen für Neutronen und Positronen, Accessed: 18.01.2022. URL https://www.frm2.tum.de/frm2/sekundaere-quellen/.

[46] Heinz Maier-Leibnitz Zentrum (MLZ). Experimental facilities - Heinz Maier-Leibnitz Zentrum (MLZ), Accessed: 18.01.2022. URL https://www.frm2.tum.de/fileadmin/w00bnv/www/content_uploads/experimental-facilities_online.pdf.

[47] J. B. Forsyth and A. Freund. Materials problems in neutron devices, 1979. URL https://www.sciencedirect.com/science/article/pii/B9780123418159500185.

[48] D. C. Tennant. Performance of a cooled sapphire and beryllium assembly for filtering of thermal neutrons. *Review of Scientific Instruments*, 59(2):380–381, 1988. ISSN 0034-6748, 1089-7623. doi: 10.1063/1.1140212. URL http://aip.scitation.org/doi/10.1063/1.1140212.

[49] LND Inc. neutron beam monitors, Accessed: 14.02.2022. URL https://www.lndinc.com/product-category/neutron-detectors/fission-chambers/neutron-beam-monitors/.

[50] C. Wagemans and A. J. Deruytter. Sub-thermal fission cross-section measurements. *Radiation Effects*, 93(1):163–167, 1986. ISSN 0033-7579. doi: 10.1080/00337578608207444. URL https://www.tandfonline.com/doi/full/10.1080/00337578608207444.

[51] Internationale Atomenergie-Organisation. Handbook on nuclear activation data, 1987.

[52] NIST Center for Neutron Research. Neutron scattering lengths and cross sections, Accessed: 14.02.2022. URL https://www.ncnr.nist.gov/resources/n-lengths/.

[53] NNDC Brookhaven National Laboratory. Evaluated nuclear data file, Accessed: 14.02.2022. URL https://www.nndc.bnl.gov/endf/.

[54] Walter Soller. A new precision X-ray spectrometer. *Physical Review*, 24(2):158–167, 1924. ISSN 0031-899X. doi: 10.1103/PhysRev.24.158. URL https://link.aps.org/doi/10.1103/PhysRev.24.158.

[55] G. Caglioti, A. Paoletti, and F.P. Ricci. Choice of collimators for a crystal spectrometer for neutron diffraction. *Nuclear Instruments*, 3(4):223–228, 1958. ISSN 0369643X. doi: 10.1016/0369-643X(58)90029-X. URL https://linkinghub.elsevier.com/retrieve/pii/0369643X5890029X.

[56] Swiss Neutronics AG. collimators, Accessed: 14.02.2022. URL https://www.swissneutronics.ch/products/equipment-for-instruments/collimators/.

[57] M. J. Cooper and R. Nathans. The resolution function in neutron diffractometry. I. the resolution function of a neutron diffractometer and its application to phonon measurements. *Acta Crystallographica*, 23(3):357–367, 1967. ISSN 0365110X. doi: 10.1107/S0365110X67002816. URL http://scripts.iucr.org/cgi-bin/paper?S0365110X67002816.

[58] G. Eckold and O. Sobolev. Analytical approach to the 4d-resolution function of three axes neutron spectrometers with focussing monochromators and analysers. *Nuclear Instruments and Methods in Physics Research Section A: Accelerators, Spectrometers, Detectors and Associated Equipment*, 752:54–64, 2014. ISSN 01689002. doi: 10.1016/j.nima.2014.03.019. URL https://linkinghub.elsevier.com/retrieve/pii/S0168900214002940.

[59] T. Weber, D. M. Fobes, J. Waizner, P. Steffens, G. S. Tucker, M. Böhm, L. Beddrich, C. Franz, H. Gabold, R. Bewley, D. Voneshen, M. Skoulatos, R. Georgii, G. Ehlers, A. Bauer, C. Pfleiderer, P. Böni, M. Janoschek, and M. Garst. Topological magnon band structure of emergent landau levels in a skyrmion lattice. *Science*, 375(6584): 1025–1030, 2022. ISSN 0036-8075, 1095-9203. doi: 10.1126/science.abe4441. URL https://www.science.org/doi/10.1126/science.abe4441.

[60] T. Weber, J. Waizner, G. S. Tucker, R. Georgii, M. Kugler, A. Bauer, C. Pfleiderer, M. Garst, and P. Böni. Field dependence of nonreciprocal magnons in chiral MnSi. *Physical Review B*, 97(22):224403, 2018. ISSN 2469-9950, 2469-9969. doi: 10.1103/PhysRevB.97.224403. URL https://link.aps.org/doi/10.1103/PhysRevB.97.224403.

[61] K. Schmalzl, W. Schmidt, S. Raymond, H. Feilbach, C. Mounier, B. Vettard, and T. Brückel. The upgrade of the cold neutron three-axis spectrometer IN12 at the ILL. *Nuclear Instruments and Methods in Physics Research Section A: Accelerators, Spectrometers, Detectors and Associated Equipment*, 819:89–98, 2016. ISSN 01689002. doi: 10.1016/j.nima.2016.02.067. URL https://linkinghub.elsevier.com/retrieve/pii/S0168900216002436.

[62] Institut Laue-Langevin. In12 - cold neutron three-axis spectrometer, Accessed: 18.01.2022. URL https://www.ill.eu/users/instruments/instruments-list/in12/description/instrument-layout.

[63] R. Georgii, T. Weber, G. Brandl, M. Skoulatos, M. Janoschek, S. Mühlbauer, C. Pfleiderer, and P. Böni. The multi-purpose three-axis spectrometer (TAS) MIRA at FRM II. *Nuclear Instruments and Methods in Physics Research Section A: Accelerators, Spectrometers, Detectors and Associated Equipment*, 881:60–64, 2018. ISSN 01689002. doi: 10.1016/j.nima.2017.09.063. URL https://linkinghub.elsevier.com/retrieve/pii/S0168900217310331.

[64] Heinz Maier-Leibnitz Zentrum (MLZ). KOeln-Münchner auf Polarisations-Analyse Spezialisiertes Spektrometer, Accessed: 18.01.2022. URL https://mlz-garching.de/kompass/de.

[65] Institut Laue-Langevin. Thermal neutron three-axis spectrometer with polarization analysis in20, Accessed: 18.01.2022. URL https://www.ill.eu/users/instruments/instruments-list/in20/description/instrument-layout.

[66] Tobias Weber, Robert Georgii, and Peter Böni. Takin: An open-source software for experiment planning, visualisation, and data analysis. *SoftwareX*, 5:121–126, 2016. ISSN 23527110. doi: 10.1016/j.softx.2016.06.002. URL https://linkinghub.elsevier.com/retrieve/pii/S2352711016300152.

[67] Tobias Weber. Update 1.5 to "takin: An open-source software for experiment planning, visualisation, and data analysis", (PII: S2352711016300152). *SoftwareX*, 6:148–149, 2017. ISSN 23527110. doi: 10.1016/j.softx.2017.06.002. URL https://linkinghub.elsevier.com/retrieve/pii/S2352711017300183.

[68] M. D. Lumsden, J. L. Robertson, and M. Yethiraj. UB matrix implementation for inelastic neutron scattering experiments. *Journal of Applied Crystallography*, 38(3):405–411, 2005. ISSN 0021-8898. doi: 10.1107/S0021889805004875. URL http://scripts.iucr.org/cgi-bin/paper?S0021889805004875.

[69] F. Mezei. Neutron spin echo: A new concept in polarized thermal neutron techniques. *Zeitschrift für Physik A Hadrons and nuclei*, 255(2):146–160, 1972. ISSN 0939-7922. doi: 10.1007/BF01394523. URL http://link.springer.com/10.1007/BF01394523.

[70] R. Gähler, R. Golub, and T. Keller. Neutron resonance spin echo—a new tool for high resolution spectroscopy. *Physica B: Condensed Matter*, 180-181:899–902, 1992. ISSN 09214526. doi: 10.1016/0921-4526(92)90503-K. URL https://linkinghub.elsevier.com/retrieve/pii/092145269290503K.

[71] R. Golub and R. Gähler. A neutron resonance spin echo spectrometer for quasi-elastic and inelastic scattering. *Physics Letters A*, 123(1):43–48, 1987. ISSN 03759601. doi: 10.1016/0375-9601(87)90760-2. URL https://linkinghub.elsevier.com/retrieve/pii/0375960187907602.

[72] Masahiro Hino. Current status of BL06 beam line for VIN ROSE at j-PARC/MLF. *Physics Procedia*, page 6, 2013. doi: 10.1016/j.phpro.2013.03.187. URL https://doi.org/10.1016/j.phpro.2013.03.187.

[73] C. Franz, O. Soltwedel, C. Fuchs, S. Säubert, F. Haslbeck, A. Wendl, J.K. Jochum, P. Böni, and C. Pfleiderer. The longitudinal neutron resonant spin echo spectrometer RESEDA. *Nuclear Instruments and Methods in Physics Research Section A: Accelerators, Spectrometers, Detectors and Associated Equipment*, 939:22–29, 2019. ISSN 01689002. doi: 10.1016/j.nima.2019.05.056. URL https://linkinghub.elsevier.com/retrieve/pii/S0168900219307120.

[74] C. Pappas, E. Lelièvre-Berna, P. Bentley, E. Bourgeat-Lami, E. Moskvin, M. Thomas, S. Grigoriev, and V. Dyadkin. Polarimetric neutron spin echo: Feasibility and first results. *Nuclear Instruments and Methods in Physics Research Section A: Accelerators, Spectrometers, Detectors and Associated Equipment*, 592(3):420–427, 2008. ISSN 01689002. doi: 10.1016/j.nima.2008.04.078. URL https://linkinghub.elsevier.com/retrieve/pii/S0168900208006517.

[75] Christian Franz, Steffen Säubert, Andreas Wendl, Franz X. Haslbeck, Olaf Soltwedel, Johanna K. Jochum, Leonie Spitz, Jonas Kindervater, Andreas Bauer, Peter Böni, and Christian Pfleiderer. MIEZE neutron spin-echo spectroscopy of strongly correlated electron systems. *Journal of the Physical Society of Japan*, 88 (8):081002, 2019. ISSN 0031-9015, 1347-4073. doi: 10.7566/JPSJ.88.081002. URL https://journals.jps.jp/doi/10.7566/JPSJ.88.081002.

[76] Thomas Krist and Ferenc Mezei. Solid state neutron polarizers and collimators. pages 88–95. Proc. SPIE, 2001. doi: 10.1117/12.

448063. URL http://proceedings.spiedigitallibrary.org/proceeding.aspx?articleid=895068.

[77] A. Stunault, K.H. Andersen, S. Roux, T. Bigault, K. Ben-Saidane, and H.M. Rønnow. New solid state polarizing bender for cold neutrons. *Physica B: Condensed Matter*, 385-386:1152–1154, 2006. ISSN 09214526. doi: 10.1016/j.physb.2006.05.396. URL https://linkinghub.elsevier.com/retrieve/pii/S0921452606012877.

[78] Thomas Keller, Robert Golub, and Roland Gähler. Neutron spin echo—a technique for high-resolution neutron scattering. In *Scattering in microscopic physics and chemical physics*, pages 1264–1286. Elsevier, 2002. ISBN 978-0-12-613760-6. doi: 10.1016/B978-012613760-6/50068-1. URL https://linkinghub.elsevier.com/retrieve/pii/B9780126137606500681.

[79] F. Mezei. Zeeman energy, interference and neutron spin echo: A minimal theory. *Physica B+C*, 151(1):74–81, 1988. ISSN 03784363. doi: 10.1016/0378-4363(88)90148-9. URL https://linkinghub.elsevier.com/retrieve/pii/0378436388901489.

[80] E. Krueger. Acceleration of polarized neutrons by rotating magnetic fields. *Nukleonika*, 25(6):889–894, 1980. ISSN 0029-5922. URL https://inis.iaea.org/search/searchsinglerecord.aspx?recordsFor=SingleRecord&RN=12611684. Place: Poland INIS Reference Number: 12611684.

[81] Maximilian Krautloher, Jonas Kindervater, Thomas Keller, and Wolfgang Häußler. Neutron resonance spin echo with longitudinal DC fields. *Review of Scientific Instruments*, 87(12):125110, 2016. ISSN 0034-6748, 1089-7623. doi: 10.1063/1.4972395. URL http://aip.scitation.org/doi/10.1063/1.4972395.

[82] R. Gähler, R. Golub, K. Habicht, T. Keller, and J. Felber. Space-time description of neutron spin echo spectrometry. *Physica B: Condensed Matter*, 229(1):1–17, 1996. ISSN 09214526. doi: 10.1016/S0921-4526(96)00509-1. URL https://linkinghub.elsevier.com/retrieve/pii/S0921452696005091.

[83] S. Säubert, J. Kindervater, F. Haslbeck, C. Franz, M. Skoulatos, and P. Böni. Dipolar interactions in Fe: A study with the neutron larmor precession technique MIEZE in a longitudinal field configuration. *Physical Review B*, 99(18):184423, 2019. ISSN 2469-9950, 2469-9969. doi: 10.1103/PhysRevB.99.184423. URL https://link.aps.org/doi/10.1103/PhysRevB.99.184423.

[84] Steffen Säubert. Experimental studies of ultraslow magnetisation dynamics, 2018. URL https://mediatum.ub.tum.de/603821?query=S%C3%A4ubert&show_id=1448818&srcnodeid=603821.

[85] P. Bender, J.K. Jochum, M. Wolf, W. Lohstroh, and C. Pfleiderer. Analysis of MIEZE data beyond the neutron spin-echo approximation. to be published.

[86] Christian Franz and Thorsten Schröder. RESEDA: Resonance spin echo spectrometer. *Journal of large-scale research facilities JLSRF*, 1:A14, 2015. ISSN 2364-091X. doi: 10.17815/jlsrf-1-37. URL http://jlsrf.org/index.php/lsf/article/view/37.

[87] Heinz Maier-Leibnitz Zentrum (MLZ). RESEDA - Resonanz-Spin-Echo-Spektrometer, Accessed: 20.01.2022. URL https://mlz-garching.de/reseda/de.

[88] J K Jochum, A Wendl, T Keller, and C Franz. Neutron MIEZE spectroscopy with focal length tuning. *Measurement Science and Technology*, 31(3):035902, 2020. ISSN 0957-0233, 1361-6501. doi: 10.1088/1361-6501/ab5358. URL https://iopscience.iop.org/article/10.1088/1361-6501/ab5358.

[89] G. Brandl, R. Georgii, W. Häußler, S. Mühlbauer, and P. Böni. Large scales–long times: Adding high energy resolution to SANS. *Nuclear Instruments and Methods in Physics Research Section A: Accelerators, Spectrometers, Detectors and Associated Equipment*, 654(1):394–398, 2011. ISSN 01689002. doi: 10.1016/j.nima.2011.07.003. URL https://linkinghub.elsevier.com/retrieve/pii/S0168900211014057.

[90] T. Weber, G. Brandl, R. Georgii, W. Häußler, S. Weichselbaumer, and P. Böni. Monte-Carlo simulations for the optimisation of a TOF-MIEZE instrument. *Nuclear Instruments and Methods in Physics Research Section A: Accelerators, Spectrometers, Detectors and Associated Equipment*, 713:71–75, 2013. ISSN 01689002. doi: 10.1016/j.nima.2013.03.010. URL https://linkinghub.elsevier.com/retrieve/pii/S0168900213002842.

[91] N. Martin. On the resolution of a MIEZE spectrometer. *Nuclear Instruments and Methods in Physics Research Section A: Accelerators, Spectrometers, Detectors and Associated Equipment*, 882:11–16, 2018. ISSN 01689002. doi: 10.1016/j.nima.2017.11.021. URL https://linkinghub.elsevier.com/retrieve/pii/S016890021731207X.

[92] Simon Foner. Vibrating sample magnetometer. *Review of Scientific Instruments*, page 2, 1956. doi: 10.1063/1.1715636. URL https://aip.scitation.org/doi/10.1063/1.1715636.

[93] D. O. Smith. Development of a vibrating-coil magnetometer. *Review of Scientific Instruments*, 27(5):261–268, 1956. ISSN 0034-6748, 1089-7623. doi: 10.1063/1.1715538. URL http://aip.scitation.org/doi/10.1063/1.1715538.

[94] S. Legl, C. Pfleiderer, and K. Krämer. Vibrating coil magnetometer for milli-kelvin temperatures. *Review of Scientific Instruments*, 81(4):043911, 2010. ISSN 0034-6748, 1089-7623. doi: 10.1063/1.3374557. URL http://aip.scitation.org/doi/10.1063/1.3374557.

[95] Felix S A Rucker. Transverse susceptibility of complex magnetic textures, 2018. URL https://mediatum.ub.tum.de/1452722.

[96] M. Bałanda. AC susceptibility studies of phase transitions and magnetic relaxation: Conventional, molecular and low-dimensional magnets. *Acta Physica Polonica A*, 124(6):964–976, 2013. ISSN 0587-4246, 1898-794X. doi: 10.12693/APhysPolA.124.964. URL http://przyrbwn.icm.edu.pl/APP/PDF/124/a124z6p12.pdf.

[97] Quantum Design GmbH. System zur messung physikalischer eigenschaften (ppms), Accessed: 21.01.2022. URL https://qd-europe.com/de/de/produkt/system-zur-messung-physikalischer-eigenschaften-ppms/.

[98] Quantum Design GmbH. Ppms® platform measurement options, Accessed: 22.01.2022. URL https://qd-europe.com/fileadmin/Mediapool/products/magnetometers/pdf/PPMS_Platform_measurement_options.pdf.

[99] H Eugene Stanley. Scaling, universality, and renormalization: Three pillars of modern critical phenomena. *Rev. Mod. Phys.*, 71(2):9, 1999. doi: 10.1103/RevModPhys.71.S358. URL https://journals.aps.org/rmp/abstract/10.1103/RevModPhys.71.S358.

[100] F. Mezei. Role of spin-nonconserving forces in the critical dynamics of fe at the curie point. *Physical Review Letters*, 49(15):1096–1099, 1982. ISSN 0031-9007. doi: 10.1103/PhysRevLett.49.1096. URL https://link.aps.org/doi/10.1103/PhysRevLett.49.1096.

[101] J. Kindervater, S. Säubert, and P. Böni. Dipolar effects on the critical fluctuations in Fe: Investigation by the neutron spin-echo technique MIEZE. *Physical Review B*, 95(1):014429, 2017. ISSN 2469-9950, 2469-9969. doi: 10.1103/PhysRevB.95.014429. URL https://link.aps.org/doi/10.1103/PhysRevB.95.014429.

[102] S. Schorr, P. Vorderwisch, and F. Mezei. Critical dynamics in EuO below the Curie point. *Physica B: Condensed Matter*, 234-236:749–751, 1997. ISSN 09214526. doi: 10.1016/S0921-4526(96)01147-7. URL https://linkinghub.elsevier.com/retrieve/pii/S0921452696011477.

[103] O. W. Dietrich, J. Als-Nielsen, and L. Passell. Neutron scattering from the Heisenberg ferromagnets EuO and EuS. III. Spin dynamics of EuO. *Physical Review B*, 14(11):4923–4945, 1976. ISSN 0556-2805. doi: 10.1103/PhysRevB.14.4923. URL https://link.aps.org/doi/10.1103/PhysRevB.14.4923.

[104] J. Als-Nielsen, O. W. Dietrich, and L. Passell. Neutron scattering from the Heisenberg ferromagnets EuO and EuS. II. Static critical properties. *Physical Review B*, 14(11):4908–4922, 1976. ISSN 0556-2805. doi: 10.1103/PhysRevB.14.4908. URL https://link.aps.org/doi/10.1103/PhysRevB.14.4908.

[105] P. Böni, M. Hennion, and J. L. Martínez. Magnon dispersion of the dipolar ferromagnet EuS near the zone center. *Physical Review B*, 52(14):10142–10149, 1995. ISSN 0163-1829, 1095-3795. doi: 10.1103/PhysRevB.52.10142. URL https://link.aps.org/doi/10.1103/PhysRevB.52.10142.

[106] J. Als-Nielsen, L. M. Holmes, and H. J. Guggenheim. Wave-vector-dependent susceptibility at $T > T_c$ in a dipolar Ising ferromagnet. *Physical Review Letters*, 32(11):610–613, 1974. ISSN 0031-9007. doi: 10.1103/PhysRevLett.32.610. URL https://link.aps.org/doi/10.1103/PhysRevLett.32.610.

[107] P. Böni, H. A. Mook, J. L. Martínez, and G. Shirane. Comparison of the paramagnetic spin fluctuations in nickel with asymptotic renormalization-group theory. *Physical Review B*, 47(6):3171–3179, 1993. ISSN 0163-1829, 1095-3795. doi: 10.1103/PhysRevB.47.3171. URL https://link.aps.org/doi/10.1103/PhysRevB.47.3171.

[108] V. J. Minkiewicz, M. F. Collins, R. Nathans, and G. Shirane. Critical and spin-wave fluctuations in nickel by neutron scattering. *Physical Review*, 182(2): 624–631, 1969. ISSN 0031-899X. doi: 10.1103/PhysRev.182.624. URL https://link.aps.org/doi/10.1103/PhysRev.182.624.

[109] B. I. Halperin and P. C. Hohenberg. Generalization of scaling laws to dynamical properties of a system near its critical point. *Physical Review Letters*, 19(12): 700–703, 1967. ISSN 0031-9007. doi: 10.1103/PhysRevLett.19.700. URL https://link.aps.org/doi/10.1103/PhysRevLett.19.700.

[110] T. Holstein and H. Primakoff. Field dependence of the intrinsic domain magnetization of a ferromagnet. *Physical Review*, 58(12):1098–1113, 1940. ISSN 0031-899X. doi: 10.1103/PhysRev.58.1098. URL https://link.aps.org/doi/10.1103/PhysRev.58.1098.

[111] B. I. Halperin and P. C. Hohenberg. Scaling laws for dynamic critical phenomena. *Physical Review*, 177(2):952–971, 1969. ISSN 0031-899X. doi: 10.1103/PhysRev.177.952. URL https://link.aps.org/doi/10.1103/PhysRev.177.952.

[112] J. C. Le Guillou and J. Zinn-Justin. Critical exponents for the n-vector model in three dimensions from field theory. *Physical Review Letters*, 39(2):95–98, 1977. ISSN 0031-9007. doi: 10.1103/PhysRevLett.39.95. URL https://link.aps.org/doi/10.1103/PhysRevLett.39.95.

[113] A. Brooks Harris. Energy width of spin waves in the Heisenberg ferromagnet. *Physical Review*, 175(2):674–679, 1968. ISSN 0031-899X. doi: 10.1103/PhysRev.175.674. URL https://link.aps.org/doi/10.1103/PhysRev.175.674.

[114] P. Böni, J. L. Martnez, and J. M. Tranquada. Longitudinal spin fluctuations in nickel. *Physical Review B*, 43(1):575–584, 1991. ISSN 0163-1829, 1095-3795. doi: 10.1103/PhysRevB.43.575. URL https://link.aps.org/doi/10.1103/PhysRevB.43.575.

[115] R. Folk and H. Iro. Paramagnetic neutron scattering and renormalization-group theory for isotropic ferromagnets at T_c. *Physical Review B*, 32(3):1880–1882, 1985. ISSN 0163-1829. doi: 10.1103/PhysRevB.32.1880. URL https://link.aps.org/doi/10.1103/PhysRevB.32.1880.

[116] P. Résibois and C. Piette. Temperature dependence of the linewidth in critical spin fluctuation. *Physical Review Letters*, 24(10):514–516, 1970. ISSN 0031-9007. doi: 10.1103/PhysRevLett.24.514. URL https://link.aps.org/doi/10.1103/PhysRevLett.24.514.

[117] P. Böni, D. Görlitz, J. Kötzler, and J. L. Martnez. Dynamics of longitudinal and transverse fluctuations above T_c in EuS. *Physical Review B*, 43(10):8755–8758, 1991. ISSN 0163-1829, 1095-3795. doi: 10.1103/PhysRevB.43.8755. URL https://link.aps.org/doi/10.1103/PhysRevB.43.8755.

[118] F Mezei. Critical dynamics in EuO at the ferromagnetic Curie point. *Physica B*, 136: 3, 1986. doi: 10.1016/S0378-4363(86)80106-1. URL https://www.sciencedirect.com/science/article/pii/S0378436386801061?via%3Dihub.

[119] P. Böni and G. Shirane. Paramagnetic neutron scattering from the Heisenberg ferromagnet EuO. *Physical Review B*, 33(5):3012–3019, 1986. ISSN 0163-1829. doi: 10.1103/PhysRevB.33.3012. URL https://link.aps.org/doi/10.1103/PhysRevB.33.3012.

[120] E Frey and F Schwabl. On the critical dynamics of ferromagnets. *Z. Physik B - Condensed Matter*, 71:14, 1988. doi: 10.1007/BF01312495. URL https://link.springer.com/article/10.1007/BF01312495.

[121] E. Frey and F. Schwabl. Critical dynamics of magnets. *Advances in Physics*, 43 (5):577–683, 1994. ISSN 0001-8732, 1460-6976. doi: 10.1080/00018739400101535. URL http://www.tandfonline.com/doi/abs/10.1080/00018739400101535.

[122] J. Kötzler. Universality of the dipolar dynamic crossover of cubic ferromagnets above T_c. *Physical Review B*, 38(16):12027–12030, 1988. ISSN 0163-1829. doi: 10.1103/PhysRevB.38.12027. URL https://link.aps.org/doi/10.1103/PhysRevB.38.12027.

[123] J. Kötzler. Critical phenomena in dipolar magnets. *Journal of Magnetism and Magnetic Materials*, 54-57:649–654, 1986. ISSN 03048853. doi: 10.1016/0304-8853(86)90197-6. URL https://linkinghub.elsevier.com/retrieve/pii/0304885386901976.

[124] B. Legendre and M. Sghaier. Curie temperature of nickel. *Journal of Thermal Analysis and Calorimetry*, 105(1):141–143, 2011. ISSN 1388-6150, 1572-8943. doi: 10.1007/s10973-011-1448-2. URL http://link.springer.com/10.1007/s10973-011-1448-2.

[125] Alexander Schober, Andreas Wendl, Franz X Haslbeck, Johanna K Jochum, Leonie Spitz, and Christian Franz. The software package MIEZEPY for the reduction of MIEZE data. *Journal of Physics Communications*, 3(10):103001, 2019. ISSN 2399-6528. doi: 10.1088/2399-6528/ab497d. URL https://iopscience.iop.org/article/10.1088/2399-6528/ab497d.

[126] Tobias Unruh. Instrument control at the FRM-II using TACO and NICOS, 2002. URL http://arxiv.org/abs/cond-mat/0210433. Number: arXiv:cond-mat/0210433.

[127] H. Iro. The dynamical correlation function of an isotropic Heisenberg ferromagnet in the critical region. *Journal of Magnetism and Magnetic Materials*, 73(2):175–178, 1988. ISSN 03048853. doi: 10.1016/0304-8853(88)90289-2. URL https://linkinghub.elsevier.com/retrieve/pii/0304885388902892.

[128] T. Strutz. *Data fitting and uncertainty: a practical introduction to weighted least squares and beyond*. Vieweg + Teubner, 1. aufl edition, 2011. ISBN 978-3-8348-1022-9.

[129] I. Antcheva, M. Ballintijn, B. Bellenot, M. Biskup, R. Brun, N. Buncic, Ph. Canal, D. Casadei, O. Couet, V. Fine, L. Franco, G. Ganis, A. Gheata, D. Gonzalez Maline, M. Goto, J. Iwaszkiewicz, A. Kreshuk, D. Marcos Segura, R. Maunder, L. Moneta, A. Naumann, E. Offermann, V. Onuchin, S. Panacek, F. Rademakers, P. Russo, and M. Tadel. ROOT — a c++ framework for petabyte data storage, statistical analysis and visualization. *Computer Physics Communications*, 182 (6):1384–1385, 2011. ISSN 00104655. doi: 10.1016/j.cpc.2011.02.008. URL https://linkinghub.elsevier.com/retrieve/pii/S0010465511000701.

[130] Hans Dembinski and Piti Ongmongkolkul et al. scikit-hep/iminuit. Dec 2020. doi: 10.5281/zenodo.3949207. URL https://doi.org/10.5281/zenodo.3949207.

[131] Boualem Hammouda and David F. R. Mildner. Small-angle neutron scattering resolution with refractive optics. *Journal of Applied Crystallography*, 40(2):250–259, 2007. ISSN 0021-8898. doi: 10.1107/S002188980605638X. URL http://scripts.iucr.org/cgi-bin/paper?S002188980605638X.

[132] Paul T Boggs and Janet E Rogers. Orthogonal distance regression. *Contemporary Mathematics*, page 16, 1990. URL https://docs.scipy.org/doc/external/odr_ams.pdf.

[133] J Crangle. The magnetization of pure iron and nickel. *Proceedings of the Royal Society of London A*, 321:15, 1971. doi: 10.1098/rspa.1971.0044. URL https://royalsocietypublishing.org/doi/epdf/10.1098/rspa.1971.0044.

[134] C. A. Neugebauer. Temperature dependence of the saturation magnetization of nickel films of thickness less than 100a. *Journal of Applied Physics*, 31(5): S152–S153, 1960. ISSN 0021-8979, 1089-7550. doi: 10.1063/1.1984641. URL http://aip.scitation.org/doi/10.1063/1.1984641.

[135] S. J. Pickart, H. A. Alperin, V. J. Minkiewicz, R. Nathans, G. Shirane, and O. Steinsvoll. Spin-wave dispersion in ferromagnetic Ni and fcc Co. *Physical Review*, 156(2):623–626, 1967. ISSN 0031-899X. doi: 10.1103/PhysRev.156.623. URL https://link.aps.org/doi/10.1103/PhysRev.156.623.

[136] M W Stringfellow. Observation of spin-wave renormalization effects in iron and nickel. *Journal of Physics C: Solid State Physics*, 1(4):950–965, 1968. ISSN 00223719. doi: 10.1088/0022-3719/1/4/315. URL https://iopscience.iop.org/article/10.1088/0022-3719/1/4/315.

[137] H. A. Mook, R. M. Nicklow, E. D. Thompson, and M. K. Wilkinson. Spin-wave spectrum of nickel metal. *Journal of Applied Physics*, 40(3):1450–1451, 1969. ISSN 0021-8979, 1089-7550. doi: 10.1063/1.1657713. URL http://aip.scitation.org/doi/10.1063/1.1657713.

[138] H. A. Mook, J. W. Lynn, and R. M. Nicklow. Temperature dependence of the magnetic excitations in nickel. *Physical Review Letters*, 30(12):556–559, 1973. ISSN 0031-9007. doi: 10.1103/PhysRevLett.30.556. URL https://link.aps.org/doi/10.1103/PhysRevLett.30.556.

[139] A. T. Aldred. Temperature dependence of the magnetization of nickel. *Physical Review B*, 11(7):2597–2601, 1975. ISSN 0556-2805. doi: 10.1103/PhysRevB.11.2597. URL https://link.aps.org/doi/10.1103/PhysRevB.11.2597.

[140] N. B. Brookes, D. Betto, K. Cao, Yi Lu, K. Kummer, and F. Giustino. Spin waves in metallic iron and nickel measured by soft X-ray resonant inelastic scattering. *Physical Review B*, 102(6):064412, 2020. ISSN 2469-9950, 2469-9969. doi: 10.1103/PhysRevB.102.064412. URL https://link.aps.org/doi/10.1103/PhysRevB.102.064412.

[141] H. A. Alperin, O. Steinsvoll, R. Nathans, and G. Shirane. Magnon scattering of polarized neutrons by the diffraction method: Measurements on magnetite. *Physical Review*, 154(2):508–514, 1967. ISSN 0031-899X. doi: 10.1103/PhysRev.154.508. URL https://link.aps.org/doi/10.1103/PhysRev.154.508.

[142] C. J. Glinka, V. J. Minkiewicz, and L. Passell. Small-angle critical neutron scattering from cobalt. *Physical Review B*, 16(9):4084–4103, 1977. ISSN 0556-2805. doi: 10.1103/PhysRevB.16.4084. URL https://link.aps.org/doi/10.1103/PhysRevB.16.4084.

[143] G. Parette and R. Kahn. Étude de la diffusion critique des neutrons par le fer dans les régions « hydrodynamique » et « quasi hydrodynamique ». *Journal de Physique*, 32(5):447–459, 1971. ISSN 0302-0738. doi: 10.1051/jphys:01971003205-6044700. URL http://www.edpsciences.org/10.1051/jphys:01971003205-6044700.

[144] M. Kohgi, Y. Endoh, Y. Ishikawa, H. Yoshizawa, and G. Shirane. High-temperature spin dynamics of a cubic ferromagnet Pd_2MnSn. *Physical Review B*, 34(3):1762–1769, 1986. ISSN 0163-1829. doi: 10.1103/PhysRevB.34.1762. URL https://link.aps.org/doi/10.1103/PhysRevB.34.1762.

[145] P. Böni and G. Shirane. Paramagnetic neutron scattering from Ni (invited). *Journal of Applied Physics*, 57(8):3012–3016, 1985. ISSN 0021-8979, 1089-7550. doi: 10.1063/1.335197. URL http://aip.scitation.org/doi/10.1063/1.335197.

[146] V G Vaks and S A Pikin. Spin waves and correlation functions in a ferromagnetic. *Soviet Physics JETP*, 26(3):9, 1968. URL http://www.jetp.ras.ru/cgi-bin/dn/e_026_03_0647.pdf.

[147] J. A. Tarvin, G. Shirane, R. J. Birgeneau, and H. S. Chen. High-temperature spin dynamics in an amorphous ferromagnet. *Physical Review B*, 17(1):241–248, 1978. ISSN 0163-1829. doi: 10.1103/PhysRevB.17.241. URL https://link.aps.org/doi/10.1103/PhysRevB.17.241.

[148] Lars Onsager. Crystal statistics. i. a two-dimensional model with an order-disorder transition. *Physical Review*, 65(3):117–149, 1944. ISSN 0031-899X. doi: 10.1103/PhysRev.65.117. URL https://link.aps.org/doi/10.1103/PhysRev.65.117.

[149] René Plumier. Neutron diffraction study of magnetic stacking faults in antiferromagnetic K_2NiF_4. *Journal of Applied Physics*, 35(3):950–951, 1964. ISSN 0021-8979, 1089-7550. doi: 10.1063/1.1713554. URL http://aip.scitation.org/doi/10.1063/1.1713554.

[150] R. Plumier and E. Legrand. Structure magnétique de K_2NiF_4. *Journal de Physique et le Radium*, 23(8):474–476, 1962. ISSN 0368-3842. doi: 10.1051/jphysrad:01962002308-9047400. URL http://www.edpsciences.org/10.1051/jphysrad:01962002308-9047400.

[151] M.E. Lines. Examples of two dimensional ordered magnetic systems. *Physics Letters A*, 24(11):591–592, 1967. ISSN 03759601. doi: 10.1016/0375-9601(67)90632-9. URL https://linkinghub.elsevier.com/retrieve/pii/0375960167906329.

[152] R. J. Birgeneau, H. J. Guggenheim, and G. Shirane. Neutron scattering from K_2NiF_4: A two-dimensional Heisenberg antiferromagnet. *Physical Review Letters*, 22(14):720–723, 1969. ISSN 0031-9007. doi: 10.1103/PhysRevLett.22.720. URL https://link.aps.org/doi/10.1103/PhysRevLett.22.720.

[153] K.G. Srivastava. A magnetic study of some compounds having the K_2NiF_4 structure. *Physics Letters*, 4(1):55–56, 1963. ISSN 00319163. doi: 10.1016/0031-9163(63)90585-7. URL https://linkinghub.elsevier.com/retrieve/pii/0031916363905857.

[154] J G Bednorz. Possible high - T_c superconductivity in the Ba-La-Cu-O system. *Z. Physik B - Condensed Matter*, 64:5, 1986. doi: 10.1007/BF01303701. URL https://link.springer.com/10.1007/BF01303701.

[155] Shin-ichi Uchida, Hidenori Takagi, Koichi Kitazawa, and Shoji Tanaka. High-T_c superconductivity of La-Ba-Cu oxides. *Japanese Journal of Applied Physics*, 26(1):L1, 1987. ISSN 0021-4922, 1347-4065. doi: 10.1143/JJAP.26.L1. URL https://iopscience.iop.org/article/10.1143/JJAP.26.L1.

[156] Shin-ichi Uchida, Hidenori Takagi, Koichi Kitazawa, and Shoji Tanaka. High - T_c superconductivity of La-Ba-Cu oxides. III - electrical resistivity measurement. *Japanese Journal of Applied Physics*, 26:L151–L152, 1987. ISSN 0021-4922. doi:

10.1143/JJAP.26.L151. URL https://iopscience.iop.org/article/10.1143/JJAP.26.L151.

[157] Hidenori Takagi, Shin-ichi Uchida, Koichi Kitazawa, and Shoji Tanaka. High - T_C superconductivity of La-Ba-Cu oxides. II. -specification of the superconducting phase. *Japanese Journal of Applied Physics*, 26:L123–L124, 1987. ISSN 0021-4922. doi: 10.1143/JJAP.26.L123. URL https://iopscience.iop.org/article/10.1143/JJAP.26.L123.

[158] Bella Lake, D. Alan Tennant, Chris D. Frost, and Stephen E. Nagler. Quantum criticality and universal scaling of a quantum antiferromagnet. *Nature Materials*, 4(4):329–334, 2005. ISSN 1476-1122, 1476-4660. doi: 10.1038/nmat1327. URL http://www.nature.com/articles/nmat1327.

[159] B. Willenberg, H. Ryll, K. Kiefer, D. A. Tennant, F. Groitl, K. Rolfs, P. Manuel, D. Khalyavin, K. C. Rule, A. U. B. Wolter, and S. Süllow. Luttinger liquid behavior in the alternating spin-chain system copper nitrate. *Physical Review B*, 91(6): 060407, 2015. ISSN 1098-0121, 1550-235X. doi: 10.1103/PhysRevB.91.060407. URL https://link.aps.org/doi/10.1103/PhysRevB.91.060407.

[160] Yi Zhou, Kazushi Kanoda, and Tai-Kai Ng. Quantum spin liquid states. *Reviews of Modern Physics*, 89(2):025003, 2017. ISSN 0034-6861, 1539-0756. doi: 10.1103/RevModPhys.89.025003. URL http://link.aps.org/doi/10.1103/RevModPhys.89.025003.

[161] Claudine Lacroix, Philippe Mendels, and Frédéric Mila. Introduction to frustrated magnetism, 2011. URL http://link.springer.com/10.1007/978-3-642-10589-0.

[162] Christopher P. Landee and Mark M. Turnbull. Recent developments in low-dimensional copper(II) molecular magnets. *European Journal of Inorganic Chemistry*, 2013(13):2266–2285, 2013. ISSN 14341948. doi: 10.1002/ejic.201300133. URL https://onlinelibrary.wiley.com/doi/10.1002/ejic.201300133.

[163] Jie Li, Yang Zhu, Pei-Zhi Huang, Da-Wei Fu, Qiang-Qiang Jia, and Hai-Feng Lu. Ferroelasticity in organic–inorganic hybrid perovskites. *Chemistry - A European Journal*, 28(59), 2022. ISSN 0947-6539, 1521-3765. doi: 10.1002/chem.202201005. URL https://onlinelibrary.wiley.com/doi/10.1002/chem.202201005.

[164] L. J. de Jongh. Magnetic properties of layered transition metal compounds, 1990. URL http://link.springer.com/10.1007/978-94-009-1860-3.

[165] Seong-Hun Park and Cheol Eui Lee. Layered copper hydroxide *n*-alkylsulfonate salts: Synthesis, characterization, and magnetic behaviors in relation to the basal spacing. *The Journal of Physical Chemistry B*, 109(3):1118–1124, 2005. ISSN 1520-6106, 1520-5207. doi: 10.1021/jp046902u. URL https://pubs.acs.org/doi/10.1021/jp046902u.

[166] F. Matthew Woodward, Pamela J. Gibson, Geoffrey B. Jameson, Christopher P. Landee, Mark M. Turnbull, and Roger D. Willett. Two-dimensional Heisenberg antiferromagnets: Syntheses, x-ray structures, and magnetic behavior of $[Cu(pz)_2](ClO_4)_2$, $[Cu(pz)_2](BF_4)_2$ and $[Cu(pz)_2(NO_3)]PF_6$. *Inorganic Chemistry*, 46(10):4256–4266, 2007. ISSN 0020-1669, 1520-510X. doi: 10.1021/ic0621392. URL https://pubs.acs.org/doi/10.1021/ic0621392.

[167] M. Skoulatos, M. Månsson, C. Fiolka, K. W. Krämer, J. Schefer, J. S. White, and Ch. Rüegg. Dimensional reduction by pressure in the magnetic framework material $CuF_2(d_2o)_2(pyz)$: From spin-wave to spinon excitations. *Physical Review B*, 96 (2):020414, 2017. ISSN 2469-9950, 2469-9969. doi: 10.1103/PhysRevB.96.020414. URL http://link.aps.org/doi/10.1103/PhysRevB.96.020414.

[168] Fernando Aguado, Fernando Rodríguez, Rafael Valiente, Jean-Paul Itiè, and Michael Hanfland. Pressure effects on jahn-teller distortion in perovskites: The roles of local and bulk compressibilities. *Physical Review B*, 85(10):100101, 2012. ISSN 1098-0121, 1550-235X. doi: 10.1103/PhysRevB.85.100101. URL https://link.aps.org/doi/10.1103/PhysRevB.85.100101.

[169] Tetsuya Matsumoto, Yuji Miyazaki, Andrew S. Albrecht, Christopher P. Landee, Mark M. Turnbull, and Michio Sorai. Heat capacities of the $S = {}^1/_2$ two-dimensional Heisenberg antiferromagnet bis(2-amino-5-chloropyridinium) tetrabromocuprate(II) $[(5CAP)_2CuBr_4]$ and its diamagnetic analogue $[(5CAP)_2ZnBr_4]$. *The Journal of Physical Chemistry B*, 104(43):9993–10000, 2000. ISSN 1520-6106, 1520-5207. doi: 10.1021/jp0020081. URL https://pubs.acs.org/doi/10.1021/jp0020081.

[170] F.M Woodward, C.P Landee, J Giantsidis, M.M Turnbull, and C Richardson. Structure and magnetic properties of $(5BAP)_2CuBr_4$: magneto-structural correlations of layered S=1/2 Heisenberg antiferromagnets. *Inorganica Chimica Acta*, 324(1):324–330, 2001. ISSN 00201693. doi: 10.1016/S0020-1693(01)00671-5. URL https://linkinghub.elsevier.com/retrieve/pii/S0020169301006715.

[171] F. M. Woodward, A. S. Albrecht, C. M. Wynn, C. P. Landee, and M. M. Turnbull. Two-dimensional S = 1/2 Heisenberg antiferromagnets: Synthesis, structure, and magnetic properties. *Physical Review B*, 65(14):144412, 2002. ISSN 0163-1829, 1095-3795. doi: 10.1103/PhysRevB.65.144412. URL https://link.aps.org/doi/10.1103/PhysRevB.65.144412.

[172] Seong-Hun Park, In-Hwan Oh, Sungil Park, Younbong Park, Ji Hyun Kim, and Young-Duk Huh. Canted antiferromagnetism and spin reorientation transition in layered inorganic–organic perovskite $(C_6H_5CH_2CH_2NH_3)_2MnCl_4$. *Dalton Trans.*, 41(4):1237–1242, 2012. ISSN 1477-9226, 1477-9234. doi: 10.1039/C1DT11544H. URL http://xlink.rsc.org/?DOI=C1DT11544H.

[173] Christoph Fiolka, 2022.

[174] P.A. Goddard et al. Csd entry: Uxowek, Accessed: 10.03.2022. URL https://www.ccdc.cam.ac.uk/structures/Search?Ccdcid=683411&DatabaseToSearch=Published.

[175] George A. Baker, G. S. Rushbrooke, and H. E. Gilbert. High-temperature series expansions for the spin-½ Heisenberg model by the method of irreducible representations of the symmetric group. *Physical Review*, 135(5):A1272–A1277, 1964. ISSN 0031-899X. doi: 10.1103/PhysRev.135.A1272. URL https://link.aps.org/doi/10.1103/PhysRev.135.A1272.

[176] G.A. Baker, H.E. Gilbert, J. Eve, and G.S. Rushbrooke. On the Heisenberg spin-½ ferromagnetic models. *Physics Letters*, 20(2):146–147, 1966. ISSN 00319163. doi: 10.1016/0031-9163(66)90911-5. URL https://linkinghub.elsevier.com/retrieve/pii/0031916366909115.

[177] Kei Yosida. On the antiferromagnetism of ($CuCl_2$) $2H_2O$ single crystal. *Progress of Theoretical Physics*, 7(1):14, 1952. doi: 10.1143/ptp/7.1.25. URL https://academic.oup.com/ptp/article/7/1/25/1925352?login=true.

[178] Toru Moriya and Kei Yosida. On the origin of the anisotropy energy of ($CuCl_2$) $2H_2O$. *Progress of Theoretical Physics*, 9(6):13, 1953. doi: 10.1143/ptp/9.6.663. URL https://academic.oup.com/ptp/article/9/6/663/1941203?login=true.

[179] F. Xiao, F. M. Woodward, C. P. Landee, M. M. Turnbull, C. Mielke, N. Harrison, T. Lancaster, S. J. Blundell, P. J. Baker, P. Babkevich, and F. L. Pratt. Two-dimensional x y behavior observed in quasi-two-dimensional quantum Heisenberg antiferromagnets. *Physical Review B*, 79(13):134412, 2009. ISSN 1098-0121, 1550-235X. doi: 10.1103/PhysRevB.79.134412. URL https://link.aps.org/doi/10.1103/PhysRevB.79.134412.

[180] H. P. J. Wijn. Ferromagnetism / ferromagnetismus, 1966. URL http://link.springer.com/10.1007/978-3-642-46035-7.

[181] M. E. Zhitomirsky and T. Nikuni. Magnetization curve of a square-lattice Heisenberg antiferromagnet. *Physical Review B*, 57(9):5013–5016, 1998. ISSN 0163-1829, 1095-3795. doi: 10.1103/PhysRevB.57.5013. URL https://link.aps.org/doi/10.1103/PhysRevB.57.5013.

[182] Anders W. Sandvik. Stochastic series expansion method with operator-loop update. *Physical Review B*, 59(22):R14157–R14160, 1999. ISSN 0163-1829, 1095-3795. doi: 10.1103/PhysRevB.59.R14157. URL https://link.aps.org/doi/10.1103/PhysRevB.59.R14157.

[183] Olav F. Syljuåsen and Anders W. Sandvik. Quantum Monte Carlo with directed loops. *Physical Review E*, 66(4):046701, 2002. ISSN 1063-651X, 1095-3787. doi: 10.1103/PhysRevE.66.046701. URL https://link.aps.org/doi/10.1103/PhysRevE.66.046701.

[184] C Paulsen, J Souletie, and P Rey. Critical scaling in a pure organic ferromagnet. *Journal of Magnetism and Magnetic Materials*, page 3, 2001. doi: 10.1016/S0304-8853(01)00005-1. URL https://www.sciencedirect.com/science/article/abs/pii/S0304885301000051.

[185] Marc Drillon, Pierre Panissod, Pierre Rabu, Jean Souletie, Vadim Ksenofontov, and Philipp Gütlich. Pressure effect on the magnetism of layered copper(II) compounds with interlayer spacing up to 40.7 Å: Nature of the magnetic ordering. *Physical Review B*, 65(10):104404, 2002. ISSN 0163-1829, 1095-3795. doi: 10.1103/PhysRevB.65.104404. URL https://link.aps.org/doi/10.1103/PhysRevB.65.104404.

[186] M. Bałanda, T. Korzeniak, R. Pełka, R. Podgajny, M. Rams, B. Sieklucka, and T. Wasiutyński. AC susceptibility study of the bilayered cyano-bridged CuW and CuMo ferromagnets. *Solid State Sciences*, 7(9):1113–1124, 2005. ISSN 12932558. doi: 10.1016/j.solidstatesciences.2005.04.011. URL https://linkinghub.elsevier.com/retrieve/pii/S1293255805001184.

[187] Maria Bałanda, Robert Pełka, Tadeusz Wasiutyński, Michał Rams, Yasuhiro Nakazawa, Yuji Miyazaki, Michio Sorai, Robert Podgajny, Tomasz Korzeniak, and Barbara Sieklucka. Magnetic ordering in the double-layered molecular magnet Cu(tetren)[W(CN)$_8$]: Single-crystal study. *Physical Review B*, 78(17):174409, 2008. ISSN 1098-0121, 1550-235X. doi: 10.1103/PhysRevB.78.174409. URL https://link.aps.org/doi/10.1103/PhysRevB.78.174409.

[188] A. Jeżowski, Z. Litwicki, V. V. Sumarokov, and P. Stachowiak. Temperature dependence of the magnetic susceptibility of solid oxygen. *Low Temperature Physics*, 32(11):1082–1085, 2006. ISSN 1063-777X, 1090-6517. doi: 10.1063/1.2389017. URL http://aip.scitation.org/doi/10.1063/1.2389017.

[189] E. Kanda, T. Haseda, and A. Ötsubo. Paramagnetic susceptibility of solid oxygen. *Physica*, 20(1):131–132, 1954. ISSN 00318914. doi: 10.1016/S0031-8914(54)80024-3. URL https://linkinghub.elsevier.com/retrieve/pii/S0031891454800243.

[190] Garam Park, In-Hwan Oh, J.M. Sungil Park, Seong-Hun Park, Chang Seop Hong, and Kwang-Sei Lee. Investigation of magnetic phase transition on the layered inorganic-organic hybrid perovskites $(C_6H_5CH_2CH_2NH_3)_2MnCl_4$ by single-crystal neutron diffraction. *Physica B: Condensed Matter*, 551:89–93, 2018. ISSN 09214526. doi: 10.1016/j.physb.2017.11.004. URL https://linkinghub.elsevier.com/retrieve/pii/S0921452617308736.

[191] C. H. Wang, M. D. Lumsden, R. S. Fishman, G. Ehlers, T. Hong, W. Tian, H. Cao, A. Podlesnyak, C. Dunmars, J. A. Schlueter, J. L. Manson, and A. D. Christianson. Magnetic properties of the S = 1/2 quasisquare lattice antiferromagnet $CuF_2(H_2O)_2$(pyz) (pyz=pyrazine) investigated by neutron scattering. *Physical Review B*, 86(6):064439, 2012. ISSN 1098-0121, 1550-235X. doi: 10.1103/PhysRevB.86.064439. URL https://link.aps.org/doi/10.1103/PhysRevB.86.064439.

[192] N. Tsyrulin, F. Xiao, A. Schneidewind, P. Link, H. M. Rønnow, J. Gavilano, C. P. Landee, M. M. Turnbull, and M. Kenzelmann. Two-dimensional square-lattice S = 1/2 antiferromagnet $Cu(pz)_2(ClO_4)_2$. *Physical Review B*, 81(13):134409, 2010. ISSN 1098-0121, 1550-235X. doi: 10.1103/PhysRevB.81.134409. URL https://link.aps.org/doi/10.1103/PhysRevB.81.134409.

[193] Faculty of Physics (TUM). Crystal and material laboratory - sample characterization, Accessed: 30.03.2022. URL https://einrichtungen.ph.tum.de/kristallabor/index-Dateien/Page480.htm.

[194] R. J. Birgeneau, H. J. Guggenheim, and G. Shirane. Neutron scattering investigation of phase transitions and magnetic correlations in the two-dimensional antiferromagnets K_2NiF_4, Rb_2MnF_4, Rb_2FeF_4. *Physical Review B*, 1(5):2211–2230, 1970. ISSN 0556-2805. doi: 10.1103/PhysRevB.1.2211. URL https://link.aps.org/doi/10.1103/PhysRevB.1.2211.

[195] R J Birgeneau, J Skalyo, and G Shirane. Phase transitions and magnetic correlations in two-dimensional antiferromagnets. *Journal of Applied Physics*, 41(3):9, 1970. doi: 10.1063/1.1658917.

[196] J. Skalyo, G. Shirane, R. J. Birgeneau, and H. J. Guggenheim. Magnons at low and high temperatures in the planar antiferromagnet K_2NiF_4. *Physical Review Letters*, 23(24):1394–1397, 1969. ISSN 0031-9007. doi: 10.1103/PhysRevLett.23.1394. URL https://link.aps.org/doi/10.1103/PhysRevLett.23.1394.

[197] R. J. Birgeneau, H. J. Guggenheim, and G. Shirane. Spin waves and magnetic ordering in K_2MnF_4. *Physical Review B*, 8(1):304–311, 1973. ISSN 0556-2805. doi: 10.1103/PhysRevB.8.304. URL https://link.aps.org/doi/10.1103/PhysRevB.8.304.

[198] H. N. Bordallo, L. Chapon, J. L. Manson, J. Hernández-Velasco, D. Ravot, W. M. Reiff, and D. N. Argyriou. S = 1/2 Ising behavior in the two-dimensional molecular magnet $Fe(NCS)_2(pyrazine)_2$. *Physical Review B*, 69(22):224405, 2004. ISSN 1098-0121, 1550-235X. doi: 10.1103/PhysRevB.69.224405. URL https://link.aps.org/doi/10.1103/PhysRevB.69.224405.

[199] J P Hague, E M L Chung, D Visser, G Balakrishnan, E Clementyev, D McK Paul, and M R Lees. Spin wave dispersion and magnons from short range order in tapiolite ($FeTa_2O_6$); a quasi-two-dimensional antiferromagnet. *Journal of Physics: Condensed Matter*, 17(46):7227–7235, 2005. ISSN 0953-8984, 1361-648X. doi: 10.1088/0953-8984/17/46/007. URL https://iopscience.iop.org/article/10.1088/0953-8984/17/46/007.

[200] E M L Chung, M R Lees, G J McIntyre, C Wilkinson, G Balakrishnan, J P Hague, D Visser, and D McK Paul. Magnetic properties of tapiolite ($FeTa_2O_6$); a quasi two-dimensional (2d) antiferromagnet. *Journal of Physics: Condensed Matter*, 16(43):7837–7852, 2004. ISSN 0953-8984, 1361-648X. doi: 10.1088/0953-8984/16/43/023. URL https://iopscience.iop.org/article/10.1088/0953-8984/16/43/023.

[201] M. Skoulatos, J.P. Goff, N. Shannon, E.E. Kaul, C. Geibel, A.P. Murani, M. Enderle, and A.R. Wildes. Spin correlations in the frustrated square lattice $Pb_2VO(PO_4)_2$. *Journal of Magnetism and Magnetic Materials*, 310(2): 1257–1259, 2007. ISSN 03048853. doi: 10.1016/j.jmmm.2006.10.379. URL https://linkinghub.elsevier.com/retrieve/pii/S0304885306015873.

[202] M. Skoulatos, J. P. Goff, C. Geibel, E. E. Kaul, R. Nath, N. Shannon, B. Schmidt, A. P. Murani, P. P. Deen, M. Enderle, and A. R. Wildes. Spin correlations and exchange in square-lattice frustrated ferromagnets. *EPL (Europhysics Letters)*, 88 (5):57005, 2009. ISSN 0295-5075, 1286-4854. doi: 10.1209/0295-5075/88/57005. URL https://iopscience.iop.org/article/10.1209/0295-5075/88/57005.

[203] N. Ashcroft and D. Mermin. *Solid State Physics*. Saunders College Publishing, 1976. ISBN 978-3-486-71301-5.

[204] Jayanta K. Bhattacharjee and Richard A. Ferrell. Dynamic scaling for the isotropic ferromagnet: ε expansion to two-loop order. *Physical Review B*, 24(11):6480–6485, 1981. ISSN 0163-1829. doi: 10.1103/PhysRevB.24.6480. URL https://link.aps.org/doi/10.1103/PhysRevB.24.6480.

[205] H. Iro. The dynamical correlation function for isotropic ferromagnets for $T \geq T_c$. *Zeitschrift für Physik B Condensed Matter*, 68(4):485–492, 1987. ISSN 0722-3277, 1434-6036. doi: 10.1007/BF01471079. URL http://link.springer.com/10.1007/BF01471079.

[206] Hermann Träuble. 11. Magnetisierungskurve und magnetische Hysterese ferromagnetischer Einkristalle. In *Magnetisierungskurve der Ferromagnetika*, page 319. Springer-Verlag Berlin, 1966. doi: 10.1007/978-3-642-87531-1_3. URL https://link.springer.com/chapter/10.1007/978-3-642-87531-1_3.

List of own Publications

1. **L. Beddrich**, J. K. Jochum, C. Franz, S. Säubert, P. Ruiz-Cuevas, P. Böni, *High resolution neutron spin echo studies of the critical dynamics of the dipolar ferromagnet Ni* (in preparation)

2. T. Weber, D. M. Fobes, J. Waizner, P. Steffens, G. S. Tucker, M. Böhm, **L. Beddrich**, C. Franz, H. Gabold, R. Bewley, D. Voneshen, M. Skoulatos, R. Georgii, G. Ehlers, A. Bauer, C. Pfleiderer, P. Böni, M. Janoschek, M. Garst, *Topological magnon band structure of emergent Landau levels in a skyrmion lattice.* Science, 375, 6584, 1025-1030 (2022). doi: 10.1126/science.abe4441

3. A. Eich, M. Hölzle, Y. Su, V. Hutanu, R. Georgii, **L. Beddrich**, A. Grzechnik, *Clamp cells for high pressure neutron scattering at low temperatures and high magnetic fields at Heinz Maier-Leibnitz Zentrum (MLZ).* High Pressure Research, 41, 1, 88-96 (2021). doi: 10.1080/08957959.2020.1841759

4. T. Weber, J. Waizner, G. S. Tucker, **L. Beddrich**, M. Skoulatos, R. Georgii, A. Bauer, C. Pfleiderer, M. Garst, P. Böni, *Non-reciprocal magnons in non-centrosymmetric MnSi*, AIP Advances, 101328 (2018). doi: 10.1063/1.5041036